Controlled nano-patterning using focused electron beam induced deposition

Mahgoub, A.M.I.M.

DOI
10.4233/uuid:9a773783-9771-4537-85d3-341fd00ac376

Publication date
2023

Document Version
Final published version

Citation (APA)
Mahgoub, A. M. I. M. (2023). *Controlled nano-patterning using focused electron beam induced deposition*. [Dissertation (TU Delft), Delft University of Technology]. https://doi.org/10.4233/uuid:9a773783-9771-4537-85d3-341fd00ac376

Controlled nano-patterning using focused electron beam induced deposition

Controlled nano-patterning using focused electron beam induced deposition

Proefschrift

ter verkrijging van de graad van doctor
aan de Technische Universiteit Delft,
op gezag van de Rector Magnificus prof.dr.ir. T.H.J.J. van der Hagen,
voorzitter van het College voor Promoties,
in het openbaar te verdedigen op 7 Juni 2023 om 12:30 uur

door

Aya Mohamed Ibrahim Mohamed MAHGOUB

Master of science in electrical engineering and information technology,
Eidgenössische Technische Hochschule (ETH) Zürich, Zwitserland,
geboren te Caïro, Egypte.

Dit proefschrift is goedgekeurd door de

promotor: dr. C.W. Hagen
promotor: prof. dr. ir. P. Kruit

Samenstelling promotiecommissie:

Rector Magnificus,	voorzitter
Dr. C.W. Hagen,	Technische Universiteit Delft, promotor
Prof. dr. ir. P. Kruit,	Technische Universiteit Delft, promotor

Onafhankelijke leden:

Dr. W.J. van der Zande	ARCNL
Prof. dr. B. Rieger	Technische Universiteit Delft
Prof. dr. U. Staufer	Technische Universiteit Delft
Prof. dr. J. Aarts	Universiteit Leiden

Overige leden:

Prof. dr. O. Ingólfsson	University of Iceland

TU Delft Delft University of Technology

ELECTRON DRIVEN CHEMISTRY FOR THE ADVANTAGE OF EMERGING NANO-FABRICATION METHODS

This project has received funding from the European Union's Horizon 2020 research and innovation programme under the Marie Skłodowska-Curie grant agreement No 722149.

The work in this dissertation was conducted at the Microscopy Instrumentation & Techniques group in the department of Imaging Physics, Faculty of Applied Sciences, Delft University of Technology.

Printed by: Ridderprint | www.ridderprint.nl

Cover design: Rana Nasser & Begad Alomrany

ISBN 978-94-6366-685-5

An electronic version of this dissertation is available at
http://repository.tudelft.nl/.

Contents

Summary

Focused electron beam induced processing (FEBIP) comprising FEBID (deposition) and FEBIE (etching) is a direct write or etch, single step technique for high resolution nano-patterning. The whole process takes place inside a single tool, the scanning electron microscope (SEM). A focused electron beam hits the sample in the presence of a precursor gas which contains the element to be deposited. The precursor molecules adsorb to the surface of the substrate. The adsorbed precursor molecules are dissociated with a certain probability (given by the dissociation cross section) by the primary, secondary and back scattered electrons into a deposited fragment and volatile byproducts. FEBID provides great potential for 3D nano-printing due to its flexibility and the absence of resists and subsequent processing steps.

The work described in this thesis was part of a Marie Skłodowska-Curie Training Network on 'Low energy ELEctron driven chemistry for the advantage of emerging NAno-fabrication methods' (ELENA). In particular, three challenges to the FEBID process were addressed to achieve control over the process for nanofabrication, i) the purity of the deposits, ii) the speed of the process and iii) control over the 3D-shape of deposits.

The purity of the deposits is a challenge because most precursors used for FEBID contain carbon atoms resulting in a high percentage of carbon in the deposit. This drives the need, on the one hand, for more research and synthesis of novel precursors that result in a higher metal content in the deposit, and on the other hand for strategies to remove the carbon from the deposits. Two novel platinum precursors were synthesized, by our ELENA partner at the university of Florida, $PtCl_2(CO)_2$ and $PtBr_2(CO)_2$. Both precursors were successful in deposition. $PtCl_2(CO)_2$ showed an improvement in the growth rate (under specific conditions) and composition compared to the widely used $MeCpPtMe_3$ while $PtBr_2(CO)_2$ behaved the worst in terms of growth rate and composition.

Seven novel Au(I) N-heterocyclic carbene (NHC) precursors ((Cl,Me)AuCl, (Cl,Et)AuCl, (Cl,iPr)AuCl, (Cl,Et)AuBr, (Cl,Et)AuI, (N,Et)AuCl and (Cl,Et)$AuCF_3$) were synthesized by our ELENA partner at the university of Oslo, and tested and characterized in an SEM. A special reservoir-on-substrate setup was implemented to heat the precursor and substrate together. The highest gold content was achieved by (N,Et)AuCl precursor (15 at% Au). The highest growth rate was achieved by (Cl,Et)$AuCF_3$. From the characterization of the deposits formed from this series of precursors, we learned that the methyl group in the precursor molecule resulted in a higher Au content compared to isopropyl or ethyl groups. On the other hand, the isopropyl group led to a higher growth rate. On the backbone of the precursor

molecule, N resulted in a higher Au content compared to Cl. Regarding the ancillary ligand, CF_3 and Cl behaved best compared to Br and I in terms of Au content in the deposit, but CF_3 was even better in terms of growth rate. This study serves as a guide for future choices of best performing ligands in the synthesis of novel precursors. The first choice would be to try (N,Me)AuCF_3 and maybe(N,iPr)AuCF_3 and (N,Me)AuCl as well.

To get rid of carbon contamination the use of water vapor during deposition is a very attractive option. Unfortunately, the maximum allowable pressure in a HV SEM remains a limitation to the maximum amount of water vapor that can be used in the SEM chamber. However, the Phenom XL desktop SEM from Thermo Fisher Scientific operates at a much higher pressure, enabling the use of more water in the specimen chamber. The Phenom XL system was modified such that water vapor could be fed into the specimen chamber at pressures up to about 1 mbar. It was demonstrated that water assisted electron beam exposure led to local removal of carbon contamination from the specimen. Further research is still needed to test the effectiveness of using the water vapor to purify FEBID deposits.

The second challenge is the deposition speed. Since FEBID is a serial process and deposition occurs point by point, the process is inherently slow compared to resist-based lithography where light exposure through a mask exposes a whole wafer at once. But the process is also limited by the precursor flux which is limited by the pressure limit of the SEM chamber. To partly lift this pressure restriction, a desktop SEM (Phenom XL G2) was used to increase the precursor flux by increasing the temperature of the precursor reservoir. The Phenom XL G2 system was not designed for performing FEBID, lacking ports that can be used for a GIS and patterning software. Therefore, the instrumentation needed to perform FEBID inside the desktop SEM was developed. The generic sample holder was equipped with a small GIS (Kleindiek Nanotechnik) and filled with the $MeCpPtMe_3$ precursor. All the required electrical connections were designed and implemented. The Phenom programming interface (PPI), which is the interface used to control the Phenom system through python scripts, was used and a script was developed for patterning. FEBID was successfully performed at precursor temperatures between 40 and 90°C. As expected, the growth rate increased as the precursor temperature, and thus flux, increased. The results were compared to deposits performed in a HV SEM under similar conditions and the growth rate in the Phenom system was found to increase more rapidly with the precursor temperature than in the HV SEM (0.065 vs 0.016 $\mu m^3/(min.K)$). On the other hand, the Pt content was slightly lower in the deposits made in the Phenom compared to the HV SEM deposits.

The third challenge concerns shape control, required to use FEBID for building high resolution complex 3D structures. A simple method was developed for building 3-dimensional closed-wall shapes, in particular truncated hollow cones. It is very similar to 3D printing, basically arranging tiny building blocks such that the designed shape is obtained. Unlike other 3D fabrication methods using FEBID presented in literature, the method (FDTM) employs a

fixed dwell time, to deposit each building block, throughout the entire process to grow a cone. Once the in-plane pitch and the out-of-plane pitch have been set, the only parameter that changes throughout the deposition of a cone is the number of building blocks per layer, decreasing from bottom to top as the cone radius decreases. Two different approaches were followed, one aimed at utilizing proximity effects to enhance the growth, using large separate building blocks, and the other aimed at achieving smooth walls and higher resolution structures, using very small closely packed building blocks. A parameter study is presented leading to specific choices of the deposition parameters. Cones were successfully deposited matching the design parameters. A small irregularity was observed at the top of most of the deposited cones. It was found that changing the starting point of deposition in every layer by 180 degrees (referred to as π shift) improves the shape and leads to a more uniform top. So, the deposition strategy matters. Even very small cones were built successfully using FDTM. The smallest deposited cone was only 100 nm high. FDTM was also successfully used to fabricate other closed-wall shapes such as cylinders and boxes.

The particular choice to fabricate truncated hollow cones originated from the need for such cones in a novel electron impact ion source, called the Nano aperture ion source (NAIS). In this source ions are generated by a focused electron beam ionizing a gas in between two thin membranes. The application requires double cones to be built concentrically, one on each membrane of the NAIS chip. The fabrication of the NAIS chip is described and the procedure for building the double cones is presented. Before the cones were built, two holes, one on each membrane, were milled using a focused ion beam (FIB). One hole serves to let the electron beam pass through from one side and ionize the gas atoms and the other hole serves to extract the ions out. Preliminary test results of the NAIS chip with cones in the prototype ion beam test setup are shown, with an ion beam of 200 pA successfully generated. Unfortunately, the cones deformed under continued electron exposure. This work is still in progress and cones of better shape integrity are needed before source brightness measurements can be performed.

To compare FDTM to other 3D-fabrication methods using FEBID, truncated hollow cones were also fabricated with two simulation-guided tools: CAD 3BID, developed for open mesh-like shapes at Oak Ridge National Lab, and the layer-by-layer approach developed at the University of Glasgow. All three methods were successful in depositing a cone shape, but none met the design dimensions right away. With FDTM, small fine tuning of some parameters was needed to match the required dimensions. For both simulation-guided tools, some input had to be provided based on previous knowledge developed in this work. It was expected that, by using the simulation-guided tools after having performed the required calibrations, the deposited shape would match the design, however, this was not the case. The cone deposited using the layer-by-layer approach was successful and close to the designed dimensions. The cone produced by CAD 3BID had a very irregular top and did not meet the required dimensions. As CAD 3BID is meant for open mesh-type structures

it will probably be hard to optimize for closed wall shapes.

The thesis ends with the conclusions and an outlook on the FEBID process in general and its use in 3D nano-printing in particular.

Samenvatting

Gefocusseerde elektronenbundel-geïnduceerde verwerking (FEBIP) bestaande uit FEBID (depositie) en FEBIE (etsen) is een eenstapstechniek voor het direct deponeren of etsen van hoge resolutie nanopatronen. Het hele proces vindt plaats in een enkel instrument, de scanning elektronenmicroscoop (SEM). Een elektronen bundel wordt gefocusseerd op het monster in de aanwezigheid van een precursorgas dat het te deponeren element bevat. De precursormoleculen adsorberen aan het oppervlak van het monster. De geadsorbeerde precursormoleculen worden gedissocieerd met een bepaalde waarschijnlijkheid (gegeven door de dissociatie-waarschijnlijkheid) door de primaire, secundaire en terugverstrooide elektronen resulterend in een neergeslagen fragment en vluchtige bijproducten. FEBID heeft potentie voor 3D-nanoprinten vanwege de flexibiliteit en de afwezigheid van het gebruik van resists en de daarbij benodigde processen.

Het werk beschreven in dit proefschrift maakte deel uit van een Marie Skłodowska-Curie Trainingsnetwerk over 'Low energy ELectron driven chemistry for the benefit of emerging NAno-fabrication methods' (ELENA). In het bijzonder worden drie uitdagingen behandeld om controle te krijgen over het FEBID-proces voor nanofabricage, i) de zuiverheid van de deposieten, ii) de snelheid van het proces en iii) controle over de 3D-vorm van deposieten. De zuiverheid van de deposieten is een uitdaging omdat de precursors die meestal worden gebruikt voor FEBID koolstofatomen bevatten, hetgeen resulteert in een hoog percentage koolstof in het deposiet. Dit stimuleert enerzijds meer onderzoek aan, en de synthese van, nieuwe precursors resulterend in een hoger metaalgehalte, en anderzijds de ontwikkeling van strategieën om de koolstof uit de deposieten te verwijderen. Onze ELENA partner aan de universiteit van Florida heeft twee nieuwe platinaprecursors gesynthetiseerd, $PtCl_2(CO)_2$ en $PtBr_2(CO)_2$. Beide precursors waren succesvol voor FEBID. $PtCl_2(CO)_2$ presteerde beter qua groeisnelheid (onder specifieke omstandigheden) en samenstelling, vergeleken met de veelgebruikte $MeCpPtMe_3$ precursor, terwijl $PtBr_2(CO)_2$ minder goed presteerde wat groeisnelheid en samenstelling betreft. Zeven nieuwe Au(I) N-heterocyclische carbeen (NHC) precursors ((Cl,Me)AuCl, (Cl,Et)AuCl, (Cl,iPr)AuCl, (Cl,Et)AuBr, (Cl,Et)AuI, (N,Et)AuCl en (Cl,Et)$AuCF_3$) werden gesynthetiseerd door onze ELENA-partner aan de universiteit van Oslo, en getest en gekarakteriseerd in een SEM. Er werd een speciale reservoir-op-substraat opstelling geïmplementeerd om de precursor en het substraat samen te verwarmen. Het hoogste goudgehalte werd bereikt met de (N,Et)AuCl-precursor (15 at% Au). De hoogste groeisnelheid werd behaald met (Cl,Et)$AuCF_3$. Uit de karakterisering van de deposieten, gevormd uit deze reeks precursors, leerden we dat het Au-gehalte

van de deposieten hoger is voor precursormoleculen met een methylgroep dan met isopropyl- of ethylgroepen. Daarentegen zorgde de isopropylgroep voor een hogere groeisnelheid. En de aanwezigheid van stikstof (N) in de ruggengraat van het precursormolecuul resulteerde in een hoger Au-gehalte dan de aanwezigheid van chloor (Cl). Wat betreft het hulp-ligand presteerden CF_3 en Cl beter dan Br en I, qua Au-gehalte in het deposiet, maar CF_3 presteerde het best in termen van groeisnelheid. Deze studie dient als leidraad voor toekomstige keuzes van de best presterende liganden bij de synthese van nieuwe precursors. De eerste keuze zou zijn om (N,Me)$AuCF_3$ te proberen en daarna misschien (N,iPr)$AuCF_3$ en (N,Me)AuCl.

Om de koolstofverontreiniging te verwijderen is het gebruik van waterdamp tijdens de depositie een zeer aantrekkelijke optie. Helaas is de maximaal toegestane druk in een HV SEM een beperking voor de maximale hoeveelheid waterdamp die in de SEM-kamer kan worden gebruikt. Echter, de Phenom XL desktop SEM van Thermo Fisher Scientific werkt bij veel hogere drukken, waardoor er meer water in de monsterkamer kan worden gebruikt. Het Phenom XL-systeem werd zodanig aangepast dat er waterdamp in de monsterkamer kon worden gevoerd tot een druk van ongeveer 1 mbar. Er is aangetoond dat bestraling met elektronen in de aanwezigheid van waterdamp leidt tot lokale verwijdering van koolstof uit het monster. Verder onderzoek is nog nodig om de effectiviteit te testen van het gebruik van waterdamp voor het zuiveren van FEBID-deposieten.

De tweede uitdaging is de depositiesnelheid. Aangezien FEBID een serieel proces is en depositie puntsgewijs plaatsvindt, is het proces inherent traag vergeleken met op resist gebaseerde lithografie, waarbij een groot oppervlak van het monster in één keer wordt belicht met behulp van een masker. Maar het proces wordt ook beperkt door de precursorflux die gelimiteerd is door de druklimiet van de SEM-kamer. Om deze drukbeperking gedeeltelijk op te heffen, is een desktop SEM (Phenom XL G2) gebruikt om de precursorflux te kunnen verhogen door middel van de temperatuur van het precursor reservoir. Het Phenom XL G2-systeem is niet ontworpen voor het uitvoeren van FEBID, omdat er geen poorten zijn die gebruikt kunnen worden voor een gas injectiesysteem (GIS) en er geen patronering-software op beschikbaar is. De benodigde instrumentatie om FEBID in de desktop SEM te kunnen doen is daarom ontwikkeld. De generieke monsterhouder werd uitgerust met een kleine GIS (Kleindiek Nanotechnik) en gevuld met de $MeCpPtMe_3$ precursor. Alle benodigde elektrische aansluitingen werden ontworpen en uitgevoerd. Het Phenom-programmeerinterface (PPI), om het Phenom-systeem te besturen via python-scripts, werd gebruikt om een script te maken voor patronering. FEBID is met succes uitgevoerd bij precursortemperaturen tussen 40 en 90 ^{o}C. Volgens verwachting nam de groei snelheid toe naarmate de temperatuur van de precursor, en dus de flux, toenam. De resultaten zijn vergeleken met depositie uitgevoerd in een HV SEM onder vergelijkbare omstandigheden en de groeisnelheid in het Phenom-systeem bleek sneller toe te nemen met de precursortemperatuur dan in de HV SEM (0,065 vs 0,016 $\mu m^3/(min.K)$). Daarentegen was het Pt-gehalte van de Phenom deposieten iets lager dan dat van

de HV SEM-deposieten.

De derde uitdaging betreft controleerbaarheid van de 3D-vorm van deposieten, nodig om FEBID te gebruiken voor het maken van complexe 3D-structuren met hoge resolutie. Met name voor het bouwen van 3-dimensionale gesloten wand strukturen, en in het bijzonder afgeknotte holle kegels. Het lijkt erg op 3D-printen, en is in feite het in volgorde plaatsen van kleine bouwstenen zodat de ontworpen vorm wordt verkregen. In tegenstelling tot andere in de literatuur gepresenteerde 3D-fabricagemethoden die gebruik maken van FEBID, maakt de hier gebruikte methode (FDTM) gebruik van een vaste verblijftijd, voor de depositie van een enkele bouwsteen, gedurende het hele proces van het groeien van een kegel. Zodra de afstand tussen de bouwstenen in het horizontale vlak en het verticale vlak zijn ingesteld, is de enige parameter die verandert tijdens de depositie van een kegel het aantal bouwstenen per laag, afnemend van onder naar boven, alwaar de straal van de kegel afneemt. Er zijn twee verschillende strategien onderzocht, één gericht op het benutten van nabijheidseffecten om een hogere groeisnelheid te krijgen, gebruikmakend van grote losse bouwstenen, en de ander gericht op het bereiken van gladde oppervlakken en hoge-resolutie structuren, gebruikmakend van zeer kleine, dicht opeengepakte, bouwstenen. Een parameterstudie wordt gepresenteerd die leidt tot specifieke keuzes van de depositieparameters. Kegels werden met succes gedeponeerd in overeenstemming met de ontwerp parameters. Er werd vaak een kleine onregelmatigheid geconstateerd aan de top van de gedeponeerde kegels. Het bleek dat het veranderen van het beginpunt van de depositie in elke laag met 180 graden (aangeduid als π shift) de vorm verbetert en leidt tot een meer uniforme top. De depositie strategie is dus van belang. Zelfs zeer kleine kegels werden met succes gebouwd, gebruikmakend van FDTM. De kleinste kegel was slechts 100 nm hoog. FDTM is ook met succes gebruikt om andere vormen met een gesloten wand te vervaardigen, zoals cilinders en rechthoekige dozen.

De bijzondere keuze om afgeknotte holle kegels te fabriceren is ontstaan uit de behoefte aan dergelijke kegels in een nieuwe elektronenimpact-ionenbron, genaamd de 'Nano Aperture Ion Source' (NAIS). In deze bron worden ionen gegenereerd door een gefocusseerde elektronenbundel die een gas tussen twee dunne membranen ioniseert. De toepassing vereist dat twee concentrische kegels worden gemaakt, één op elk membraan van de NAIS-chip. De fabricage van de NAIS-chip wordt beschreven en de procedure voor het bouwen van de dubbele kegels wordt gepresenteerd. Voordat de kegels werden gemaakt, werden twee gaten, één in elk membraan, gemaakt met behulp van een gefocusseerde ionenbundel (FIB). Eén gat dient om de elektronenbundel door te laten, teneinde de gasatomen te ioniseren, en het andere gat dient om de ionen eruit te halen. Voorlopige testresultaten, verkregen met de NAIS-chip met dubbele kegels in een prototype ionenbundelopstelling, worden getoond, met als resultaat een ionenbundel van 200 pA. Helaas bleek dat de kegels vervormen onder voortdurende blootstelling aan elektronen. Dit werk wordt nog voortgezet omdat kegels van betere vormvastheid nodig zijn voordat metingen van de bronhelderheid kunnen worden uitgevoerd.

Om FDTM te vergelijken met andere 3D-fabricagemethoden die gebruik maken van FEBID, werden ook afgeknotte holle kegels vervaardigd met twee simulatiegestuurde tools: CAD 3BID, ontwikkeld voor open mesh-achtige vormen bij Oak Ridge National Lab, en de laag-voor-laag-benadering ontwikkeld aan de Universiteit van Glasgow. Alle drie de methoden waren succesvol in het deponeren van een kegelvorm, maar geen enkele voldeed meteen aan de ontwerpafmetingen. Met FDTM, fijn afstemming van enkele parameters was nodig om aan de vereiste afmetingen te voldoen. Voor de beide simulatiegestuurde tools was input nodig gebaseerd op eerdere kennis ontwikkeld in dit werk. De verwachting was dat door het gebruik van de simulatiegestuurde tools, na het uitvoeren van de vereiste kalibraties, de gedeponeerde vorm zou overeenkomen met het ontwerp, maar dit was niet het geval. De kegel die met behulp van de laag-voor-laag-benadering werd gemaakt, was succesvol en voldeed ruwweg aan de ontwerp afmetingen. De kegel geproduceerd door CAD 3BID had een zeer onregelmatige bovenkant en voldeed niet aan de vereiste afmetingen. Aangezien CAD 3BID is bedoeld voor open mesh-achtige structuren, zal het waarschijnlijk moeilijk te optimaliseren zijn voor gesloten wand vormen. Het proefschrift eindigt met de conclusies en een vooruitblik op het FEBID-proces in het algemeen en het gebruik ervan bij 3D-nanoprinten in het bijzonder.

1

Introduction

1

The main drive for the development of nano-patterning techniques is the semiconductor and integrated circuits (IC) industry. One of the main components in an IC is the transistor and the smaller and more compact the transistors are, the larger the density of the components on the IC can be. An IC can include millions of transistors, therefore a small decrease in size of a transistor drastically increases the packing density and the performance of the IC. It all started in 1965 with Moore's law. Gordon Moore predicted a doubling of the number of components per IC every year [1]. This was not just a simple prediction, but rather led Intel to become one of the world's largest manufacturers of semiconductor chips and microprocessors. This rather economic law remained valid until now and became a motivation for semiconductor industries to push the resolution limits. There is no guarantee of course that this law will continue forever, but it certainly was a motivation and drive for many developments in nanofabrication techniques.

Photolithography, with all its varieties, is the main patterning technology used for the fabrication of devices. In simple words, lithography is a process to define a specific pattern on a chip. It is used to build the layers that define the architecture of the device. After the desired material for a layer is deposited on the chip, a layer of a photosensitive material is coated on top of it [2]. Then a mask is used with the desired pattern and the chip is exposed to UV light [2]. Depending on the type of resist, after its development, either the desired pattern remains or is etched away from the resist. Etching can be performed afterwards through the areas that are unprotected by the resist. The resist is then removed and the process can be repeated to build several layers of the device. Many processes can be involved depending on the design such as atomic layer deposition (ALD) [3], chemical or physical vapor deposition (CVD, PVD), sputtering and lift off [4]. There are several types of etching as well, depending on the required shape, such as wet etching, dry etching and reactive ion etching (RIE) [4].

There are different types of lithography, the most common types are extreme UV lithography (EUVL), e-beam lithography (EBL), and nanoimprint lithography (NIL). The oldest types are proximity and contact followed by projection lithography. In contact or proximity lithography the mask is either in contact or in close proximity of the resist. Mechanical problems occurred in the case of contact and proximity lithography which led to the development of projection lithography in the 1980s [4]. The resolution went from 0.25 and 2 µm in the case of contact and proximity lithography to about 80 nm in projection lithography [4].

The resolution was diffraction limited, therefore lowering the wavelength of the UV light used was one way towards improving the resolution, following the famous Rayleigh formula. In the 1980s, mercury vapor lamps were used with the 'i-line' wavelength of 365 nm [4–6]. In the late 1990s, the source was replaced by KrF lasers with a wavelength of 248 nm, entering the deep UV range [5, 6]. Shortly after, in the early 2000s, the wavelength was reduced to 193 nm by using ArF excimer lasers [4–6]. Then, immersion lithography was introduced and the wavelength decreased further to 157 nm with the F2

laser [6]. The latest transition went into the 'extreme UV' with a wavelength of 13.5 nm in 2010 [5, 6]. EUV lithography tools are now being developed by ASML. The systems are extremely complex and have to operate in vacuum since EUV is easily absorbed by air [5]. Although the resolution of EUV lithography is getting better than 10 nm, there are still challenges involving line edge roughness, sensitivity of the resist and defects [7, 8]. There is a lot of research about new resist materials which could help in finding solutions for these issues. Another widely used type of lithography is EBL. The substrate is first covered with an electron-sensitive resist. Without a physical mask, the electron beam is programmed to scan the substrate in the specified positions that determine the pattern. As opposed to EUVL, EBL is a sequential process where the beam moves and scans the required locations, point by point [4]. EBL is therefore much slower than optical lithography. To achieve the highest resolution, there is a limit on the field of view that can be exposed by deflecting the beam. Exceeding this area, the sample has to be moved. Additionally, due to the scattering of the electrons, proximity effect corrections are required in EBL [4]. EBL achieves a sub-10 nm resolution [9].

NIL is another parallel patterning lithography technique where a stamp with the required pattern is pressed against a wafer coated with a NIL resist [10]. NIL achieves 3D structures with sub-10 nm resolution [10]. The stamps need to be manufactured first, which can be done using EBL [10].

In all these lithography processes, several steps of using a resist, exposing it, transferring the pattern, development of the resist, etching, removing the resist, maybe lift off and other steps are required. For large scale industrial production, EUVL or NIL are more suitable due to the high throughput. Some applications, however, may require a specific, small and local structure either alone or complementary to large scale industrial patterning. In this case, it becomes very time and resource consuming to carry out all these steps for a small local pattern. Furthermore, in the case of any small damage or defect that happens to the very expensive masks of EUVL for example, it would be a huge waste to have to get rid of the mask. This drives the demand for methods to directly and locally pattern in a controlled manner without the need of using resist and the multiple steps related to transferring a pattern.

Focused electron beam induced processing (FEBIP) is a direct write/etch nano-patterning technique which includes deposition (FEBID) and etching (FEBIE). FEBIP can all be performed inside one tool, usually a scanning electron microscope (SEM). FEBID is a single step process, where a focused electron beam hits the sample at a specified position in the presence of a precursor gas which contains the element to be deposited. The precursor molecules adsorb to the surface of the substrate. The primary, secondary and back scattered electrons, generated by the scattered primary beam, all can contribute to the dissociation of the precursor molecule into a fragment that is deposited and some volatile byproducts that are pumped away. The process is illustrated in Figure 1.1. The dissociation may take place either through dissociative electron attachment (DEA), dissociative ionization (DI) or neutral dissociation (ND) [11, 12]. In the case of FEBIE, the non-volatile fragment

reacts with the substrate to form volatile byproducts leading to etching at the positions exposed to the beam in the presence of the precursor [13]. The main advantage of FEBIP is the direct write of nanostructures at specified locations in one process step, inside the SEM. With FEBID sub-10 nm resolution in SEM was achieved and even 1 nm structures were deposited on thin membranes [14].

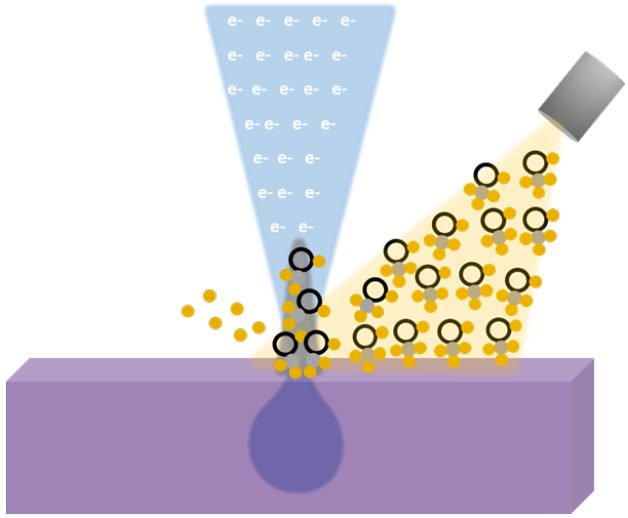

Figure 1.1: Illustration of the FEBID process. The electron beam hits the sample in the presence of the adsorbed layer of precursor molecules. The precursor molecules are dissociated into a fragment that forms the deposit and some volatile byproducts.

There are many parameters that affect the FEBID process. There are beam, precursor gas and patterning parameters. The beam parameters include: beam energy, current, focus, stigmation and operation in either immersion or field free mode [15]. The gas parameters include the precursor temperature, the local gas pressure, the geometry of the gas injection system (GIS), the distance between the nozzle (the end part of the GIS needle from which the gas exits) and the sample, the surface diffusion and the dissociation cross section. The patterning parameters include the spacing between the exposure points (pixels), the order of deposition, dwell time, the writing strategy, the choice of continuous exposure versus interlacing or intermittent exposure and the resolution (how many pixels correspond to 1 nm, as is adjusted through the magnification). These parameters affect the growth regime. If the precursor flux is abundant and the limiting factor is the electron flux, the growth is in the current/electron/reaction rate limited regime. If the growth is limited by the amount of precursor, meaning that if the current increases there will be no further growth since the precursor is depleted, the growth is in the precursor/gas/mass transport limited regime. A third, intermediate, regime is the diffusion enhanced regime.

FEBID is commonly used in photolithography mask repair [16] and to build AFM tips [17, 18]. It was also used to fabricate stamps for NIL [19] and different types of sensors such as strain sensors [20], gas and dielectric sensors [21] and magnetic sensors [22]. In addition to that, FEBID was used in biomedical applications such as the fabrication of nano-patterns to kill bacteria on bone implants [23]. Despite the flexibility and versatility provided by FEBIP, several challenges remain on the way towards developing it to a mature patterning or lithography technique. The composition of the deposit usually includes undesired ligands from the precursor molecule. This leads to low purity of the deposits. Moreover, the process speed is significantly lower than in common lithography techniques since it is a serial point by point deposition process similar to EBL. The speed is limited by the incoming precursor flux which is limited by the maximum allowable pressure in the SEM. There have been some studies on carrying out FEBID in a multibeam SEM to speed up the deposition process [24]. Full and accurate shape control is not yet reached which limits the exploitation of the great 3D capabilities of FEBID. This work contributes in addressing these challenges aiming towards developing FEBID into a reliable and stable lithography technique. Chapters 2 and 3 and part of chapter 4 address the purity problem. The rest of chapter 4 addresses the deposition speed problem. Chapters 5, 6 and 7 discuss procedures to use FEBID in building 3D shapes. We will now briefly introduce the content of these chapters.

The precursor chemistry usually limits the metal content in the deposits. Most FEBID precursors are originally designed for CVD and ALD [13, 25, 26]. Due to the high operating temperature in the CVD and ALD processes, the unwanted ligands dissociate thermally yielding pure metal deposition. However, this is not the case in the FEBID process which results in the co-deposition of impurities. Most of these precursors are organometallic and contain several carbon atoms, some of which usually stay in the deposit. Other precursors that have fewer carbon atoms might have a low volatility and require heating to high temperatures to reach the vapor phase. Therefore, there is a need to investigate and synthesize novel and better precursors. The desired properties include stability, insensitivity to air and humidity, volatility and reaching the vapor phase at a temperature that is possible to achieve in the SEM, safe to handle and safe to use in the SEM [26]. This work was part of a Marie-Curie collaborative project (ELENA) in which the involved partners synthesized novel precursors. Our partners synthesized novel Pt and Au precursors, to be tested as FEBID precursors. The whole testing procedure, which included the method of loading and inserting the precursors in the SEM, finding the temperature required to reach the vapor phase and achieve a suitable vapor pressure for deposition, deposition and growth rate determination and characterization of deposit composition, is presented in chapter 2 for the Pt-precursors, and in chapter 3 for the Au-precursors.

Chapter 4 describes the modification of a Phenom XL desktop SEM from Thermo Fisher Scientific to adapt it for FEBID processing. Because the desktop SEM allows high operating pressures, higher precursor pressures

can be employed leading to higher deposition rates. The desktop SEM was used to test the effect of increasing the precursor temperature and thus the flux on the composition and the growth rate of FEBID structures. The desktop SEMs are not designed for FEBID, so there were no ports available for a GIS. Therefore, the instrumentation for FEBID was developed in this work and integrated in the Phenom XL, after which FEBID was successfully performed. The deposits were compared to deposits fabricated in a high vacuum SEM. The Phenom XL system also allowed adding water vapor at high pressure which was used to investigate the possibility of removing carbon contamination from the substrate and from deposits using EBIE with water.

Recently, the use of FEBID to make three dimensional nano-structures, basically 3D nano printing, has received quite some attention. The flexibility of building 3D shapes locally, using FEBID in a single step, has made it appealing to apply it in fields such as nano-magnetism [27], plasmonics [28], biomedical engineering and more. Structures include vertical nanowires, helices, membranes and others. Many challenges are faced when trying to build nanostructures using resist-based lithography, such as precise alignment of multiple layers, roughness and resolution issues, fabricating overhanging and sloping structures and under-etching. FEBID facilitates building 3D shapes that are very challenging if not impossible to build with existing lithography techniques. Recent work on 3D fabrication with FEBID often focused on open, cage-like structures, and made use of simulation guided deposition [29–31]. That is, computationally intensive electron-matter interaction simulations aided in choosing the deposition parameters. To avoid this, in this work a different procedure for building 3D structures using FEBID was investigated, which is presented in chapter 5. The focus is on closed wall structures and especially truncated hollow cones. The latter shapes find application in a novel nano aperture ion source (NAIS). The procedure is focused on simplicity, keeping the parameters constant throughout the deposition of a shape, and increasing the growth rate. The pool of FEBID parameters is described and the choices of the values of the parameters are explained to achieve a specific design. The same building block is used repeatedly to build the full shape, which is different from the methods published in literature where the dwell time is adapted in each point, resulting in different building blocks. Two approaches are presented, one with large building blocks separated from each other where proximity effects are utilized to enhance the growth rate. The other approach employs small building blocks overlapping with each other to achieve smooth layers. The importance of the writing strategy is highlighted and the challenges in the deposition process are explained. To test the capabilities of the procedure in achieving high resolution 3D shapes, smaller cones were deposited successfully with dimensions of about 200 nm. The method was successfully used to deposit other shapes as well such as cylinders and boxes.

In chapter 6 the application of the cones in the NAIS is addressed. A special chip consists of two parallel membranes in between which gas is supplied. Two coaxial circular holes are milled in the membranes using the focused ion

beam (FIB) and around each hole a cone is deposited, concentrically, one on each membrane. An electron beam, incident along the cone axis on the gas leaving the space between the two cones, produces ions that can be further accelerated and focused into an ion beam. The challenges in the fabrication of this double cone structure are discussed and some preliminary results are shown. Due to electron scattering, FEBID suffers from proximity effects which lead to broadening of deposited structures. Similarly, EBL suffers from proximity effects and there are already existing mature proximity effect correction methods. This should be taken into account in FEBID as well, especially when designing 3D shapes. In our procedure for 3D FEBID, these effects are to be considered based on experiments. But other researchers have developed simulations attempting to compensate for broadening of structures, proximity effects and other problems, such as heating effects. The main software solutions available are the layer by layer approach in [29], CAD 3BID [30] and another pattern generation software developed by Keller and Huth [31]. The differences between CAD 3BID and the latter pattern generation software have been described in [31] and [32]. In chapter 7, a comparison between our method, CAD 3BID and the layer by layer approach, applied to the same shape, is presented.

Finally, the thesis ends with the conclusion chapter where the main conclusions of this work are summarized.

2

FEBID of platinum from $PtCl_2(CO)_2$ and $PtBr_2(CO)_2$

Two platinum precursors, $PtCl_2(CO)_2$ and $PtBr_2(CO)_2$, were designed for Focused Electron Beam Induced Deposition (FEBID) with the aim of producing platinum deposits of higher purity than those deposited from commercially available precursors. In this work, we present the first deposition experiments in a scanning electron microscope (SEM), wherein series of pillars were successfully grown from both precursors. Their growth was studied as a function of electron dose and compared to deposits grown from the commercially available precursor $MeCpPtMe_3$. The composition of the deposits was determined using energy dispersive X-ray spectroscopy (EDX) and compared to the composition of deposits from $MeCpPtMe_3$, as well as deposits made in an ultra-high-vacuum (UHV) environment. A slight increase in metal content and a higher growth rate are achieved in the SEM for deposits from $PtCl_2(CO)_2$ compared to $MeCpPtMe_3$. However, deposits made from $PtBr_2(CO)_2$ show slightly less metal content and a lower growth rate compared to $MeCpPtMe_3$. With both $PtCl_2(CO)_2$ and $PtBr_2(CO)_2$, a marked difference in composition was found between deposits made in the SEM and deposits made in UHV. In addition to Pt, the UHV deposits contained halogen species and little or no carbon, while the SEM deposits contained only small amounts of halogen species but high carbon content. Results from this study highlight the effect that deposition conditions can have on the composition of deposits created by FEBID.

This chapter has been published as *Electron beam-induced deposition of platinum from $PtCl_2(CO)_2$ and $PtBr_2(CO)_2$. Beilstein Journal of Nanotechnology.* **11, 1789-1800** (2020)

2.1. Introduction

Focused electron beam induced deposition (FEBID) is a direct write nanopatterning technique. FEBID has very high design flexibility and does not require masks or resist and development. Moreover, it does not need to be performed in a clean room with multiple process stages such as spin coating, deposition, development, etching, etc.; it is a single step process [33]. The process starts by injecting a precursor gas into the vacuum chamber of an electron microscope [13, 34]. At specific locations on the substrate exposed to the electron beam, the transiently adsorbed precursor molecules decompose, forming a deposit while the volatile byproducts of the reaction desorb into the vacuum [11, 35–37].

One of the main challenges associated with FEBID is the typical low purity of the deposits. Many FEBID precursors are organometallic, leading to high carbon content in the deposit [26, 36, 38]. Often, unwanted fragments of the precursor molecules stay behind in the deposits [39]. Some precursors perform better in this respect but are thermally unstable, for instance, ClAuCO and $ClAuPF_3$ [40–42]. Therefore, it is desirable to design new, stable precursors that enable the deposition of pure metals. In this work, two novel platinum precursors ($PtCl_2(CO)_2$ and $PtBr_2(CO)_2$) were synthesized and tested. The synthesis was performed by our partners at the university of Florida in the group of prof. Lisa McElwee-White. Both $Pt(CO)_2X_2$ complexes were compared to the widely used commercially available precursor $MeCpPtMe_3$. The design of $Pt(CO)_2X_2$ takes advantage of the known tendency for CO and halogens to dissociate from metal centres upon electron irradiation [43–45]. Other organometallic compounds that include a halide and CO ligands, such as $(\eta^3\text{-}C_3H_5)Ru(CO)_3Br$, showed the loss of CO upon electron irradiation [46, 47], as have CO-containing precursors without halides such as $W(CO)_6$ [48] and $Co(CO)_3NO$ [49]. In addition, the use of four-coordinate Pt(II) centres minimizes the number of metal-ligand bonds that must be broken for complete precursor decomposition [43]. Electron-induced decomposition of adsorbed $PtCl_2(CO)_2$ has been previously studied using X-ray photoelectron spectroscopy (XPS) and mass spectrometry, and some deposits were produced in the ultra-high vacuum (UHV) environment of an Auger electron spectroscopy (AES) setup [50, 51]. In the work presented here, $PtCl_2(CO)_2$ and $PtBr_2(CO)_2$ were used for FEBID in a regular scanning electron microscope (SEM) and $PtBr_2(CO)_2$ was also used for deposition in the aforementioned AES setup. A comparison of the two precursors is interesting because the bromide derivative is more volatile than the chloride (vide infra), facilitating delivery to the substrate, but study of the electron-induced reactivity of $(\eta^3\text{-}C_3H_5)Ru(CO)_3Br$ and $(\eta^3\text{-}C_3H_5)Ru(CO)_3Cl$ under UHV conditions demonstrated that the response of the halides to electron flux was similar for both compounds [46]. The typical issues to be addressed when testing novel precursors include: (i) precursor storage, (ii) gas injection system (GIS) loading, (iii) optimal precursor temperature for deposition, (iv) precursor volatility and transport from the SEM chamber, (v) ability of precursor to form solid deposits upon electron exposure, and (vi) deposition rate and deposit composition. We now report

an investigation of these practical aspects of $PtCl_2(CO)_2$ and $PtBr_2(CO)_2$ in the context of their potential use in FEBID of Pt nanostructures.

2.2. Experimental Methods

2.2.1. Synthesis

$PtCl_2(CO)_2$. The compound was synthesized by a modified literature procedure [44, 52]. A suspension of PtI_2 (0.4 g, 0.9 mmol) in toluene (15 mL) was prepared in a Schlenk flask under N_2 and CO was bubbled through the suspension for 2 hours. SO_2Cl_2 (0.6 g, 4.5 mmol) was then added into the system. The reaction mixture was stirred at room temperature under N_2 for 6 additional hours, during which the black suspension became a dark purple solution. Anhydrous *n*-heptane (30 mL) was added into the solution and the flask was stored in the freezer overnight. The product was obtained as pale white crystals. The solvent was removed by cannulation and the solid was washed with *n*-heptane until the washes were colourless. After drying under vacuum for several hours, the product was obtained as needle-shaped crystals (0.15 g, yield 52%). The compound was identified by comparison to literature data [53].^{13}C NMR (C_6D_6): δ 151.01. IR: ν_{CO} 2127, 2171 cm^{-1}. $PtCl_2(CO)_2$ sublimes at 35 - 40 °C at 125 ± 1 mTorr.

$PtBr_2(CO)_2$. The compound was synthesized using a modified literature method [54]. $PtBr_2$ (0.51 g) was stirred in 1,2- dichloroethane (42 mL) in a 300 mL Parr reactor with a glass liner for 1.5 h at room temperature under CO (150 psi). The Parr reactor was then heated to 70 °C using a water bath and the stirring was continued for another 3 h. After the reactor was cooled to room temperature, the reaction mixture was stirred overnight. After changing the atmosphere back to N_2, the Parr reactor was opened in the glove box. The yellow-brown suspension was transferred into a Schlenk flask and the solvent was removed on a Schlenk line. A light yellow solid (0.47 g, yield 80%) was collected after purification by sublimation at 30 - 35 °C at 125 ±1 mTorr. The compound was identified by comparison to literature data [54]. ^{13}C NMR ($CDCl_3$): δ 152.34. IR (CH_2Cl_2): ν_{CO} 2129, 2170 cm^{-1}. Both precursors are very sensitive to air and humidity and decompose immediately, discolouring to brown if exposed to air. For comparison, commercial samples of the commonly used Pt precursor $MeCpPtMe_3$ are crystalline and colourless at room temperature and the compound is not sensitive to air or humidity.

2.2.2. Thermogravimetric Analysis (TGA)

TGA was performed at the university of central Florida by the group of Dr. Titel Jurca. TGA of $Pt(CO)_2X_2$ was conducted on an ISI TGA-1000 instrument housed inside a nitrogen-atmosphere glove box, using Pt sample pans, with a 5 cc/min flow of UHP N_2. The complexes were measured non-isothermally at a steady ramp rate of 10 °C/min (sample masses: $PtCl_2(CO)_2$ 2.99 mg, $PtBr_2(CO)_2$ 3.01 mg), and isothermally at 90 °C (sample masses: $PtCl_2(CO)_2$ 2.99 mg, $PtBr_2(CO)_2$ 2.98 mg) following the protocol 25 – 90 °C at a ramp rate

of 10 °C/min, hold 240 min. @90 °C, 90 – 400 °C at a ramp rate of 10 °C/min.

2.2.3. FEBID in the SEM

Deposition was performed in a Thermo Fisher Scientific (TFS) Nova Nano Lab 650 dual beam system. Standard TFS gas injection systems (GIS) were used to introduce the new precursors into the SEM chamber, using a separate GIS for each precursor. Since $PtCl_2(CO)_2$ and $PtBr_2(CO)_2$ are both very sensitive to O_2 and H_2O, they were stored in a nitrogen-filled glove box and GIS filling was carried out in the box. The GIS needles were positioned about 150 µm from the electron beam and about 150 µm above the sample surface, which was at the eucentric height (5 mm working distance) in all deposition experiments. This allows for some thermal expansion of the needle when the GIS is heated. After installing each precursor-filled GIS, its crucible temperature was determined. The desired temperature should generate a pressure rise that is sufficient for deposition without exceeding the maximum pressure allowed in the SEM chamber (approximately 10^{-4} mbar).

A silicon substrate was used for all deposition experiments, patterned such that circular areas of pristine silicon are surrounded by black silicon (obtained by reactive ion etching). The black silicon area aids in focusing the electron beam close to the circular Si areas in which the deposition was done. Unless stated otherwise, the beam energy used during deposition was 18 kV and the beam current was varied from 12 – 140 pA between experiments. To achieve high spatial resolution, all deposition experiments were done in ultra-high resolution (immersion) mode. Specific patterning parameters such as electron beam dwell time and the refresh time between exposure passes will be detailed for each experiment. To characterize FEBID growth, the height and base diameter of pillars were measured using 35° tilt images.

2.2.4. Energy dispersive X-ray (EDX) Analysis

EDX was performed using an Oxford XMax150 detector on a Zeiss Supra 55 SEM. For EDX measurements, 250 x 250 nm^2 squares were deposited, thick enough to minimize the signal from the Si substrate during the analysis with a 5 keV beam. The beam current during EDX was 5 nA and the sample was mounted at a working distance of 7.5 mm and tilted by 35° to maximise the EDX signal. The system was plasma cleaned before the EDX measurements were taken to minimize carbon contamination.

2.2.5. UHV Deposition

The UHV deposition experiments were performed in Johns Hopkins University by the group of dr. Howard Fairbrother by introducing the $Pt(CO)_2X_2$ precursor into a chamber (base pressure of $3x10^{-9}$ mbar) furnished with a PHI 610 Scanning Auger Microprobe system (LaB_6 filament). The precursor was heated to 85 – 90 °C ($PtBr_2(CO)_2$) or approx. 80°C ($PtCl_2(CO)_2$) and leaked through an UHV-compatible leak valve equipped with a directional doser, which was used to increase the partial pressure of the precursor at

the surface of the substrate (silicon in the case of $PtBr_2(CO)_2$, Ru-capped Si/Mo multilayers in the case of $PtCl_2(CO)_2$). Deposits were produced over 12 hours under steady state deposition conditions using a 3 kV electron beam with a substrate current of 0.5 – 1.0 μA. A pressure of 5–7x10^{-8} mbar was maintained throughout deposition, with the substrate at room temperature. Deposits made under UHV conditions were imaged using a JEOL JSM-IT100 SEM with a 5 kV primary electron beam (8 nm resolution) and analysed using the JEOL-made EDX unit. While deposit thickness was not measured, UHV-deposited samples were thick enough to yield minimal silicon substrate signal during EDX measurements.

2.3. Results and Discussion

2.3.1. Thermal properties of the precursor

Thermogravimetric analysis was used to make a preliminary assessment of the thermal stability of $PtCl_2(CO)_2$ and to study its volatility at near-atmospheric pressure (approx. 1.2 atm positive pressure under N_2). In the standard TGA experiment (figure 2.1a), the compound underwent an initial mass loss beginning at roughly 80 °C, resulting in an intermediate residual mass of approximately 83% at 125 °C. This initial mass drop is consistent with loss of both CO ligands to form $PtCl_2$ (82.6% calculated residual mass). Additional mass loss occurred until approximately 200 °C was reached, leaving a residual mass of around 20% which plateaued until 350 °C at which point further mass loss ensued to yield a final residual mass of 14%; far below the initial Pt content of 60.5%. $PtBr_2(CO)_2$ displayed a similar three step mass loss (Figure 2.1b). Initial mass loss began at roughly 80 °C, resulting in an intermediate residual mass of approximately 80% at 125 °C. The second step did not occur until approximately 200 °C was reached, leaving a residual mass of around 46%, which plateaued until 330 °C at which point further mass loss ensued until a final residual mass of 26% was reached; significantly below the initial Pt content of 47.5%. The low final residual masses are characteristic of a combination of decomposition and sublimation during the experiment.

When data were obtained at an isothermal temperature of 90 °C (figure 2.2), the mass losses were consistent with a mixture of sublimation and decomposition. For $PtCl_2(CO)_2$, a plateau corresponding to ca. 58% of original mass is likely indicative that prolonged heating at 90 °C will result in precursor decomposition (figure 2.2a,b). Conversely, for $PtBr_2(CO)_2$, prolonged heating at 90 °C facilitated a greater degree of sublimation vs. decomposition whereupon approximately 29% of the original mass remained (figure 2.2b,c). This is reasonably below the initial Pt content of 47.5%. The TGA studies indicate that $PtBr_2(CO)_2$ is more stable under prolonged heating leading to increased volatility, but $PtCl_2(CO)_2$ is more efficient under a faster ramped-temperature process (10 °C/min).

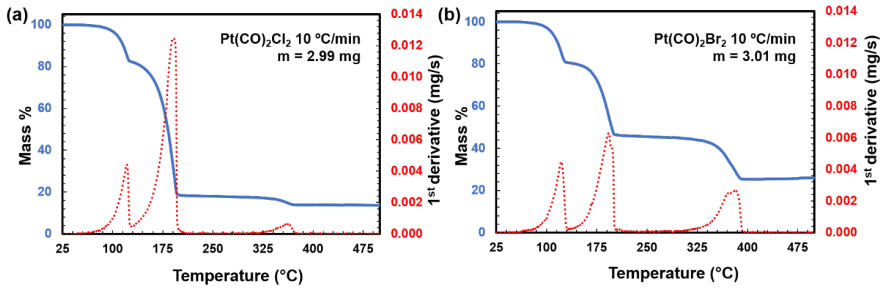

Figure 2.1: Thermogravimetric analysis (TGA) and 1st derivative DTG of (a) $PtCl_2(CO)_2$ and (b) $PtBr_2(CO)_2$.

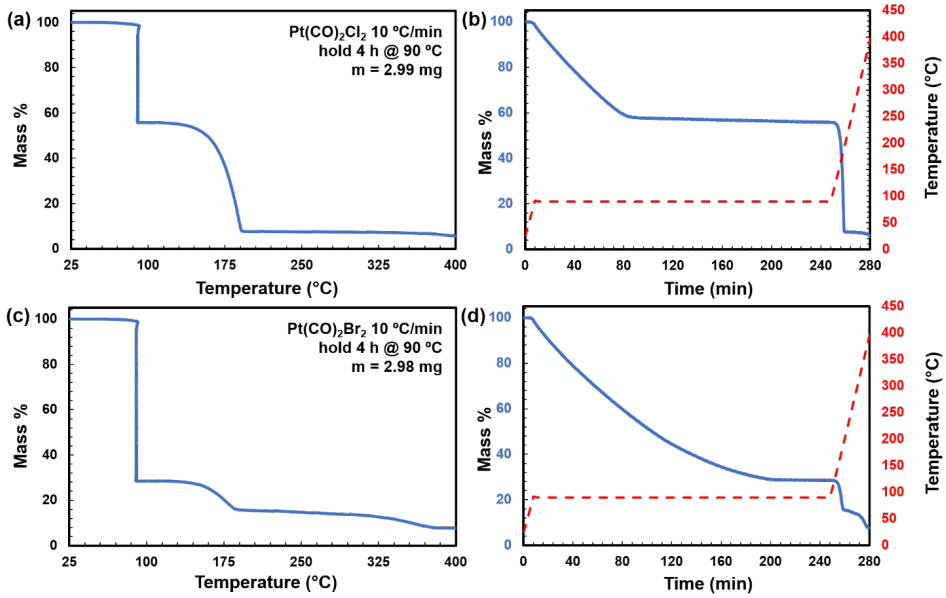

Figure 2.2: Isothermal TGA traces plotted as a function of temperature and time for (a,b) $PtCl_2(CO)_2$ and (c,d) $PtBr_2(CO)_2$ for isothermal analysis at 90°C for 4h.

2.3.2. Precursor gas properties

Precursor crucible temperature was determined for both precursors by gradually increasing the temperature of the GIS while monitoring the pressure in the SEM vacuum chamber until a pressure rise is observed, suitable for deposition and not exceeding the maximum allowable pressure in the SEM. Temperatures suitable for deposition were found to be 80 °C and 60 °C for $PtCl_2(CO)_2$ and $PtBr_2(CO)_2$, respectively, with corresponding pressures in the SEM chamber of about $4x10^{-6}$ mbar. All SEM deposition experiments done with these precursors were carried out at these crucible temperatures. Both $Pt(CO)_2X_2$

precursors produced a steep pressure rise upon opening the GIS valve, followed by a somewhat slower pressure drop. Starting at a background pressure of about $2x10^{-6}$ mbar, the pressure rises to about $8x10^{-6}$ mbar upon opening the valve of the $MeCpPtMe_3$ GIS and decreases to the background level when the valve is closed. Starting at about the same background pressure, opening the valve of the $PtCl_2(CO)_2$ GIS increases the chamber pressure to about $4x10^{-6}$ mbar after an initial sharp pressure rise and subsequent pressure drop. Figure 2.3a shows the chamber pressure after the valve of the $PtCl_2(CO)_2$ GIS was opened and then closed after some time. Almost identical behaviour is observed for $PtBr_2(CO)_2$. The observation of rapid pressure rise with the $PtCl_2(CO)_2$ crucible at 80 °C is consistent with the TGA results in which mass loss corresponding to dissociation of the CO ligands was observed to begin at 80°C (figure 2.1). The sharp pressure increase upon opening the valve may be caused by a partial precursor decomposition in the GIS crucible, resulting in a mixture of precursor molecules and CO [26, 40]. When opening the valve, the CO then escapes rapidly, giving rise to a sharp pressure increase in the SEM chamber. When all the CO has left the GIS and the needle, the vapour pressure of the parent molecule remains. This is in sharp contrast with the behaviour of $MeCpPtMe_3$, shown in figure 2.3b, which does not cause an initial sharp pressure rise in the chamber. This is consistent with TGA data for $MeCpPtMe_3$, which do not indicate facile thermal ligand loss reaction such as the loss of CO from metal carbonyls [55].

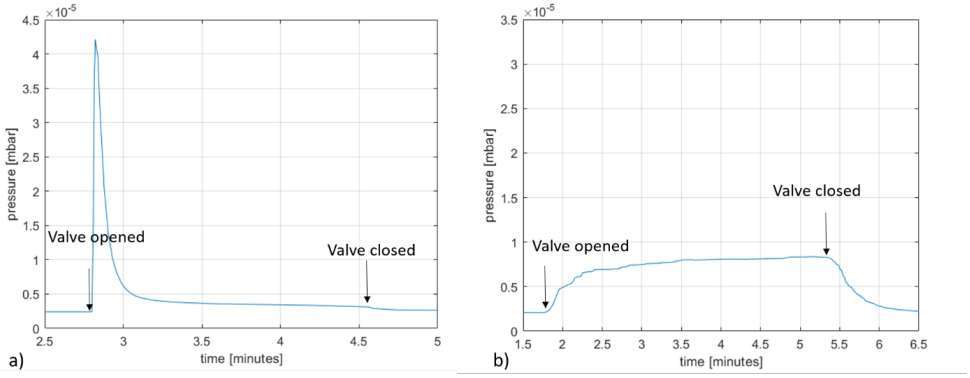

Figure 2.3: chamber pressure after opening and closing the GIS valve containing a) $PtCl_2(CO)_2$ and b) $MeCpPtMe_3$.

2.3.3. Deposition

The first set of experiments was aimed at finding the right parameters for deposition in an SEM. Because successful deposition [50], and surface science studies [44, 51], from $PtCl_2(CO)_2$ were reported already, this precursor was chosen to start with. Because the bromine compound is expected to perform similarly, as mentioned in the introduction section, it was anticipated that the same set of parameters could be used for the deposition from that precursor.

In the first experiment (hereafter referred to as experiment 1), pillars of different height were deposited using point exposures with varying dwell times. The parameters chosen were based on previous studies using $MeCpPtMe_3$ that demonstrated growth of visible pillars such that the height could be determined easily [15, 30]. A primary beam energy of 18 kV was used with beam currents of 12 pA, 38 pA, and 140 pA. A writing strategy was employed wherein a 4 x 5 array of locations at a 200 nm pitch was exposed in a serial fashion. At each location, the electron beam remained for a different dwell time, starting with 0.5 ms and increasing by 1 ms at each further location. Exposure of each location within the 4 x 5 array is considered a single pass. After each pass, a waiting time of 10 ms was introduced, during which the beam was blanked and the precursor allowed to replenish the area of deposition. This entire process was repeated for 100 passes. Without the inclusion of a waiting time, minimal growth was observed for the first few pillars with the lowest dwell times. Figure 2.4a shows an array of the resulting pillars. For reference, a similar array of pillars was deposited from $MeCpPtMe_3$ using the same parameters (figure 2.4b), except for a higher chamber pressure ($8x10^{-6}$ mbar). The pillars deposited from $PtCl_2(CO)_2$ have a conical shape, and the height is smaller and seems to saturate much more rapidly with electron dose than for the pillars deposited from $MeCpPtMe_3$ (figure 2.5). Note that in figure 2.5 the dose is plotted as the total number of incident electrons used to grow a pillar i.e., the beam current multiplied by the total dwell time at the location of exposure, excluding the waiting time. For point exposures, this is a better-defined measure than the dose per unit area. Although the diameters of the pillars from $PtCl_2(CO)_2$, as judged from figure 2.4, appear slightly larger than those of pillars deposited from $MeCpPtMe_3$, figure SI-Pt.4 in the supporting information shows that they are equal within experimental error. The aspect ratio of the $MeCpPtMe_3$ pillars (ca. 6 for the largest pillars) is larger than for the $PtCl_2(CO)_2$ pillars (ca. 2.5 for the largest pillars). The decreasing growth rate (here defined as the increase in height per incident electron, i.e. the slope of the curves in figure 2.5a) with increasing dose indicates that the growth is still limited by the precursor supply for both precursors, but more so for $PtCl_2(CO)_2$ [11, 56]. The larger height of the $MeCpPtMe_3$ pillars compared to the $PtCl_2(CO)_2$ pillars is presumably caused by the higher partial pressure of $MeCpPtMe_3$, but may also be caused by many other factors governing FEBID such as the surface residence time, the dissociation cross section and surface diffusion [12].

From both precursors, $PtCl_2(CO)_2$ and $MeCpPtMe_3$, arrays of pillars were also deposited at both a lower and a higher beam current of 12 pA and 140 pA, respectively. Figure 2.5a displays the heights of those pillars as well. For $MeCpPtMe_3$ the growth rate is highest at 12 pA and lowest at 140 pA. This indicates that at 140 pA the growth is severely limited by the precursor supply, whereas at 12 pA the growth tends towards a linear increase with dose, approaching current-limited growth [56]. For pillars deposited from $PtCl_2(CO)_2$, the growth rates at 12 and 38 pA are quite similar in the dose range probed in the experiment. At 140 pA the pillar heights are smaller than at lower cur-

rents and the growth is clearly limited by the precursor supply. At all currents no linear height increase with dose is observed, which means that the growth is still limited by the precursor supply.

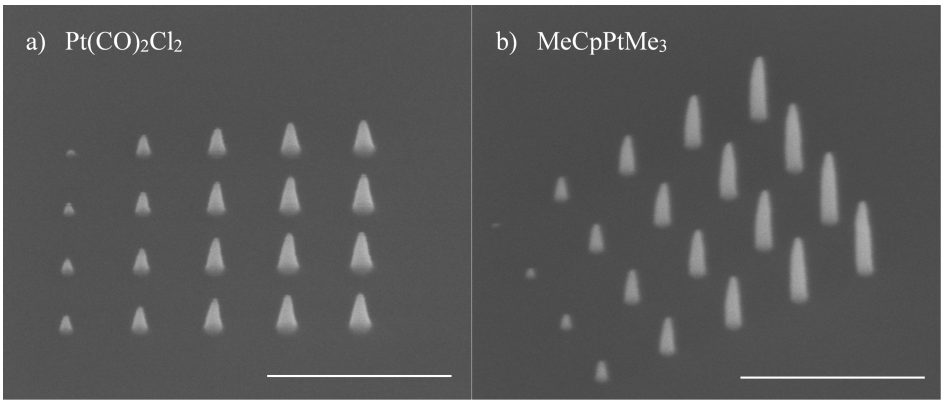

Figure 2.4: Pillars deposited at 38 pA. a) 35° tilt image of pillars deposited from top to bottom and from left to right from $PtCl_2(CO)_2$. b) 35° tilt image of pillars from $MeCpPtMe_3$, rotated for better visibility. Scale bars are 500 nm.

Figure SI-Pt.4 shows the base diameters of the pillars grown from $PtCl_2(CO)_2$ and $MeCpPtMe_3$. The diameters of pillars grown from both precursors are largest at 12 pA, presumably due to a larger contribution of precursor surface diffusion to the growth [56]. At low currents, the pillars grow more slowly in height but faster in width; this makes it interesting to plot the deposited volume as a function of the electron dose and compare the growth rates with those at higher currents. Approximating the shape of the pillars either as a cone (shorter pillars) or as a cylinder with a conical top (taller pillars), the pillar volumes were calculated and plotted in figure 2.5b. For example, the deposits in figure 2.4a and in figure 2.4b the first 2 columns of are approximated as cones, while the other deposits more closely resemble cylinders with conical tops. It is noted here that the volume of halos deposited around pillars were assumed to be negligible, as no visible halos were observed in the SEM images. At all currents the volume (figure 2.5b) shows a nonlinear initial increase with dose followed by a more linear increase. This reflects the isotropic growth in the early stages of the deposition, when both the diameter and the height increase. At a later stage, when the diameter tends to saturate because secondary electrons generated in the pillar cannot reach the surface to contribute to further lateral growth, the volume increases more or less linearly with height and thus linearly with dose [56]. At this stage pillars grown from $MeCpPtMe_3$ grow at a rate approximately 2.5 times faster than those grown from $PtCl_2(CO)_2$, irrespective of the beam current. This can also be observed for the heights of pillars shown in Figure 2.5a.

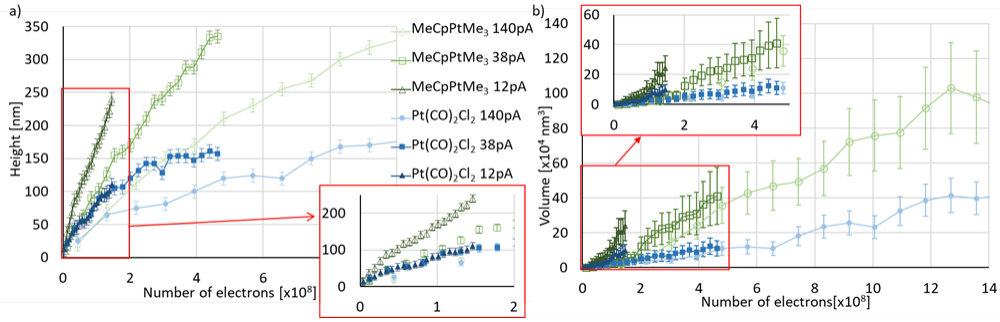

Figure 2.5: Pillars deposited at 38 pA. a) 35° tilt image of pillars deposited from top to bottom and from left to right from $PtCl_2(CO)_2$. b) 35° tilt image of pillars from $MeCpPtMe_3$, rotated for better visibility. Scale bars are 500 nm.

The second set of experiments aimed to grow pillars whose heights vary more linearly with exposure dose. In order to do so, a refresh time equal to ten times the dwell time was introduced immediately after each exposed location, so that the growth should be less limited by the precursor supply. Further, the waiting time between passes was doubled to 20 ms and the number of passes was doubled to 200. This experiment will be referred to as experiment 2. Four pillars were grown at a 200 nm pitch with dwell times of 0.5, 1, 1.5, and 2 ms, from the precursors $MeCpPtMe_3$ and $PtCl_2(CO)_2$, and now also from $PtBr_2(CO)_2$, at two beam currents (12 pA and 38 pA) and a beam energy of 18 kV. Figure 2.6 shows SEM 35° tilt images of the pillars deposited at 12 and 38 pA. First, it is observed that deposits can also be grown from $PtBr_2(CO)_2$, albeit at a lower growth rate than for the other two precursors.

In experiment 1, at 12 pA, the pillars grown from $MeCpPtMe_3$ were taller than those grown from $PtCl_2(CO)_2$ (see figure 2.5a). Conversely, using the deposition strategy of experiment 2, with more time for precursor replenishment, the heights of pillars grown from both precursors at 12 pA were almost the same (figures 2.6a and 2.6b). At 38 pA, however, the pillars grown from $PtCl_2(CO)_2$ were taller than those grown from $MeCpPtMe_3$ (figures 2.6d and 2.6e). Figures 2.6b and 2.6e show the difference in shape and size for pillars deposited from $PtCl_2(CO)_2$ at 12 and 38 pA. The heights and volumes of the pillars grown at 38 pA from $PtCl_2(CO)_2$ are plotted in figure 2.7 and reveal a distinctly enhanced growth with increasing dose via experiment 2 compared to the strategy employed in experiment 1. The results for the other two precursors, as well as the results of experiment 1 using a beam current of 38 pA for comparison, are also included in figure 2.7. The pillar diameters are shown in figure SI-Pt.5 in the supporting information. We observe that the addition of the refresh time in experiment 2 significantly increased the growth in terms of height, diameter and volume.

Although the purpose of this work was not to find the optimum deposition conditions, the highest growth rates we observed (using experiment

2 at 38 pA) were 0.045nm^3/electron (22 e$^-$/nm^3) for $PtCl_2(CO)_2$, 0.0035 nm^3/electron (290 e$^-$/nm^3) for $PtBr_2(CO)_2$, and 0.020 nm^3/electron (50 e$^-$/nm3) for $MeCpPtMe_3$. These rates were obtained from the slope of the curves taken at 38 pA in experiment 2 and shown in figure 2.7. For all three precursors, the growth was still limited by the precursor flux. To further enhance the growth rate, the local precursor pressure must be increased.

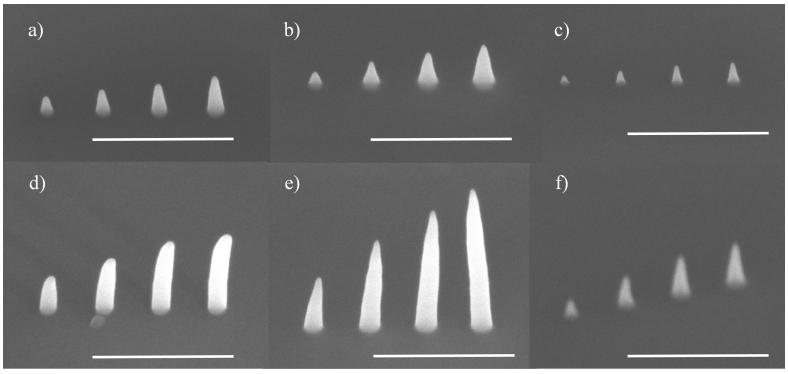

Figure 2.6: Comparison of pillars grown in experiment 2 from all three precursors a) and d) $MeCpPtMe_3$, b) and e) $PtCl_2(CO)_2$ and c) and f) $PtBr_2(CO)_2$. The dwell times for each pillar were 0.5, 1, 1.5 and 2 ms (left to right) and this was repeated for 200 passes. a), b) and c) are deposited at 12 pA. This corresponds to electron doses of 7.5, 15, 22.5, and 30x10^6 electrons. d), e) and f) are deposited at 38 pA, corresponding to electron doses of 24, 47, 71 and 95x10^6 electrons, respectively. All scale bars are 500 nm.

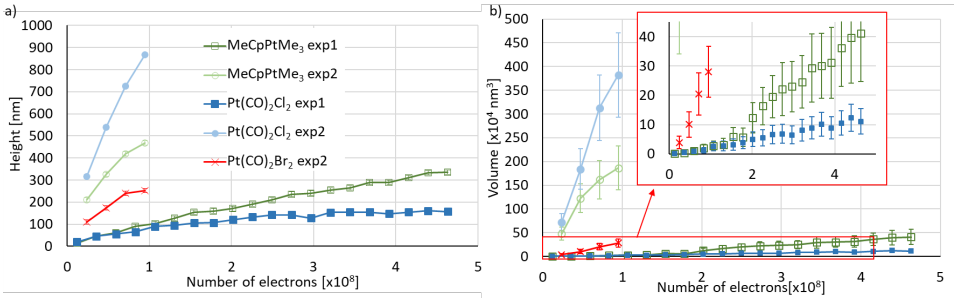

Figure 2.7: Pillar height a) and volume b) versus number of electrons deposited at 38 pA from $MeCpPtMe_3$, $PtCl_2(CO)_2$, and $PtBr_2(CO)_2$. For comparison, the graph also contains the heights obtained from $MeCpPtMe_3$ and $PtCl_2(CO)_2$ in experiment 1. The error bars originate from $\pm$10 nm errors in size measurements taken manually from SEM images. The lines between the points serve as a guide to the eye and the inset shows an expansion of the data in the rectangular (red) area.

Based on these experiments, we conclude that both new precursors $PtCl_2(CO)_2$ and $PtBr_2(CO)_2$ can be successfully used for FEBID, the former showing faster growth and the latter showing slower growth than the well-known precursor $MeCpPtMe_3$.

2.3.4. Composition

In order to directly compare the composition of the deposits grown from these precursors, square deposits of 250 x 250 nm^2 were deposited from each precursor in the SEM using the following parameters: 5 kV, 400 pA, 12 ms dwell time, 50 passes, pitch between exposed pixels of 20 nm, and exposure dose of 596 $nC/\mu m^2$. The total deposition time was 100 s.

EDX measurements were performed on these deposits. Typical spectra are shown in the supporting information, figure SI-Pt.1. The $PtCl_2(CO)_2$ square contained about 55 at% C and 20 at% Pt (figure SI-Pt.1, top), while the $PtBr_2(CO)_2$ square had about 65 at% C and 12 at.% Pt (figure SI-Pt.1, middle). These results contrast sharply with previous deposits from $PtCl_2(CO)_2$ made in a UHV chamber, which did not contain any carbon and instead consisted of 35 at% Pt and 65 at% Cl, as determined from EDX [50]. Deposits from $PtBr_2(CO)_2$ performed under UHV were similarly composed primarily of platinum and bromine (36 at% Pt and 55 at% Br), with minimal carbon and oxygen contamination. For reference, the composition of a square deposited in the SEM from $MeCpPtMe_3$ was measured (figure SI-Pt.1, bottom) whose composition (18 at% Pt and 70 at% C) agreed well with literature values [26, 38, 57]. It is noted that the deposition conditions in the UHV system and in the SEM were quite different. In the UHV system, deposits from $PtCl_2(CO)_2$ were made over 23 hours at a chamber pressure between 2 and $7x10^{-8}$ mbar with a beam energy of 3 kV and a beam current of 300 nA, resulting in a deposit size of approximately 20 x 57 μm^2. Assuming that the deposit size represents the beam size, the current density was 26 $mAcm^2$ and the power density was 78 W/cm^2. The deposit from $PtBr_2(CO)_2$ was made in UHV at a pressure of approx. $5x10^{-8}$ mbar, at 3 kV and a beam current of approx. 750 nA, resulting in a deposited area of $4.6x10^{-2}mm^2$. The corresponding current density was 1.6 mA/cm^2 and the power density was 4.9 W/cm^2. In the SEM, at a chamber pressure of typically 10^{-6} mbar, a square area was exposed with a finely focused beam in a serial fashion (20 nm pitch between pixels) in 50 passes. The current density, calculated as the current per 20 nm diameter pixel, was 127 A/cm^2 and the corresponding power density was $6.3x10^5$ W/cm^2. Although there is a huge difference in current density between the UHV and the SEM deposition experiments, it is unclear how this would lead to the observed difference in composition. It is more likely that the different vacuum conditions play a crucial role here.

The two potential sources of carbon in the SEM deposits are the precursor molecules themselves or hydrocarbon contamination in the SEM chamber. The latter is clearly absent in the UHV system. To endeavour to reduce the contribution of carbon contamination from the SEM chamber, deposition was done in the SEM after plasma cleaning the chamber. EDX spectra of deposits

made after plasma cleaning are shown in the supporting information (figure SI-Pt.2). The composition of all SEM deposits, made before and after plasma cleaning, and the UHV deposits, as determined from EDX, are summarized in Table 2.1. The Si detected in the spectra is most probably coming from the substrate. The origin of the N is not clear. It could arise from the window of the detector or it could be a Si escape peak caused by the Pt Mα1 photons hitting the detector. The Si Kα escape peak shows up at 1.74 keV below the Pt Mα1 peak [58]. The Pt Mα1 peak is at 2.2 keV and the N peak detected is at about 0.46 keV as shown in Figures S1 and S2 in the supporting information. Only the composition of the deposits from $PtCl_2(CO)_2$ are affected by plasma cleaning, increasing the platinum content by 6 at.% and decreasing the carbon content by the same amount. Although there is a small carbon contribution from contamination, it does not explain the entire carbon content in the deposits. In order to estimate the contamination level of the SEM chamber before plasma cleaning, a deposit was made from contamination only, using the same deposition time as was used for the EDX deposit (100 sec), while the heated GIS needle was inserted but with the valve closed. From a tilt image of the deposit, its volume is estimated as $1.4 \times 10^7 nm^3$. The volume of the EDX deposit from $PtCl_2(CO)_2$ was approximately $1.67 \times 10^8 nm^3$. Thus, the volume contribution of contamination from the chamber is only about 8.5 %. After plasma cleaning the SEM chamber, the contamination test was repeated, but no visible growth of a deposit was observed. This indicates that plasma cleaning successfully removes most of the contamination from the chamber and from the GIS needle as well. To verify that the substrate itself did not contain appreciable amounts of carbon, EDX was performed at a position on the substrate far away from the deposit. The resulting composition was 95.9 at.% Si, only 3 at.% C and 1.1 at.% O and the spectrum is shown in figure SI-Pt.3 in the supporting information. The fact that no N is seen in this spectrum rules out the possibility that the N originates from the detector window.

An alternative reason for the differences observed between the high vacuum (HV) environment of the SEM and UHV may lie in the presence of water in the SEM. In HV, the deposits are almost halogen free but contain a lot of carbon, whereas in UHV the deposits are almost carbon-free but suffer from a large halogen content.

The water present in HV could play a role in two different ways. First, upon electron irradiation, the water is ionized and could react with the halogen species to form HBr or HCl, both of which are volatile, explaining the low halogen content of the deposits. The reactive OH radical that remains could react with carbon and convert it to the volatile CO. From this reaction, the deposit can lose both the halogen and some carbon content. In this way water has been used for purification of FEBID of platinum [59, 60] and gold [61]. An analogous reaction occurs with ammonia to get rid of the halogen in deposits from $(\eta^3 - C_3H_5)Ru(CO)_3Cl$ precursor [62]. However, this reaction scheme would lead to a much lower carbon content in the deposit than what has been observed. The second possibility is the formation of formic acid and formaldehyde. Recent studies show that electron irradiation of CO and H_2O

does not just lead to the formation of CO_2, which is volatile, but can also lead to the formation of formic acid and formaldehyde [63]. Both compounds may stay in the deposit and contribute to the observed high carbon content. Detailed reaction schemes can be found in [63]. But this would also lead to a significant amount of oxygen in the deposit, at least as much as carbon if not more. In order to lose this oxygen, the formic acid and formaldehyde should further decompose. At present it is unclear what the reaction mechanisms are that lead to the observed composition of the deposits.

	$PtCl_2(CO)_2$			**$PtBr_2(CO)_2$**			**$MeCpPtMe_3$**	
Element	**SEM**		**UHV**	**SEM**		**UHV**	**SEM**	
	Before	After		Before	After		Before	After
C	55.4	50	..	65.4	66.4	6.5	69.5	67.3
Pt	20.2	25.8	37.6	12.1	11.3	35.9	18.4	18.8
Si	5.4	5.3	3.7	3.7	3.9	1.4	5.8	7.3
O	7.2	6.5	..	10.8	9.7	1.2	6.3	6.6
N	4.3	4.8	..	..	1.6	..	..	..
Br	..	..	..	8	7	54.9	..	..
Cl	7.5	7.6	58.7	..	..	..	..	..

Table 2.1: Composition (in at.%), as determined by EDX, of deposits made in the SEM from the three platinum precursors. Deposition was done before (Before) and after (After) plasma cleaning the SEM chamber. The composition of deposits made in UHV were added for comparison.

2.3.5. Post deposition e-beam irradiation

As mentioned above, the deposits grown in the UHV system contained a high percentage of Cl or Br for $PtCl_2(CO)_2$ and $PtBr_2(CO)_2$, respectively [50]. A major motivation for the synthesis of these precursors was the possibility that the halogen ligand could be removed by post deposition e-beam exposure; however, e-beam exposure has been previously shown to remove the halogen only from the surface of deposits [50]. In that study, after exposing a $PtCl_2(CO)_2$ deposit to a 3 keV, 300 nA, e-beam in the AES system for 7 hours, EDX and AES measurements were performed to evaluate the composition in the bulk and at the surface, respectively. EDX measurement showed no change in the Pt content while AES measurement showed an increase from 36 to 56 at% Pt [50]. This proves that e-beam post deposition exposure removes the Cl from the surface only, and not from the bulk. Indeed, for much thinner deposits created in the AES system post-deposition e-beam irradiation purified deposits to a level of 87% Pt [50]. Thus, it may be useful only for very thin deposits. The deposits that were grown in the SEM have a much lower halogen content, so the more relevant purification would be to remove the carbon. Nevertheless,

we tested the effect of post deposition e-beam exposure on the composition of the SEM-grown $PtCl_2(CO)_2$ deposit. The deposit was exposed to a 10 keV, 2.1 nA, e-beam in the SEM, for one hour. This was done before plasma cleaning. Using EDX, no change in the composition was detected, which confirms that the e-beam exposure does not remove Cl from the deposit bulk. Furthermore, no increase was observed in the carbon content which supports that the carbon in the deposits does not originate from contamination of the SEM chamber.

2.4. Conclusion

The main conclusion of this study is that the two compounds $PtCl_2(CO)_2$ and $PtBr_2(CO)_2$ can both be successfully used as FEBID precursors to make platinum containing deposits. The shapes of deposits and their growth rates were addressed and compared to deposits made from the frequently used $MeCpPtMe_3$ precursor. Although this work did not focus on optimization of deposition conditions, the highest growth rates we found were $0.045nm^3$/electron for $PtCl_2(CO)_2$, $0.0035nm^3$/electron for $PtBr_2(CO)_2$, and 0.020nm3/electron for $MeCpPtMe_3$. Apart from platinum, the deposits grown from the two novel precursors in the SEM, revealed a high carbon content, similar to deposits from the $MeCpPtMe_3$ precursor. This is markedly different from deposits grown in UHV, which contained no carbon, but a large halogen content. Contrary to expectations based on volatility, $PtBr_2(CO)_2$ turned out to perform worse than $PtCl_2(CO)_2$ as a FEBID precursor with the lowest growth rate and the lowest platinum content. Results from this investigation provide added motivation for studies designed specifically to unravel the reasons as to why and how deposition conditions influence the composition of deposits created by FEBID.

Supporting Information

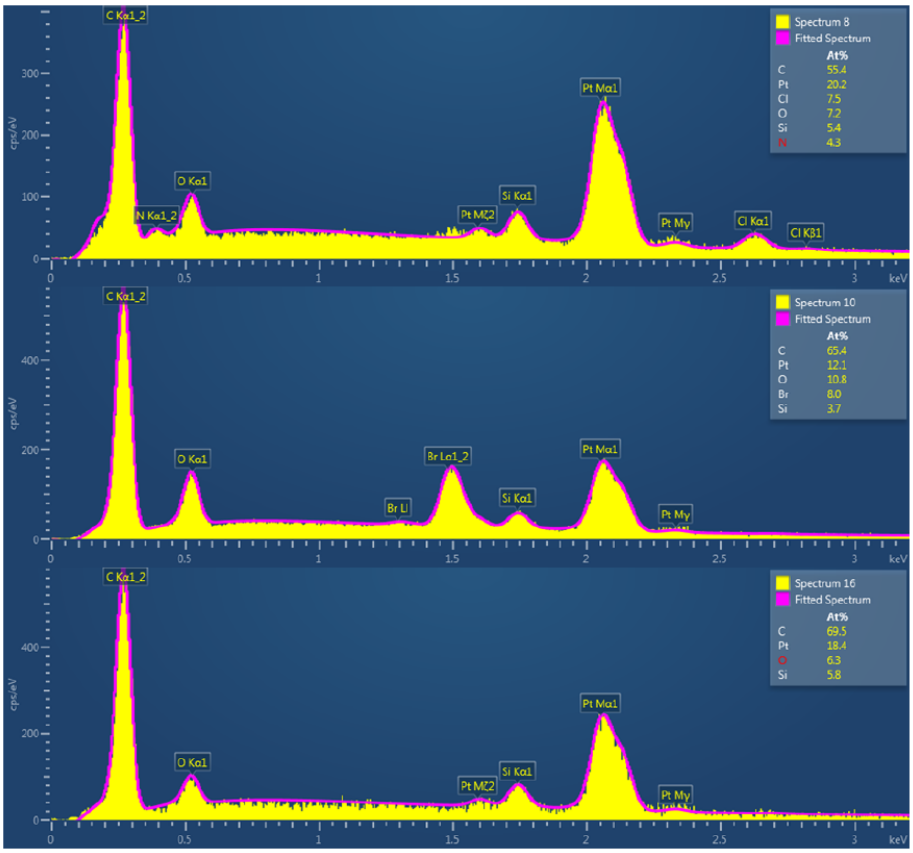

Figure SI-Pt.1: EDX spectra of deposits from the three platinum precursors. Top graph: $PtCl_2(CO)_2$, middle graph: $PtBr_2(CO)_2$, bottom graph: $MeCpPtMe_3$. The deposition was done before plasma cleaning the SEM chamber. All values are in atom %

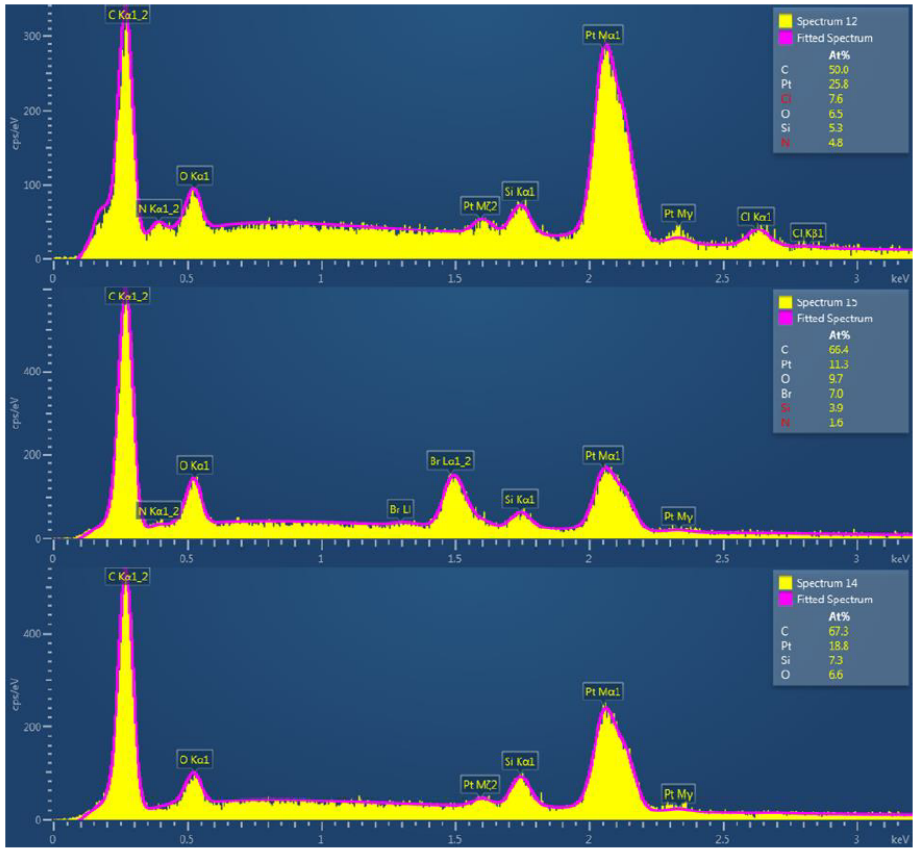

Figure SI-Pt.2: EDX spectra of deposits from the three platinum precursors. Top graph: $PtCl_2(CO)_2$, middle graph: $PtBr_2(CO)_2$, bottom graph: $MeCpPtMe_3$. The deposits were made after plasma cleaning the SEM chamber. All values are in atom %.

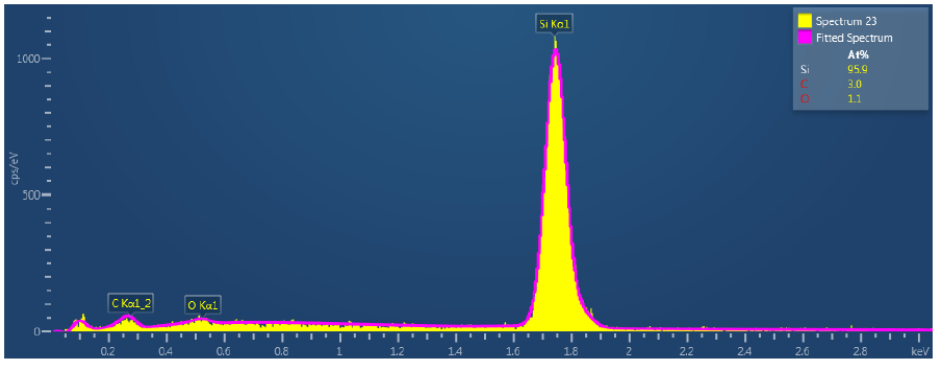

Figure SI-Pt.3: EDX spectrum of the Si substrate. All values are in atom %.

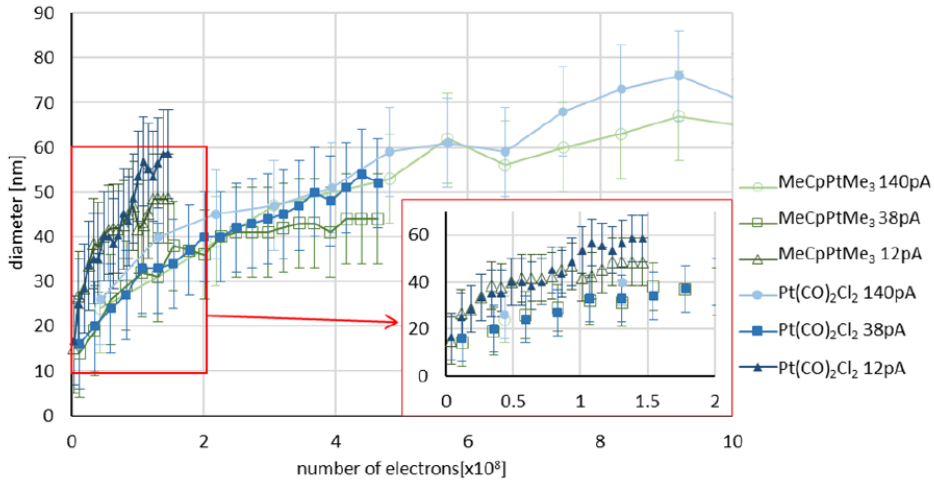

Figure SI-Pt.4: Pillar diameter versus number of electrons per pillar, for pillars deposited at 12, 38 and 140 pA from $MeCpPtMe_3$ (open symbols) and $PtCl_2(CO)_2$ (closed symbols). The ±10 nm error bars originate from size measurements taken manually from SEM images. The lines between the points serve as a guide to the eye and the inset shows an expansion of the data in the rectangular (red) area.

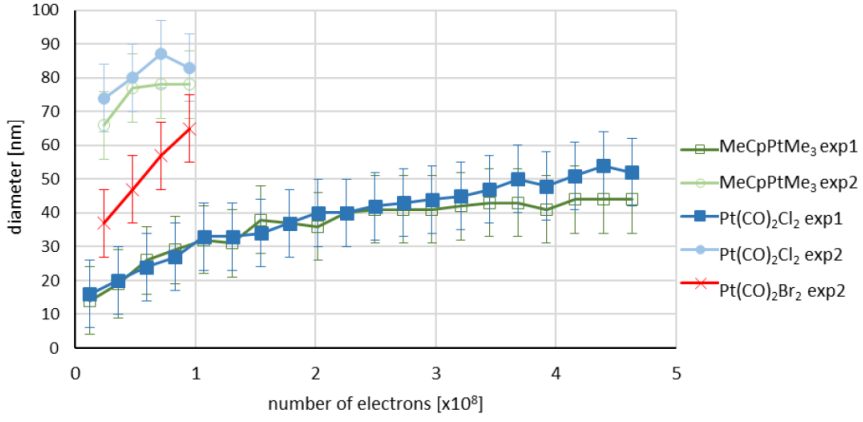

Figure SI-Pt.5: Pillar diameter versus number of electrons per pillar, for pillars deposited at 38 pA from $MeCpPtMe_3$, $PtCl_2(CO)_2$ and $PtBr_2(CO)_2$. For comparison the graph also contains the diameters obtained from $MeCpPtMe_3$ and $PtCl_2(CO)_2$ in experiment 1. The ±10 nm error bars originate from size measurements taken manually from SEM images. The lines between the points serve as a guide to the eye.

3

Gold(I) N-heterocyclic carbene precursors for FEBID

Seven gold(I) N-heterocyclic carbene (NHC) complexes were synthesized, characterized, and identified as suitable precursors for focused electron beam-induced deposition (FEBID). Several variations on the core Au(NHC)X moiety were introduced, that is, variations of the NHC ring (imidazole or triazole), of the alkyl N-substituents (Me, Et, or iPr), and of the ancillary ligand X (Cl, Br, I, or CF_3). The seven complexes were tested as FEBID precursors in an on-substrate custom setup. The effect of the substitutions on deposit composition and growth rate indicates that the most suitable organic ligand for the gold precursor is triazole-based, with the best deposit composition of 15 at% gold, while the most suitable anionic ligand is the trifluoromethyl group, leading to a growth rate of $1 \times 10^{-2} nm^3/e^-$.

This chapter has been published as *Gold(I) N-heterocyclic carbene precursors for focused electron beam-induced deposition. Beilstein Journal of Nanotechnology.* **12, 257–269** (2021)

3.1. Introduction

Focused electron beam-induced deposition (FEBID) is a nanofabrication technique that allows for the growth of three-dimensional free-standing nanostructures [11–13, 37].This mask-less nanofabrication technique uses gaseous molecules as precursors. The gas molecules are introduced in the specimen chamber of a scanning electron microscope (SEM), adsorb onto a substrate, and dissociate upon electron irradiation, leaving a solid deposit on the substrate and some volatile fragments. The technique has been employed in applications such as the fabrication of nanoconnectors [64], extreme ultra-violet lithography (EUVL) mask repair [65], AFM probe tips [66–68], nanodevices for plasmonics [69], gas sensors [22, 70], optoelectronics [71], and magnetic [72, 73] and biomedical applications [74]. FEBID provides a flexible direct-write technique to fabricate complex 3D structures, which are hard to realize using resist-based planar lithography processes. However, when using organometallic precursors, usually, undesired dissociation fragments also end up in the deposit. A major challenge is therefore to achieve control over the composition of the deposited material through a proper design of the precursor molecule [75, 76].

Gold deposition has been one of the earliest interests in FEBID [77], as gold 3D-nanostructures can find a wide range of applications from plasmonics [69] to optoelectronics [71]. Gold FEBID precursors (Figure 3.1) have had a similar history as other metal precursors, as the first tested compounds were taken from the existing library of gold precursors for chemical vapour deposition (CVD). The first compounds tested were gold dimethyl acetylacetonate, Au(acac)Me_2, and its trifluorinated and hexafluorinated derivatives, Au(tfac)Me_2 and Au(hfac)Me_2 [77]. While for the former two compounds the gold content in the deposits varied over a large range (3–28 at% [38, 69, 78, 79] and 3–39 at% [78, 80–82]), the latter complex yielded only traces of gold (2–3 at% [77]). Within the series of gold acetonate complexes, the highest gold content has been achieved with Au(tfac)Me_2 when water was co-injected as an oxidizing agent during the deposition (91 at% gold) [61]. To circumvent carbon contamination, a series of inorganic gold(I) complexes has been explored, such as Au(PF_3)Cl [17, 41, 42, 83] and Au(CO)Cl [40], which gave high-purity deposits. Unfortunately, the high instability of these precursor molecules has severely hindered their use as FEBID precursors.

For the compounds $[AuMe_2Cl]_2$ and Au(PMe_3)Me [84], it was demonstrated that the presence of alkyl ligands in gold FEBID precursors has a highly positive effect on the stability of the compounds [85, 86] and can lead to a satisfactory purity of the obtained nanostructures (19–25 and 29–41 at% Au, respectively) [84]. The most recent organometallic gold complexes that were tested are Au(CNMe)CF_3 and Au(CN(t−Bu))CF_3. These complexes are stabilized by the presence of a good σ-donor ligand (isocyanide) and their volatility is enhanced by the presence of a trifluoromethyl ligand. Deposits from these precursors contained 22 and 14 at% of gold, respectively [86]. Although many different ligand architectures of gold organometallic complexes were tested as FEBID gold precursors, the effect of different substitutions in the core struc-

ture of the molecule on the composition and growth rate of deposits is still largely unexplored. Such studies may reveal groups or ligands in precursors that perform better in FEBID and can perhaps lead to a generalized precursor design.

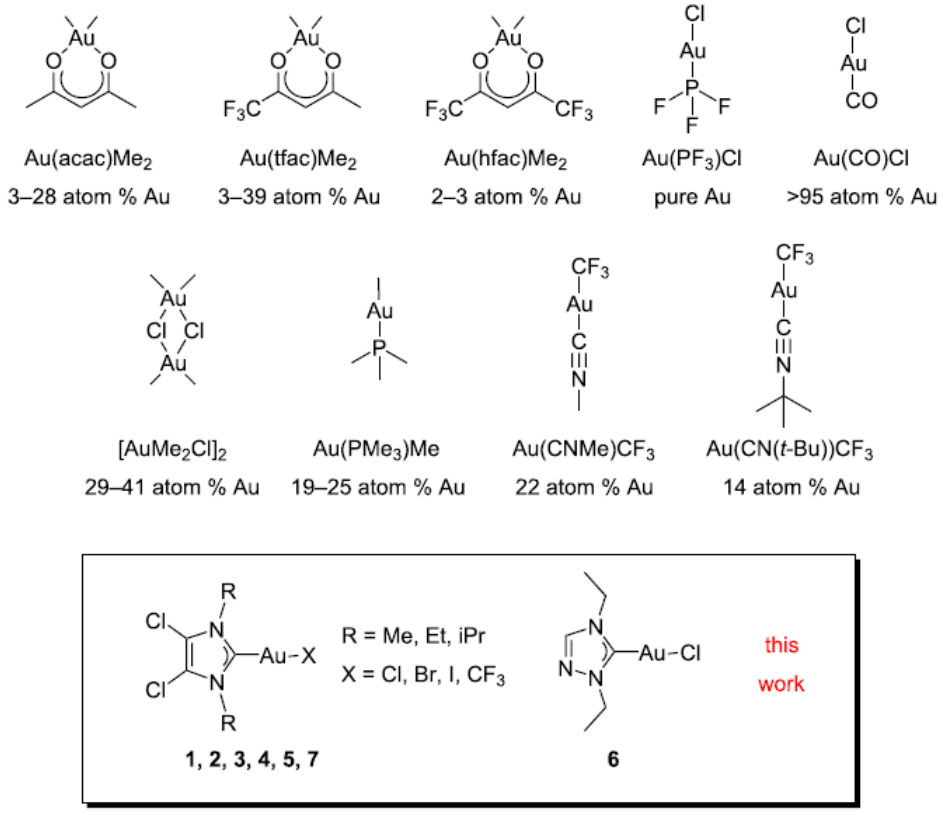

Figure 3.1: Overview of previously reported FEBID gold precursors, $Au(acac)Me_2$ [38, 69, 78, 79], $Au(tfac)Me_2$ [78, 80–82], $Au(hfac)Me_2$ [77], $Au(PF_3)Cl$ [17, 41, 42, 83], Au(CO)Cl [40], [AuMe2Cl]2 [32], $Au(PMe_3)Me$ [84, 85], $Au(CNMe)CF_3$ [86], and $Au(CN(t-Bu))CF_3$ [86], and the compounds studied in this work, labelled as 1–7.

The objective of this work is to expand the already existing library of gold(I) FEBID precursors and to study the effect of various substitutions at the core structure of a series of gold(I) N-heterocyclic carbene (NHC) complexes on the growth rate and composition of deposits. The precursors that were synthesized had the general formula Au(NHC)X, and the effect of the variation of both the NHC ligand and the ancillary ligand X (X = Cl, Br, I, CF_3) (figure 3.1) was studied. Because the sublimation temperatures of these precursors exceeded the maximum operating temperature of standard gas injection systems (GIS) in the SEM, an unconventional method was chosen to introduce the precurs-

ors from a custom-built reservoir mounted directly on top of a heated substrate on which also the deposits were directly grown. The growth of the deposited pillars was studied as a function of the deposition time, and some larger cube-shaped deposits were made to determine the composition of the deposited material using energy-dispersive X-ray (EDX) spectrometry.

3.2. Experimental

3.2.1. Synthesis and characterization

The synthesis and characterization were performed at the university of Oslo by the group of prof. Mats Tilset. All chemicals and solvents needed were commercially available and were used as received. $Au(SMe_2)Cl$ was prepared according to a procedure reported in [87]. 1,4-Diethyl-1,2,4-triazolium iodide was prepared according to the procedure reported in [88]. In order to more easily refer to the complexes, we denote the compounds as (Y,R)AuX, where Y is the backbone substitution of the NHC ligand, R is the N-substituent, and X is the negatively charged ancillary ligand. The precursors (Cl,Me)AuCl (1), (Cl,Et)AuCl (2) and (Cl,iPr)AuCl (3) were prepared according to [89]. All reactions were performed under ambient conditions unless specified otherwise. NMR spectra were recorded on Bruker Advance DPX200, DPX300, AVII400, AVIII400 and AVII600 instruments at ambient temperature. ^{1}H and ^{13}C NMR spectra were referenced relative to the residual solvent system (CD_2Cl_2). ^{19}F NMR spectra were referenced to hexafluorobenzene (−164.9 ppm). Mass spectra were obtained on a Micromass QTOF II spectrometer and a Bruker Daltronics maXis II spectrometer. Melting point determinations were performed on a Stuart SMP10 melting point apparatus, using flame-sealed capillaries at a pressure of ca. 0.2 mbar in order to mimic a vacuum environment.

[(Cl,Et)AuBr] (4): A solution of 2 (100.6 mg, 0.24 mmol, 1 equiv) and LiBr (211.6 mg, 2.4 mmol, 10 equiv) in dried acetone (10 mL) was stirred in the dark under Ar for 20 h. Solvent was removed by rotary evapouration and the resulting white solid was partially dissolved in dichloromethane (DCM) and purified through column chromatography (DCM, silica). The product was obtained as an off-white powder (100.3 mg, 89%). ^{1}H NMR (400 MHz, CD_2Cl_2) δ 4.29 (q, J = 7.3 Hz, 4H, $-CH_2-$), 1.44 (t, J = 7.3 Hz, 6H, $-CH_3$); ^{13}C NMR (101 MHz, CD_2Cl_2) δ 174.1 (NHC-C), 116.9 (=C-Cl), 46.3 ($-CH_2-$), 16.0 ($-CH_3$); MS (ESI^+, MeOH): m/z 490.896 ($[M(^{35}Cl^{35}Cl^{79}Br) + Na]^+$, 62.3%), 492.894 ($[M(^{37}Cl^{35}Cl^{79}Br) + Na]^+$, $[M(^{35}Cl^{35}Cl^{81}Br) + Na]^+$,100%), 494.891 ($[M(^{37}Cl^{37}Cl^{79}Br) + Na]^+$, $[M(^{37}Cl^{35}Cl^{81}Br) + Na]^+$, 46.6%); HRMS (MeOH): m/z meas. 490.8963, calcd. 490.8962 for $[C_7H_{10}Au^{79}Br^{35}Cl_2N_2Na]^+$ (Δ = −0.1 ppm); mp 204–205 °C; elemental analysis: calcd. for $C_7H_{10}AuBrCl_2N_2$: C, 17.89; H, 2.14; N, 5.96; found: C, 17.76; H, 2.13; N, 5.82%.

[(Cl,Et)AuI] (5): A suspension of 2 (100.3 mg, 0.24 mmol,1 equiv) and NaI (358.2 mg, 2.4 mmol, 10 equiv) in dried acetone (10 mL) was stirred in the dark under Ar for 20 h. Solvent was removed by rotary evapouration and the resulting white solid was partially dissolved in dichloromethane (DCM), filtered, and purified through column chromatography (DCM, silica). The obtained or-

ange powder was precipitated from layering of DCM and pentane. The product was obtained as a white powder (89.2 mg, 72%). ^{1}H NMR (600 MHz, CD_2Cl_2) δ 4.30 (q, J = 7.3 Hz, 4H, CH2-), 1.45 (t, J = 7.2 Hz, 6H, -CH_3); ^{13}C NMR (151 MHz, CD_2Cl_2) δ 181.0 (NHC-C), 117.0 (=C-Cl), 46.0 (-CH_2-), 16.0 (-CH_3); MS (ESI$^+$, MeOH): m/z 538.882 ([M(^{35}Cl^{35}Cl) + Na]$^+$, 100%), 540.880 ([M(^{37}Cl^{35}Cl) + Na]$^+$ 64.5%), 581.010 ([(NHC)$_2$Au]$^+$, 74.1%), 583.007 ([(NHC)$_2$Au]$^+$, 95.9%), 585.005 ([(NHC)$_2$Au]$^+$, 46.3%); HRMS (MeOH): m/z meas. 538.8824, calcd. 538.8824 for $[C_7H_{10}Au^{35}Cl_2IN_2Na]$+ (Δ = −0.1 ppm); mp 178–179 °C; elemental analysis: calcd. for $C_7H_{10}AuC_2lIN_2$: C, 16.26; H, 1.95; N, 5.42; found: C, 16.07; H, 1.91; N, 5.28%.

[(N,Et)AuCl] (6): 1,4-Diethyl-1,2,4-triazolium iodide (400.6 mg, 1.58 mmol, 1 equiv) was solubilized in 60 mL of DCM. Ag_2O (185 mg, 0.80 mmol, 0.5 equiv) was added and the resulting suspension was left stirring in the dark for 15 h. To the resulting white suspension solid Au(SMe_2)Cl (467.3 mg,1.58 mmol, 1 equiv) was added and immediately a yellow coloration of the suspension was observed. After 4 h of stirring in the dark the yellow suspension was filtered and concentrated to dryness. The solid was purified by column chromatography (silica, DCM) and an orange product was obtained. Upon recrystallization from layered DCM and pentane, white crystals were obtained (565 mg, 84%). ^{1}H NMR (400 MHz, CD_2Cl_2) δ 8.05 (s, 1H, =CH-), 4.41 (q, J = 7.3 Hz, 2H, -CH_2-, N side), 4.24 (q, J = 7.4 Hz, 2H, -CH_2-, CH side), 1.53 (t, J = 7.4 Hz, 3H, -CH_3, CH side), 1.51 (t, J = 7.3 Hz, 3H, -CH_3, N side); ^{13}C NMR (101 MHz, CD_2Cl_2) δ 173.2 (NHC-C), 142.2 (=CH-), 49.2 (-CH_2-, N side), 44.9 (-CH_2-, CH side), 16.6 (-CH_3, CH side), 15.7 (-CH_3, N side); MS (ESI$^-$, MeOH): m/z 356.023 ([[M(^{35}Cl)-H]$^-$, 100%), 358.020 ([M(^{37}Cl)-H]$^-$ 31.9%), 392.000 ([M(^{35}Cl)+Cl]$^-$ 40.3%); HRMS (MeOH): m/z meas. 356.0233, calcd. 356.0234 for $[C_6H_{10}Au^{35}ClN_3]^-$ (Δ = 0.3 ppm); mp 131–132 °C; elemental analysis: calcd. for $C_6H_{11}AuClN_3$: C, 20.15; H, 3.10; N, 11.75; found: C, 20.09; H, 3.13; N, 11.78%.

[(Cl,Et)AuCF_3] (7): AgF (104.0 mg, 0.82 mmol, 2 equiv) was added in a Schlenk flask. Upon addition of dry acetonitrile (10 mL) a grey suspension was obtained under vigorous stirring. Me_3SiCF_3 (0.3 mL, 2.1 mmol, 5 equiv) was added and a white/grey suspension was immediately formed. After a few minutes, the white suspension turned grey. The reaction mixture was stirred in the dark for 1 h. Solid 2 (176 mg, 0.41 mmol, 1 equiv) was added and the mixture turned into a light grey suspension. After 1 day the reaction mixture was concentrated to dryness and the obtained solid was partially dissolved in DCM, filtered, and concentrated. The dark product was purified by column chromatography (DCM, silica) and the product was obtained as a white powder (122.1 mg, 66%). 1H NMR (400 MHz, CD_2Cl_2) δ 4.28 (q, J = 7.3 Hz, 4H, -CH_2-), 1.45 (t, J = 7.3 Hz, 6H, -CH_3); ^{13}C NMR (101 MHz, CD_2Cl_2) δ 184.5 (q, J = 14.9 Hz, NHC-C), 162.8 (q, J = 344.2 Hz, -CF_3), 117.4 (=C-Cl), 46.1 (-CH_2-), 16.5 (-CH_3); 19F NMR (188 MHz, CD_2Cl_2) δ −30.61 (s, 3F, -CF_3); MS (ESI$^+$, MeOH): m/z 480.973 ([M(^{35}Cl^{35}Cl) + Na]$^+$ 100%), 482.970 ([M(^{37}Cl^{35}Cl) + Na]$^+$ 63.4%); HRMS (MeOH): m/z meas. 480.9730, calcd. 480.9731 for

$[C_8H_{10}Au^{35}Cl_2F_3N_2Na]^+$ (Δ = 0.2 ppm); mp 146–149 °C; elemental analysis: calcd. for $C_8H_{10}AuCl_2F_3N_2$:C, 20.93; H, 2.20; N, 6.10; found: C, 20.99; H, 2.17; N, 6.05%.

3.2.2. Determination of the sublimation temperature

The experiments for determining the sublimation temperatures and the NMR measurements were performed at the university of Oslo by the group of prof. Mats Tilset. Sublimation temperatures for compounds 1–7 were obtained by cold finger sublimation. The cold finger sublimation setup was immersed in an oil bath and heated by a heating plate. The temperature was controlled and registered by an immersion thermometer immersed in the oil bath at the same height as the bulk material and connected to the heating plate. The pressure measured for each experiment was $1x10^{-3}$ mbar on a VACUU.VIEW or DCP 3000 Vacuubrand manometer mounted on the Schlenk line used. The cold finger was cooled down with continuous water flow. 20 ± 1.5 mg of bulk material were charged in the sublimation apparatus, which was then evacuated and conditioned with Ar or N_2 before being evacuated again. The dynamic heating of the sample was carried out at a heating rate of 1 K per 10 min. The sublimation temperature was determined as the point at which the formation of a white film was observed on the initially transparent cold finger. The material was left subliming at this temperature in order to accumulate a small quantity of sublimate, sufficient for further analysis. The sublimed material was then collected and analyzed by ^{1}H NMR spectroscopy. The identity of the sublimed material was assessed by comparison with the ^{1}H NMR spectrum of the bulk material (see Supporting Information).

3.2.3. Deposition setup

All deposition experiments were performed in a Thermo Fisher Scientific Nova Nanolab 600 dual-beam SEM. The base chamber pressure was about $1x10^{-6}$ mbar. Silicon substrates were used for all experiments. The silicon substrates were cleaned by ultrasonication in acetone for 15 min, followed by ultrasonication in isopropanol for 15 min and blow drying with N_2, and were kept in a dust free environment. For each precursor a different substrate was used to avoid cross contamination. The substrate was mounted on a custom-built heater [90] shown in figure 3.2 and crystals of the precursor were placed directly on the substrate. The low volatility of the compounds required heating above the maximum allowable temperature of a standard GIS to effectively sublime the material. An aluminium plate covered the substrate, leaving a central circular area free for deposition. The precursor material was contained in a recessed hole in the bottom of the plate, connected by a small channel to the deposition area. For each precursor to be tested a new plate was taken to avoid cross contamination.

Precursors were tested for deposition upon e-beam irradiation. When deposition was successful, two types of deposits were created. Firstly, large deposits for composition analysis were written by repeatedly (2000 passes)

exposing a 250x250nm^2 area, using point exposures with a dwell time of 500 µs and a pitch of 10 nm between the exposure points. Secondly, to characterize the growth, square arrays of 3 × 3 pillars, each pillar grown at a different dwell time, were fabricated. In each array, the pillar separation was 1 µm. Two types of arrays were deposited, one with short dwell times of 0.1, 0.2, 0.5, 1, 2, 5, 10, 20, and 50 s (referred to as type 1), and one with longer dwell times for slow-growth precursors of 1, 5, 10, 20, 40, 60, 80, 100, and 120 s (referred to as type 2).

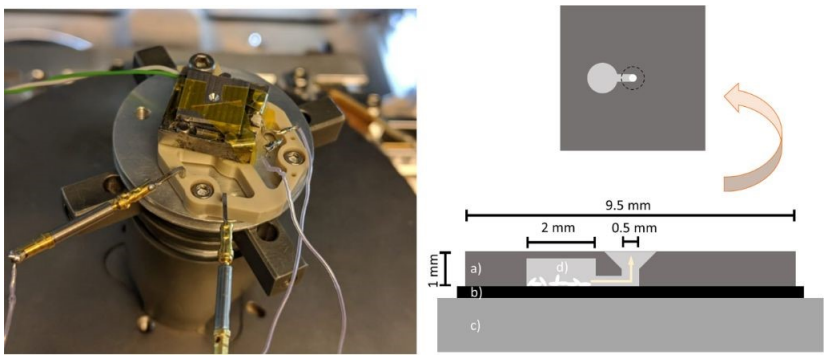

Figure 3.2: Substrate heater and precursor supply system of the deposition setup. Only the conical hole in the centre, through which the deposition is done, is visible. The precursor crystals are stored underneath the top metal cover. (a) Vapour guide, (b) silicon substrate, (c) substrate heater, and (d) precursor crystals. The sketch on top shows the bottom view of the vapour guide.

The Nova Nanolab has a 12-bit DAC to control the beam position. Therefore, the addressable grid runs from 0 to 4095 pixels in the X direction and from 280 to 3816 pixels in the Y direction. The horizontal field width (4.1 µm) is equivalent to 4096 pixels, that is, one pixel corresponds to 1 nm.

Dimensions of deposits were measured from SEM images, and, in case of tilt images, corrected for the tilt angle. For the determination of the deposited volume, pillars were approximated either as a cone or a cylinder with a cone on top, depending on their shape. The error was calculated based on an error of ±10 nm in measuring the height and diameters of the pillars, except for a few pillars where the height error was ±100 nm. These few pillars were much longer and were thus measured at a lower magnification than the other pillars. Beam energy and current used for all deposits were 5 keV and 40 pA, respectively.

3.2.4. Composition determination

EDX measurements were performed in the same Nova Nanolab 600 dual-beam SEM using an Oxford Instruments X-MAX 80 EDX detector. Beam energy and current used during the measurements were 5 keV and 600 pA, respectively.

The working distance was kept around 5 mm to have the optimum EDX signal. All spectra were analysed using the Oxford Instruments AZtec software.

3.3. Results and Discussion

3.3.1. Precursor design

The properties of a FEBID precursor molecule are crucial for the deposition process. The precursor molecule should be volatile in a suitable range of pressures and temperatures. Under these conditions, it needs to be easily deliverable in the gas phase, adsorb on a substrate, be sensitive to the electron beam, and decompose in a clean manner to the desired products. Furthermore, it should be inexpensive and easy to prepare, nontoxic, environmentally safe and easy to store and handle [75]. The choice of such molecules requires a compromise to be made between volatility,stability, and reactivity induced by electron irradiation of the molecule. This must then be translated into a structure that can lead to the deposition of the desired material [85]. Most FEBID precursors are organometallic complexes designed with the aim to obtain pure metal deposits. Normally, the metal content is quite limited, and the deposits are often heavily contaminated with carbon. Therefore, it makes sense to use as little carbon as possible in the design of the molecule [75]. Furthermore, it has been observed that large ligands, such as the methylcyclopentadienyl group in $MeCpPtMe_3$ and acetylacetonate in $Au(acac)Me_2$, do not decompose favourably under electron irradiation. However, this trend is not extended to the recently reported silver carboxylates [69, 91]. In gold(I) complexes, only two ligands are present in the coordination sphere, a neutral ligand L and an anionic ligand X. Both ligands influence the complex stability, with an increased stability after the introduction of Au–C bonds [85]. The X ligand has shown to control the volatility of the complex by means of steric hindrance; as the size of X increases, the intramolecular interactions between the precursor molecules, specifically the aurophilic interactions, decrease substantially, rendering the precursor more volatile. This is valid only if the compounds maintain a constant lattice [85, 86, 92].

Gold(I) NHC complexes are known for their versatility in different applications such as catalysis [93], biomedicine [94], and photochemistry [95]. While chemically very different species are classified as NHCs, they all share a common moiety, a carbene carbon stabilized by two α-nitrogen atoms. NHCs are neutral two-electron donors, analogous to the more extensively studied CO and PR_3 derivatives. The coordinative capability of the NHCs depends in fact primarily on the sp^2-hybridized lone pair of the carbene carbon atom, which has a strong σ-donor capability [96]. Moreover, the presence of back donation of π electrons into the empty p_z orbital of the carbene carbon atom further strengthens the C–Au bond [96]. Such features hint at a strong organometallic bond that precludes ligand dissociation under the temperature and pressure conditions involved in FEBID experiments.

Gold(I) NHC complexes owe their widely ranged adaptability to the great variability of the NHC ligand itself [97]. The NHC ligand can, in principle, be

tailored to the desired application. For FEBID the main aim is to diminish the number of carbons in the molecular formula as much as possible in order to minimize the tendency to form contaminated deposits. Furthermore, we aim at the introduction of various heteroatoms such as halogens and nitrogen, in an effort to increase the volatility of the compound. These criteria were fulfilled in the NHC gold(I) complexes 1–7 (Figure 3.3). Compounds 1–5 and 7 are imidazole-based NHC complexes with short aliphatic substituents on the nitrogen atoms (N-substituents) and two chlorine atoms on the backbone of the aromatic structure. While compounds 1–3 have a chloride as the other ancillary ligand, this has been modified in compounds 4, 5, and 7 with the introduction of a bromide, iodide, or trifluoromethyl group, respectively. The effect of the halogen substitution on the performance of FEBID precursors has, to the best of our knowledge, not been investigated yet for gold compounds. The difference between the bromide and chloride ligands has been investigated [98] for platinum precursors. It was shown that under the tested conditions, the chloro compound performed better than the bromo compound in terms of composition and growth rate [98].

Compound 6 is a triazole-based NHC gold(I) complex that presents a further reduced number of carbon atoms compared to the imidazole-based compounds with the replacement of one of the backbone carbon atoms by a nitrogen atom.

Based on the design of these precursors, the expectation is that electron irradiation will decompose the ligands under the formation of nitrogen- and chlorine-containing organic fragments, hopefully leading to more volatile byproducts, compared to precursors with purely carbon-based ligands. Furthermore, the synthesis aimed for a series of thermally robust compounds that can be straightforwardly handled and tested.

3.3.2. Synthesis

The chemical precursors to the selected NHC ligands are salts of their respective imidazolium or triazolium cations. The imidazolium salts were obtained starting from the unsubstituted 4,5-chloroimidazole through two sequential alkylation reactions using the selected alkyl iodides [99]. For the triazolium salt the two alkylation reactions were carried out together in a one-pot synthesis [88]. The resulting salts were then reacted with silver oxide to generate the respective Ag(I) NHC complexes. Upon the addition of 1 equiv of gold precursor $Au(SMe_2)Cl$ in situ, a transmetalation reaction took place that yielded the desired Au(NHC)Cl complexes 1, 2, 3, and 6 (figure 3.4 a,b) [89]. Compounds 4 and 5 were synthesized through a halide metathesis reaction when a solution of 2 in acetone was stirred with a large excess of a bromide [100] or iodide [101] salt (figure 3.4c). Compound 7 was obtained by reaction of 2 with a mixture of AgF and Me_3SiCF_3 [102]. This reaction created in situ a $AgCF_3$ species that, through a transmetalation reaction, yielded compound 7 (figure 3.4c). All these compounds are, under ambient conditions, inert colourless crystals or white powders that are stable to air and moisture and safe to handle.

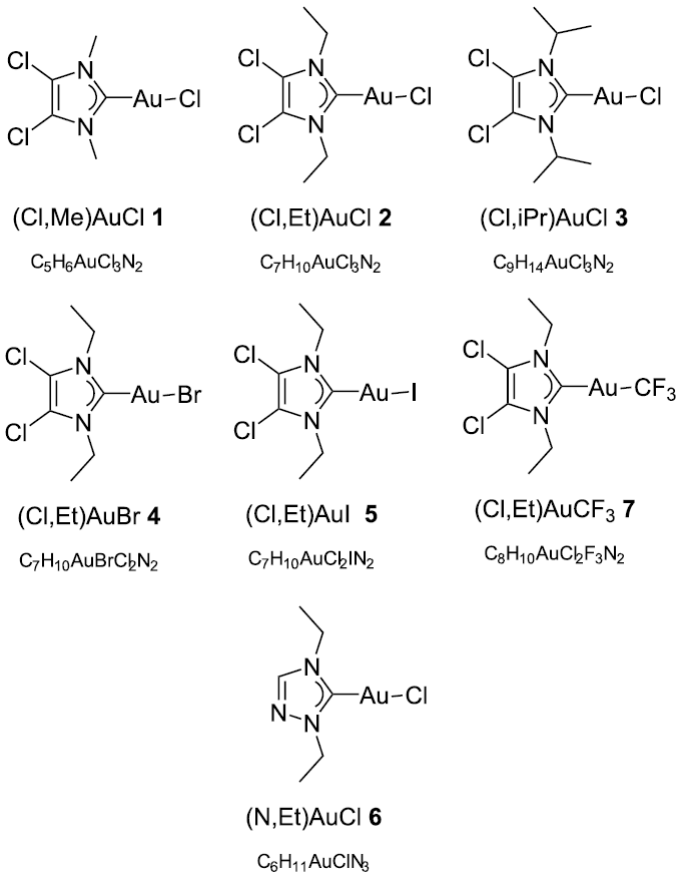

Figure 3.3: The selected Au(NHC)X complexes studied and their molecular formulae.

3.3.3. Precursor volatility and thermal stability

Table 3.1 shows the sublimation temperature, obtained from the cold finger setup, for each precursor. No decomposition was observed in the collected sublimed materials by comparison of their ^{1}H NMR spectra with those of the bulk material, and no change of the bulk material was observed during the sublimation experiments by visual observation. The correlation between halogen ligand and volatility was recently discussed for a series of isocyanide gold(I) complexes [92]. Halogens with larger radii have been observed to lead to the formation of more volatile complexes, presumably due to the increased intermolecular distances in the packing of the crystals, mainly through weakening of aurophilic interactions [92]. The same trend was observed during cold finger sublimation experiments on the synthesized compounds. However, the magnitude of the sublimation temperature variation was found to be only modest for the halogen series Cl, Br, and I. This can be related to the presence of the NHC moiety, which is predominant in the packing of the molecules, thus re-

ducing the weight of aurophilic interaction in the overall packing energy [103]. The variation of sublimation temperature is more important when a trifluoromethyl group is introduced on the gold atom inducing a decrease of more than 20 °C, in line with observations on isocyanide gold(I) complexes [86]. With the increase of the steric bulk of the N-substituents, the sublimation temperature is decreased. Going from Me to Et substituents causes a decrease in sublimation temperature of 22 °C, while the decrease from Et to iPr is minor (3 °C). Furthermore, the triazole-based gold complex was shown to be more volatile than its imidazole-based counterpart (table 3.1).

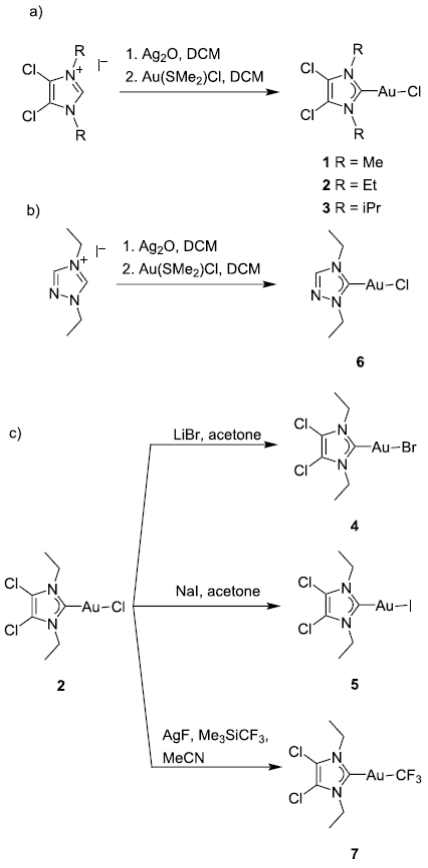

Figure 3.4: Synthesis routes for 1–7.

The melting temperatures of the compounds are found not to be correlated directly with the sublimation temperatures. The sublimation temperature is a lower boundary of the FEBID operating range, to achieve a useful vapour pressure. The upper boundary is the upper pressure limit of the SEM. All deposition experiments were performed in this operating range. A temperature of 100 °C was chosen to explore all precursors, except for the least volatile compound 1 for which a temperature of 120 °C (20 °C more than its sublim-

ation temperature) was necessary to provide a sufficient precursor flow. It is noted that all deposits reported in this work are grown on heated substrates and the resulting growth rates are valid only at the corresponding temperature. A beneficial side effect of heating the substrates to at least 100 °C is that adsorbed water is removed from the substrates, diminishing its influence on the FEBID process.

Compound	**Sublimation temperature (°C)**	**Melting point (°C)**	**Deposition temperature (°C)**
(Cl,Me)AuCl (1)	100	266–269	120
(Cl,Et)AuCl (2)	78	185–186	100
(Cl,iPr)AuCl (3)	75	202–203	100
(Cl,Et)AuBr (4)	77	204–205	100
(Cl,Et)AuI (5)	73	178–179	100
(N,Et)AuCl (6)	60	131–132	100
(Cl,Et)AuCF$_3$ (7)	53	146–149	100

Table 3.1: Sublimation temperatures, melting points, and the chosen temperature for deposition of the studied precursors.

3.3.4. Testing apparatus

A more flexible setup than a traditional GIS was required for the exploration and testing of a large series of precursors. Commercially available GIS have a limited temperature range. For example, the maximum allowable temperature of the Thermo Fisher Scientific GIS, used with $W(CO)_6$ or $MeCpPtMe_3$, is limited by the software to 65 °C. As the precursors tested here are inert under normal conditions and stable to air and moisture, they lend themselves for exploration in an open system, and they pose no known health hazard to the user. They were first tested by positioning free precursor crystals on a heated substrate, and observing their disappearance upon heating. Furthermore, electron beam-induced deposition was observed in close vicinity of the crystals. A small and easy to handle setup mounted on a substrate surface was then developed, resembling a GIS, comprising a reservoir, an injection channel, and a deposition area (figure 3.2). The cylindrical precursor reservoir of 2.5 mm^3 (2 mm diameter, 0.8 mm height) and a 1 mm long and 0.5 mm wide channel, which separates the reservoir from the circular deposition area (0.5 mm diameter), were milled from the bottom of an aluminium plate (9.5 × 9.5 × 1 mm^3). The plate lies directly on the 10 × 10 mm^2 silicon substrate, covering some precursor crystals positioned on the substrate, and is kept in place with vacuum-compatible Kapton tape. Only small quantities are needed to test a precursor, and a wide range of temperatures can be achieved (tested up to 160 °C).

3.3.5. Deposition and composition results

All compounds were tested for electron beam-induced deposition, after which deposits were made large enough for compositional analysis using EDX. Slightly larger deposits were grown from the (N,Et)AuCl precursor, in order to reduce the silicon signal from the substrate and to obtain EDX measurements with a silicon content comparable to that of the other studied materials (<10 at%). Figure 3.5 shows typical deposits, defined as 250 × 250 nm^2 squares, from all seven tested precursors. The deposits clearly differ in size and shape. The deposits have grown considerably in the lateral direction, almost doubling in size. Clear differences are seen in the vertical dimension ranging from about 0.5 µm (figure 3.5 a,f) to 3 µm (figure 3.5g). While a minor halo is observed for all precursors, only for (N,Et)AuCl (6) a significant granular halo is obtained (see Supporting Information, figure SI-Au.19), for reasons yet unknown.

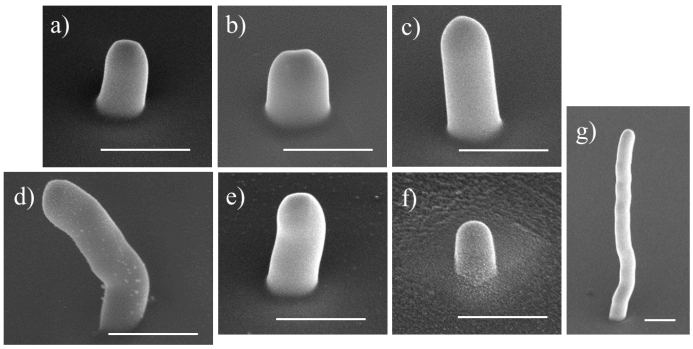

Figure 3.5: SEM images, tilted by 50°, of 250 × 250 nm^2 square deposits made using a beam energy and current of 5 keV and 40 pA, respectively.(a) 1 (Cl,Me)AuCl, (b) 2 (Cl,Et)AuCl, (c) 3 (Cl,iPr)AuCl, (d) 4 (Cl,Et)AuBr, (e) 5 (Cl,Et)AuI, (f) 6 (N,Et)AuCl, and (g) 7 (Cl,Et)AuCF_3. The deposition was performed using the reservoir-on-substrate setup, heated to 100 °C for all compounds except for 1, which was heated to 120 °C. The scale bars are 1 µm.

The average composition of seven or eight EDX spectra from at least three deposits as those shown in figure 3.5 is listed for each precursor in Table 3.2. The values reported are the mean ± standard error. All deposits have a consistent atomic fraction (at%) of gold, indicating the successful delivery of the intact parent molecule to the beam incidence area. For the series (Cl,Et)AuX with X = Cl, Br, I, and CF_3 (2, 4, 5, and 7), a Au content of 7.3–8.8 at% was obtained. Although the differences in Au content are only modest, the compounds X = Cl and X = CF_3 (2 and 7) were observed to contain the highest percentage of gold. Going from Cl over Br to I, the Au content steadily decreased. The decrease in metal content from Cl to Br compounds has been observed for deposits from Pt compounds as well [98]. The relatively high chlorine content of compounds 1–3, compared to that of compounds 4–7, indicates that the backbone and the gold-bonded Cl are co-deposited. Br, I, and

F are also present in negligible quantities, demonstrating their suitability as elements to be used in FEBID precursors. Iodine is detected in EDX analysis only at 8 keV incident energy, and is therefore not shown in table 3.2 (see Supporting Information).

	(1)	(2)	(3)	(4)	(5)	(6)	(7)
C	61.2 ± 0.58	66.7 ± 1.23	68.7 ± 0.96	67.0 ± 0.76	69.0 ± 0.53	60.7 ± 0.61	68.0 ± 0.41
N	14.9 ± 0.38	10.9 ± 0.37	10.0 ± 0.11	11.7 ± 0.30	11.9 ± 0.27	11.3 ± 0.35	12.3 ± 0.32
Au	10.3 ± 0.32	8.80 ± 0.40	7.30 ± 0.15	8.00 ± 0.26	7.30 ± 0.12	14.6 ± 0.41	8.80 ± 0.19
Si	7.40 ± 0.53	6.80 ± 0.67	6.90 ± 0.77	6.80 ± 0.39	7.30 ± 0.50	7.80 ± 0.42	7.20 ± 0.48
O	2.90 ± 0.10	3.70 ± 0.24	4.80 ± 0.25	3.30 ± 0.12	3.30 ± 0.04	4.00 ± 0.16	1.70 ± 0.07
Cl	3.30 ± 0.11	3.10 ± 0.07	2.40 ± 0.08	0.80 ± 0.04	1.30 ± 0.04	1.60 ± 0.08	1.90 ± 0.23
Br	0	0	0	2.50 ± 0.10	0	0	0
F	0	0	0	0	0	0	0.20 ± 0.07
C/Au observed	5.9	7.6	9.4	8.4	9.5	4.2	7.7
C/Au parent	5	7	9	7	7	6	8

Table 3.2: Elemental composition of deposits obtained by EDX with all values given in at%. In addition, the ratio between carbon content and gold content in the deposits and the corresponding parent molecules are given.

	C/Au ratio	N/Au ratio	Cl/Au ratio
parent molecule of 6	6	3	1
deposit from 6	4.2	0.8	0.1
fragment 6a	4	1	0

Table 3.3: Ratios between the atomic percentages of elements present in the precursor molecule of 6, the deposit from 6 and a putative fragment 6a (see Figure 3.6).

For the series (Cl,R)AuCl with R = Me, Et, and iPr (1–3) a wider range of gold content was found. This variation can be directly correlated to the number of carbon atoms in the precursor molecule. Going from R = Me over Et

to iPr, the Au percentage decreases from 10.3 over 8.8 to 7.3 at%, respectively, following the trend of the Au/C ratio of the starting material. For all compounds, the C/Au ratio observed in the deposits is comparable to, if not slightly larger than, the ratio in the parent molecules. While the gold composition is highly influenced by the variation of the R substituents, the carbon atomic fraction does not proportionally increase with the increase of carbon atoms in the precursor. Br, Cl, I, and F are partially or mostly removed upon irradiation, while N is mostly co-deposited. A similar behaviour was observed for isocyanide-based gold(I) precursors, where N is also partially co-deposited [34]. Recently, it was further demonstrated that nitrogen can be embedded in pre-existent carbon material upon the use of N-containing precursors under electron irradiation [62]. EDX analyses of the deposits show the presence of silicon and oxygen, which are not present in the precursor molecules. Their presence is likely to come from the silicon substrate with its native oxide surface layer.

The triazole-based compound 6 is the best-performing precursor, yielding the highest Au content of 14.6 at%. In this case, the C/Au ratio in the deposit is considerably lower than in the parent molecule (tables 3.2 and 3.3). This could be indicative of the effective fragmentation of the triazole-based ligand. Also in this case, Cl is mostly removed, while N is partially removed, leaving carbon and gold as the mainly deposited atoms.

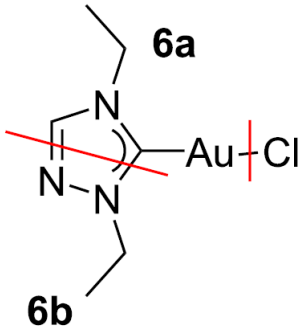

Figure 3.6: Possible fragmentations of (N,Et)AuCl (6), with the loss of Cl and a volatile fragment 6b, and the deposition of 6a.

Based on the N/Au, C/Au, and Cl/Au ratios for compound 6 (Table 3.3), it is evident that the chloride ligand is removed and that the triazole-ring is fragmented. However, the fragmentation of the NHC ligand is not simple and unambiguous, as various fragmentations can take place either by the removal of the N-substituents or by the effective fragmentation of the NHC ring. Since no fragmentation of the ring occurs for the imidazole-based compounds, the presence of a N–N bond appears to be a requirement. Thus, we postulate that the most plausible fragmentation is the removal of a N=N–Et fragment (6b) with the co-deposition of the metal centre and the strongly bonded carbene

moiety 6a, for which the molecular structure is comparable to the imidazole-based precursors (figure 3.6). However, we cannot rule out the possibility of different fragmentations occurring at the same time.

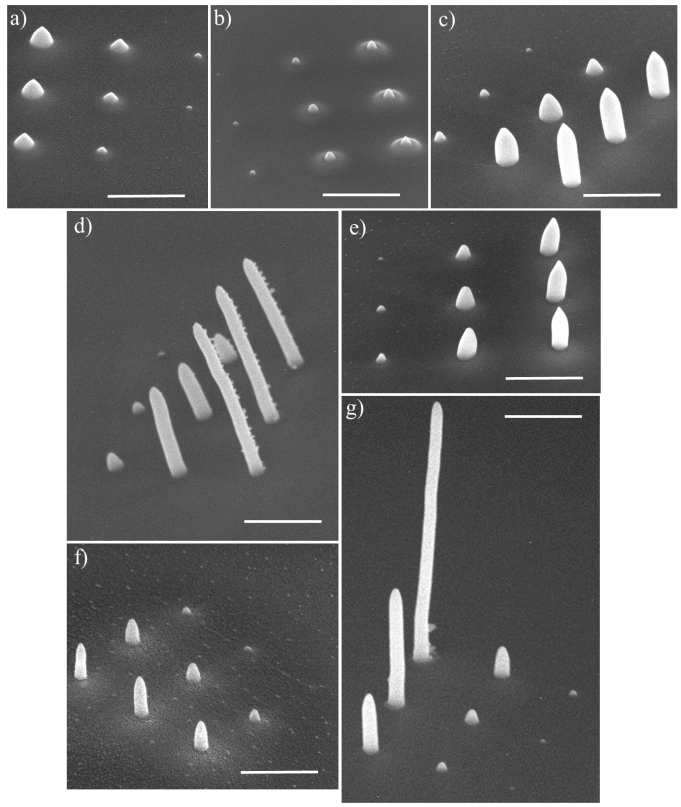

Figure 3.7: Typical SEM images, tilted by 50°, of pillar arrays deposited from all precursors. (a) 1 (Cl,Me)AuCl, (b) 2 (Cl,Et)AuCl, (c) 3 (Cl,iPr)AuCl,(d) 4 (Cl,Et)AuBr, (e) 5 (Cl,Et)AuI, (f) 6 (N,Et)AuCl, and (g) 7 (Cl,Et)AuCF$_3$. The deposition was performed using the reservoir-on-substrate setup heated to 100 °C for all compounds except for 1, which was heated to 120 °C. The scale bars are 1 µm.

3.3.6. Growth Rate

To evaluate the deposition rate of these novel precursors, square arrays of 3 × 3 pillars were deposited, with each pillar grown with a different deposition time as explained in the Experimental section. Arrays with short deposition times (type 1) were deposited from (Cl,Et)AuCF$_3$, due to its high deposition rate. For all other precursors, arrays with long deposition times (type 2) were fabricated. Figure 3.7 shows SEM tilt images (at 5 keV and 40 pA) of a typical array of deposited pillars for each precursor. For each deposited pillar its

total deposition time is converted to the total number of incident electrons, or electron dose, used to deposit that pillar.

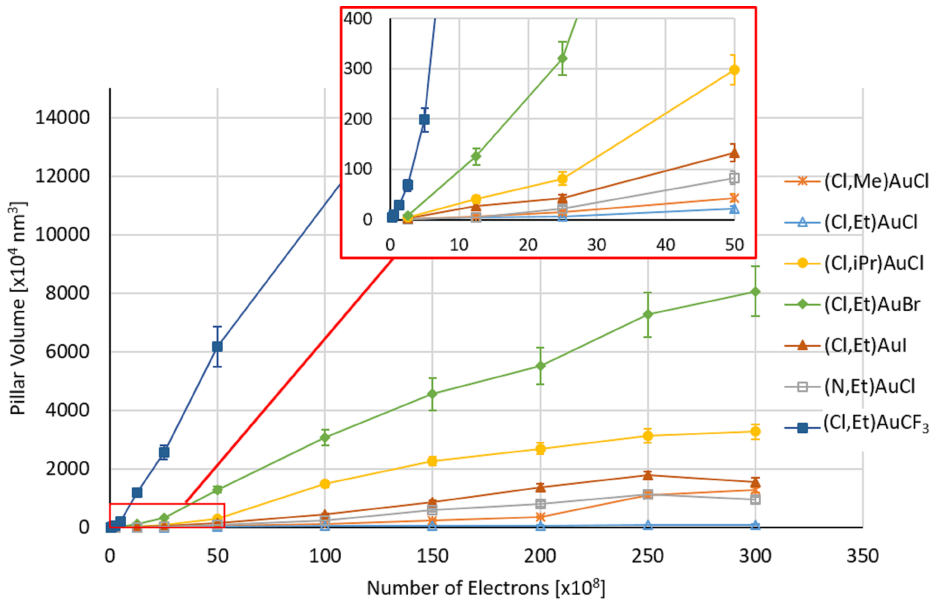

Figure 3.8: Calculated volume of pillars grown using a 5 kV, 40 pA beam, as a function of the electron dose given as total number of primary electrons used to deposit a pillar. During all experiments the substrate and the precursor were heated together to 100 °C, except for (Cl,Me)AuCl, which was heated to 120 °C. For each precursor an array of 3 × 3 pillars was deposited. The lines between the points merely serve as a guide to the eye.

Figure 3.7 shows that the shapes of the pillar deposits from different precursors are different. Therefore, the volume was chosen to fairly compare the growth rate of the different precursors. The height and diameter of the pillars were measured and used to calculate the volume. Figure 3.8 shows the calculated deposit volumes as a function of the electron dose. Clearly different deposition rates are found ranging from $3x10^{-5}$ to $1x10^{-2}nm^3/e-$, assuming linear growth. For the well-known Pt precursor $MeCpPtMe_3$, the deposition rate was recently reported as $2x10^{-2}nm^3/e-$, although deposited under very different conditions [98]. Except for the compound (Cl,Et)$AuCF_3$, the growth rates of the presently studied gold precursors are considerably lower, which may be due to the elevated substrate temperature at which the deposition was performed. Arranging the precursors according to their growth rate, in increasing order, the following sequence is obtained: (Cl,Et)AuCl < (Cl,Me)AuCl < (N,Et)AuCl < (Cl,Et)AuI < (Cl,iPr)AuCl < (Cl,Et)AuBr < (Cl,Et)$AuCF_3$. No clear correlation between sublimation temperature and growth rate is observed. However, it should be noted that the most volatile compound (Cl,Et)$AuCF_3$

(7) led to the highest growth rate. Height and diameter of pillars grown from all precursors 1–7, used to calculate the volume, are plotted in figure SI-Au.20 in Supporting Information. Deposits from all precursors show a rather linear increase in height with electron dose (figure SI-Au.20a, Supporting Information), whereas the deposit diameter increases at first but saturates at higher doses (figure SI-Au.20b, Supporting Information). The saturation values differ between precursors, probably reflecting the difference in composition, which influences the electron scattering in the pillars.

3.4. Conclusion

Seven gold NHC complexes of the form (Y,R)AuX were synthesized and thermally characterized at the university of Oslo. The sublimation temperature T_s of the compounds was observed to decrease with the increase of the steric bulk of the N-substituent in the series R = Me, Et, and iPr, that is, $T_{s,Me} > T_{s,Et}$ > Ts,iPr, and with the variation of the halide ligand X in the series X = Cl , Br, I, and CF_3,that is, $T_{s,Cl} \approx T_{s,Br} > T_{s,I} > T_{s,CF_3}$. Minor structural variations were observed to cause a sublimation temperature difference of 47 °C between the least volatile compound (Cl,Me)AuCl (1) and the most volatile compound (Cl,Et)AuCF$_3$ (7). Furthermore, the introduction of a triazole-based ring in (N,Et)AuCl (6) leads to a more volatile complex than the imidazole-based counterpart (Cl,Et)AuCl (2). The compounds were tested as FEBID precursors on a heated substrate equipped with an on-substrate precursor reservoir. We analyzed the influence of the variation of the NHC ring, of the N-substituents and of the halogen or pseudo halogen ligand X both on composition and deposition rate. The variation of the R group expectedly led to better composition results for the smaller alkyl substituents (R = Me), accompanied by a decrease in volatility. Minor composition differences were registered for the variation of the X group, with X = Cl and CF_3 leading to the best results. Of the tested precursors, the most promising is the triazole-based complex 6, which leads to an un-optimized gold composition of 14.6 at%. Modest atomic percentages of gold have been achieved, in line with previously reported gold(I) precursors, but still below the best-performing unstable gold(I) precursors and Au(tfac)Me$_2$. However, there is much room for improvement regarding the deposition conditions, which could lead to better composition of the deposits. The growth rate measurements of the compounds, at the temperature of deposition, have shown that under constant conditions the variation of the X group from a halogen to a trifluoromethyl group is highly beneficial. (Cl,Et)AuCF$_3$ (7) shows the highest growth rate while retaining the same gold composition as the halogen-based complexes. This comparison offers an interesting perspective to further explore trifluoromethylated FEBID precursors, rather than the halide counterparts.

Supporting Information

S1. NMR characterization and cold finger sublimation experiments of the precursors 1–7

1 (Cl,Me)AuCl

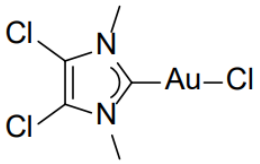

Sublimation. From top to bottom in order: 1, sublimed obtained for three different experiments at a registered temperature of: 100.7 °C, 99.6 °C, 100.9 °C.

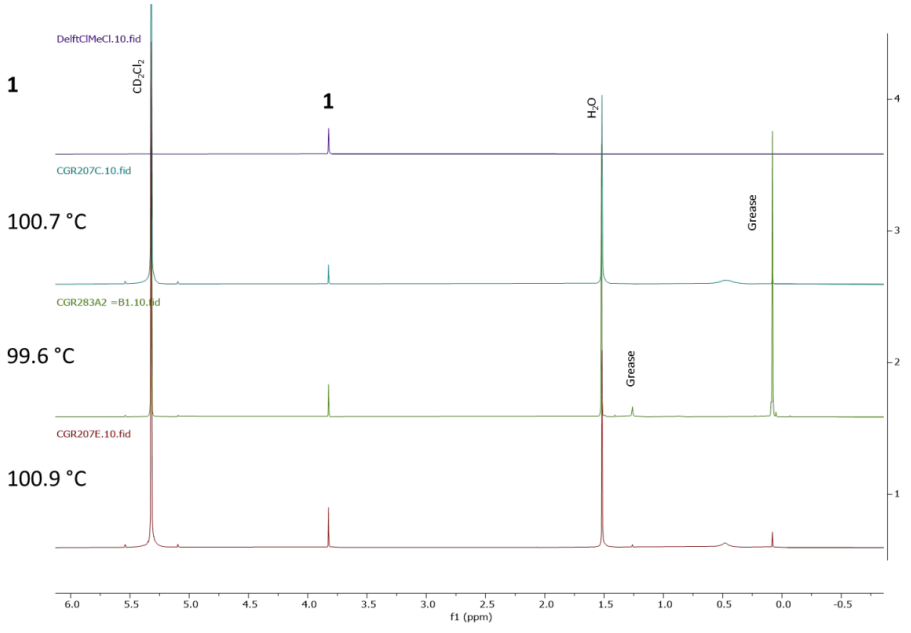

Figure SI-Au.1: ^{1}H NMR spectra stack plot for 1 and the obtained sublimation materials (400 MHz or 300 MHz, CD_2Cl_2).

2 (Cl,Et)AuCl

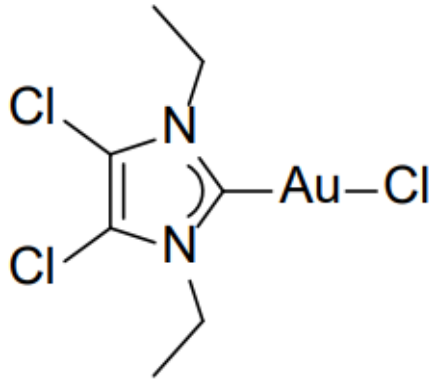

Elemental analysis: Calcd. for $C_7H_{10}AuCl_3N_2$: C, 19.76; H, 2.37; N, 6.58%. Found: C,19.80; H, 2.35; N, 6.56%. Sublimation. From top to bottom in order: 2, sublimed obtained for three different experiments at a registered temperature of: 78.3 °C, 78.3 °C, 78.2 °C.

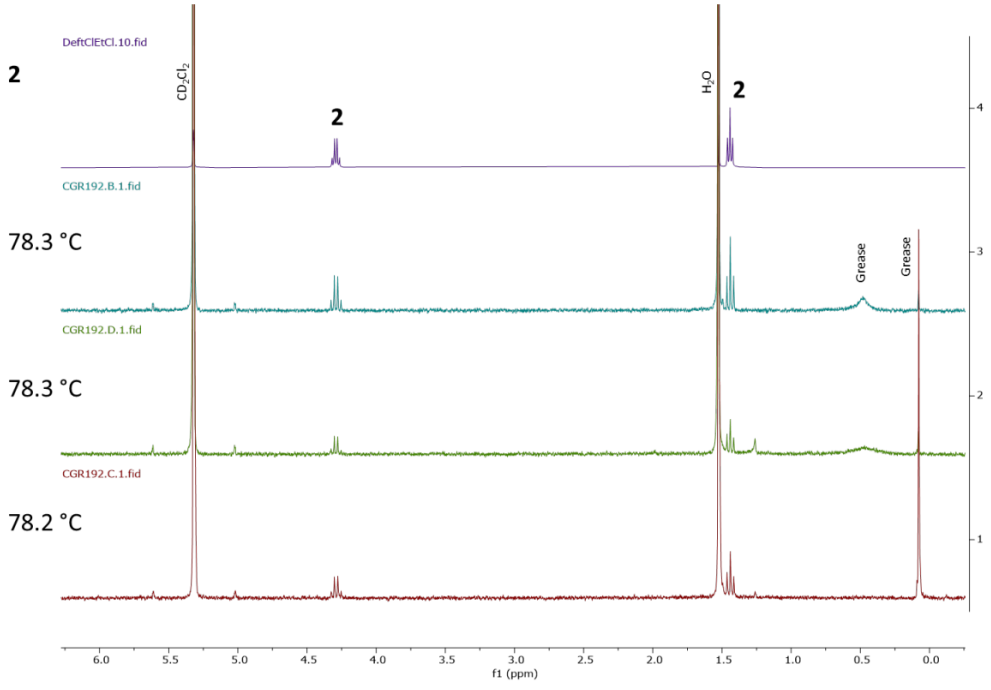

Figure SI-Au.2: ^{1}H NMR spectra stack plot for 2 and the obtained sublimation materials (400 MHz or 300 MHz, CD_2Cl_2).

3 (Cl,iPr)AuCl

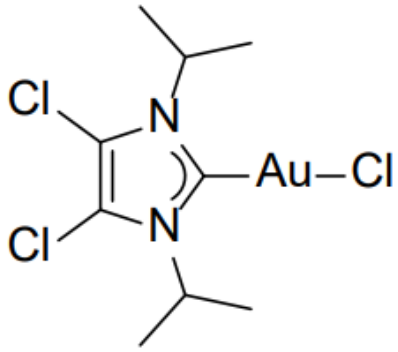

Elemental analysis: Calcd. for $C_9H_{14}AuCl_3N_2$: C, 23.83; H, 3.11; N, 6.18%. Found: C, 23.81; H, 3.09; N, 6.%. Sublimation. From top to bottom in order: 3, sublimed obtained for three different experiments at a registered temperature of: 75.2 °C, 76.2 °C, 75.2 °C.

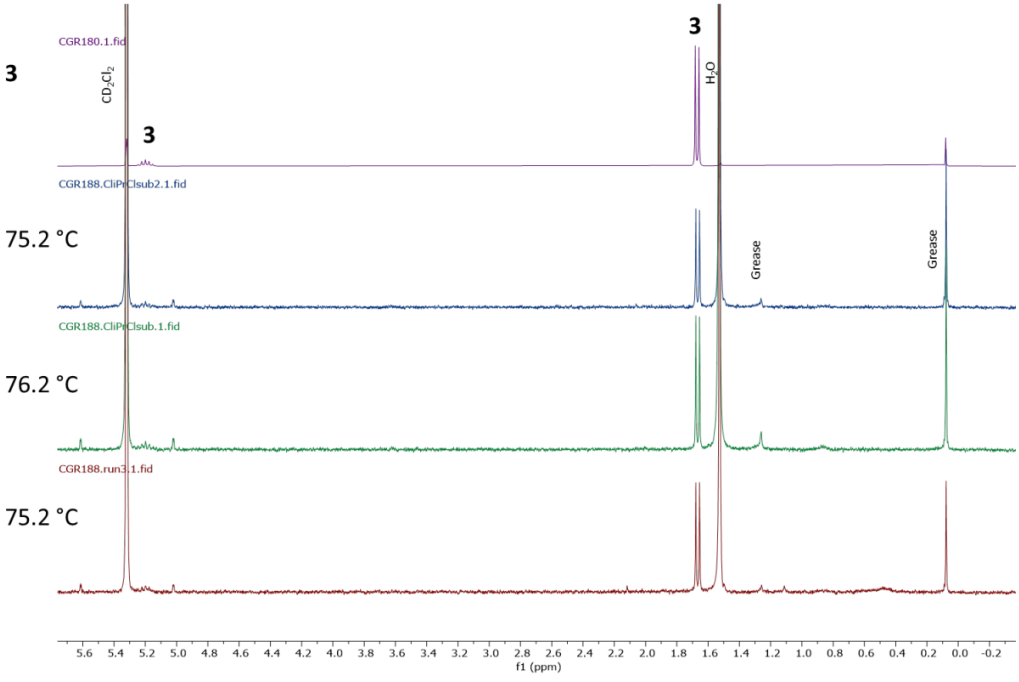

Figure SI-Au.3: ^{1}H NMR spectra stack plot for 3 and the obtained sublimation materials (400 MHz or 300 MHz, CD_2Cl_2).

4 (Cl,Et)AuBr

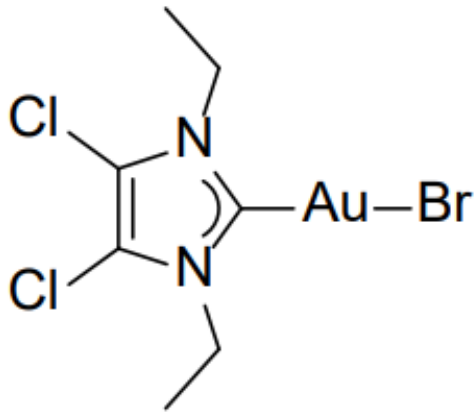

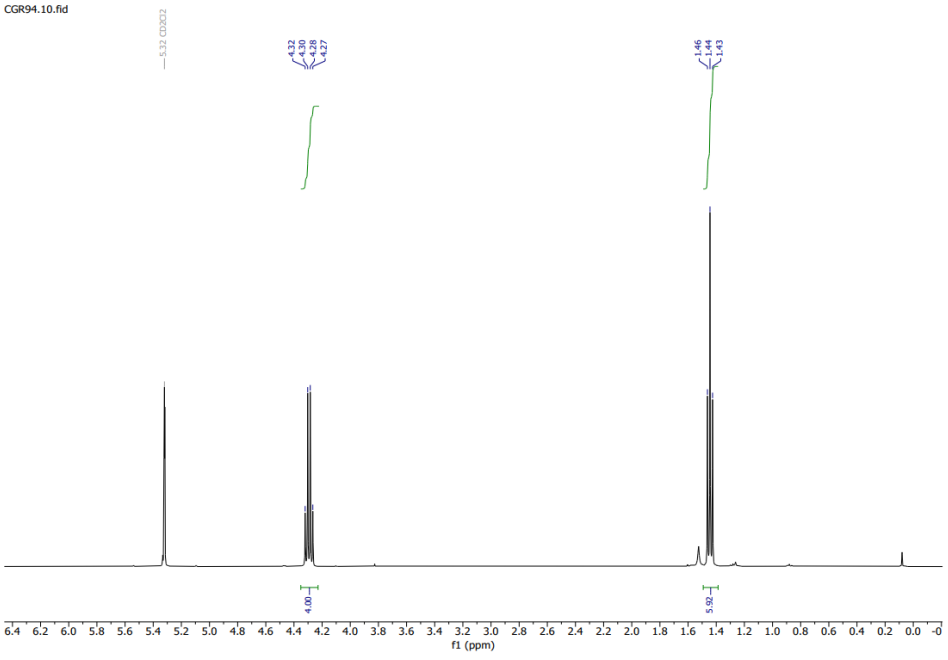

Figure SI-Au.4: ^{1}H NMR spectrum of 4 (400 MHz, CD_2Cl_2)

Sublimation. From top to bottom in order: 4, sublimed obtained for three different experiments at a registered temperature of: 77.3 °C, 77.2 °C, 77.4 °C.

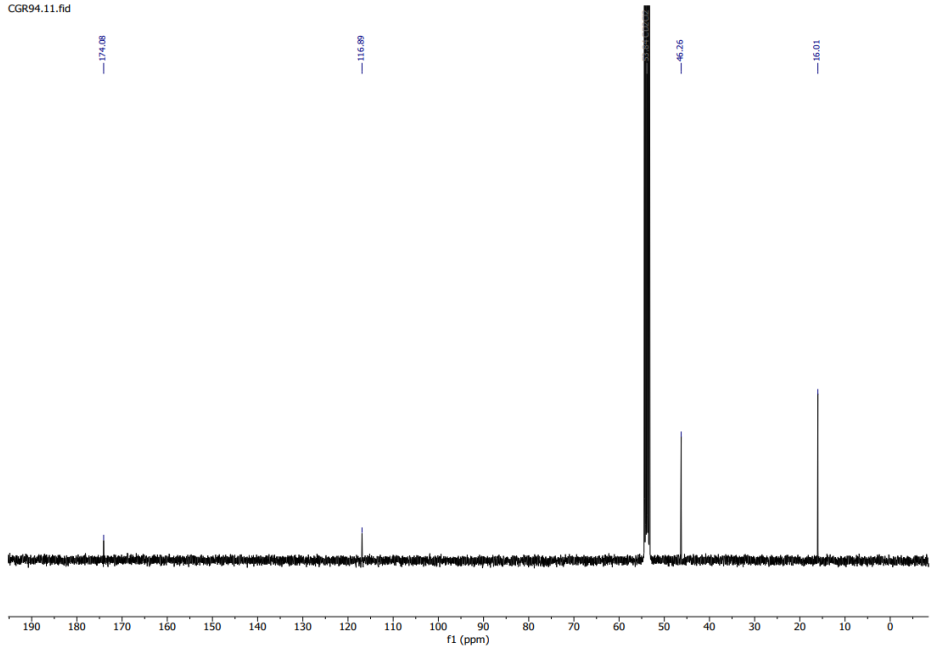

Figure SI-Au.5: ^{13}C NMR spectrum of 4 (101 MHz, CD_2Cl_2)

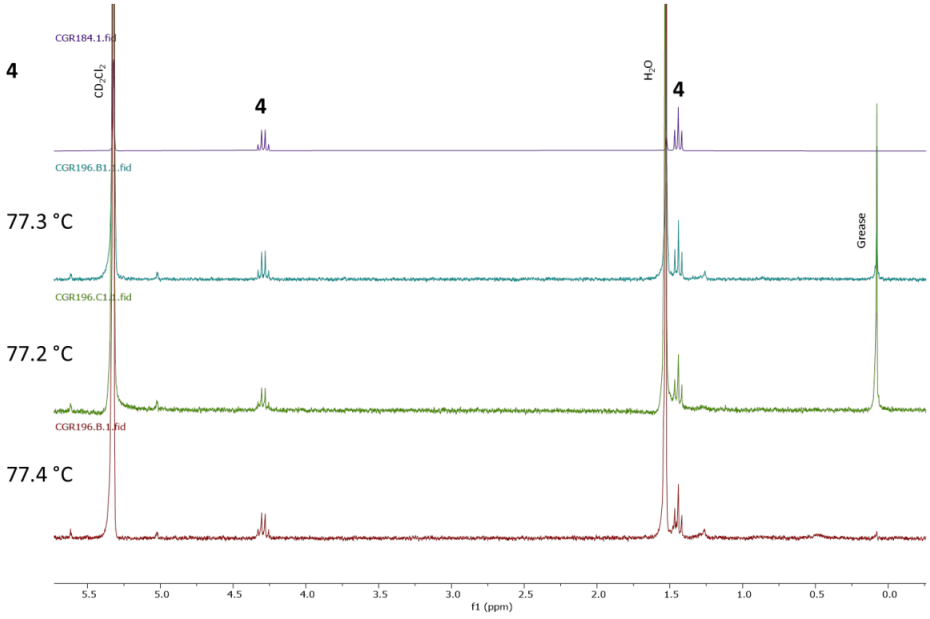

Figure SI-Au.6: ^{1}H NMR spectra stack plot for 4 and the obtained sublimation materials (400 MHz or 300 MHz, CD_2Cl_2).

5 (Cl,Et)AuI

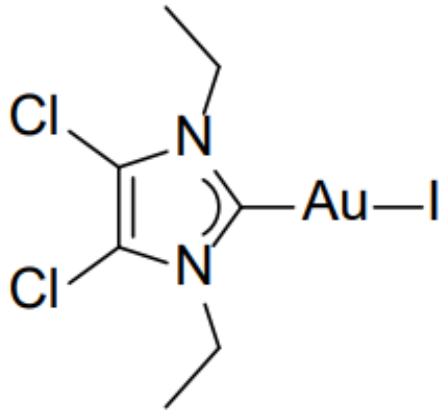

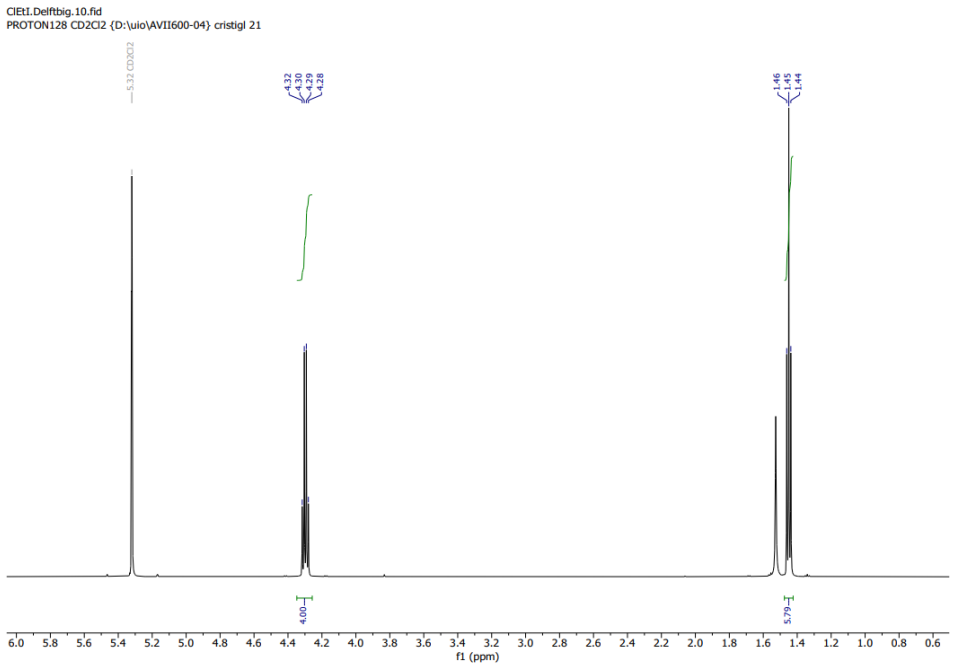

Figure SI-Au.7: ^{1}H NMR spectra stack plot for 5 and the obtained sublimation materials (600 MHz , CD_2Cl_2).

Sublimation. From top to bottom in order: 5, sublimed obtained for three different experiments at a registered temperature of: 73.3 °C, 73.2 °C, 73.3 °C.

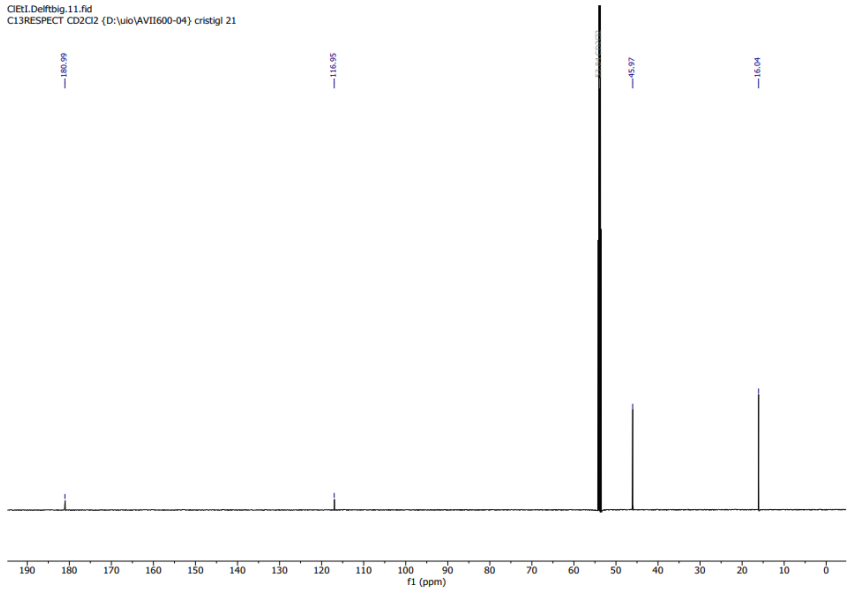

Figure SI-Au.8: ^{13}C NMR spectrum of 5 (151 MHz, CD_2Cl_2).

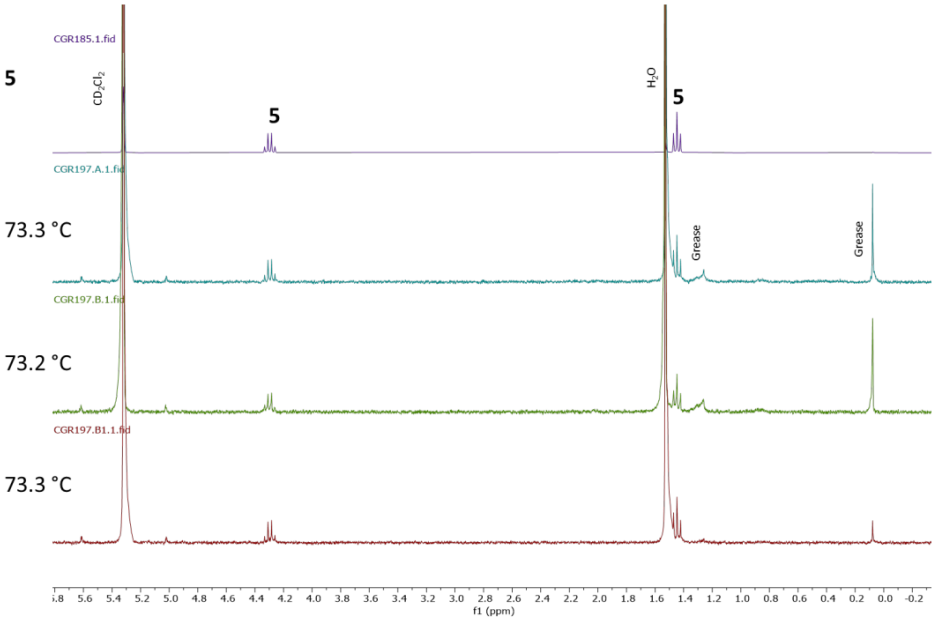

Figure SI-Au.9: ^{1}H NMR spectra stack plot for 5 and the obtained sublimation materials (400 MHz or 300 MHz, CD_2Cl_2).

6 (N,Et)AuCl

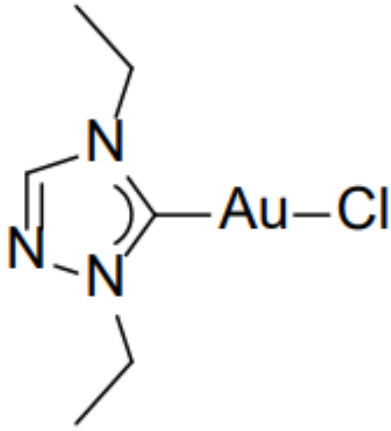

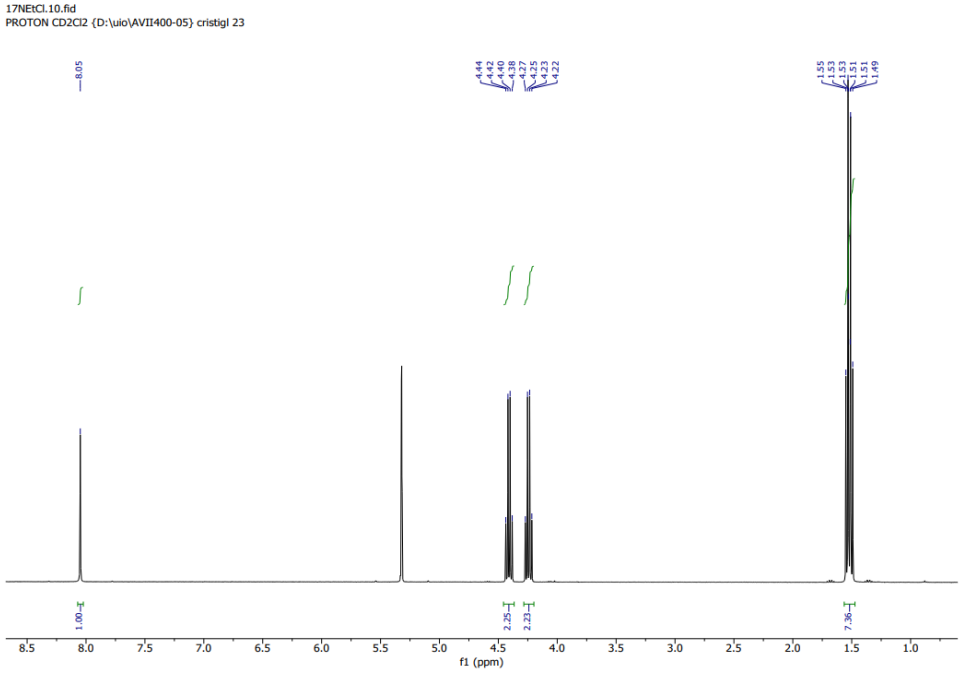

Figure SI-Au.10: ^{1}H NMR spectrum of 6 (400 MHz, CD_2Cl_2).

Sublimation. From top to bottom in order: 6, sublimed obtained for three different experiments at a registered temperature of: 60.2 °C, 59 °C, 60.2 °C.

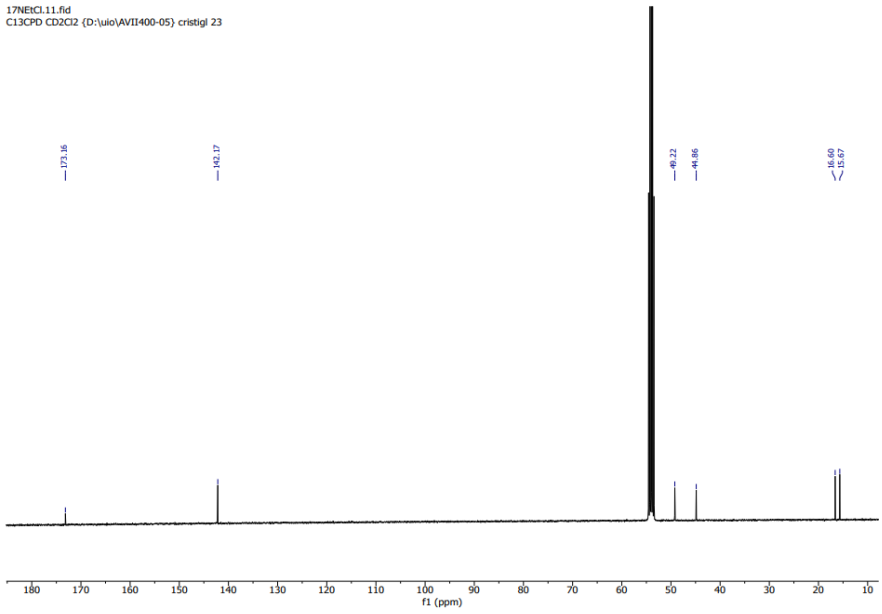

Figure SI-Au.11: ^{1}H NMR spectrum of 6 (101 MHz, CD_2Cl_2).

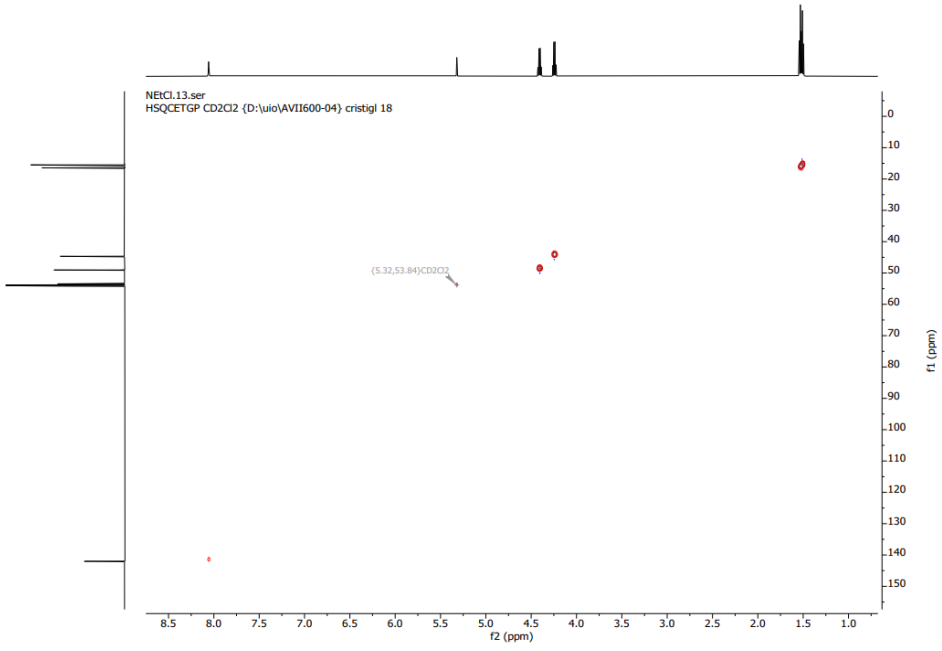

Figure SI-Au.12: ^{1}H–^{13}C HSQC spectrum of 6 (600 MHz, CD_2Cl_2).

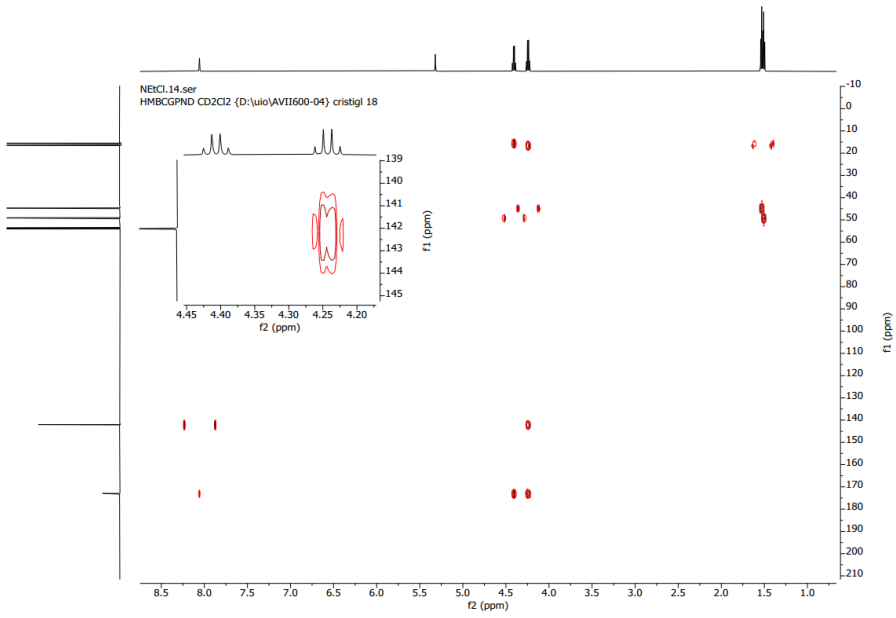

Figure SI-Au.13: $^{1}H–^{13}C$ HMBC spectrum of 6 (600 MHz, CD_2Cl_2).

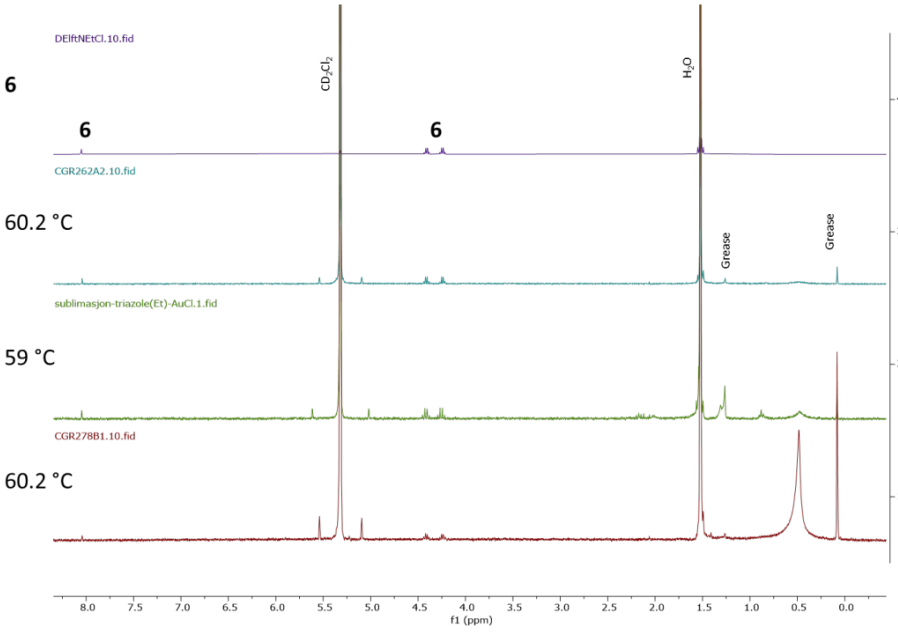

Figure SI-Au.14: ^{1}H NMR spectra stack plot for 6 and the obtained sublimation materials (400 MHz or 300 MHz, CD_2Cl_2).

7 (Cl,Et)$AuCF_3$

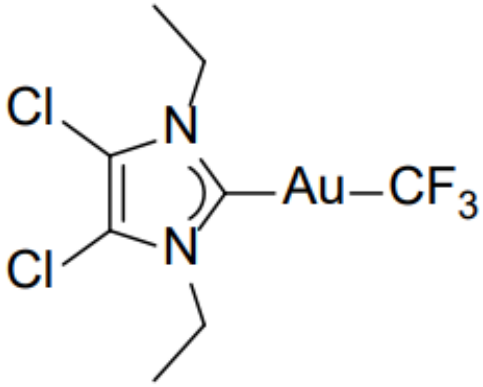

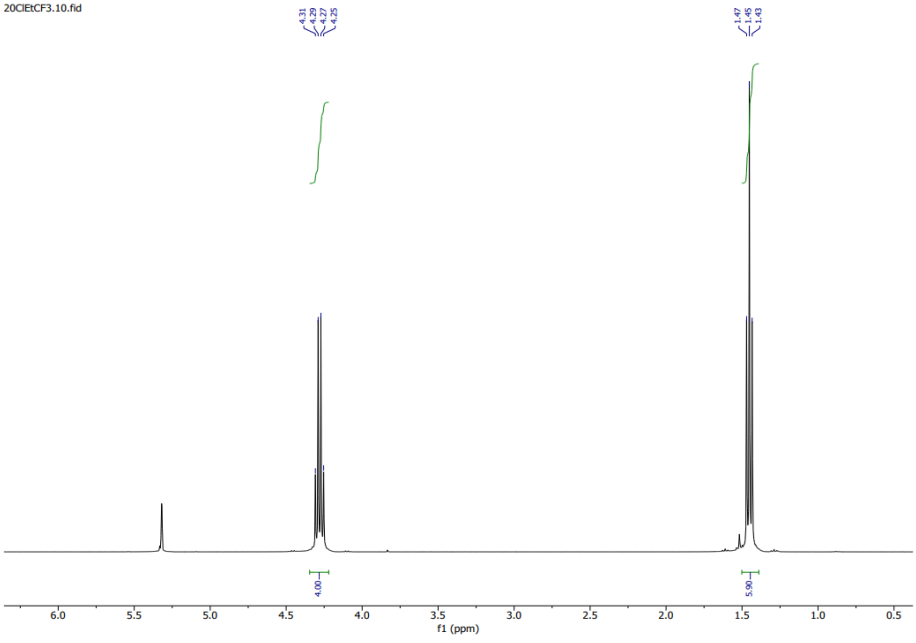

Figure SI-Au.15: ^{1}H NMR spectrum of 7 (400 MHz, CD_2Cl_2).

Sublimation. From top to bottom in order: 7, sublimed obtained for three different experiments at a registered temperature of: 54.9 °C, 52.8 °C, 53.1 °C. For the first experiment no heating rate is applied as immediate sublimation is observed.

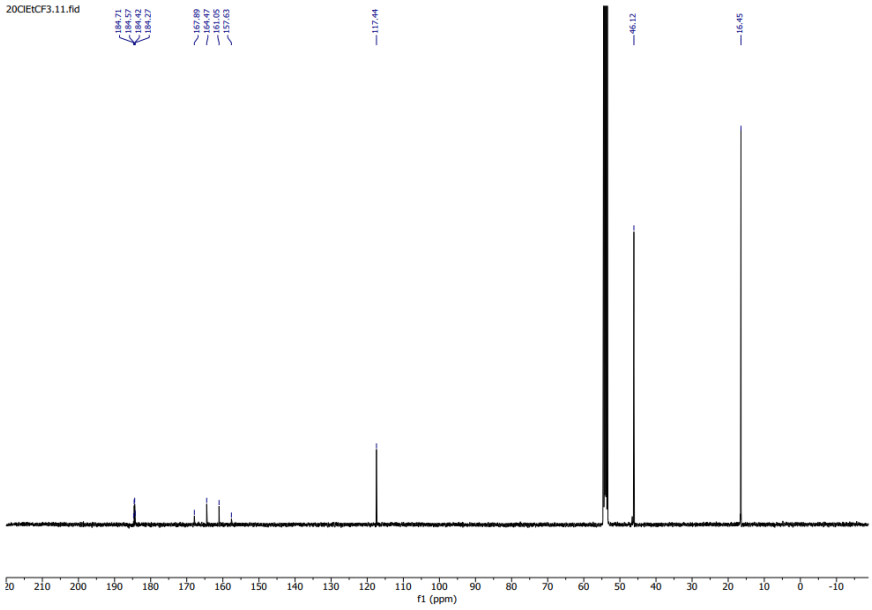

Figure SI-Au.16: ^{13}C NMR spectrum of 7 (101 MHz, CD_2Cl_2).

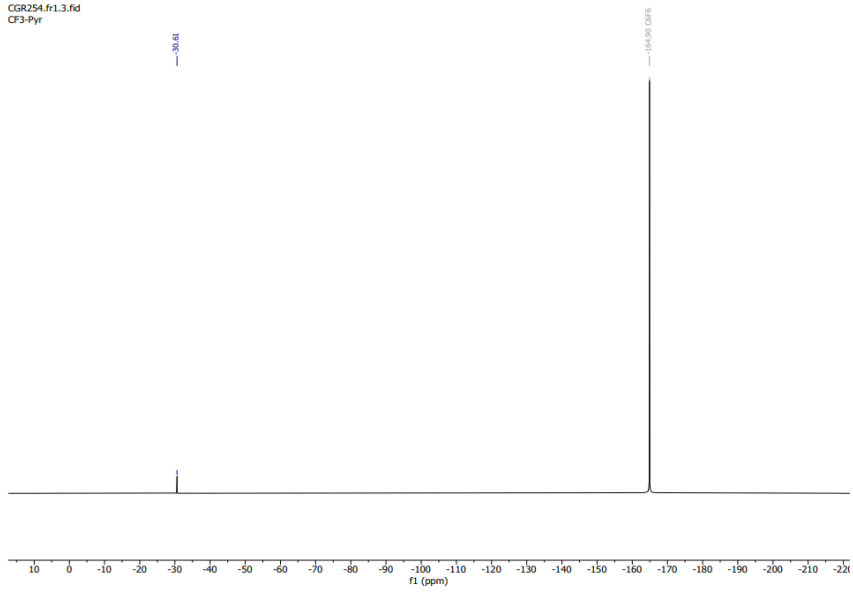

Figure SI-Au.17: ^{19}F NMR spectrum of 7 (188 MHz, CD_2Cl_2).

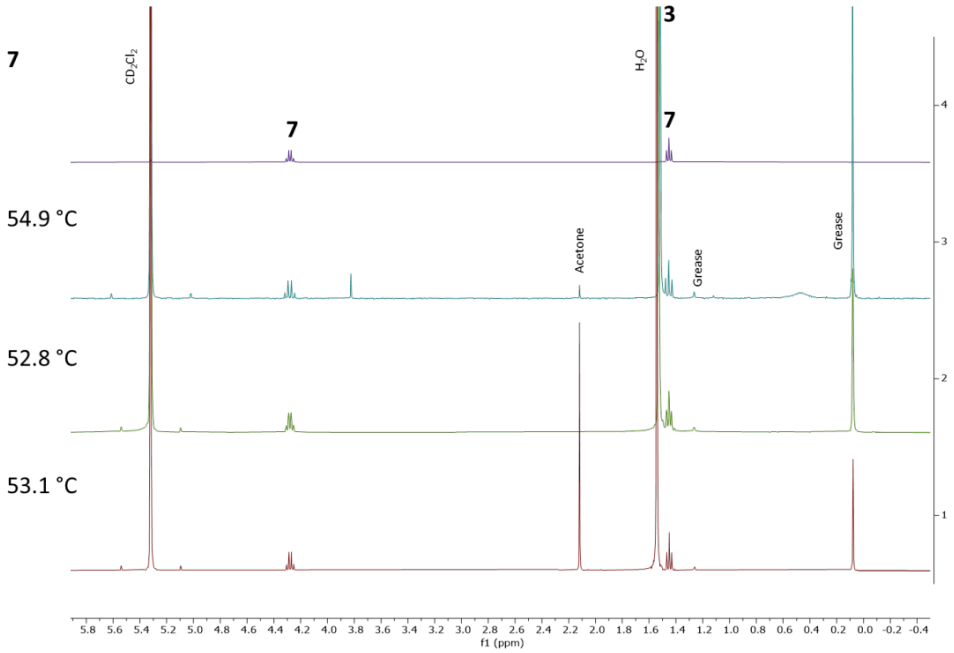

Figure SI-Au.18: ^{1}H NMR spectra stack plot for 7 and the obtained sublimation materials (400 MHz or 300 MHz, CD_2Cl_2).

S2. Supplemental deposition data for 1–7

Element	Average	Standard error
C	65.4	0.23
N	10.5	0.23
Au	5.0	0.07
Si	13.4	0.13
O	2.8	0.04
Cl	0.9	0.02
I	2.0	0.05

Table S4: EDX of 5 performed at 8 keV and 600 pA.

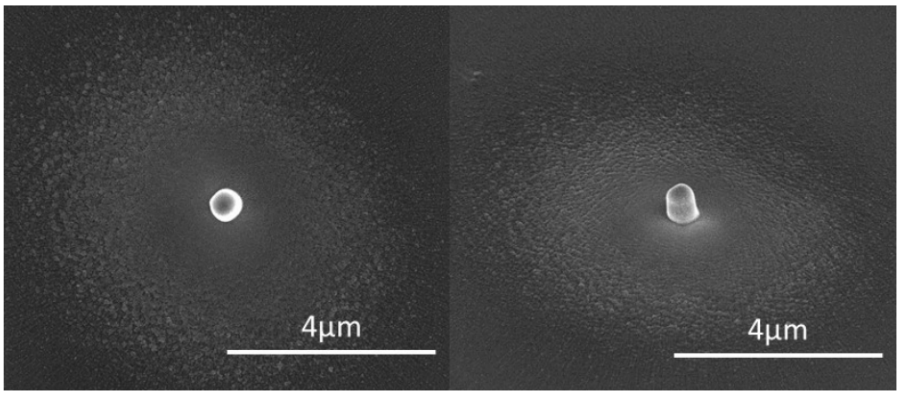

Figure SI-Au.19: 250 × 250 nm^2 square deposits of 6 at 100 °C, pitch 10 nm, dwell 500 µs, 5 kV, 2000 passes, 600 pA, top down and 50° tilt. A round, very granular halo is visible.

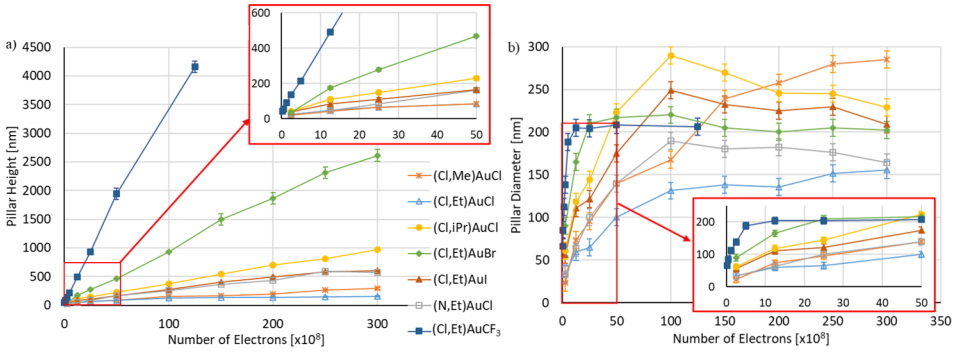

Figure SI-Au.20: (a) Height and (b) diameter of pillars grown using a 5 kV, 40 pA beam as a function of the electron dose given as total number of primary electrons used to deposit a pillar. During all experiments the substrate and the precursor are heated together to 100 °C, except for (Cl,Me)AuCl, which was heated to 120 °C. For each precursor an array of 3 × 3 pillars was deposited. The lines between the points merely serve as a guide to the guide.

4

FEBIP in a Desktop SEM

4.1. Introduction

One of the limitations of the FEBID process is the low growth rate caused by the precursor supply being limited by the maximum allowable pressure in the SEM chamber (usually $10^{-5} - 10^{-7}$ mbar) [104–106]. However, in desktop SEM's, such as the PhenomWorld systems (now part of Thermo Fisher Scientific, but the original name will be used throughout this chapter), which operate at much higher pressure, higher growth rates would be achievable.

Another limitation of FEBID is the usually large carbon content in the deposits. It is well known that focused electron beam induced etching (FEBIE), using water vapor as a precursor, can assist in the removal of carbon and help in the purification of FEBID structures. FEBIE with water vapor has been used to etch graphene, carbon, diamond and has been used to create holes in carbon films [35, 107–113]. It has been used to remove the carbon halo around FEBID deposits and to etch, in a controlled way, parts of FEBID deposits to achieve vertical side walls [114]. Not only that, but water vapor has been used to purify FEBID deposits during deposition achieving pure gold deposits [61]. FEBIE using residual H_2O molecules was also shown to etch carbon [112]. The possibility of operating at relatively high pressure in the desktop SEM allows to work in a water vapor environment (similar to an environmental SEM) which can help in removing the carbon from FEBID structures [76, 115].

FEBIP in a desktop SEM has not been investigated before, as far as we know. This chapter describes modifications of a PhenomWorld desktop SEM to allow for FEBIP experiments aimed at two goals: i) FEBID at precursor fluxes higher than possible in high-end SEM's, and ii) the removal of carbon using FEBIE at water precursor pressures higher than possible in standard SEM's. In the next section the PhenomWorld desktop system will be introduced, after which the modifications will be described in section 4.3 and 4.4.

4.2. The PhenomWorld desktop SEM

PhenomWorld is a company that makes small desktop SEMs, which are about the size of a desktop computer. The PhenomWorld system (or for short Phenom system) is a smaller, simpler and easier to operate, version of an SEM with a somewhat lower resolution and less stringent requirements on the vacuum level of the specimen chamber, which makes it interesting for our goals.

There are some similarities between a Phenom system and an environmental SEM (ESEM). The ESEM [105, 106] operates under high chamber pressure due to the presence of water. However, the pressure at the source, and also in the optical column, needs to be kept much lower and to achieve that, differential pumping is applied in combination with pressure limiting apertures between the column and the specimen chamber [116]. The same concept is applied in the Phenom system to allow for a high pressure in the chamber without affecting the pressure in the column and the source. The Phenom XL allows the user to operate under different chamber pressures: 60 Pa, 10 Pa and 1 Pa by connecting the chamber to the pump through different aper-

tures and by the opening or closing of valves (see Appendix 4.1, Figure A1. 3). The operation of the valves and the variation of the chamber pressure are explained in more detail in Appendix 4.1.

	Pharos	**Phenom XL**	**Phenom XL G2**
Magnification	200–1,000,000x	80 – 100,000x	160 – 200,000x
Acceleration voltage	2 - 15 kV	4.8 – 15 kV	4.8 – 20.5 kV
Resolution	2.5 nm SED and 4 nm BSD	≤ 20 nm	< 10 nm

Table 4.1: Selected specification differences between the Phenom Pharos, XL and XL G2 systems.

There are different systems produced by PhenomWorld. All experiments presented here were carried out in Phenom XL and XL G2 systems because of their large sample holder and the possibility of electrical connections to the sample holder. The main differences between the two systems are shown in table 4.1. All experiments in section 4.3 with the Pt precursor were performed in the Phenom XL G2 while the experiments in section 4.4 with water were performed in the Phenom XL. The Pt deposits in section 4.3 were imaged in the Phenom Pharos to have higher resolution. The main differences between the Pharos and both XL systems are also presented in table 4.1. The operation of the gas injection system (GIS), selected to be built in, requires ± 80 V for the piezo drive, but the driver board of the Phenom XL can only hold up to 30 V. Therefore the Phenom XL G2 was used for the Pt experiments. The electron source used in both systems is CeB6. The vacuum at the source is usually between 10^{-8} and 10^{-7} mbar. The sample holder in the XL fills basically all of the specimen chamber. The latter, being much smaller than the specimen chamber in a regular SEM, allows for a very short pump-down time, typically less than 1 minute between loading the sample and starting to image. Figure 4.1 a) shows the standard sample holder of the Phenom XL, containing an array of sample stubs. With the thumb wheel at the lower front side the height of the plate holding the stubs can be adjusted. Different types of holders exist. There is also a simple sample holder, called “generic sample holder”, shown in figure 4.1 b), which does not contain the plate with stubs, offering the possibility to mount non-standard samples. The generic sample holder also contains electrical connections to the outside world. In this work both the generic and standard sample holders were used. Other types of sample holders exist, but they were not used in this project.

All Phenom systems have a back scatter detector (BSD), but some systems also have a secondary electron detector (SED) and/or a detector for energy dispersive X-ray spectroscopy (EDX). The Phenom is equipped with a four-quadrant semiconductor backscatter detector (BSD) [105, 117] that provides composition and topography information. The highly energetic back scattered

electrons (BSE) produce electron-hole pairs when they undergo inelastic scattering after penetrating the depletion region in the semiconductor [105, 118]. Operating the detector quadrants in pairs and adding the signals provides material contrast [119]. By enabling specific quadrants and subtracting the signals, topographic information is collected [119]. The detector is placed under the objective lens above the sample and the electron beam passes through a central hole as illustrated in figure 4.2. The BSD can operate at moderate vacuum levels (up to a few mbar) [116] which is useful in the experiments with precursors or water vapor.

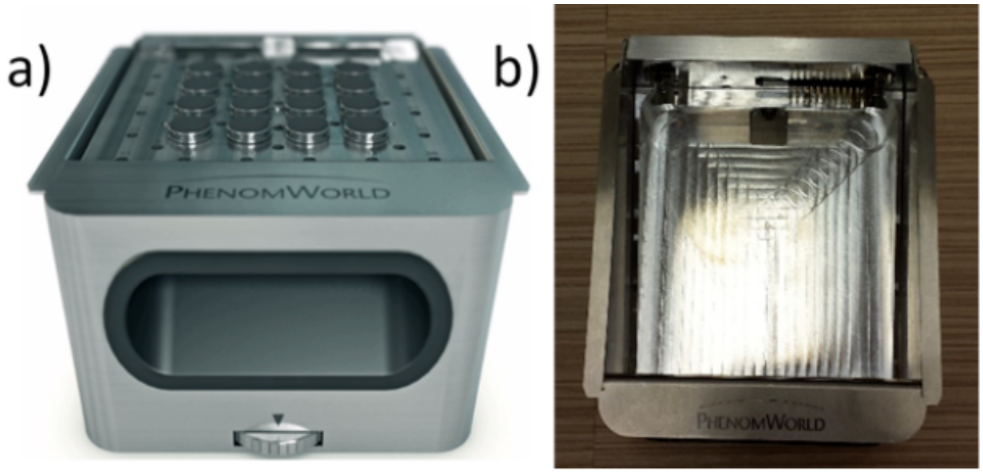

Figure 4.1: a) Standard XL sample holder which can accommodate nine 25 mm diameter stubs or thirty six 12 mm diameter. b) The generic sample holder with electrical connections (top right).

The SED used in the Phenom system is an Everhart-Thornley detector (ETD). It can only operate up to a pressure of 1 Pa. The position of the SED can be seen from figure 4.3 (top view) and 4.4 (side view). It is placed at an angle to the horizontal plane to maximize the efficiency. The detector consists of a scintillator surrounded by a Faraday cage. A positive potential is applied to the Faraday cage to attract the low energy secondary electrons (SE). The electrons are further accelerated to the scintillator, to which an even higher positive potential is applied, where they are releasing photons [105, 118]. The photons are guided to the photomultiplier where photoelectrons are generated and amplified [118, 120].

The EDX detector used in the Phenom system is a fully embedded silicon drift detector (SDD) which is thermoelectrically cooled. The detector's active area is 25 mm^2. The detector has an ultrathin silicon nitride window allowing for a detection range from B to Am. The energy resolution is ≤ 132 eV at Mn Kα. The maximum input count is 300000 counts per second (cps). A special software package was created for element identification (EID). More details about the EDX detector can be found in the datasheet in [121].

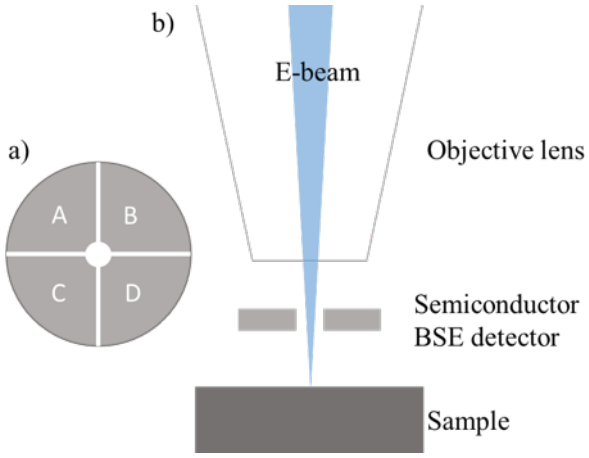

Figure 4.2: a) Top view of the four quadrant semiconductor back scatter detector. b) side view of the position of the detector with respect to the pole piece and the sample.

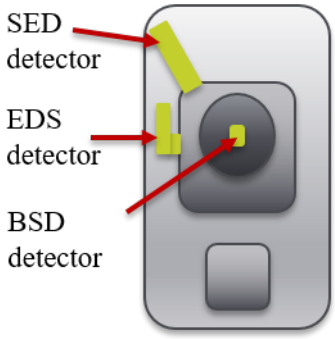

Figure 4.3: Top view of detectors present in the Phenom XL system. The EDX detector is placed at an angle of 29° to the horizontal plane.

The vacuum of the Phenom system is controlled through a manifold with vacuum valves. A simplified diagram of the system operation is illustrated in figure 4.5. The starting position of the sample holder is under the navigation camera, then it moves downwards (due to the pumping of the lift) and then to the left till it is below the lens. These movements are controlled through the valves that pump and vent the lift and the shuttle. The details of the system operation are described in Appendix 4.1.

The Phenom operation is controlled through the Phenom Programming Interface (PPI) using python scripts. This helps to automate processes. Scripts can be used to do various things from setting parameters to reading out data, acquiring images, saving them, moving the beam or the sample, changing the state of the system (standby/ wakeup/etc.). This will be used in the experiments of this study to control the beam and the stage during deposition and imaging.

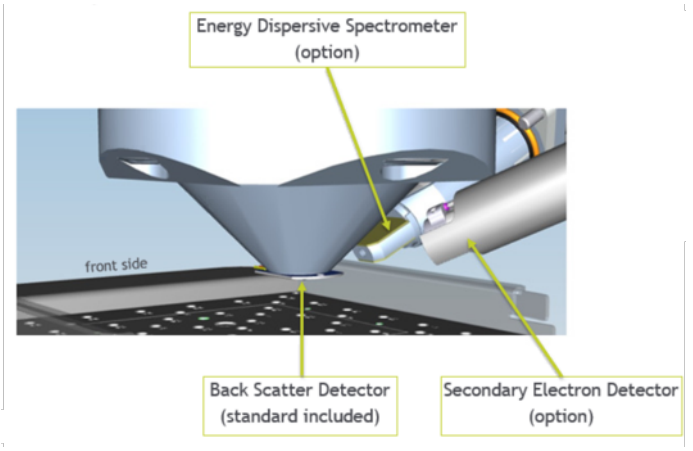

Figure 4.4: Side view of the detectors with respect to the pole piece and the sample holder.

4.3. FEBID from $MeCpPtMe_3$ under high pressure in the Phenom XL G2

As mentioned in the introduction, the typical operating pressure in an SEM chamber is $10^{-5} - 10^{-7}$ mbar. The SEM will be automatically vented if the threshold pressure (10^{-4} mbar) is exceeded. This limits the maximum possible precursor flux throughout a FEBID process. In this work, it is investigated whether FEBID growth in the Phenom increases when the precursor flux is increased by further heating and thus operating at much higher chamber pressure than what is allowed in a high vacuum (HV) SEM.

FEBID was never performed in a Thermo Fisher Desktop SEM before. Unlike a HV SEM, a desktop SEM is not equipped with ports or a gas injection system (GIS). Therefore a method of inserting and heating the precursor was required. The precursor used for platinum deposition was Trimethyl (methylcyclopentadienyl)platinum(IV) ($MeCpPtMe_3$). The threshold pressure in a regular SEM allows heating the precursor up to about 55 °C. Further increasing the precursor temperature increases the chamber pressure approaching the limit. In the Phenom desktop SEM, the chamber pressure can reach about 1 mbar while the source pressure stays in the order of 10^{-7} mbar. This allows heating the precursor to 90 °C and higher, thereby increasing the precursor flux.

4.3.1. Gas Injection System (GIS) built in to the Phenom XL G2 Sample Holder

The solution chosen to insert the precursor in the Phenom XL G2 chamber was to install a small GIS inside the sample holder. Kleindiek Nanotechnik is a company that manufactures nano-manipulators and a small GIS that can fit inside an SEM chamber.

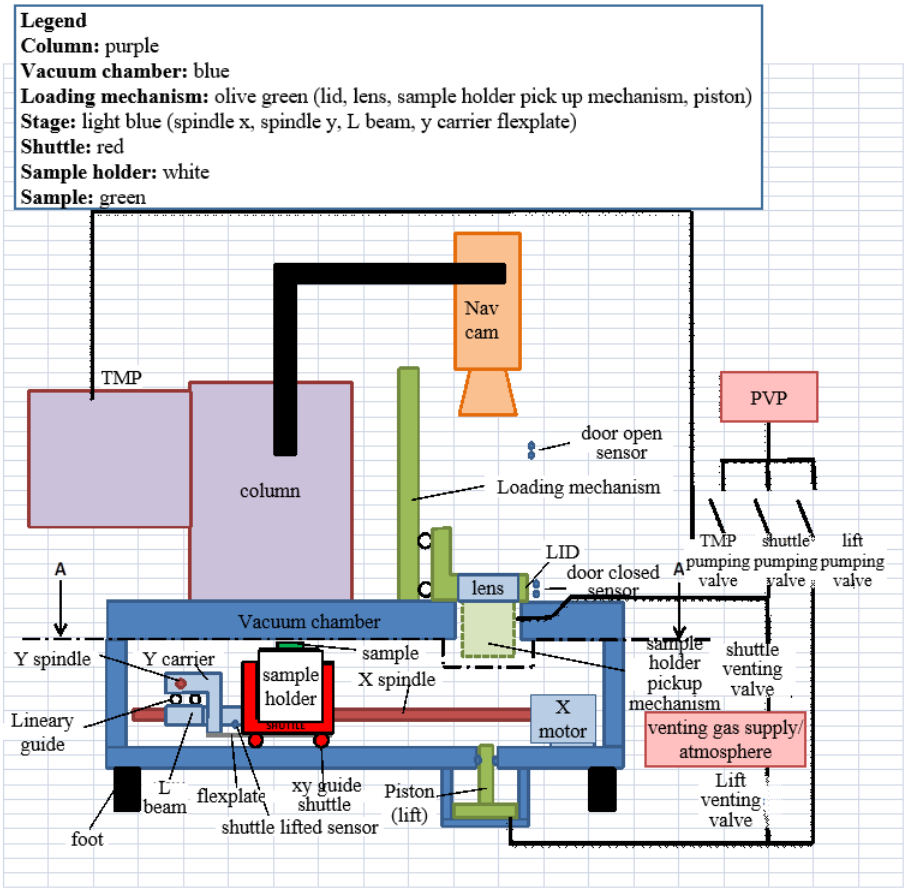

Figure 4.5: Simplified diagram of parts of the Phenom XL system. PVP is pre-vacuum pump, TMP is turbo molecular pump.

Figure 4.6 shows the Kleindiek GIS together with its 2 connectors. One connector is for the temperature control and the other is for the nano-controller that controls the valve in steps, such that it is possible to have it partially open. The two GIS controllers and the power supply are shown in figure 4.7. First the precursor was filled in to the Kleindiek GIS. Then it was mounted in the XL G2 generic sample holder pointing towards the sample as shown in figures 4.8 and 4.9. Special cables were designed and manufactured to connect the GIS to the sample holder feedthroughs and to connect the controllers to the Phenom XL G2. Details of the cabling are shown in Appendix 4.3.

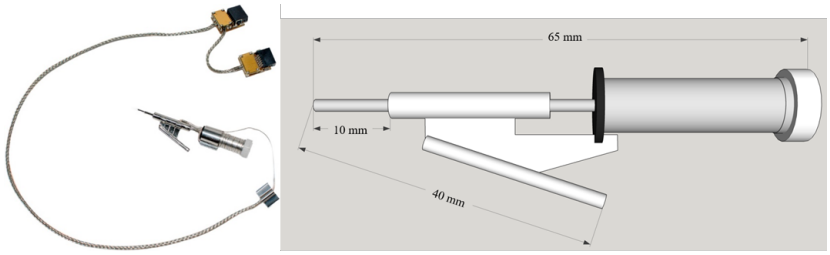

Figure 4.6: Kleindiek GIS with 2 connectors for the temperature controller and the nano-controller that controls the valve.

Figure 4.7: Kleindiek controllers. The top one is the temperature controller, the black knob allows the user to set the temperature. The reading below the horizontal line in the display is the target temperature and the one above is the current temperature. The middle box is the nano-controller which controls the valve. The bottom one is the power supply.

In order to fit everything in the existing sample holder such that the sample is below the nozzle of the GIS, the working distance turned out to be quite large, unfortunately. The optimal working distance for the XL system is about

8 mm, but in this setup the working distance was about 28-29 mm. Moreover, the sample and the whole stub plate had to be tilted to have the sample mounted below the nozzle at the smallest possible working distance. The distance between the nozzle and the sample was not an accurately controlled parameter since everything was placed manually. The distance was estimated by focusing on the nozzle, then focusing on the sample and subtracting the working distances in both cases. For most experiments the distance between the nozzle and the sample was about 4 mm.

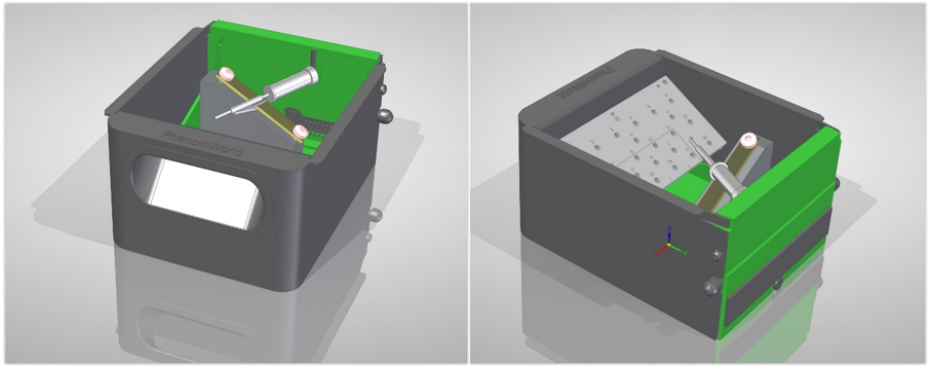

Figure 4.8: Cartoons of the generic sample holder modified with a gas injection system (GIS) for letting in precursor gas. The stub plate was cut and tilted to fit together with the GIS inside the sample holder.

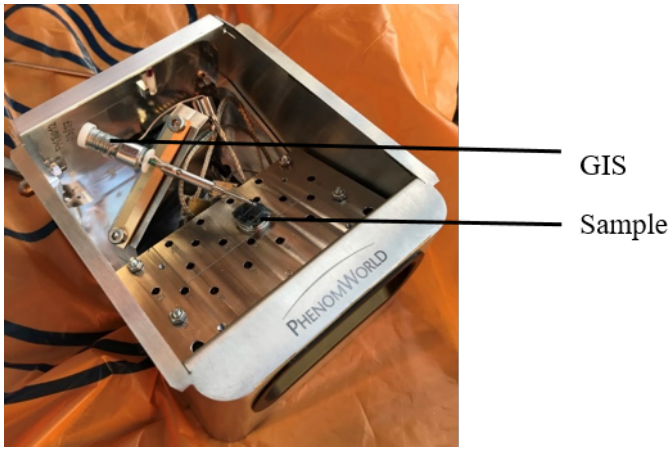

Figure 4.9: Picture of the generic sample holder with the GIS and a Si sample mounted.

A silicon sample was used for all the deposition experiments providing a flat surface for deposition. The chamber pressure was monitored using a Pfeiffer Pirani pressure gauge. The temperature of the precursor was controlled with the temperature controller (the top one in figure 4.7) in the range between 40

and 90 °C. The thermal decomposition temperature of this precursor is above 360 °C which is far above the temperature range used in all experiments [38].

All depositions were performed at 5 kV and a beam current, as measured using a Faraday cup, of 1.93 nA. The Phenom systems are designed for fast and easy imaging, but not for patterning using FEBID. Therefore, the user control of the beam deflection is very limited even with the use of PPI. In a typical FEBID process in a HV SEM, the beam is controlled through the SEM patterning software. A stream file with the dwell time and coordinates of points to be exposed is created and serves as input to the software. In the patterning process the beam is focused on each specified pair of coordinates in the specified order and then moves to the next coordinates. The stream file can contain instructions for blanking the beam for a specified time after exposing a certain position. In a Phenom system most of this is inaccessible to the user. Through PPI, the stage position and the magnification can be controlled as well as the beam blanking. However, when the beam is un-blanked it is continuously scanning the full field of view. This doesn't allow for high resolution FEBID patterning, but creating big deposits is still possible by exposing the entire field of view. More tricks will be discussed later to facilitate patterning, but for the first experiments no high resolution patterning was required. Square deposits were made to compare the growth and composition at different precursor reservoir temperatures. In the XL G2, the highest magnification was achieved at a horizontal field width (HFW) of 1.07 µm. Most of the depositions were done by exposing the whole field of view at this magnification for either 2 or 5 minutes. This HFW corresponds to 684 pixels and thus a spacing of about 1.56 nm between pixels. The dwell time per pixel is 200 ns for every scan. This means that there are about 641 scans per minute.

For comparison deposits were also made in the HV Nova Nanolab650 SEM (Thermo Fisher Scientific) with the same precursor and attempting to achieve deposition conditions as similar as possible to those in the Phenom system. The same writing strategy was applied at the same beam energy and approximately the same current (5 keV and 1.6 nA), dwell time per pixel (200 ns), pitch (2 nm) and a total deposition time of either 2 or 5 minutes. However, the precursor pressure, the GIS design, the working distance and the distance between the nozzle and the substrate were different between the Nova and the Phenom. In the Nova, the distance between the nozzle and the substrate is about 150 µm. Depositions were done on a horizontal and on a 40 degree tilted substrate, the latter to mimic the conditions in the Phenom. Due to the vacuum restrictions in the Nova Nanolab650 SEM it was not possible to heat the precursor up to 90 °C, as in the Phenom. Depositions were done at 40, 45, 50 and 55 °C reaching a maximum chamber pressure of about 3.4×10^{-5} mbar.

4.3.2. Results and Discussion

Deposition in the Desktop SEM

SED and BSD images were taken of the deposits formed in the desktop SEM. Figure 4.10 shows the SE images of the shapes that were deposited for 2

minutes each. The GIS heating temperature was varied from 50 °C to 90 °C in steps of 5 °C shown in images a) to i) respectively. This resulted in a chamber pressure ranging between 0.002 and 0.02 mbar. A typical graph of the variation of the chamber pressure with precursor temperature is shown in figure 4.11. It is noted here that this is the total pressure, i.e. the total of the partial pressure of the precursor and the rather high background pressure of the system, the latter clearly dominating the pressure at precursor temperatures below 65 °C. The pressure then would be expected to go up as shown by the dashed blue line in figure 4.11. The downwards shift of the curve and the pressure drop at 65 °C might indicate when the increasing flux of heavy precursor gas molecules starts to dominate the total pressure, leading to a lower pressure readout on the gas-dependent Pirani gauge.

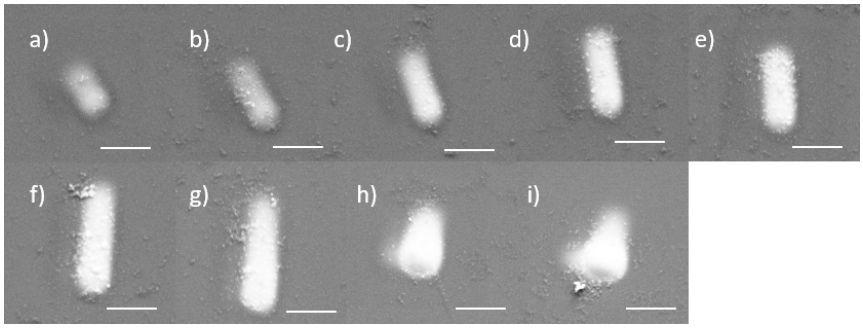

Figure 4.10: Top-down SE images of deposits made at 5 keV and 1.93 nA, exposing the full field of view (1.07µm x 1.07µm) for 2 minutes. The HFW of 1.07 µm corresponds to 684 pixels and thus a pitch of about 1.56 nm. The dwell time per pixel is 200 ns. The GIS heating temperature was varied from 50 °C to 90 °C in steps of 5 °C shown in images a) to i) respectively. Images are taken at 5 keV, 1.93 nA. The scale bars are 3 µm.

As explained in the previous section, the deposit is obtained by exposing the full field of view of 1.07 µm in length and height. Because the sample is tilted the deposition area will be the projection of the rectangular scan area on to the tilted sample surface. The resulting deposits, as shown in figure 4.10, were elongated rectangular shapes with curved corners and covered and surrounded by grains. The images were taken in the Phenom Pharos and are top-down images. It is noted here that deposition on tilted surfaces will also enhance the growth due to the increased number of secondary electrons emitted from a tilted surface. At the highest temperatures, shown in figure 4.10 h) and i) it seems that the growth was more lateral (in the substrate plane) rather than vertical (along the beam). Figure 4.12 shows the SE images of the shapes that were deposited for 5 minutes each. The GIS heating temperature was varied from 40 °C to 90 °C in steps of 5 °C shown in images a) to k) respectively. The deposits again show an elongated rectangular shape similar to the shapes in figure 4.10 or a slightly curved shape. The grains on and around the deposits

are visible in figure 4.12 as well. In both sets of deposits in figures 4.10 and 4.12, the size of the deposit increases as the precursor temperature increases. This will be quantitatively analyzed later in this section.

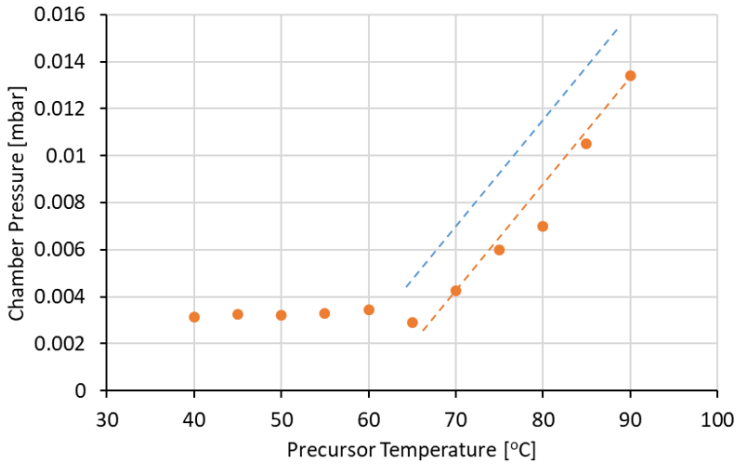

Figure 4.11: Chamber pressure at each precursor temperature in the Phenom XL G2. The dotted blue line indicates the expected pressure rise with temperature considering only the background gas. The dotted orange line is a guide to the eye through the measured lower lying total pressure data of the background pressure and the heavier precursor gas.

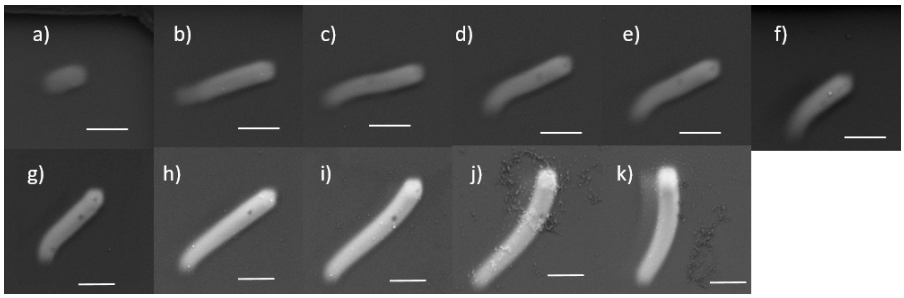

Figure 4.12: Top-down SE images of deposits made at 5 keV and 1.93 nA exposing the field of view (1.07µm x1.07µm) for 5 minutes. The HFW of 1.07 µm corresponds to 684 pixels and thus a pitch of about 1.56 nm. The dwell time per pixel is 200 ns. The GIS heating temperature was varied from 40 °C to 90 °C in steps of 5 °C shown in images a) to k) respectively. Images are taken at 5 keV, 1.93nA. The scale bars are 3 µm.

The setup explained in section 4.3.1 is a prototype and is all manually arranged in the small sample chamber available. This unfortunately led to drift of both the GIS position as well as the sample position, the latter probably

caused by the tilted sample mounting construction. Drift is the most likely cause for the designed square area of deposition to turn out as an elongated shape. Especially when depositing at the highest magnification, the drift is very high. A set of squares were deposited at a lower magnification to find out if the drift is lower in this case. Squares of 4.01 µm were deposited by exposing a full field of view of this width. Figure 4.13 shows the 4.01 µm squares deposited for 2 minutes each at temperatures between 45 and 90 °C. In this case, the deposits turn out as square shapes as defined. Indeed, the drift is most severe at the highest magnification. It is also not constant and not always in the same direction, which may have led to the curved elongated shapes observed when depositing at the highest magnification.

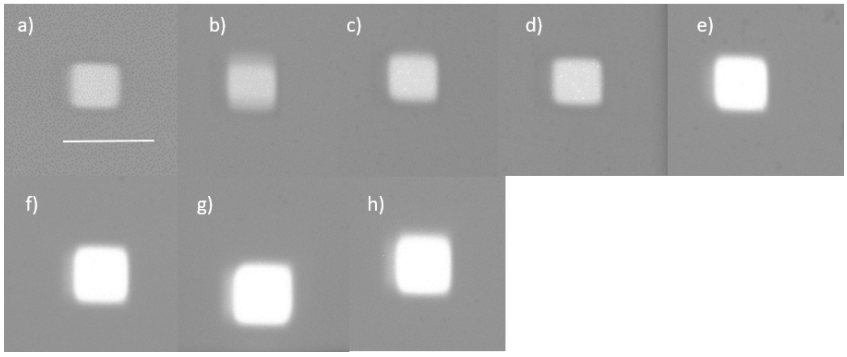

Figure 4.13: Top-down SE images of deposits made at 5 keV and 1.93 nA in Phenom XL G2, exposing the full field of view (4.01µm x 4.01µm) for 2 minutes. The HFW of 4.01 µm corresponds to 684 pixels and thus a pitch of about 5.86 nm. The dwell time per pixel is 200 ns. The GIS heating temperature was a) 45 °C, b) 50 °C, c) 55 °C, d) 60 °C, e) 75 °C, f) 80 °C, g) 85 °C, h) 90 °C. Images are taken at 5 keV, 1.93 nA. The scale bar is 8 µm.

Deposition in the high vacuum SEM

Reference deposits were made in the HV Nova Nanolab650 SEM under conditions as similar as possible to those in the Phenom. As shown in Figure 4.14, the shapes that were deposited in the HV SEM are much better controlled compared to the ones deposited in the Phenom. The designed square length was 1.07 µm and the measured lengths and widths of the deposits were between 1.1 and 1.4 µm while in the Phenom they were between 1.5 and 13 µm. In a HV SEM, using a stream file, deposition can be controlled per pixel. The beam position is defined using x and y coordinates of pixels in the desired order together with the dwell time during which the beam will stay at each pixel. Therefore, there is no need to use the highest magnification of the SEM. However in the Phenom, it was not possible to address pixels, the beam is only scanning. The scan area had to be the same size as the deposit, which was the reason to use high magnification. Furthermore, since the setup in the HV SEM is designed for deposition experiments, with a special port for the GIS,

and without a tilted sample mount, the drift is much less of a problem in the HV SEM. In the Nova Nanolab650 SEM, the working distance is about 5 mm and the needle is positioned at about 150 µm above the sample and 150 µm away from the beam. In the Phenom the working distance was about 29 mm and the needle was about 4 mm away from the sample. Figure 4.15 illustrates the differences in the setup between the Phenom and the Nova Nanolab650 SEM. The deposits in the Nova Nanolab650 SEM were performed on both a flat and a tilted sample. The smaller the working distance, the higher the resolution due to the better focus. The closer the sample to the nozzle, the higher the precursor flux arriving at the sample.

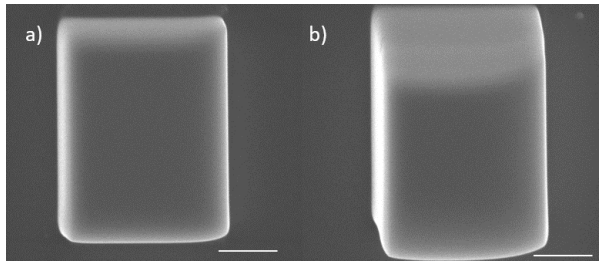

Figure 4.14: Top down SE images of squares deposited by FEBID in the HV Nova Nanolab650 SEM at 40° tilt 5 keV, 1.6nA, precursor heated up to 40 °C and a dwell time per pixel of 200 ns, pitch of 2 nm and a total deposition time of 2 and 5 minutes for a) and b) respectively. The scale bar is 500 nm.

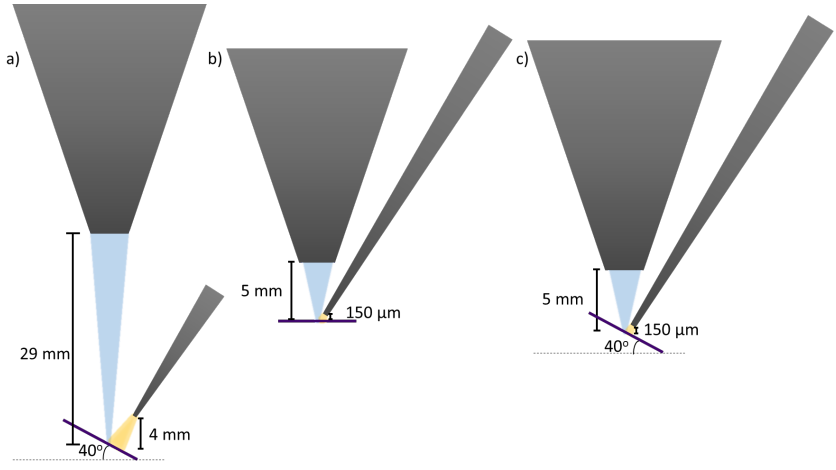

Figure 4.15: a) Illustration of the setup in the Phenom system including the pole piece, the GIS nozzle and the sample. b) and c) illustrations of the setup in the Nova Nanolab650 SEM. b) The sample is horizontal and c) the sample is tilted to mimic the setup in the Phenom system.

Another difference worth noting is the nozzle design. The Kleindiek nozzle is a bevelled nozzle (as shown in figure 4.16) where the edge is parallel to the substrate which guides the molecules closer to the substrate and it has a hole for the beam to reach the substrate surface [122]. However, in the Nova Nanolab650 SEM the GIS has a straight tube nozzle design as shown in figure 4.17. Figure 4.18 shows an illustration of the difference in the nozzle shapes between the Kleindiek and the Nova Nanolab650 SEM GIS nozzles. According to [122], the beveled nozzle shape is expected to increase the accessible precursor flux by about 4.6 times compared to the straight nozzle.

Growth rate

The growth rate determined at different precursor temperatures will indicate whether the change in the precursor flux by increasing the temperature influences the growth rate. The deposited volume divided by the total deposition time is used as a measure of the growth rate. From figures 4.10 and 4.12 it is seen that the shapes of the deposits are irregular and thus the determination of the volumes is not trivial. However, rough estimates of the dimensions were used to approximate the volume of the deposits. The shape of a deposit was approximated as half a cylinder (its cross section perpendicular to the substrate is a semicircle). Figure 4.19 shows the estimated growth rates of the '5 minute' deposits made in the Phenom XL G2 system and in the Nova Nanolab650 SEM at different precursor temperatures, and a clear increase is observed with increasing temperature. The growth rate in the Phenom system increases more rapidly with the precursor temperature than in the Nova, with 0.065 μm^3/(min.K) resp. 0.016 μm^3/(min.K), linearizing the data. It is noted that this occurs despite the larger distance between the nozzle and the sample in the Phenom, compared to the Nova, which decreases the local flux of precursor molecules at the sample considerably. The large additional supply of molecules originating from contaminants in the phenom system must be responsible for this rapid increase, perhaps in addition to an increased surface coverage [12] at higher pressures. Using figure 4.11 the growth rate for the Phenom deposits can be plotted versus chamber pressure, which is a better measure of the total supply of molecules to the substrate. This is shown in figure 4.20. Each point is an average of volumes of several structures deposited under the same conditions. The growth rate is observed to increase rapidly at low pressures and saturates at high chamber pressures, the growth probably becoming limited by the electron current. At low pressures the growth will be dominated by contamination growth, the Pt-precursor partial pressure being only a small fraction of the total pressure. The volumes of the Nova Nanolab650 deposits grown in five minutes were much smaller than those of the Phenom deposits (max. 2.5 μm^3 and 20 μm^3, respectively). Operating at higher chamber pressures, allowing for higher precursor fluxes, clearly increases the growth rate. In the next sub-section the composition of the deposits will be investigated to learn how the high contamination level of the Phenom system contributes to the deposition.

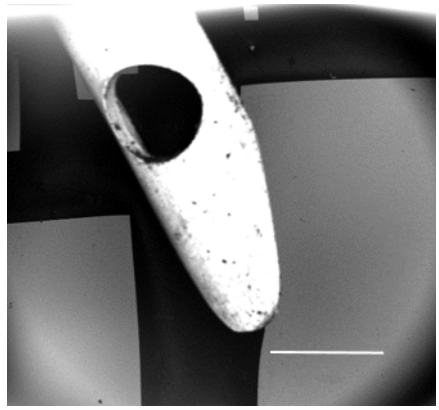

Figure 4.16: SE image of the Kleindiek GIS nozzle used for deposition experiments in the Phenom. It is a beveled nozzle with the edge parallel to the substrate and it contains a hole for the electron beam to pass through. Scale bar is 1 mm.

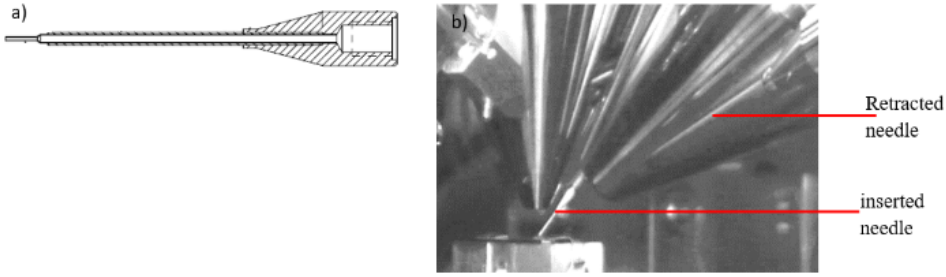

Figure 4.17: GIS nozzle in the Nova Nanolab650 SEM. a) the needle design in cross section. b) Navigation camera image of the inside of the chamber of the Nova Nanolab650 SEM where one GIS needle is inserted just above the sample and another one is retracted.

Composition

EDX was used to measure the composition of the Phenom and the Nova Nanolab650 reference deposits. The EDX measurements were performed using an EDAX detector in the Helios dual beam SEM and Nova NanoSEM 450 SEM. For all the measurements, the beam energy was 4 keV and the beam current was 1.5 – 2 nA. The beam energy was chosen such as to minimize the signal from the substrate and measure only the composition of the deposit.

An example of an EDX spectrum for a Phenom deposit which was deposited for 5 minutes at a precursor temperature of 75 °C is shown in figure 4.21. All deposits in both the Phenom and the Nova were observed to contain at least 65 at% C. The lower the Pt content in a deposit, the higher the C content. In addition to Pt and C, the deposits contained O, N and Si. The Si and O signals are likely to originate from the substrate, since the deposits are not very thick.

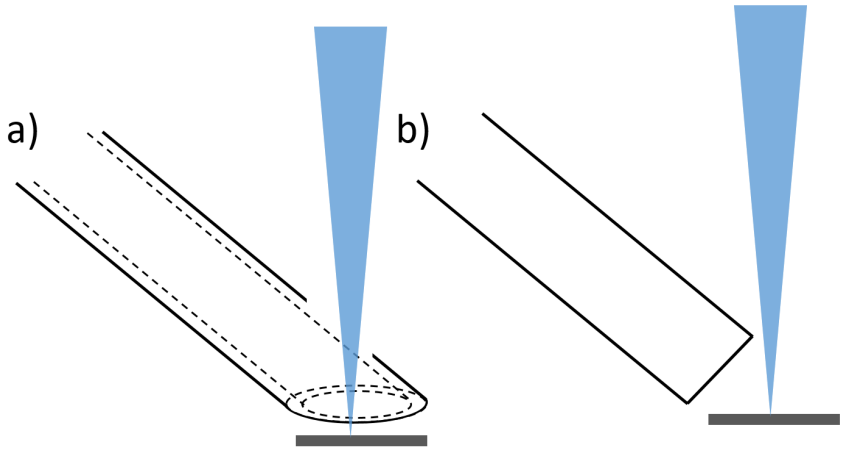

Figure 4.18: a) Beveled nozzle in the Kleindiek GIS with a hole for the e-beam. b) GIS nozzle in the Nova SEM. The images are not to scale and the dimensions are not available due to copyrights of the manufacturing companies. The electron beam and substrate positions are shown. The cartoons are not to scale.

The source of N is not clear. It might have resulted from the window of the detector or from a Si escape peak caused by the Pt Mα1 photons hitting the detector. The Si Kα escape peak shows up at 1.74 keV below the Pt Mα1 peak [58, 98]. The Pt Mα1 peak is at about 2.1 keV and the N peak detected is at about 0.4 keV as shown in figure 4.21. The atomic percentage of Pt is plotted in figure 4.22 as a function of the precursor temperature, for deposits made both in the Phenom and the Nova. The first observation is that, at the same precursor temperature, the Pt content of the Phenom deposits is about half the Pt content of the Nova deposits, and there is more carbon present in the Phenom deposits than in the Nova deposits. The highest Pt content reached in these experiments was 15 at% in the Phenom deposits, still lower than the lowest observed Pt content of ≈18 at% in the Nova deposits. The higher C content in the Phenom deposits compared to the Nova deposits must be due to the co-deposition of carbon from the rather high background pressure, containing hydrocarbons, among other molecules. The second observation is that, in both SEM's, if the precursor temperature is increased, the Pt content slightly increases in a linear fashion with a slope of 0.12 at%/K for the Phenom deposits and 0.17 at%/K for the Nova Nanolab650 deposits. The increase in the Pt content is accompanied by a corresponding decrease in the C content. In literature, no information was found about the metal content in deposits as a function of precursor temperature or pressure (the only information that was found is a report about heating the substrate [38], but not the precursor). The slight increase in the Pt content with increasing precursor temperature, in both the Nova and the Phenom, can be explained from the difference in background pressure, i.e. unwanted supply of hydrocarbons, in both systems. An

increase of the precursor flux in the Phenom SEM contributes much less to the total supply of molecules, because of the severe hydrocarbon contamination level, than the same increase of the precursor flux in the comparatively clean Nova SEM.

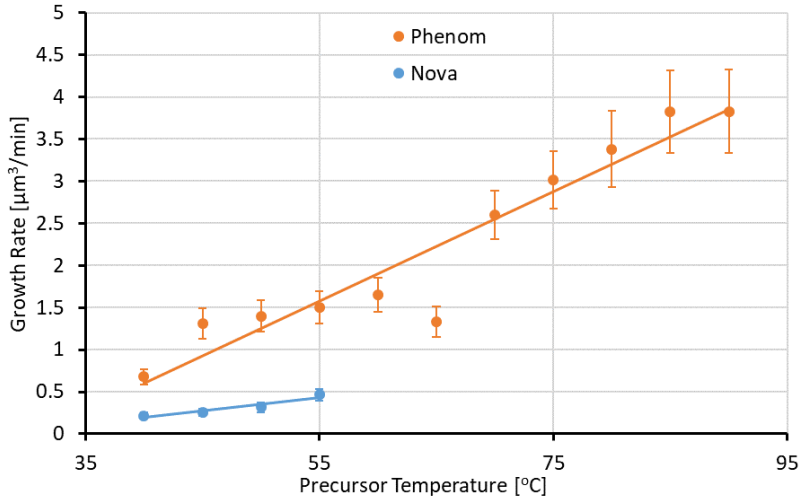

Figure 4.19: Growth rate calculated as deposited volume/deposition time for deposits made in 5 minutes in the Phenom XL G2 (orange) and in the Nova Nanolab650 SEM (blue) at different precursor temperatures. The lines are best linear fits through the data, as guides to the eye. The error bars are calculated based on the uncertainty in the dimensions as taken from the SEM images.

FEBID Patterning techniques in a Phenom desktop SEM

So far, in the deposition experiments in the Phenom, the patterning was done by exposing the full field of view at the maximum magnification. This was sufficient to create some large deposits that can be used for growth rate and composition measurements. In this section, the possibility for more controlled patterning is investigated. There is a big difference in resolution and control between the Phenom and the HV SEM. As mentioned before, the Phenom systems do not have patterning software. The PPI allows for changing the magnification and then scaling the scanning area to a fraction of this magnification. However, this feature was not tested thoroughly in the company. In addition to that, there is a command to move to certain coordinates or move by a certain distance. If the distance to be moved is smaller than a certain value, the movement is done by beam shift, otherwise it is done by moving the stage. To test the patterning, a line was deposited. A PPI script was developed to achieve control over the beam position. A line of 151 points was patterned using the script. The script reads an image of a line consisting of 151 points. It starts at the current position, zooms in to the highest magnification (HFW=1.07 µm)

and then a scaling factor of 0.1 is applied to attempt an even smaller exposure area. The scaling factor is meant to define the size of the image acquisition area as the scaling factor times the field of view. The area is exposed for 2 seconds and then the beam moves to the second point of the line with a pitch of 0.2 µm, exposes the next area for 2 s and so on. In each area there are 684 x 684 pixels and each pixel is exposed during a dwell time of 200 ns. The resulting line is shown in figure 4.23. The width of the line measured from the image is about 1.5 µm. The width of the square deposits shown in the previous sections was also between 1.5 and 2 µm. This shows that the scaling didn't really decrease the exposed area, so it is still unclear what the function of this parameter is. The line deposits also contained a kind of crystals or grains which are absent in deposits made from the same precursor in the HV SEM. The origin of these grains is not clear.

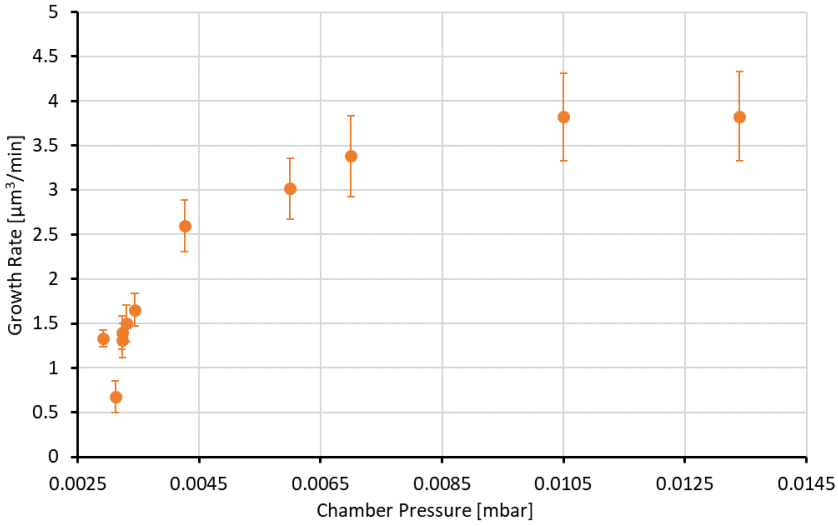

Figure 4.20: Growth rate calculated as deposited volume/deposition time for deposits made in 5 minutes in the Phenom XL G2 at different chamber pressure. Each point is an average of volumes/time of several deposits deposited under the same conditions. The error bars are calculated based on the uncertainty in the dimensions as taken from the SEM images.

With the same procedure, the logo of Thermo Fisher was deposited and is shown in figure 4.24. The conclusion is that patterning is possible in the Phenom system but only in a primitive way and at a resolution much worse than in a HV SEM. In the Phenom system, the best resolution (in FEBID) achieved with the setup presented here was about 1 µm while in a HV SEM the FEBID resolution is sub-10 nm. Further development of the PPI is required to be able to control the patterning and expose points rather than a field of view.

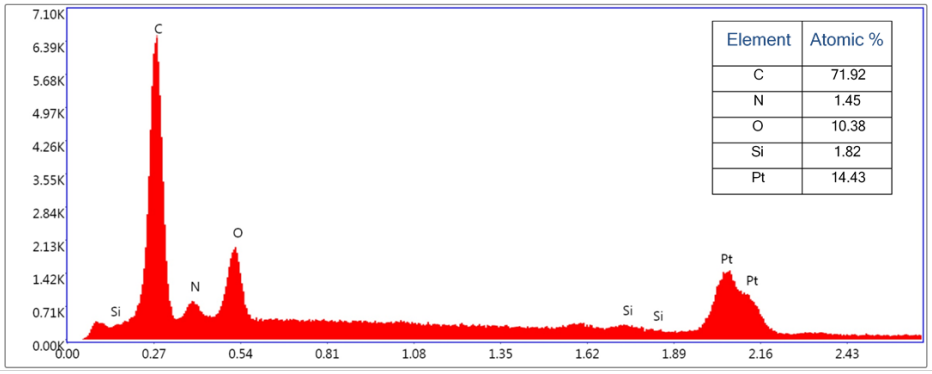

Figure 4.21: An example EDX spectrum of a Phenom deposit which was deposited for 5 minutes at 75°C precursor temperature.

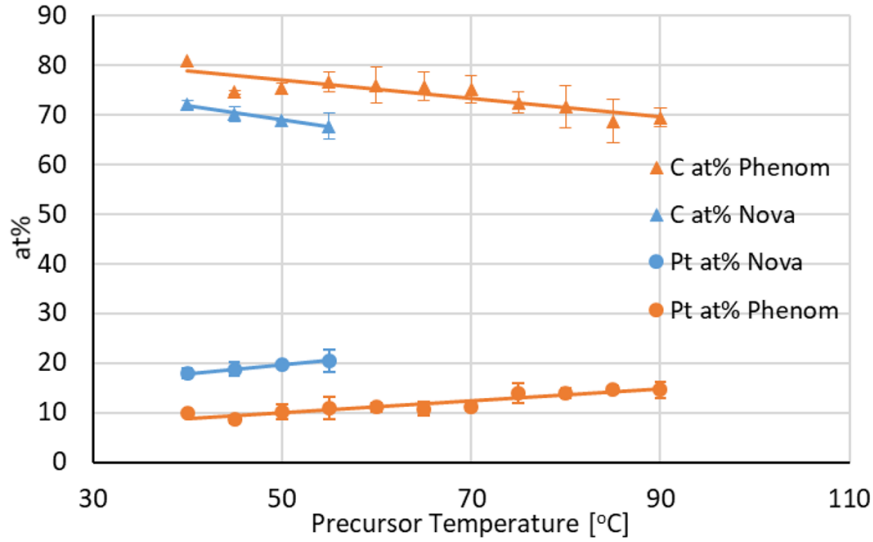

Figure 4.22: In orange: Average atomic percentage of platinum and carbon for deposits that were deposited in the Phenom XL G2 for 2 and 5 minutes at different precursor temperatures ranging from 45-90°C. The EDX measurements were performed in a Helios dual beam SEM. In blue: Average atomic percentage of platinum and carbon for deposits that were deposited in the Nova Nanolab650 SEM for 2 and 5 minutes at different precursor temperatures ranging from 40-55°C. The EDX measurements were performed in the Nova Nano SEM 450 with an EDAX system. The drawn lines are linear fits to the data. The error bars show the standard deviation for each set of deposits of different precursor temperatures.

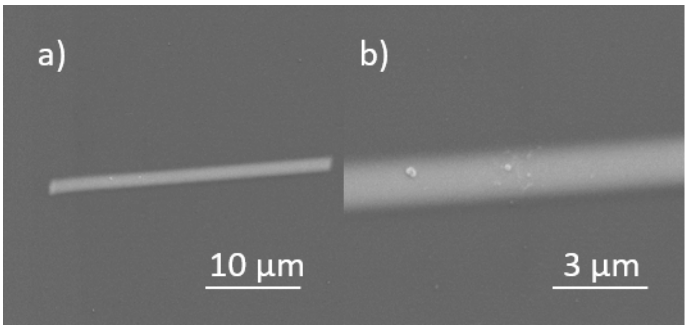

Figure 4.23: a) SE image of a line of 151 points deposited at a pitch of 0.2 µm exposing every point as a square (684x684 pixels) for 2 s. b) Enlarged image of the line in a).

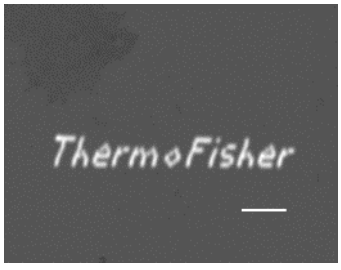

Figure 4.24: BSE image of the Thermo Fisher logo deposited using FEBID in the Phenom XL G2 system. The scale bar is 100 µm.

4.4. Focused Electron Beam Induced Etching (FEBIE) Using Water in the Phenom XL System

In the previous section we have seen that the growth rate achieved in the Phenom system is higher than that achieved in the Nova Nanolab650 SEM due to the higher precursor flux, obtained by increasing the precursor temperature and operating at a higher pressure. However, this was achieved at the expense of the platinum content in the deposit. The deposits in the Phenom had a lower Pt content and a higher C content. In this section it is investigated how carbon contamination on a sample surface can be removed (etched) by electron beam induced etching in the presence of water at pressures higher than usual. Focused electron beam induced etching (FEBIE) is a direct write high-resolution subtractive technique in the SEM [12, 36]. In the FEBIE process an electron beam scans over the sample dissociating adsorbed precursor molecules injected in to the SEM. The dissociated molecules react with the substrate forming volatile fragments which are pumped away. This could be very useful for the removal of carbon from FEBID deposits, but also as a fast, cheap and local cleaning method of a specific part of a sample surface, pre-imaging to achieve higher resolution imaging without the nuisance of contamination.

4.4.1. Modified setup

Considering the similarities between the Phenom system and the ESEM in terms of the ability to operate at higher chamber pressure without affecting the source, the Phenom system is a good candidate for operating with water. In this work the Phenom XL system was modified to accommodate for inserting water in the chamber. Instead of the connection to air for venting, a water bottle was connected to the sample holder (chamber) through valves, with apertures in between, to regulate the amount of water entering the system. An extra pump was connected to evacuate the water bottle. An extra valve is added to close the connection between the water bottle and the pump after the bottle is pumped to avoid blocking the pump with water. Pressure is monitored in the chamber, column and water bottle. It is important to note that the apertures were varied throughout experiments. The standard apertures used for differential pumping when connected to air are 12 and 40 μm in diameter. Using a 12 μm aperture for letting in water didn't cause a noticeable pressure rise. Then a 20 μm aperture was used for some experiments. To reach higher pressures and widen the range, a 100 μm aperture was installed along with a manual needle valve to control the amount of water in the system without affecting the source pressure. The manual needle valve still provided a limited pressure range, so the aperture was changed when needed and was combined with the needle valve. Appendix 4.2 explains details and diagrams of the modified setup. Experiments were performed to investigate the effect of introducing water vapor in the chamber and whether it removes the carbon contamination upon e-beam irradiation. We expect that the removal or etching of carbon results in brightening of the exposed area in BSE-images while carbon deposition causes darkening [112, 115]. The pressure was monitored at the shuttle as the closest approximation to the chamber pressure. The beam energy was 5 keV for all experiments. The measured beam current was 9.7 nA. A series of squares of 4.07 μm length was exposed, each square with an increasing exposure time. The exposure times varied from 2 to 25 minutes. This was repeated at different pressures by letting in different amounts of water vapor, controlled by the aperture sizes. Experiments were performed at the following pressures: 0.08, 0.16, 0.21, 0.56, 0.8 and 1.5 mbar making sure that the source pressure stayed just below 10^{-7} mbar. All experiments were performed on a silicon substrate.

4.4.2. Results and Discussion

Two sets of experiments were performed in the Phenom system with all parameters exactly the same except that two experiments were done without the addition of water, at a chamber pressure of 0.08 and 0.16 mbar, and the others with water added up to a pressure of 1.5 mbar. Square areas of 4.07 μm x 4.07 μm were exposed for 2, 5, 10, 12, 15 and 20 minutes. In figure 4.25 the SE images, as taken in the Phenom XL, are shown of the squares made without the addition of water. A decrease in intensity, or darkening, is seen at the boundaries of the exposure area which gets more prominent for longer exposure times. This is ascribed to the deposition of carbon from hydrocar-

bon molecules present in the specimen chamber. The fact that it occurs at the boundaries of the exposed area indicates that the supply of hydrocarbons is mostly by surface diffusion. In the center of the squares the amount of hydrocarbons gets depleted, but at the boundaries hydrocarbons are diffusing towards the depleted area but are dissociated by the electron beam before reaching the central area of the square. Figure 4.26 shows the BSE images of the same squares. These images show a much better material contrast. To quantify the intensities in the images, intensity profiles were taken. Of each image 200 horizontal cross section intensity profiles were collected around the middle of the square. The average was calculated, then smoothed and plotted in figure 4.27 for the SE images of figure 4.25 and in figure 4.28 for the BSE images of figure 4.26. For each pressure, the intensity profiles for different exposure times were aligned and plotted on the same plot.

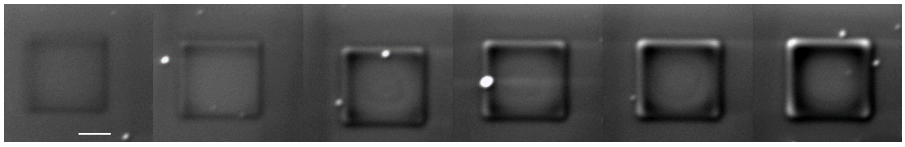

Figure 4.25: SE images of squares exposed to the e-beam for 2, 5, 10, 12, 15 and 20 minutes left to right. There was no water inserted in the system. Beam energy: 5 keV. Beam current: 9.7 nA. The chamber pressure was 0.08 mbar. The exposure area was a square with a side length of 4.07 µm. Scale bar is 2 µm.

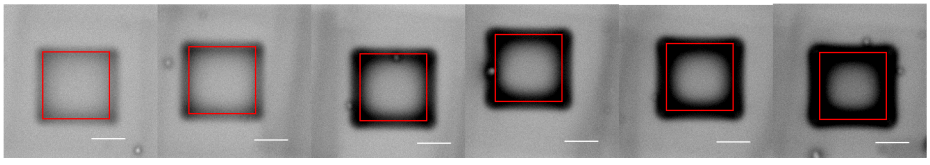

Figure 4.26: BSE images of the squares shown in figure 4.25. The exposed area is shown as red squares in each image. The scale bar is 2µm.

The center between the peaks or valleys (representing the edges of the squares) in the images were aligned to each other to better judge changes to the width of the squares. In figure 4.27 it is seen that the intensity in the center of the squares first slightly increases (at 5 min exposure time) and then decreases to a level that remains constant at longer exposure times. The initial increase in intensity might be caused by the presence of water at the substrate surface causing some removal of carbon, but then more hydrocarbons diffuse in, causing some deposition of carbon which levels off due to depletion effects. It is well-known that in the presence of both hydrocarbons and water carbon deposition (FEBID) and carbon etching (FEBIE) are two competing processes [110]. The valleys in the intensity plots clearly show the thickening and broadening of the carbon rim around the squares. Looking at figure 4.28 it is noted that the intensity plots of the BSE images provide more information on the

intensity in the central area of the squares. It is seen that the intensity at the center of the squares decreases for longer exposure times, indicating increasing deposition of carbon. It is clear that in this experiment the carbon deposition dominates over possible carbon removal by the presence of water in the system.

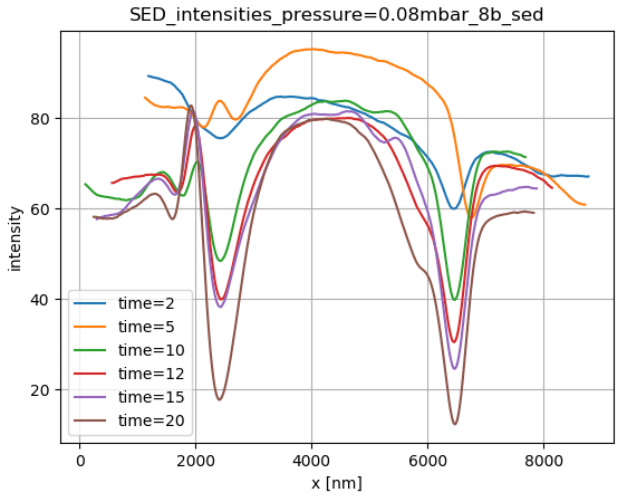

Figure 4.27: Averaged and smoothed intensity profiles for the SE images of the squares in figure 4.25. The centers between the 2 peaks are aligned to be able to see whether the square gets wider for longer exposure time. The exposure times are in minutes.

The second set of experiments was done with the addition of water into the system up to a pressure of 0.8 mbar. As the BSE images are more sensitive to the presence of carbon we choose to only show these images here. The SE images can be found in Appendix 4.4. In figure 4.29, carbon deposition is seen to occur around the squares, although much less than in the absence of water (see figure 4.26), and the central area gets brighter with increasing exposure time. Figure 4.30 shows the average intensity profiles, clearly demonstrating the brightening in the central area. The etching effect of water dominates the carbon deposition in this experiment.

To judge how clean the central area of the square becomes after exposure in the presence of water, a smaller square was exposed inside one of the cleaned squares. First two squares with a HFW of 4.07 µm were exposed for 15 minutes in the presence of water at a pressure of 0.8 mbar. Then a smaller square was exposed in the absence of water for 10 minutes, inside each of the two squares, at the smallest HFW of 2.46 µm (figure 4.31a), but one was scaled to 0.5 attempting to make it even smaller (figure 4.31b). Figure 4.31 and 4.32 show BSE and SE images, respectively, of the two cleaned squares with the smaller squares inside. The carbon rims of the small squares inside

are hardly visible and are really small compared to those of the big squares as is seen from the intensity profiles in figure 4.33. This demonstrates that even after 10 minutes of exposure the squares were still clean. This gives enough time for a user to image structures inside a cleaned area without the problems of carbon contamination, allowing for high resolution slow scan imaging.

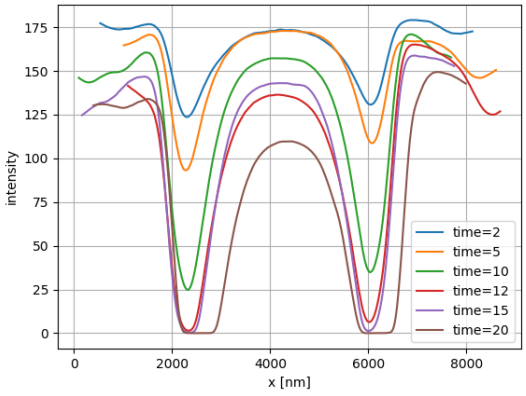

Figure 4.28: Averaged and smoothed intensity profiles for the BSE images of the squares in figure 4.26. The centers between the 2 valleys (the C walls) are aligned to be able to see whether the square gets wider for longer exposure time. The exposure times are in minutes.

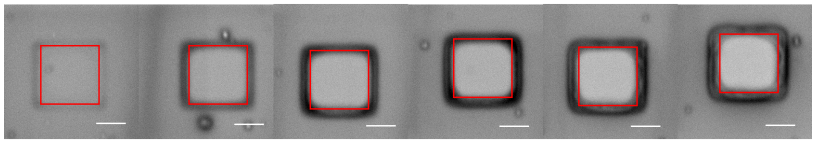

Figure 4.29: BSE images of squares exposed to the e-beam for 2, 5, 10, 12, 15 and 20 minutes left to right. Water was inserted in the system to a pressure of 0.8 mbar. Beam energy: 5 keV. Beam current: 9.7 nA. The exposure area was a square of side length 4.07 µm. The exposed area is shown as red squares in each image. The scale bar is 2 µm.

More exposure experiments were performed at different pressures: 0.16 mbar without additional water, 0.21, 0.56 and 1.5 mbar, all with added water. The SE and BSE images of the squares exposed in these experiments are shown in Appendix 4.4. To compare the brightening effect observed at different exposure times and different pressures, the intensity difference between the center of the exposed square and outside of the exposed square was determined. The intensity outside was calculated as the average intensity of a small area outside of the square in the BSE image of each square. This area was manually checked to make sure there are no particles or dirt. Figure 4.34 shows this intensity difference at different exposure times and different

pressures. The maximum brightness intensity is 255 (white) and maximum darkness intensity is 0 (black). So, the higher the intensity, the brighter the area. The change in intensity as a result of electron exposure in the presence of water indicates the efficiency in removal of carbon from the surface and is an indicator of how clean the surface is. Figure 4.34 shows that if no water is added (0.08 mbar) deposition of carbon takes place, but when some water is added the removal of carbon occurs and larger intensity differences are observed for larger exposure times. This does not necessarily mean that the surface becomes cleaner, i.e. contains less and less carbon, it could also mean that the surface gets more heavily oxidized leading to image intensity changes.

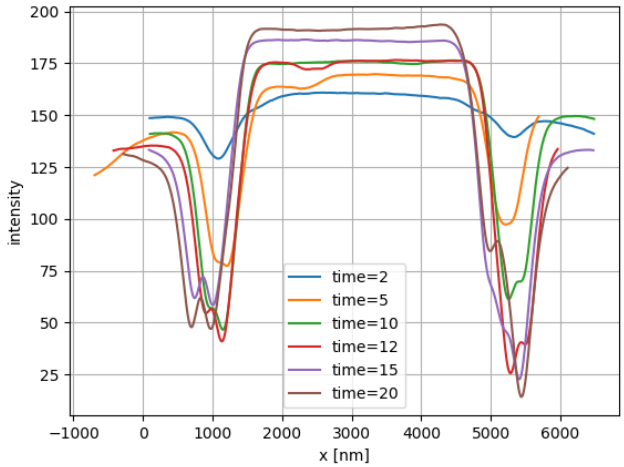

Figure 4.30: Averaged and smoothed intensity profiles for the squares in figure 4.29. The centers between the 2 valleys (the carbon rim) are aligned to be able to see whether the squares widen at longer exposure times. The exposure times are in minutes.

It is important to note that the brightening effect is stable in time. Samples were imaged several times in different systems over several months after the experiments were done and nothing really changed.

Finally, a highly contaminated gold sample was exposed in the presence of water (reaching a chamber pressure of 1.13 mbar) in the Phenom XL to test if even severe carbon contamination can be removed. The beam energy and current used were 5 keV and 9.7 nA. Figure 4.35 shows the SE image of the exposed square. The red square shows the originally scanned area. Clear brightening is observed despite the presence of a large amount of carbon. There is a wide rim observed around the exposed area, indicating a strong in-flux of hydrocarbons. The contamination was so severe that imaging the brightened area for a few seconds covered it completely with a black carbon layer. Bigger areas were attempted to clean, even up to 50 µm, but such large areas could not successfully be cleaned on this particularly dirty sample.

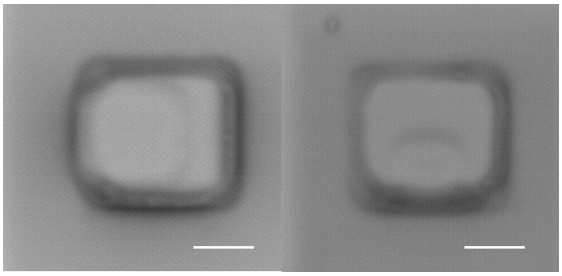

Figure 4.31: BSE images of small squares exposed inside a larger previously exposed square. The bigger squares of HFW of 4.07 µm are exposed at 5 keV, 9.7 nA for 15 minutes in the presence of water at a pressure of 0.8 mbar. The smaller squares are exposed for 10 minutes. The HFW of the smaller squares is a) 2.46 µm, b) 1.23 µm. The scale bar is 2 µm.

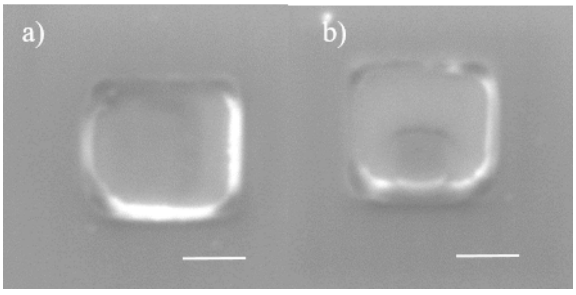

Figure 4.32: SE images of smaller square exposed inside another already exposed square. The bigger squares of HFW of 4.07 µm are exposed at 5 keV, 9.7nA for 15 minutes with water at a pressure of 0.8 mbar. The smaller squares are exposed for 10 minutes. The HFW of the smaller squares is a) 2.46 µm, b) 1.23 µm. The scale bar is 2 µm.

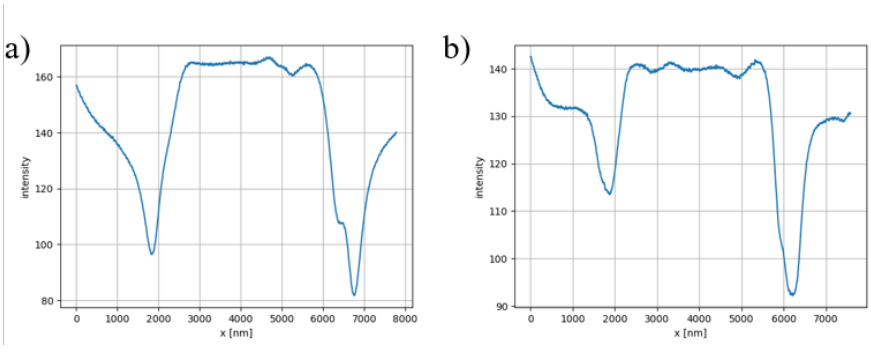

Figure 4.33: Averaged and smoothed intensity profile of horizontal cross sections of the squares in figure 4.31 a) and b) respectively. The profiles were taken at a position such that the small square is also included.

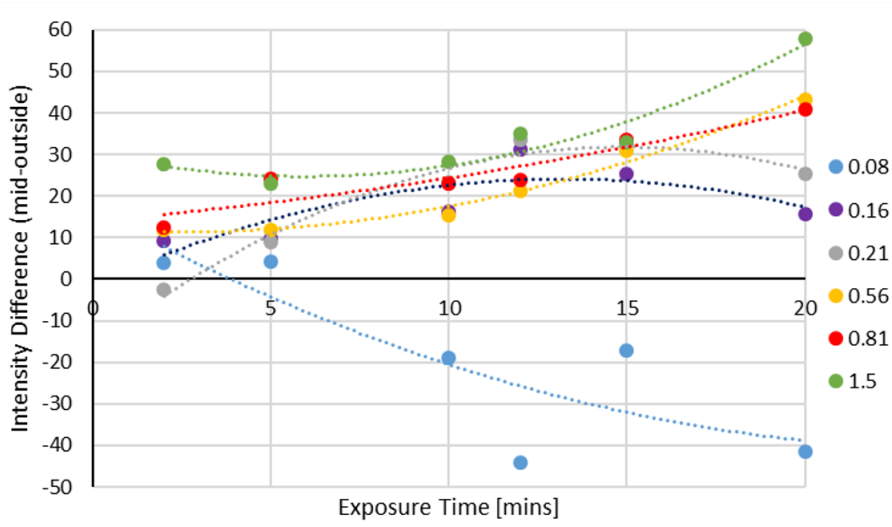

Figure 4.34: Intensity difference between the center of the exposed square and outside of the square at different exposure times and different pressures. Each trend line represents a pressure. The pressures in the legend are in mbar.

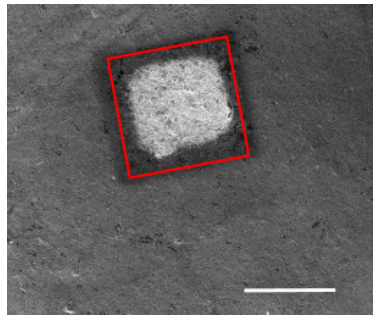

Figure 4.35: SE image of gold nanoparticles on carbon after e-beam exposure of a 4.07 µm square in the presence of water vapor. The original scanned area is shown in red. The scale bar is 3 µm.

4.5. Conclusion

The Thermofisher Desktop SEM, or Phenom system, provides a simple setup that operates at high chamber pressure, up to 1 mbar. In this system it was tested whether an increase in precursor flux increases the growth rate of FEBID. A small GIS was installed in the sample holder of the Phenom system and FEBID was performed there for the first time. Shapes were deposited under similar conditions in a HV Nova Nanolab650 SEM for comparison. The increase in the precursor flux indeed increases the growth rate but the metal content decreases compared to deposits in the HV SEM. Increasing the flux

(by increasing the temperature of the precursor reservoir) results in a small increase in the metal content in both HV and desktop SEM. Then, the effect of adding water in the desktop SEM chamber for substrate cleaning or removal of carbon contamination upon e-beam irradiation (FEBIE) was investigated. This can be very useful to purify deposits and to locally clean part of the sample. The setup was modified to connect a water supply to the chamber and the amount of water vapor reaching the chamber was controlled via apertures. Exposed square areas showed up as bright areas in backscattered electron images when water vapor was introduced, which indicates the etching of carbon. The exposed squares were surrounded by a black rim which we attribute to carbon contamination resulting from hydrocarbon molecules diffusing towards the depleted square area and getting pinned by electron induced dissociation at the boundary of the square. Experiments were performed at different amounts of water vapor and at various exposure times. The longer the exposure time, the brighter the exposed area becomes. This opens the door to further improve the method of inserting water in a more controlled way to the chamber, and turn it into a simple method to locally clean samples.

Appendix 4.1. Manifold Vacuum Valves

The Phenom system operation is regulated by valves and hoses connected through the manifold valve block. There are five directly operated 2-port, normally closed, solenoid valves and two directly operated, normally closed, 3-port solenoid valves. The functionality of the valves is as follows: The 2-port valves are the five gold-colored ones in figure A4.1. They are labelled as VPL, VVL, VPS, VVS and VPT in Figure A4.3.

VPL: connects the lift to the pre-vacuum pump (PVP).

VVL: connects the lift to the silencer (air) for venting. This valve will be open only during the venting of the lift.

VPS: connects the shuttle to the PVP.

VVS: connects the shuttle to the silencer (air) for venting. This valve will be open only during the venting of the shuttle.

VPT: connects the PVP to the turbo molecular pump (TMP).

There are also two 3-port valves which are the black ones in figure A4.1 and are labelled as V01 and V06 in figure A4.3. The CAD drawings with top and side view of the manifold with the valves and all connections are shown in figure A4.2. The numbers 01 and 06 are referring to the chamber pressures that can be chosen: 0.1 and 0.6 mbar. V01: either connects the shuttle to the PVP through the 12 µm aperture or connects the shuttle to the air also through the 12 µm aperture. V06: either connects the shuttle to the PVP through the 40 µm aperture or connects the shuttle to the air also through the 40 µm aperture. If both V01 and V06 are closed then the pressure will be 0.01 mbar. If only V01 is open, the pressure will be 0.1 mbar. If only V06 is open, the pressure will be 0.6 mbar.

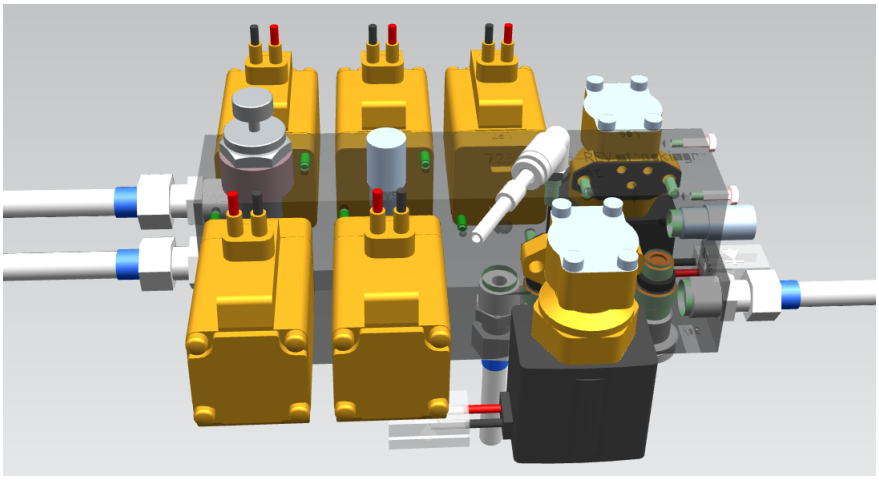

Figure A4.1: Manifold diagram with all the valves. The connections of every valve is explained in figure A4.3

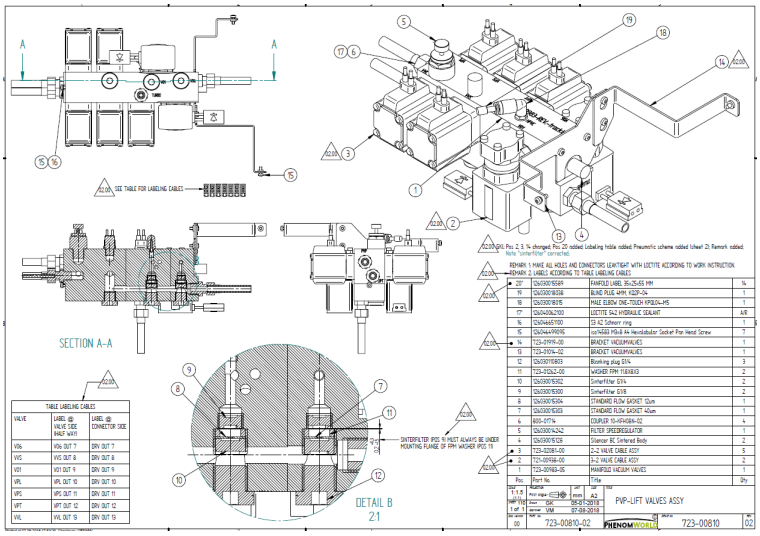

Figure A4.2: Diagram of the manifold with all connections, valves and apertures.

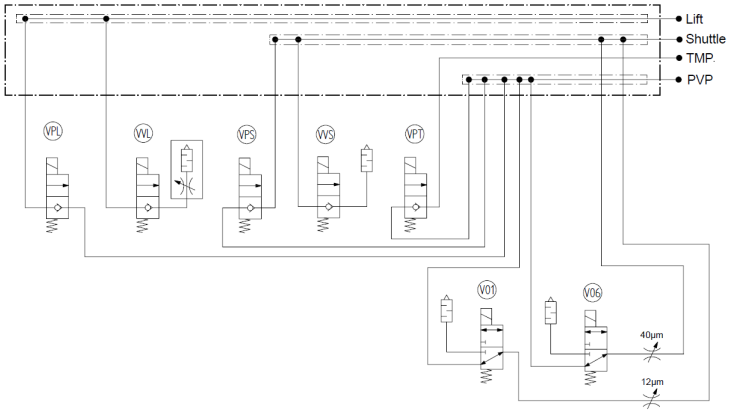

Figure A4.3: Valve block piping and instrumentation (P&ID) diagram of the manifold. There are five directly operated 2-port, normally closed, solenoid valves and two directly operated, normally closed, 3-port solenoid valves. TMP is the turbo molecular pump and PVP is the pre-vacuum pump.

Appendix 4.2. Modified setup to insert water

In the experiments, another valve block was added to allow for letting in water into the chamber. In the final setup, nothing was changed to block 1. In block 2, only V01 and V06 are connected and they have a separate power supply. The water bottle is connected to block 2 instead of air. An extra pump is connected to pump the water bottle and part of block 2. An extra valve is added to close the connection between the water bottle and the pump after the bottle is pumped, to avoid blocking the pump with water. Another extra valve is added to close the connection between block 2 and block 1 while the water is open, to avoid the escape of the water into the column and the original pump. The pressure is monitored in the shuttle, column and water bottle.

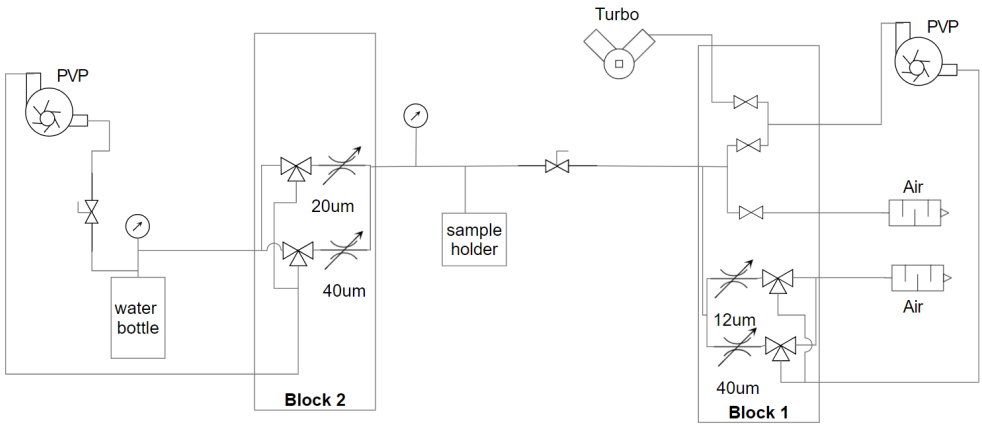

Figure A4.4: Simplified schematic showing the modified XL setup for letting in water. Block 1 is the original block as present on any standard XL and block 2 is added to allow for letting in water. For simplicity, the symbols for the valves in the schematic are general. The 2 way valves drawn inside block 1 are solenoid, normally closed, 2 port valves. The 3 port valves in block 1 and 2 are solenoid common 3 port valves. It is important to note that the apertures were varied in block 2 throughout different experiments.

The modified setup of the XL system to allow letting in water is simplified in figure A4.4. It is important to note that the apertures were varied in block 2 throughout different experiments. A standard block, as mentioned before, has a 12 µm aperture in V01 and a 40 µm aperture in V06. Some pictures of the setup are shown in figure A4.5.

Appendix 4.3. GIS Cables

The cables and connections designed to connect the Phenom XL2 to the GIS are showed in figure A4.6.

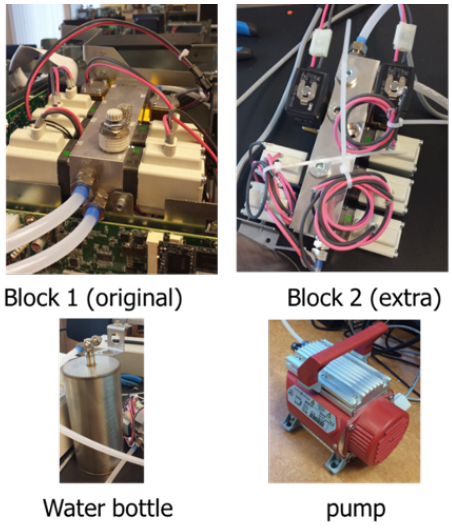

Figure A4.5: Pictures of the modified setup.

SMC12 T	SMC12 V	SSW-113-01-G-D	SUB D 26p male	SUB D 15p male	SUB D 15p male
1b		20	11	1	
2b		19	12	2	
1a, 2a,3a,4a		4 (gnd)	23	3 (gnd)	
3b		16	21	4	
4b		22	22	5	
		6 (gnd)	18	7,8,9 (gnd)	7,8,9 (gnd)
5a	1a	2 (gnd)	5		3 (gnd)
5b	1b	14	20		1

2x SMC12 connectors (f) SSW-113-01-G-D SUB D 26p (m) 2x SUB D 15p (m)

Figure A4.6: Cables and connections used to connect the GIS to the Phenom XL2

Appendix 4.4. FEBIE with water experiments

More SE and BSE images of the water exposure experiments at different pressures are shown here. The intensity profiles are also presented.

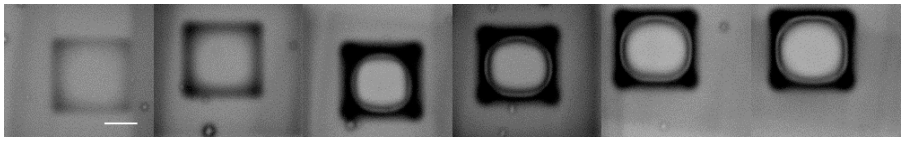

Figure A4.7: BSE images of squares exposed to the beam at 5 keV, 9.7 nA. The shuttle pressure was 0.16 mbar without letting in water. From left to right the exposure times are: 2, 5, 10, 12, 15, 20 minutes. Scale bar is 2 µm.

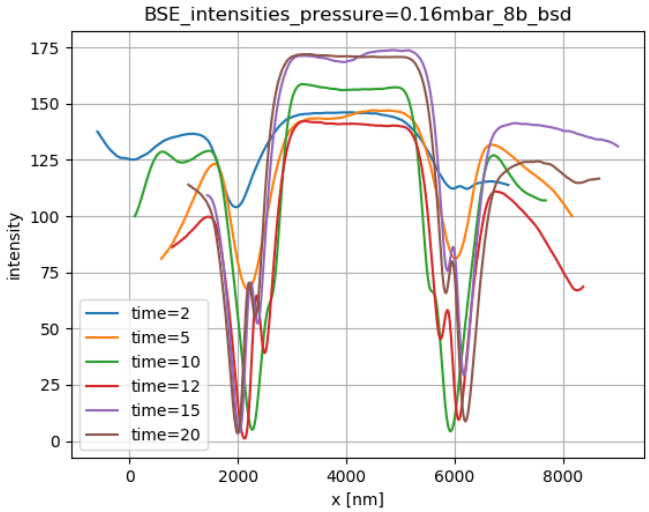

Figure A4.8: Averaged and smoothed intensity profiles for the squares in figure A4.7. The centers between the 2 peaks are aligned to be able to see whether the squares get wider for longer exposure time. The exposure times are in minutes.

Figure A4.9: SE images of the squares in Figure A4.7.

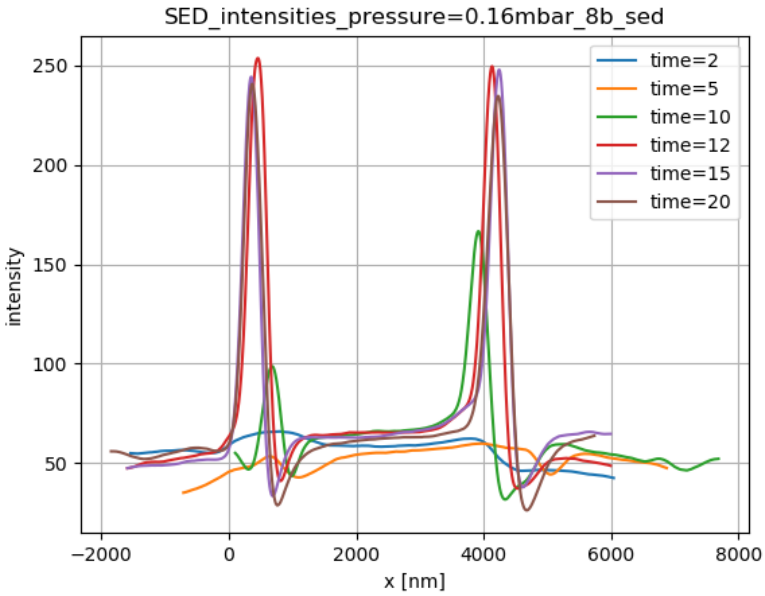

Figure A4.10: Averaged and smoothed intensity profiles for the squares in figure A4.9. The centers between the 2 peaks are aligned to be able to see whether the squares get wider for longer exposure time. The exposure times are in minutes.

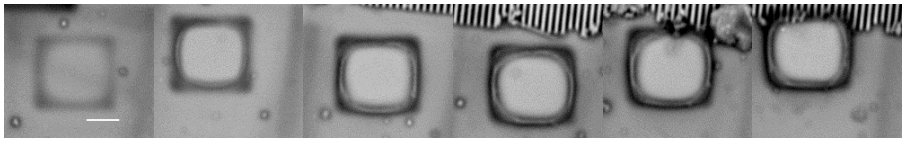

Figure A4.11: BSE images of squares exposed to the beam at 5 keV, 9.7 nA. The shuttle pressure was 0.21 mbar by letting in water through a 20µm aperture. From left to right the exposure times are: 2, 5, 10, 12, 15, 20 minutes.

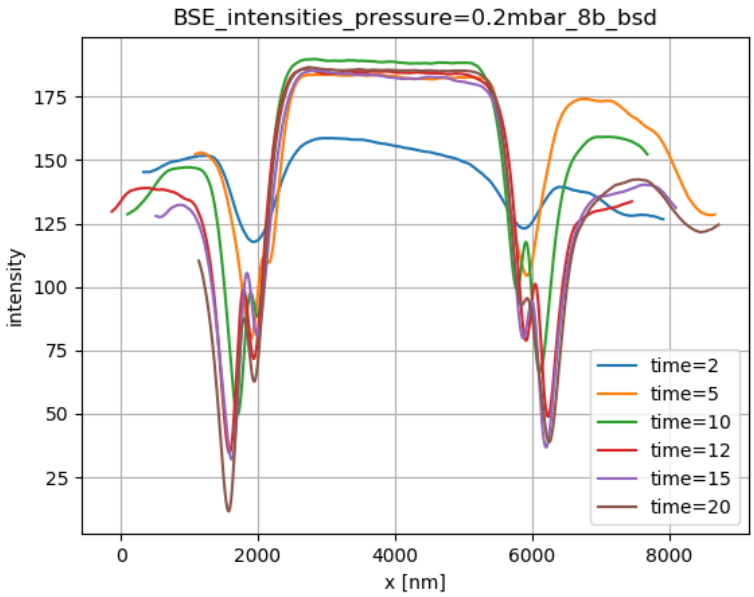

Figure A4.12: Averaged and smoothed intensity profiles for the squares in Figure A4.11. The centers between the 2 valleys are aligned to be able to see whether the squares get wider for longer exposure time. The exposure times are in minutes.

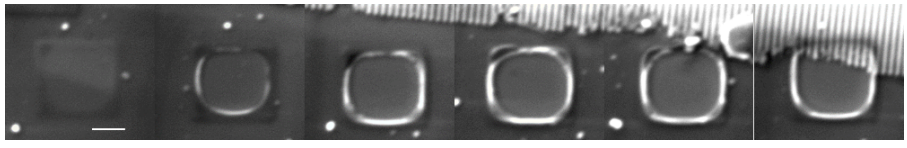

Figure A4.13: SE images of the squares in figure A4.11.

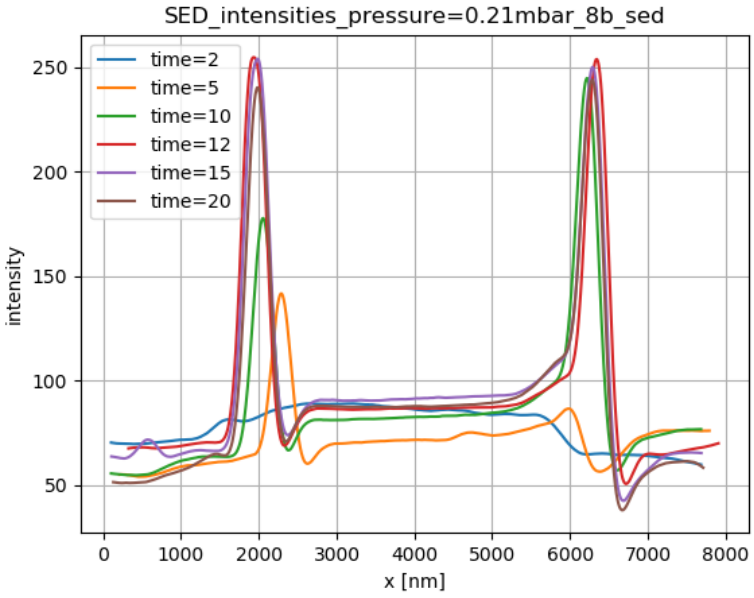

Figure A4.14: Averaged and smoothed intensity profiles for the squares in figure A4.13. The centers between the 2 peaks are aligned to be able to see whether the squares get wider for longer exposure time. The exposure times are in minutes.

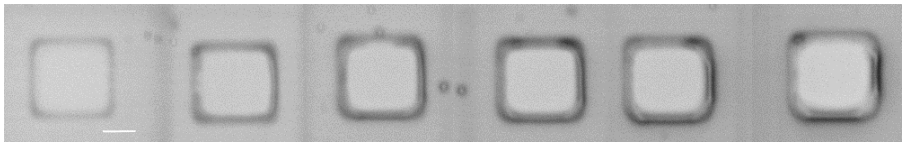

Figure A4.15: BSE images of squares exposed to the beam at 5 keV, 9.7 nA. The shuttle pressure was 0.56 mbar by letting in water through a 40µm aperture. From left to right the exposure times are: 2, 5, 10, 12, 15, 20 minutes.

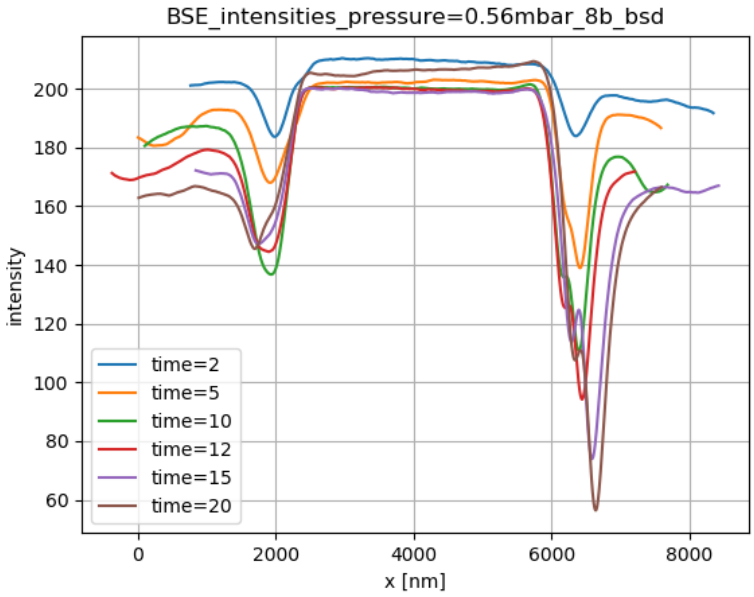

Figure A4.16: Averaged and smoothed intensity profiles for the squares in figure A4.15. The centers between the 2 peaks are aligned to be able to see whether the squares get wider for longer exposure time. The exposure times are in minutes.

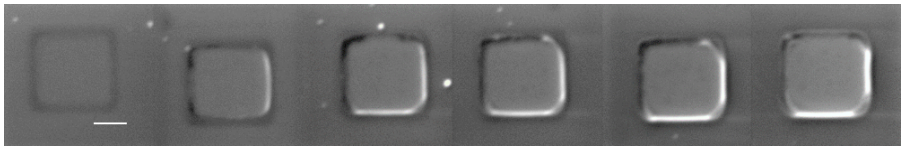

Figure A4.17: SE images of squares in figure A4.15.

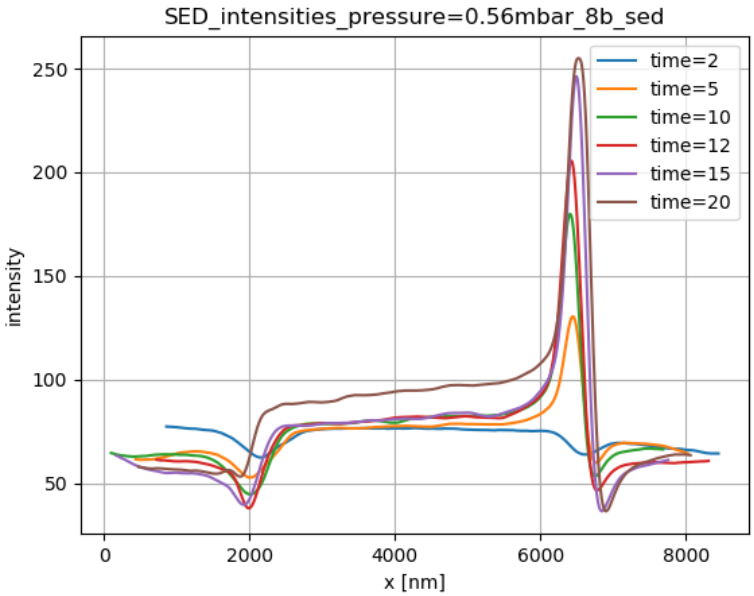

Figure A4.18: Averaged and smoothed intensity profiles for the squares in figure A4.17. The centers between the 2 peaks are aligned to be able to see whether the squares get wider for longer exposure time. The exposure times are in minutes.

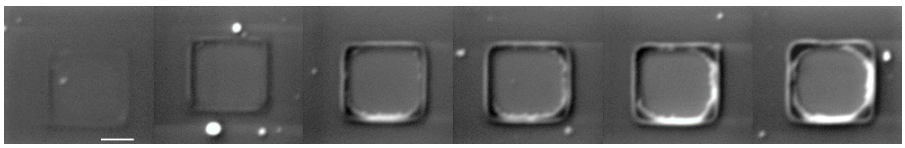

Figure A4.19: SE images of the squares in figure 4.29.

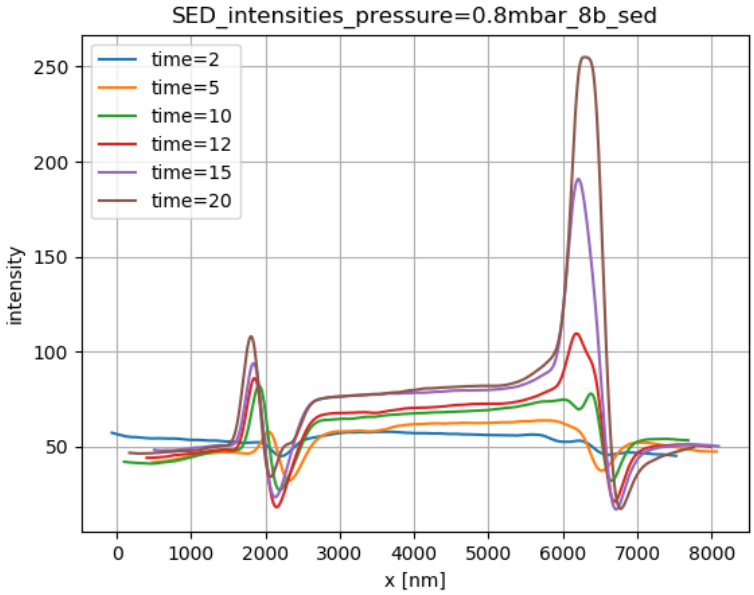

Figure A4.20: Averaged and smoothed intensity profiles for the squares in figure A4.19. The centers between the 2 peaks are aligned to be able to see whether the squares get wider for longer exposure time. The exposure times are in minutes.

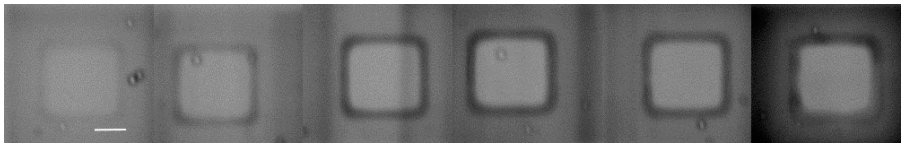

Figure A4.21: BSE images of squares exposed to the beam at 5 keV, 9.7 nA. The shuttle pressure was 1.5 mbar by letting in water. From left to right the exposure times are: 2, 5, 10, 12, 15, 20 minutes.

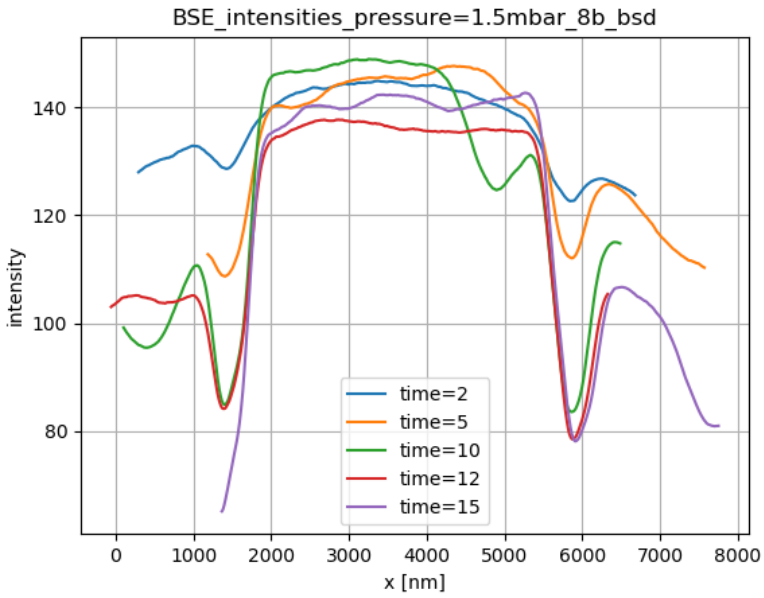

Figure A4.22: Averaged and smoothed intensity profiles for the squares in figure A4.21. The centers between the 2 peaks are aligned to be able to see whether the squares get wider for longer exposure time. The exposure times are in minutes.

5

3D FEBID fixed dwell time method (FDTM)

5.1. Introduction

The demand for 3D nanostructures is rising in fields such as nanomagnetism [27], plasmonics [28], biomedical engineering [74], strain sensors [20], mask repair [16], fabrication of AFM tips [17, 18] and more [27]. Structures include vertical nanowires, helices, membranes and others. There have been many attempts for fabrication of 3D shapes using UV or E-beam lithography in multiple steps comprising chemical or physical vapor deposition and different etching techniques. This requires multiple tools and consumes a large amount of time. Moreover, challenges exist such as precise alignments of multiple layers, reaching the desired roughness and resolution, fabricating overhanging and sloping structures and under-etching. Focused Electron Beam Induced Deposition (FEBID) provides a flexible single-step technique for creating 3D shapes that are very challenging, if not impossible, to fabricate with existing lithography processes. Not only that, but it allows for the fabrication of 3D shapes of a few microns in size in just a few minutes of time. However, there are still challenges associated with the FEBID process such as proximity effects, the broadening of deposits and purity.

For submicron structure the preferred method is FEBID. Examples of artistic structures fabricated using FEBID are shown in figure 5.1

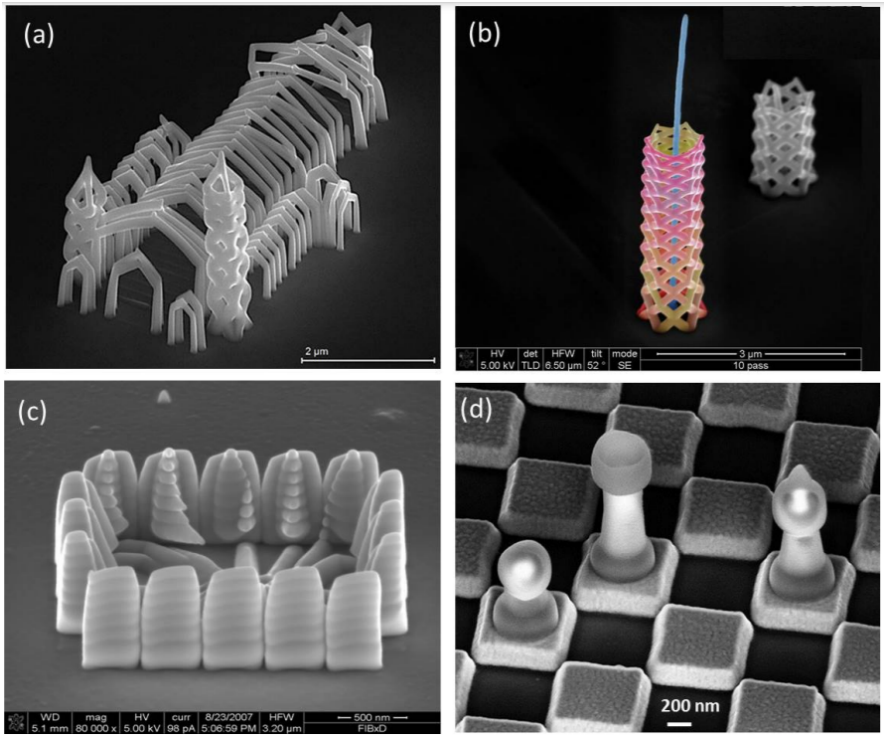

Figure 5.1: 3D shapes fabricated by FEBID. From: [123], Technische Universiteit Eindhoven, and references therein.

In 2018 Niels Noordzij (TU-Delft) developed a patterning strategy for the deposition of “shells”, i.e. closed wall structures, using FEBID. The patterning strategy consisted of arranging building blocks in concentric circles, varying the dwell time with height. He successfully built hollow cones and also double cones of which the inner one is deposited on a lower membrane while the outer one is deposited on the upper membrane of a double membrane structure. This double cone was intended to be applied in the NAIS ion source. The deposition parameters such as the building block size, distance between building blocks, beam energy, beam current, and dwell time were found in a trial and error fashion. Unfortunately this work was unpublished except for an abstract at the EIPBN2017 conference (N. Noordzij and C.W. Hagen, 3D-nanoprinting using Electron Beam Induced Deposition). In figure 5.2, an example is shown of a double cone structure that he fabricated using FEBID. The work discussed here is a continuation of the work of Niels Noordzij, intended to more systematically study the influence of the parameters on the deposition of closed wall shapes, such as hollow cones and double cones for the application in the NAIS ion source.

Recently, simulation guided deposition methods were developed, attempting to compensate for broadening of structures, proximity and heating effects and precursor diffusion. The main software solutions are CAD 3BID (2018) [30], the pattern generation software developed by Keller and Huth (2018) [31] and the layer by layer approach (2020) [29]. The differences between CAD 3BID and the latter pattern generation software have been described in [31] and [32]. The pattern generation for both simulations is based on a diving board-like structure as a building block, shown in figure 5.3 [15, 31]. Several calibration measurements are required for these simulation tools. A method almost identical to the layer by layer approach was also applied for focused ion beam (FIB) systems in [124].

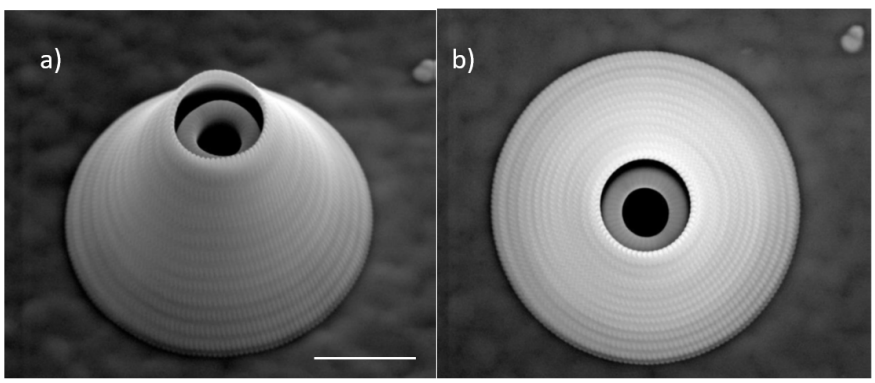

Figure 5.2: a) Outer and inner cone written on a double membrane structure. b) 30 degree tilted image. The inner diameter of the top of the outer cone is approx. 850 nm and 450 nm for the inner cone [courtesy of Niels Noordzij]. Scale bar is 1 µm.

Figure 5.3: Diving board structure used as a building block for simulation tools. The figure is reprinted (adapted) with permission from [15]. Copyright 2018 American Chemical Society.

Where the CAD 3BID software is more optimized for open mesh-like structures [30], this work focuses on structures with closed walls. A procedure for building 3D hollow cones with closed walls and without using simulation tools is presented. In the software tools mentioned in literature, models are used to calculate the dwell time for each point of the 3D shape to be deposited. All other parameters are based on calibration experiments or chosen by the user. The tools are not designed to also optimize the growth rate. The present method of building shapes with closed walls, also considers strategies to speed up the growth while maintaining the design process as simple as possible. The challenges involved in the choice of the deposition parameters and writing strategy, to achieve efficient growth and a simple writing strategy at the same time, will be discussed. The cone shape was selected to study specifically because it finds application in a nano aperture ion source (NAIS) [125–129], as will be described in the next chapter. The same cone shape has also been fabricated using the CAD 3BID and the layer by layer approach. More details on these software tools and a comparison with the method presented below, using closed wall cone fabrication, will be provided in chapter 7.

5.1.1. Shape design

The example shape to be fabricated is a truncated hollow cone, or volcano shape, as shown in figure 5.4. The cone is defined by its top radius r_t, its bottom radius r_b and its height h. The cone angle ϕ is then determined by $\tan^{-1}(h/(r_b - r_t))$. The dimensions of the desired cone were chosen as h = 2 µm, r_b=500 nm, r_t= 100 nm and consequently, $\phi \approx 78.7^o$. The challenge is to fabricate a cone with dimensions that meet the specifications. It is noted that the wall thickness is another design parameter, but because it is not very relevant for the application in the ion source it will not be considered here.

The strategy to build a 3D shape using FEBID is based on laying down small volumes of material, from now on named building blocks, one by one, in the right position and order. The shape is built point by point and layer by layer from bottom to top in an additive manner. The principle is similar to 3D

printing or additive manufacturing. In 3D printing, a 3D shape is designed using CAD software for example, forming an STL file, and is converted to 2D layers in a G-code format using slicing software. The G-code controls the movement of the nozzle that contains the molten plastic, or other material, to be printed. The printed, or deposited, shape is composed of tiny bits of plastic, or other material, that has solidified after leaving the nozzle of the 3D printer. In FEBID, the deposited shape is formed as a result of electron interaction with precursor gas molecules, coming from the nozzle of a gas injection system (GIS), which are adsorbed on the substrate surface. The stream file, which is basically similar to a G-code file, controls the position of the e-beam and how long it stays at each position. The strategy for building a 3D shape using FEBID requires to choose the size of the building blocks, the spacing between them and the order in which they are positioned. The size of a building block could be chosen based on practical considerations, as having a sufficient number of blocks per dimension of the designed shape, and fulfilling, e.g., the required surface smoothness. The parameters that determine the size of the building blocks will now be discussed first.

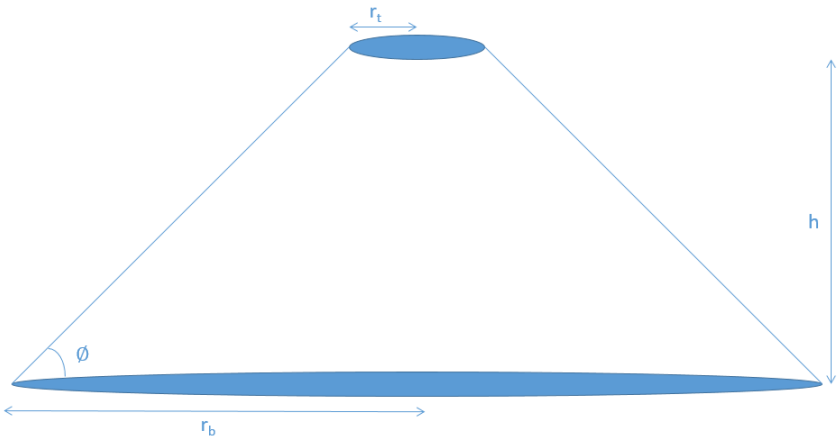

Figure 5.4: Geometry of the hollow cone. Dimensions are: top radius r_t, bottom radius r_b, height h and angle ϕ.

5.1.2. FEBID physics; factors affecting the building block size

There are multiple parameters that affect the size of the building block, some are electron beam related and some are precursor gas related. The beam related parameters include beam energy, current and dwell time. The gas related parameters include the GIS alignment, nozzle position with respect to the sample, precursor type, temperature, sticking coefficient and surface diffusion. The dwell time is the time the beam stays at a specific point. The beam current and the dwell time constitute the number of primary electrons (PEs) needed to deposit a building block. Higher beam current means more

electrons are available for the deposition process. If there is enough precursor supply, a linear relation is expected between the beam current and the volume of the deposit, or building block, and the growth is said to occur in the current limited regime [12, 13, 15]. However, this is not always the case. When the precursor flux is insufficient, the area where electrons are incident on might get depleted such that the growth is no longer governed by the electron flux but by the precursor flux instead. The growth is then said to occur in the precursor, or mass transport, limited regime [12, 13, 15]. Increasing the electron current further will then lead to a saturating growth. Apart from being supplied directly from the GIS nozzle, precursor molecules will also be supplied over the substrate surface by surface diffusion. This may lead to an intermediate regime called the diffusion enhance regime [12, 15]. FEBID growth will therefore depend on the detailed balance between the electron flux, the precursor supply from the GIS nozzle and the precursor supply by diffusion towards the deposition area. The FEBID growth regimes have been discussed extensively in literature [11, 56, 130, 131]. The dissociation of precursor molecules will not only be caused by the incident primary electrons (PE), but also by scattered electrons. When PEs hit and penetrate the surface of the substrate they will be scattered either elastically, if deflected by the nuclei of the substrate atoms without losing energy, or inelastically if they knock out an electron from the shells of the substrate atoms [120]. In case of inelastic scattering the knocked out electrons are called secondary electrons (SEs) [132]. These SEs are generated along the pathway of the PEs [12]. The electrons that are elastically scattered backwards are called back scattered electrons (BSEs). The trajectories of the PEs, SEs and BSEs are not just confined to the point of impact of the PEs but they rather spread both laterally and vertically throughout the specimen forming an interaction volume as shown in figure 5.5 [120]. The interaction volume depends on the composition of the specimen, the primary beam energy, the angle of incidence of the beam with respect to the surface and the probe size. Scattered electrons with enough energy will be able to escape from the surface. The depth from which electrons can still escape from the surface (escape depth) depends on their energy and the substrate material [12]. When the beam hits the sample under an angle, a larger portion of the interaction volume is within the escape depth, which results in the escape of a larger number of SEs, as shown in figure 5.6. There are two types of SEs. SE1 are produced directly by the PE close to the point of incidence of the PE beam [120]. SE2 result from inelastically scattered BSEs, and can emerge from the surface if they are within the escape depth [120]. During FEBID, the precursor gas inserted in the SEM chamber, adsorbs to the surface of the substrate. PEs, BSEs and SEs cause the dissociation of the adsorbed precursor molecules into non-volatile fragments that form the deposit and volatile by-products that are pumped away [133]. The efficiency of this process is determined by the energy dependent dissociation cross section [131]. When a pillar shape starts to grow vertically under a stationary electron beam, the PEs will be scattered within the deposit, may exit the pillar from the side walls and then hit the substrate [132]. These are called forward

scattered electrons (FSEs). Due to all the scattering mechanisms mentioned, the deposit formed from the interaction of a focused e-beam with a sample at a specific point will not have the same dimensions as the PE beam spot size. Some of the scattered electrons within the interaction volume that are able to escape from the surface can contribute to the deposition. In pillar deposition, the vertical growth rate is mostly caused by PEs and SE1, and the lateral growth rate is mostly due to the FSEs and SE2 [134].

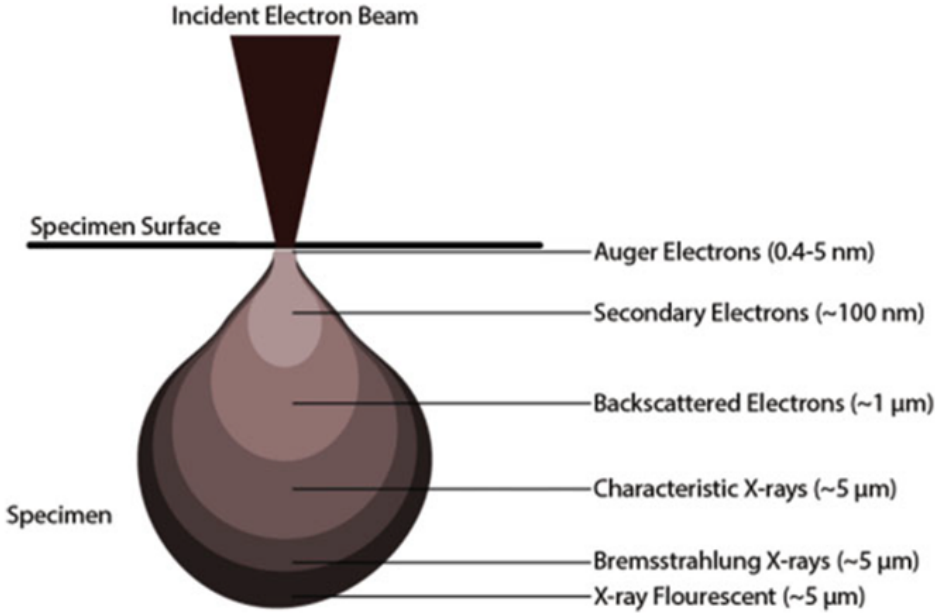

Figure 5.5: Illustration of the interaction volume upon exposure to a focused e-beam. The figure is reproduced with permission from Springer Nature [120].

The primary beam energy affects the interaction volume, as illustrated in figure 5.7. At high energy the interaction volume is pear-shaped with a tiny intersection area at the surface (figure 5.7a), whereas at low energy the interaction volume resembles more of a half sphere with a large intersection with the surface (figure 5.7b). Therefore the PE energy will influence the size of the building block. At the beginning of the deposition, the growth is governed by the PE's, SE1's [134–136] and the probe size. It is expected from the reduced brightness β_r (Equation 5.1), a conserved quantity in electron optical systems, that at a given beam current and opening angle, the smallest spot size, and thus building block size, is obtained at the highest beam energy. So, for high resolution fabrication, with tiny building blocks, a high beam energy is used. However, if a design does not require features with the highest resolution, then larger building blocks can be deposited at lower beam energies, or at a higher beam current, which scales with the probe area at a given beam en-

ergy and opening angle [137]. At low energy also small building blocks can be deposited by reducing the deposition time, which would have the advantage of a larger growth rate than at higher energy.

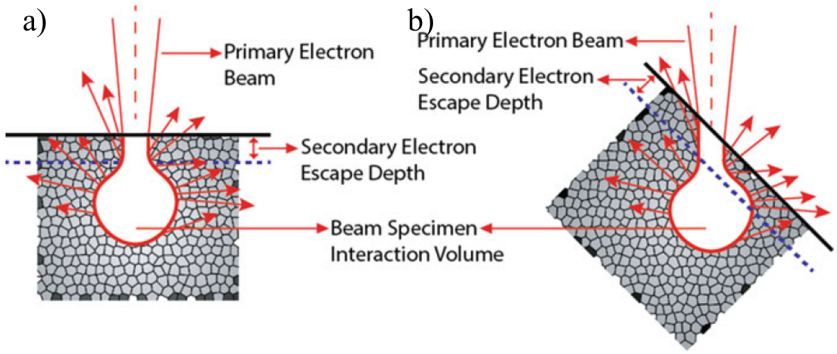

Figure 5.6: Scattering of secondary electrons (SE) from a) a flat and b) a sloped surface. The escape depth includes a larger portion of the interaction volume in the sloped surface which results in the escape of a larger number of SEs. The figure is reproduced with permission from Springer Nature [120].

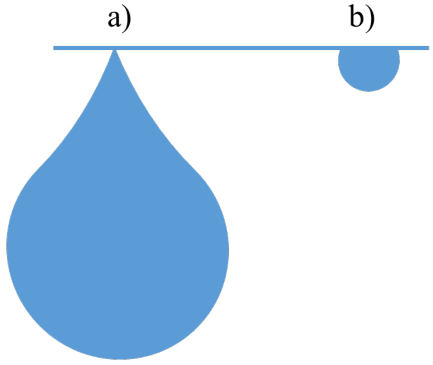

Figure 5.7: Illustration of the interaction volume for a high beam energy a) and low beam energy b) for the same substrate.

$$\beta_r = \frac{dI}{dA.d\Omega.V} \tag{5.1}$$

The reduced brightness is defined as the beam current dI passing through a surface dA within a solid angle dΩ. V is the electron acceleration voltage. For deposition from the Pt precursor $MeCpPtMe_3$, the deposition yield increases with increasing beam energy reaching a maximum at about 150 eV, and then decreases at higher energies as shown in figure 5.8 [133, 138]. For deposition from $W(CO)_6$, the peak of the deposition cross section is between 100 eV

and 1 keV as shown in figure 5.9 [12, 138]. Although in this work all experiments were performed using $MeCpPtMe_3$, these two examples show that in the energy range available in regular SEM's (1-30 keV) the deposition yield will decrease towards higher energies.

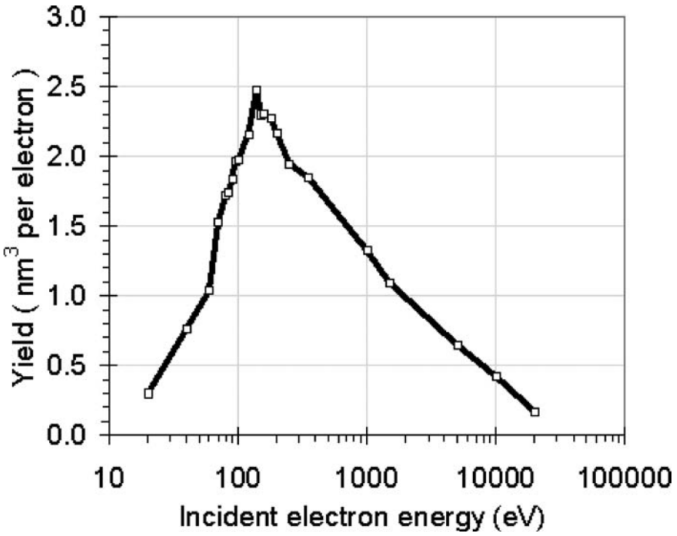

Figure 5.8: The deposition yield for $MeCpPtMe_3$. The figure is from [133, 138].

As mentioned earlier, the idea is to build a 3D shape in an additive manner arranging building blocks in a certain order and stacking them in multiple layers. The stacking of the blocks is not simply adding volumes of material because of the physics of the deposition process. Depositing a pillar affects neighboring pillars as well. These effects are called proximity effects. One type of proximity effect results in a halo created around the deposit caused by BSEs and SE2 from the substrate and by FSEs and SEs originating from the growing deposit. Depending on the substrate material and the beam energy, the BSE range will differ and thus, halo's of different size and thickness can be formed. Higher beam energy results in a larger halo around the deposit [13, 139]. If a neighboring pillar is within that halo range it will grow in size. For instance, when pillars are deposited adjacent to each other in a straight line, the last deposited pillar will be the thinnest. This has been experimentally demonstrated in [13, 140, 141]. In addition, neighboring pillars may cause pillar bending as a result of charging [13, 141]. When a new pillar is being deposited, electrons are emitted from it, leaving it positively charged and a nearby previously deposited pillar becomes negatively charged which leads to the bending of the previously deposited pillar. This is more significant in high aspect ratio structures. For these reasons, the order of deposition is very important especially in building 3D shapes. Another proximity effect arises from deposition at a sloped surface. When the deposition starts at a sloped surface, the escape depth of the scattered SE includes a larger portion of the interac-

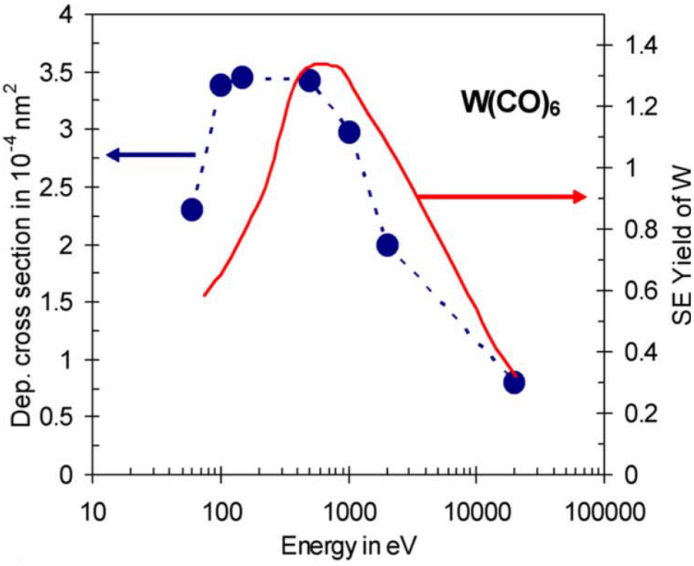

Figure 5.9: Deposition cross section for $W(CO)_6$ and SE yield for W. The figure is reprinted with permission from [12]. Copyright 2008, American Vacuum Society.

tion volume which results in the escape of a larger number of SE as illustrated in figure 5.6. This enhances the deposition rate. Furthermore, depending on the beam energy, deposited points in previous layers might thicken. The larger the beam energy, the deeper they penetrate leading to extra deposition and thickening of previous layers. However, instead of being obstacles, some of these proximity effects can be used together with controlling the writing strategy and the deposition order to enhance the growth rate.

If the dose is kept constant, the beam current and dwell time are inversely proportional. Choosing a low beam current and long deposition time ensures the most efficient growth in terms of utilizing the supplied electrons but it takes a long time. According to [15], the lowest beam currents (such as 21 pA) are the most suitable for building overhanging 3D shapes using FEBID. Higher beam currents were shown to result in co-deposition of unwanted secondary deposits and the formation of side branches underneath the overhanging shape [15]. The co-deposits were ascribed to PEs transmitted through the overhanging shape, with a small cross section for precursor dissociation, and SE's emitted from its bottom [15, 142]. An example of co-deposition is shown in figure 5.10 for a pillar deposited using 100 pA and a 2 keV beam. At higher beam energy there are fewer SEs emitted from the bottom surface of overhanging structures, because of the lower SE yield, and thus less co-deposition will occur. To avoid co-deposition and side branching is crucial for open structures based on the diving board shape as shown in figure 5.3. This forces one to choose a low beam current, leading to a long deposition time.

In closed wall structures or solid shapes, based on solid building blocks, co-deposition and side branching will much less influence the resulting shape of the deposit, such that higher beam currents can be used, thereby reducing the deposition time.

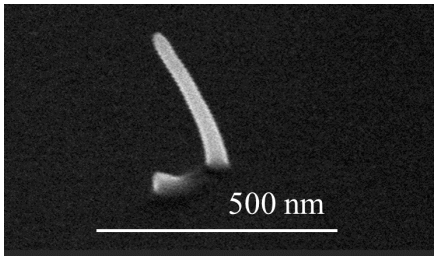

Figure 5.10: Pillar deposited from the $MeCpPtMe_3$ precursor, using a beam of 100 pA for 1.6 ms and beam energy of 2 keV, showing a co-deposited structure underneath.

An electron beam penetrating a growing pillar may cause the pillar to heat, which may lead to bending of the pillar towards the substrate and a reduction in growth rate [143]. The heating increases with increasing acceleration voltage V, as follows from Equation 5.2. The temperature increase ΔT_{bulk} is calculated by assuming that the heat due to the electron beam is evenly distributed in a hemisphere of radius R_H equal to half the electron range R_E, i.e. $R_E/2$ [12]. In Equation 5.2, I is the beam current, η is the backscatter electron yield and κ is the thermal conductivity of the bulk substrate.

$$\Delta T_{bulk} = VI\frac{1-\eta}{2\pi\kappa R_H} \tag{5.2}$$

The beam current contributes to the local heating effect as well. Simulations have shown that the heating causes a decreasing precursor residence time and an increasing precursor desorption rate [143, 144] leading to slower growth. This typically causes a growing pillar to bend towards the substrate [143]. The heat dissipation to the bulk substrate depends on the cross sectional area of the deposit [143], the larger the area, the higher the heat dissipation rate. In mesh-like shapes, with small cross sectional area, heating might have a serious slowing-down effect on the growth. In the deposition of a closed wall structure, such as a cone, with a much larger cross sectional area, the effect of heating is expected to be much less.

5.2. Experimental Method

All experiments were performed in a Helios G3 dual beam SEM (Thermo Fisher Scientific). A silicon substrate was used for all experiments, patterned such that circular areas of pristine silicon are surrounded by black silicon, as obtained by reactive ion etching. The black silicon area helps in focusing the electron beam close to the circular Si areas where the deposition is done. The

sample was mounted on an aluminum stub either with carbon tape or with a metal clamp. $MeCpPtMe_3$ was used as a precursor in all experiments. The precursor was filled in the standard GIS from Thermo Fisher Scientific. The GIS-nozzle was aligned to about 150 µm above the sample and about 50 µm from the electron beam incidence position. The precursor is heated to 45 °C and the crucible and nozzle are always kept warm as long as the chamber is pumped. The SEM background pressure is usually around $1x10^{-6}$ mbar and rises to about $1x10^{-5}$ mbar when the GIS valve is opened to allow the precursor in. When the nozzle is inserted the focus is manually readjusted. After the valve is opened, the chamber pressure is monitored and the deposition is started only after the pressure reaches a stable value. All depositions are carried out in the ultra-high resolution (UHR), or immersion, mode. The working distance was always kept at 4 mm to ensure that the distance between the sample and the nozzle is kept constant. The depositions were done using stream files which are text files that include the coordinates of all the points in the designed shape (in pixels) and the dwell time (the time that the beam stays at each pixel) in the prescribed order. The Helios G3 has a 16-bit DAC, therefore there are 65536 addressable pixels in the X-direction, and 56576 in the Y-direction. A full horizontal field width (HFW) is equivalent to 65536 pixels. This can be used to calculate how many pixels correspond to 1 nm at a specific magnification. The pattern is always placed at the center of the field of view. When cones of the same diameter are deposited, the magnification, and thus the HFW, is kept constant such that the resolution remains constant.

The stream files were generated using Matlab. The variables that define the cone are the bottom and top radii, r_b and r_t, respectively, the pitch between neighboring deposition points in a circular cone layer, pt_{pitch}, the radial decrement between consecutive cone layers, r_{pitch}, the number of passes, n_{passes}, used to revisit a cone layer before a radial decrement is applied, the dwell time, t_{dwell}, defined as the time that the beam exposes a location uninterrupted, the HFW and the total number of pixels that correspond to the HFW (65536 in the case of the Helios SEM we used). All variables with the dimension of length in nm are converted to pixels. The number of layers, n_{layers} is calculated as $(r_b\text{-}r_t)/r_{pitch}$, and consequently the layer height is $\Delta h = h/n_{layers}$. The pt_{pitch} is kept constant throughout the cone, although the actual distance between adjacent deposition points may slightly differ to achieve a uniform distribution of deposition points per cone layer. The number of points, n_{pts} for each circle of radius r is calculated by dividing the circumference by the pt_{pitch}, $n_{pts} = Int((2\pi r)/(pt_{pitch}))$. These points are uniformly distributed over a circle by letting an angle θ range from 0 to 2π in steps of $(2\pi)/n_{pts}$, excluding the value of 2π to avoid a double exposure. The x and y coordinates are calculated for each layer as $x = r\cos\theta, y = r\sin\theta$ and stored in an array. Sometimes it is beneficial to deposit a circle in several passes to allow for replenishment of the precursor molecules. In such cases each circle is revisited n_{passes} times before the radius is decreased to deposit the next smaller cone layer, and n_{passes} times the height of the building block should equal the required layer height Δh. The stream file contains the coordinates in pixels and the dwell time in

units of 0.1 µs. The range of dwell times allowed by the patterning software is 25 ns to 25 ms. Longer dwell times can be achieved by repeating lines with the same coordinates in the stream file until the desired time is achieved.

Two different approaches will be used to build the same shape. The first approach is to choose a building block as small as possible and arrange them closely packed to each other. The goal is to deposit rings, which are flat and smooth, on top of each other to avoid having to take proximity effects into account. It is also the ultimate way to fabricate high-resolution structures, using the smallest possible building blocks. As discussed in the previous section this requires a high beam energy and low beam current. The second approach utilizes the proximity effects to speed up the growth. In this approach the building blocks are larger and well separated from each other. Throughout the growth of consecutive layers, the gaps are filled. Pillar-shaped building blocks are grown on sloping parts of the pillars in the previous layer, thereby enhancing the growth. Throughout the cone growth the pt_{pitch} and the dwell time were fixed, but the number of points per layer was varied. This approach minimizes differences in proximity [140, 141, 145] and heating effects [143] and precursor flux between different layers and simplifies the design significantly. This is one of the main differences between our approach and the earlier work by Niels Noordzij (cf. section 5.1) and other simulation-guided approaches in [29–31].

5.3. Single building block study

In this section the deposition of single building blocks is studied by a variation of the parameters that influence the FEBID growth. The building blocks to be used for 3D fabrication are made using point exposures and basically consist of small pillar-shaped deposits. As discussed above the size and shape are determined by parameters such as the electron beam energy, the beam current and the deposition time. First the influence of the beam energy will be investigated.

5.3.1. Influence of beam energy

In section 5.1.2 it was argued that using a larger beam energy leads to a smaller deposited volume, when keeping the beam current and deposition time constant. To verify this experimentally, seven series of 9 pillars were deposited, each pillar at a different beam energy ranging from 1 to 20 keV, at an almost constant beam current between 79 and 85 pA, as measured using a Faraday cup. The dwell time for each series was chosen between 10 and 80 ms. SEM images of the tilted pillars deposited at 20 ms dwell time are shown in figure 5.11. It is clearly seen that the deposited volume decreases towards higher beam energies. The height and base diameter of the pillars were measured from the SEM images and plotted for all series as a function of beam energy and dwell time in figure 5.12.

As observed in figures 5.11 and 5.12, when the beam energy increases, both the height and diameter of the pillar decreases. Figure 5.13 shows that the

volume of the pillar, as obtained from the height and diameter as described in [98], decreases as the beam energy increases and then starts to saturate. A similar experiment was performed by Winkler et al. [15] using 5 pA, 5 kV up to 21 pA, 30 kV electron beams. They determined the vertical growth rate (VGR) and normalized that for the current used. It was measured for 5, 10, 15, 20 and 30 kV and was found to be highest (6.94 and 6.89 nm/(s.pA)) for 5 and 10 kV respectively. The normalized VGR at 30 kV was 47 % less than for 5 kV. For the pillars in figure 5.12, grown at 20 ms, using 10 kV and a measured beam current of about 80 pA, the normalized VGR is about 20 nm/(s.pA). This is almost three times the VGR calculated in [15] for pillars grown using 5 or 10 kV but a 21 pA beam current. This shows the clear dependence of the VGR on the beam current and energy.

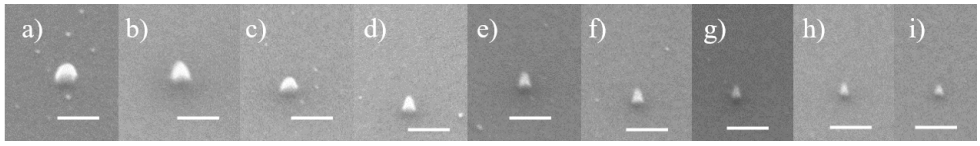

Figure 5.11: Pillars deposited using a beam current between 79 and 85 pA and a dwell time of 20 ms for different values of the beam energy: a) 1 kV b) 2 kV, c)3 kV, d)5 kV, e)7 kV, f)10 kV, g)15 kV, h)18 kV and i)20kV. All scale bars are 100 nm. Images are 50° tilted.

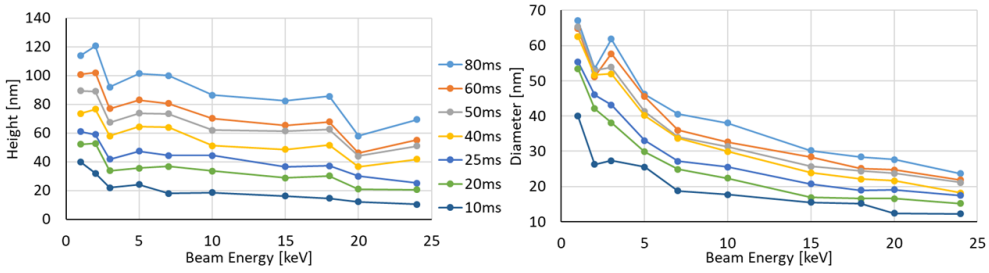

Figure 5.12: Height and diameter of pillars deposited at different beam energies for different dwell times. The beam current was between 79 and 85 pA depending on the beam energy.

5.3.2. Influence of beam current and dwell time

To investigate experimentally the effects of the beam current and dwell time on the building block, pillars were deposited using the same beam energy (10 kV) but different beam currents, as measured using a Faraday cup. The experiment was repeated at different dwell times. The pillars deposited with 80 ms dwell time are shown in figure 5.14. The height and base diameter of the pillars were measured from SEM images and plotted versus the beam current in figure 5.15. The volume of the pillars was calculated and plotted versus the

beam current in figure 5.16. Both the height and diameter saturate for beam currents of several hundreds of pA's. The same data are plotted in a different way in figures 5.17 and 5.18, i.e. versus the number of incident electrons needed to grow a pillar, as calculated from the product of the beam current and the dwell time, and divided by the electron charge. At the same electron dose, a higher beam current leads to a lower pillar height, indicative of the growth being limited by the precursor supply. Therefore the growth is less efficient for higher beam currents. Perhaps only for the smallest current of 17.1 pA the growth is in the current limited regime, following a linear variation of height with electron dose, but at higher currents a deviation from linear behavior can already be seen. The diameters are seen to vary with electron dose in a much more universal way, independent of the beam current. Even for the highest electron doses they are still increasing because the corresponding pillar heights do not yet exceed the range of the electron scattering volume at 10 keV.

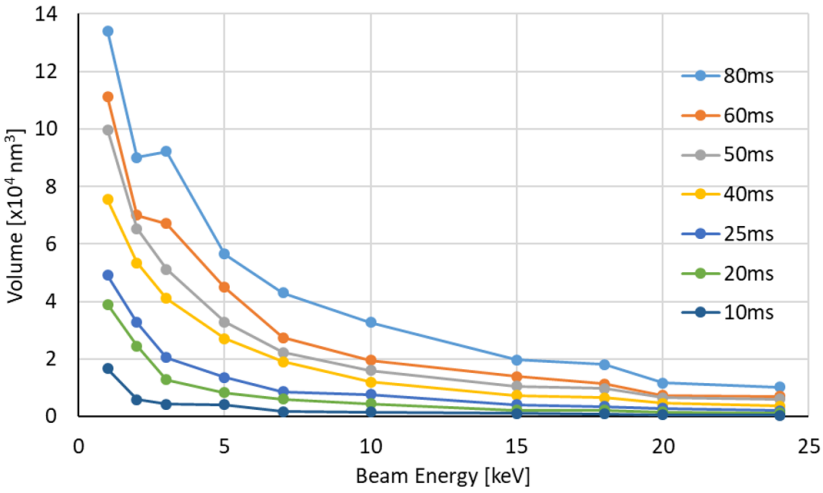

Figure 5.13: Volume of pillars deposited at different beam energies for different dwell times. The beam current was between 79 and 85 pA depending on the beam energy.

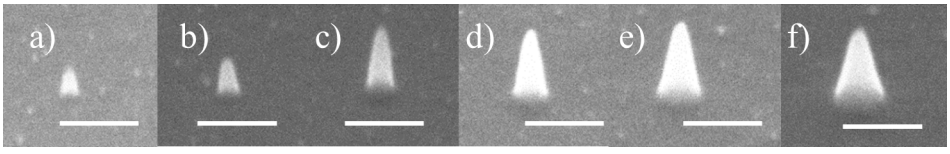

Figure 5.14: Pillars deposited using a 10 kV beam and different beam currents. The dwell time for each pillar is 80 ms. The beam currents, as measured using a Faraday cup, were: a) 17.1 pA, b) 39.8 pA, c) 77.4 pA, d) 155.5 pA, e) 314.8 pA and f) 624 pA. The scale bars are 100 nm.

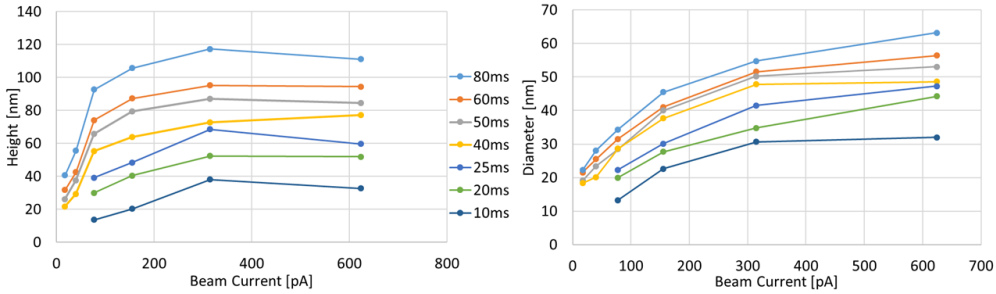

Figure 5.15: Height and diameter of pillars deposited using a 10 kV beam energy and different beam currents for different dwell times. The currents in the plots are measured currents using a Faraday cup.

An interesting observation from the two graphs in figure 5.17 is that one can choose the aspect ratio of the building block. For example, a 32-34 nm diameter pillar requires about 4×10^7 electrons, irrespective of the beam current. From the left hand graph in figure 5.17 it is seen that at a beam current of 624 pA a pillar height of about 32.7 nm is obtained and at 77 pA a height of about 92.7 nm. The respective dwell times to fabricate these pillars, of aspect ratio 1 and 2.7, are calculated as 10 ms and 80 ms. The volume growth rate of the bigger pillar is only 2.5 times smaller than for the smaller one (see Table 5.1). When a ≈15 nm diameter building block is required, 5×10^6 electrons are needed, but for such low electron doses there is much less variation in pillar height with beam current. At a beam current of 624 pA the height would be about 10 nm, and the corresponding dwell time about 1 ms, whereas at 77 pA the height would be roughly the same and the dwell time would be 10 ms.

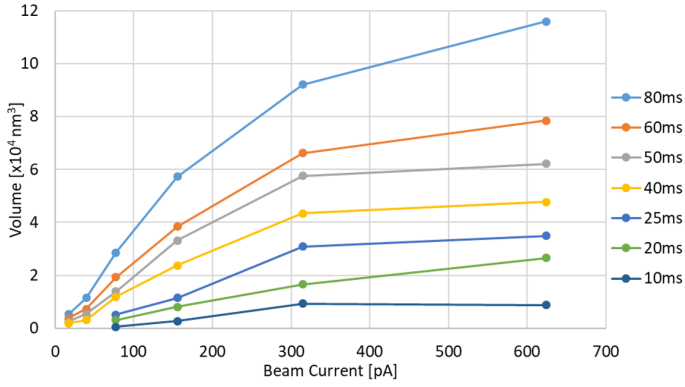

Figure 5.16: Volume of pillars deposited using a 10 kV beam energy and different beam currents for different dwell times. The currents in the plots are measured currents using a Faraday cup.

These examples, summarized in table 5.1, show that when the smallest building block is fabricated at high current and small dwell time the deposition efficiency (volume/dwell time) is almost ten times higher than at low current and high dwell time. Of course, even smaller building blocks can be fabricated by using smaller dwell times and/or higher beam energies, but it would be more difficult to image them individually and determine their dimensions. When using such small building blocks a better strategy to characterize the growth is to deposit multiple layers to a measurable thickness, image those deposits and determine average values of height, deposited volume, thickness, etc. So far in the discussion of the building block dimensions, proximity effects were not taken into account. But they do contribute to the growth rate. The above suggested strategy to deposit multiple layers and determine average dimensions would also include these effects. Which building block, beam current and dwell time to choose depends on the design priorities. If the desired shape is small (<100 nm) and has very fine and thin parts or segments, high beam energy and low beam current (e.g. 21 pA) would be the best choice to achieve the highest resolution. Although, if the probe size is not the dominant contribution to the dimensions of the building block, a larger current can be used and the accompanying gain in growth rate. For taller shapes (> 1 µm) with thick solid parts, growth rate may have priority and it is better to use higher beam currents (e.g. hundreds of pA's). Using very high beam currents (> 200 pA in case of a 10 kV beam) may not be a wise choice since the growth rate does not increase much but thermal effects may start to kick in.

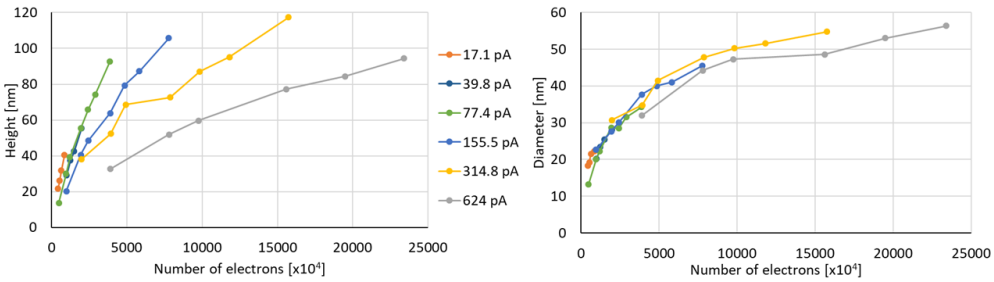

Figure 5.17: The height and diameter of the pillars at different doses expressed as number of electrons calculated from the product of the beam current and the dwell time and divided by the electron charge. All the points on a line have the same beam current but the dose is different by varying the dwell time. The currents in the legend are measured using a Faraday cup.

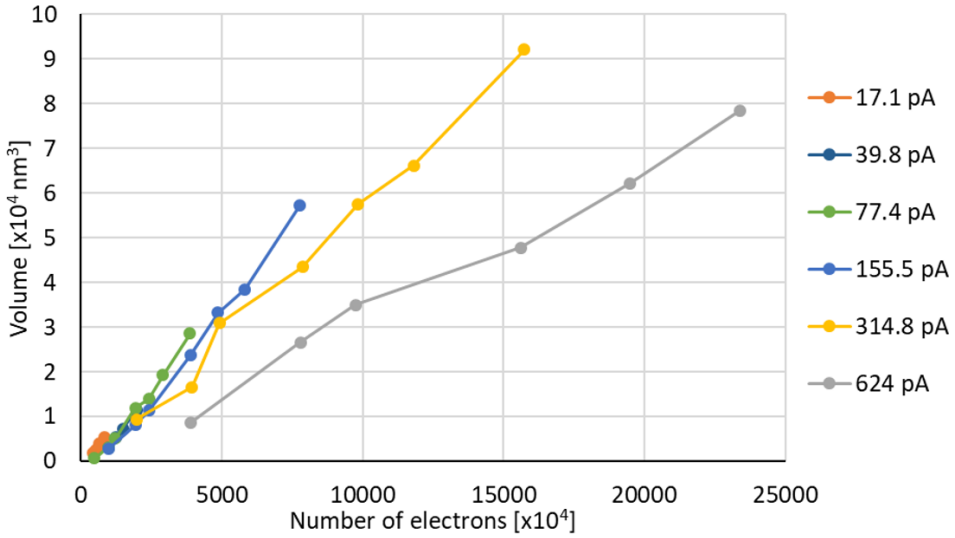

Figure 5.18: Volume of the pillars at different doses expressed as number of electrons calculated from the product of the beam current and the dwell time and divided by the electron charge. All the points on a line have the same beam current but the dose is different by varying the dwell time. The currents in the legend are measured using a Faraday cup.

d (nm)	h (nm)	I (pA)	t_{dwell} (ms)	Vol. (nm^3)	Vol. growth rate (nm^3/ms)
32	32.7	624	10	8739	874
34.3	92.7	77	80	28552	357
15	10	624	1	589	589
13.3	13.7	77	10	627	62.7

Table 5.1: Comparison of the volume growth rate of pillars deposited at the same dose but at two different current values I. The volume (Vol.) is calculated as $\pi d^2 h/12$, where d is the diameter and h the height of the deposited cones.

5.4. From building block to 3D shape – experimental results

As an illustration of the above discussion about the influence of the beam energy, current and dwell time on the dimensions of the building block and the growth rate, experiments were performed at 10 kV and 80 pA. By choosing this intermediate beam energy, the growth rates are not too low and broaden-

ing of previously deposited points is limited as the penetration depth is much smaller than at 30 kV. At the same time, the beam energy is not so low to decrease the resolution and secondary deposition will still be limited. Also an intermediate beam current of 80 pA was chosen allowing to illustrate high-resolution small building block growth as well as rapid large building block growth. As mentioned in section 5.2, two different approaches are followed, the first employing small, closely packed, building blocks and the second employing larger separated building blocks.

5.4.1. Cone fabrication using small building blocks

The first approach uses a building block as small as possible and they are closely packed to each other. The dwell time was chosen as 50 µs. The pt_{pitch} is set to 1 nm, which means that neighboring points in the circles to be deposited will largely overlap. Then each layer is repeated for 2 passes leading to a total exposure time per pixel of 100 µs in each layer. Choosing an even smaller dwell time (close to 25 ns) would require many more passes before a visible deposit is formed, and before the next layer of reduced radius is deposited. This would create a huge stream file that may exceed the maximum allowed stream file size. Another limitation may be posed by the deflection time of the beam moving from point to point [30]. If the desired 3D shape requires a large amount of beam deflections, in case the dwell time is very short and multiple passes are needed, the total deposition time will increase.

In the cone design the radii are fixed to r_b = 500 nm and r_t = 100 nm, and the desired height h = 2 µm. To study how the cone develops when the number of layers increases, the radial pitch r_{pitch} is set to 0.3 nm and the number of passes is taken as two. Figure 5.19 shows SEM tilt-images of a sequence of cones for an increasing number of layers. The small dot deposited on the right of each cone marks the starting point of the deposition. In all depositions the GIS nozzle was positioned in the top left corner of the SEM images. Figure 5.19a) already consists of 10 layers, each of slightly decreasing radius. It is easy to imagine that a single deposited circle would have been barely visible in an SEM image. The circles in the figure have smooth top surfaces as a result of the small and overlapping building blocks. The cone walls thicken on the inside when more layers are deposited.

The experiment is continued with another sequence in which more layers are added until a complete cone is obtained. Figure 5.20 shows the SEM tilt-images of the cones. The inner diameter at the cone base appears to slightly decrease as the cone height increases. This is due to the electron beam interaction volume which rises through the cone wall when the height increases. This leads to a wall thickness increase similar to the diameter increase of a single pillar during its growth: it starts as a small conical shape, which grows laterally at first, but when the height increases and the interaction volume rises through the pillar, the diameter of the pillar becomes constant, as shown in figure 5.21. In the cones of figure 5.20 a slight irregularity is observed at the top part of the cone especially in figures 5.20f and 5.20g. Looking more carefully, it is seen to develop already at an earlier stage of the growth, as

visible in figure 5.20b. Possible causes of this irregularity will be addressed in a few dedicated experiments that will be described in section 5.4.2. Also the slight deformation visible at the lower right of the cones in figure 5.20 will be discussed there. Figure 5.22 shows the top view of a complete cone. Lines and circles have been added in red to check the alignment between the top and bottom circles of the cone. A small misalignment can be observed between the centers of both circles of about 30 nm in both the x and y directions. This misalignment can possibly be attributed to stage and sample drift which will be further discussed in section 5.5. Figure 5.23 shows the height of the cones in figure 5.20, as a function of the number of layers. The height, represented with a red line shown in figure 5.20g), was measured from the dip point on the top right and corrected for the tilt, as a reference point in all images, to the surface of the sample marked with a dashed red line passing through the pillar deposited beside the cone that marks the starting point. A linear increase in height is seen up to 400 layers, after which the height increases more rapidly. The latter is probably due to the proximity effect which will increase towards the top of the cone. The initial height increase is 1.2 nm/layer which comes down to a building block height of only 0.6 nm.

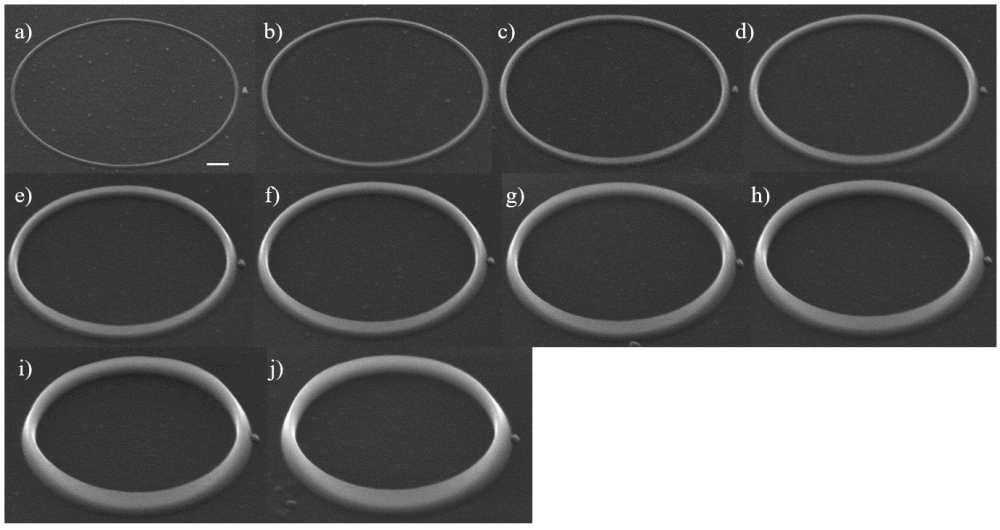

Figure 5.19: Cones grown with different numbers of layers. r_{pitch} was fixed at 0.3 nm and the number of layers was varied. r_b was 500 nm. Cones were deposited using 10 kV and a 80 pA beam current. pt_{pitch}=1 nm, dwell time= 50µs repeated for 2 passes. The number of layers was a) 10, b) 20, c) 30, d) 40, e) 50, f) 60, g) 70, h) 80, i) 90 and j) 100. All images have the same scale. The scale bar is 100 nm.

In order to study what the effect of changing r_{pitch} is on the cone growth, the number of layers was fixed to 400 and r_{pitch} was varied between 0.1 and

1 nm. Naturally, this will lead to a variation in the top radius r_t. As before, r_b was 500 nm, the dwell time was 50 µs , the pt_{pitch} = 1 nm, and each layer is repeated for 2 passes (total exposure time per pixel = 100 µs). Figure 5.24 shows the SEM images of the deposited cones. These small changes in r_{pitch} seriously affect the cone angle, but did not much affect the cone height under these conditions. This is clearly seen in figure 5.25 which shows the cone height and cone angle as a function of r_{pitch} for the cones shown in figure 5.24. It is easily seen from figure 5.25 that a value of 0.2 nm for r_{pitch} should lead to the desired angle of 78.7º and consequently to a 2 µm cone height. This was tried experimentally and figure 5.26a shows the cone deposited with r_{pitch} = 0.2 nm. The resulting cone height was 2430 nm, exceeding the desired 2 µm. This may well be due to the increased growth towards the top of the cone. Then a cone with a slightly larger r_{pitch} of 0.3 nm was deposited, which is shown in figure 5.26b. These parameters were used to deposit 8 cones at different times, over a period of one year, and the dimensions, averaged over the 8 cones, were: height=2016 nm, cone angle from the horizontal: 80.5º, r_t = 102 nm, r_b = 554 nm. Over a longer period of time, the cone height variation was between 1600 and 2200 nm when deposited using the same parameters. The variations between depositions will be discussed in the next section. The number of layers for these cones was 1333 and the total cone deposition time was 3 minutes and 45 s.

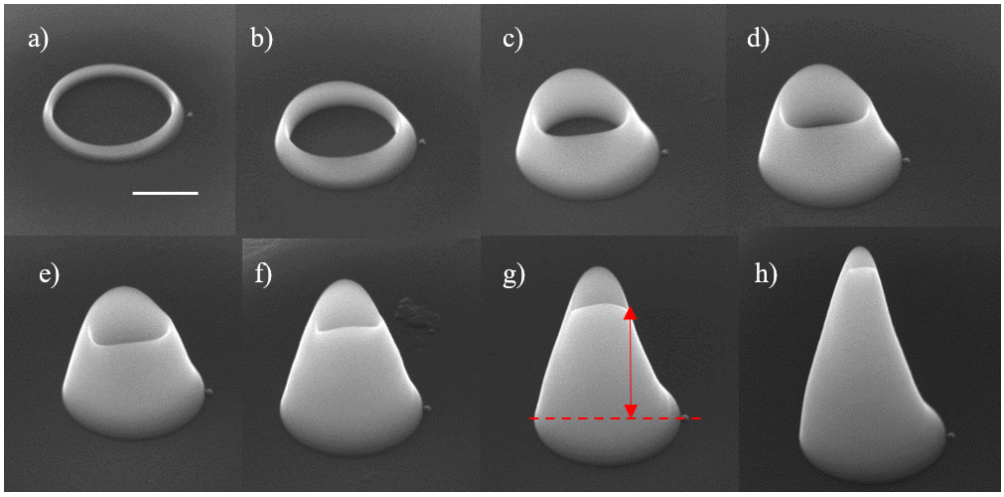

Figure 5.20: Cones grown with increasing numbers of layers. r_{pitch} was fixed at 0.3 nm and the number of layers was varied. r_b was 500 nm and the target r_t was 100 nm. The cones were deposited using 10 kV, and a 80 pA beam current. pt_{pitch}=1 nm, dwell time= 50µs repeated for 2 passes. The number of layers was a) 100, b) 200, c) 400, d) 500, e) 600, f) 800, g) 1000 and h) 1333. All images have the same scale. The scale bar is 500 nm.

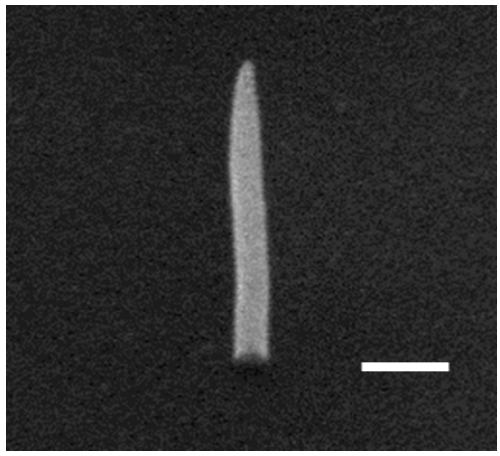

Figure 5.21: SEM 50º tilted image of a pillar deposited at 10 kV and a beam current of 25 pA beam, during 1.28 s. The scale bar is 100 nm. Note the constant diameter of the cylindrical part and the pointy conical top part.

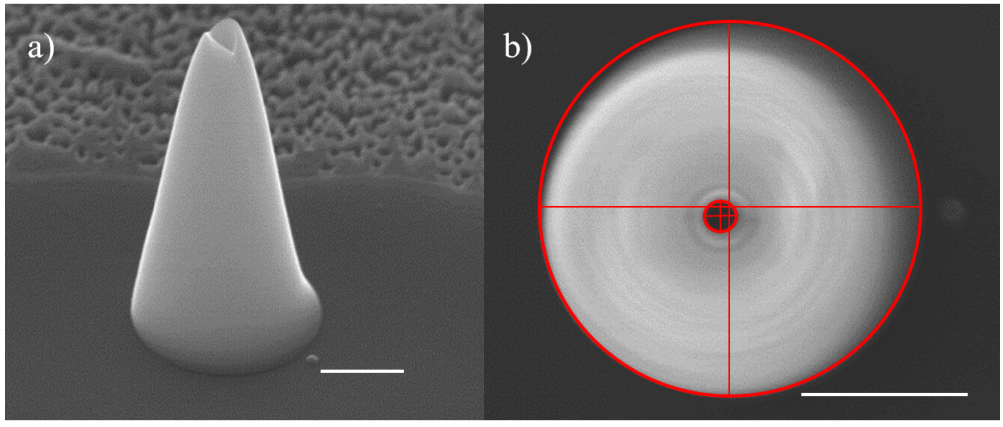

Figure 5.22: a) 50º tilt image and b) top down image of a cone deposited using 10 kV, 80 pA beam. The pt_{pitch} is 1 nm, r_b was 500 nm (measured 564 nm) and r_t was 100 nm (measured 47 nm), the dwell time was 50 µs. Each layer is deposited in 2 passes. r_{pitch} was 0.3 nm. The scale bars are 500 nm. The total number of layers is 1333. The measured height of the cone is 2010 nm.

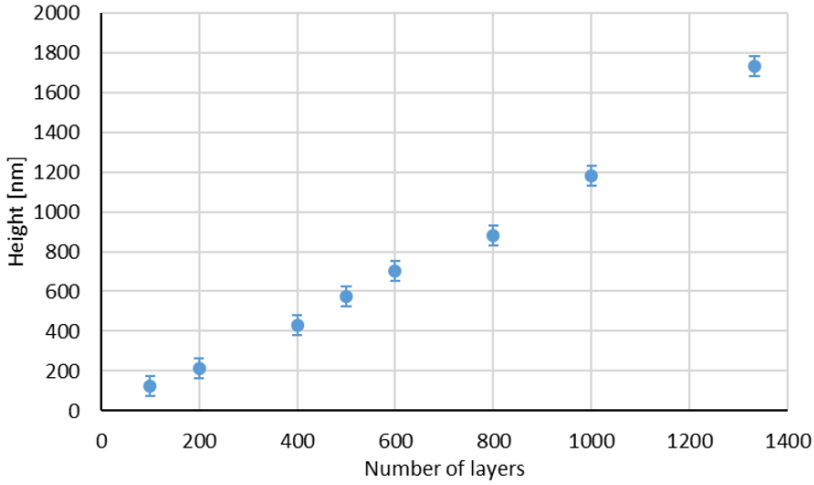

Figure 5.23: The height of cones deposited with a different number of layers, r_{pitch} was fixed at 0.3 nm and the number of layers was varied. r_b was 500 nm and the target r_t was 100 nm. The error bars are ±50 nm uncertainties in the manual height measurements from the SEM images.

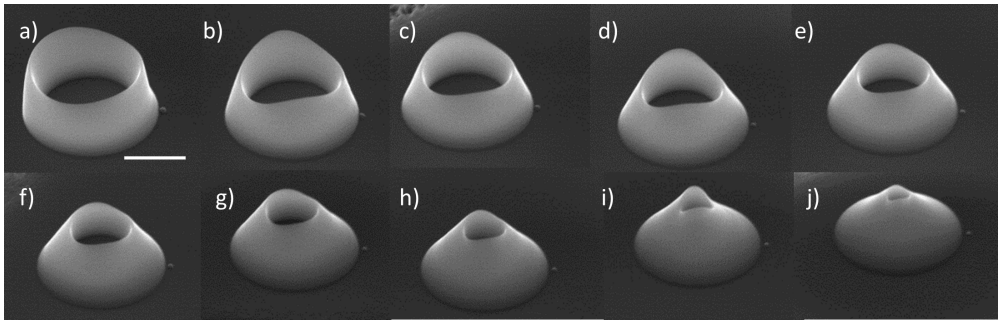

Figure 5.24: SEM 50° tilt images of cones deposited with 400 layers using 10 kV beam. The current was measured to be 88 pA using a Faraday cup. pt_{pitch} is 1 nm, dwell time is 50 µs. Each layer is deposited in 2 passes. r_{pitch} is varied between a) 0.1 and j)1 nm. All images have the same scale. The scale bar is 500 nm.

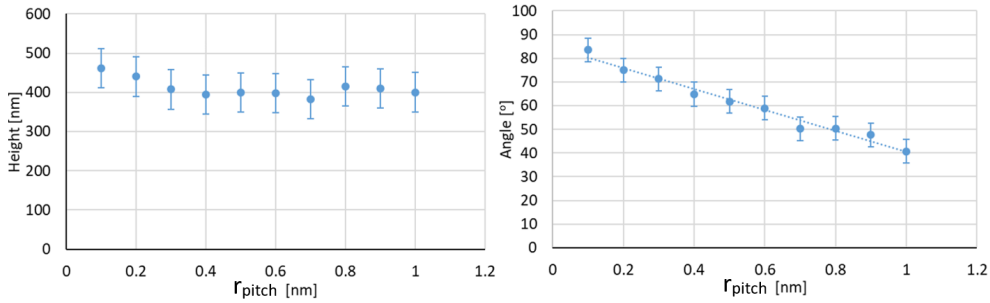

Figure 5.25: Height and angle of cones of 400 layers deposited using 10 kV beam. The current was measured to be 88 pA using a Faraday cup. pt_{pitch} is 1 nm, dwell time is 50 µs. Each layer is deposited in 2 passes. r_{pitch} is varied between 0.1 and 1 nm.

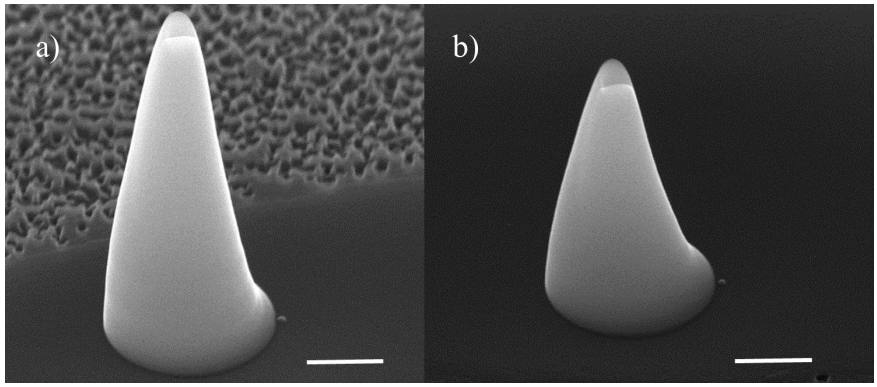

Figure 5.26: SEM 50° tilt images of cones deposited using 10 kV beam. The current was measured to be 83.6 pA using a Faraday cup. pt_{pitch} is 1 nm, r_b was 500 nm and r_t was 100 nm, dwell time is 50 µs. Each layer is deposited in 2 passes. r_{pitch} was a) 0.2 and b) 0.3 nm. The resulting number of layers was a)2000 and b)1333. The resulting cone height was a) 2430 nm and b) 1733 nm. The scale bars are 500 nm.

Smaller cones

Using the same approach, smaller cones were deposited to explore the creation of even smaller shapes. As an example, a cone of about five times smaller dimensions is fabricated, i.e. with r_b = 100 nm, r_t = 20 nm and 78.7 degree cone angle. The beam energy and current for deposition were 10 kV, 80 pA, pt_{pitch} = 1 nm, r_{pitch} = 0.3 nm, dwell time = 50 µs repeated for 2 passes. This means that there are 266 layers in the cone. Assuming we have the same VGR as the larger cones (1.2 nm/layer), then we expect a height of about 320 nm. The resulting cone is shown in figure 5.27a. The cone height was about 350 nm and the angle was about 76º which are both close to the expected values. The cone shape is much more regular than for the bigger ones and the irregularity at the top observed in the larger cones is much less pronounced. Even smaller cones can be created with the same parameters, but at a higher beam energy to achieve smaller building blocks. A cone deposited at 20 kV, with all other parameters the same, is shown in figure 5.27b. From figure 5.12, the height of the pillar at 20 kV for the lowest dwell time of 10 ms was 0.65 times the height of the pillar at 10 kV. Applying the same ratio we expect the height of the cone at 20 kV to be 0.65 times the height of the cone at 10 kV which is 228 nm. The height of the cone is measured to be 220 nm which is almost as expected, and the cone angle is about 67 degrees. This is not the limit, if smaller cone are desired, the shape can still be controllably deposited by decreasing the beam current. Another cone was deposited using a 20 kV beam, with a measured beam current of 36 pA, and the rest of the parameters are kept the same. From figure 5.15, for most of the dwell times, the height of the pillar at 40 pA is about half the height at 80 pA. Thus we expect a cone height of about 110 nm at 40 pA. The resulting cone is shown in figure 5.27c. The cone height was about 115 nm and the cone angle was about 54 degrees. These examples show the flexibility of the method and the potential to create high resolution nano-cones that are almost impossible to create using other methods or lithography techniques.

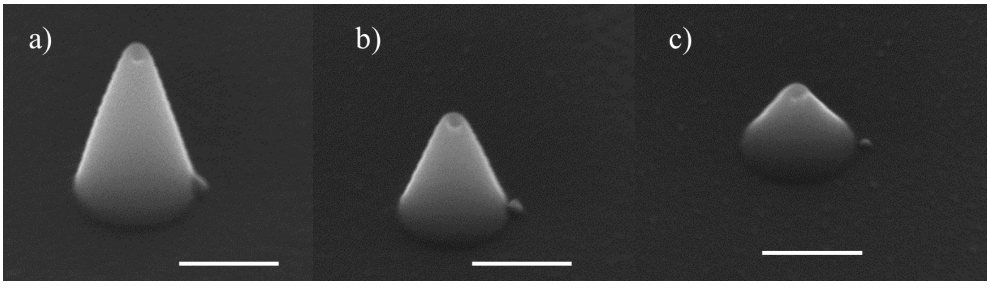

Figure 5.27: Small cones deposited using a beam of a) 10 kV and 80 pA, b) 20 kV and 80 pA, c) 20 kV and 36 pA. r_b was 100 nm and r_t was 20 nm. The pt_{pitch} = 1 nm, r_{pitch}= 0.3 nm, dwell time= 50µs repeated for 2 passes. The small pillar on the right is deposited just to mark the starting position. The scale bar is 200 nm.

5.4.2. Approach 2: Large Building Blocks

The second approach makes use of large building blocks that are well separated. This approach utilizes the proximity effects to enhance the growth rate. From figure 5.12, at a dwell time of 20 ms the height and diameter of a pillar deposited using 10 kV and a 80 pA beam are about 35 and 22 nm, respectively. The pt_{pitch} in this approach is chosen to be larger than the diameter of a single pillar such that the pillars do not overlap and the proximity effects can be utilized. Experiments were performed using a pt_{pitch} of 30, 50 and 70 nm. Values of r_{pitch} are chosen between 1 and 6 nm, i.e. smaller than the radius of the pillars.

First, the evolution of the cone growth is studied by depositing sequences of cones with an increasing number of layers, with pt_{pitch} = 50 nm and r_{pitch} = 2 and 3 nm. Figure 5.28 shows SEM images of a sequence of cones with r_{pitch} = 3 nm and with a number of layers increasing from 1 to 14. The individual pillars are well separated at the beginning of the growth. When the growth proceeds the space between pillars is seen to fill up rapidly with each new layer. The small pillar at the right of each cone marks the starting point of the deposition. Each layer starts at the same point and is written in the same order. The height of the rings in figure 5.28 was measured and plotted versus number of layers in figure 5.29.

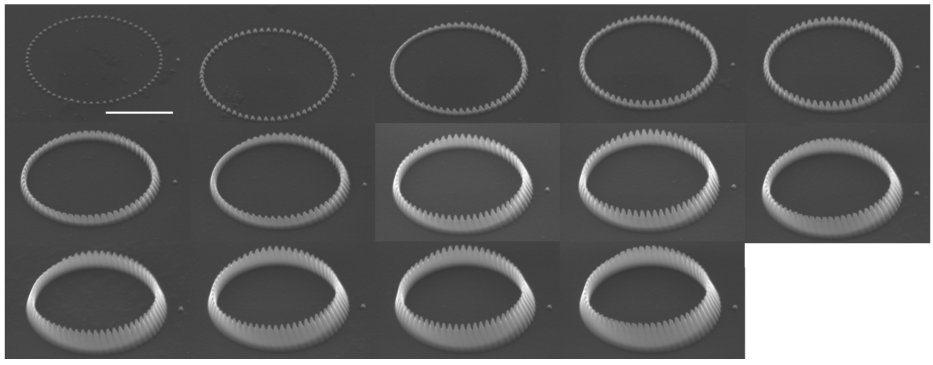

Figure 5.28: Successive layers of a cone deposited using larger building blocks at larger spacing. The beam energy was 10 keV, the beam current was 80 pA, dwell time =20 ms (single pass), pt_{pitch} = 50 nm, r_{pitch} = 3 nm, r_b =500 nm. The scale bar is 500 nm.

The right side of the cone walls in figure 5.28 seems to lean over to the left more than the left side of the cone walls. Also the top of the rings is more corrugated on the right side than on the left side of the cones. These features may eventually further develop to a similar deformation as was seen in the small building block cones at the lower right side of the cones. This raised the question how important the particular order is in which the pillars in a ring are deposited. Small differences in the overlap between pillars in subsequent layers may grow out into irregularities. As a trial experiment the starting point

of a layer was chosen on the opposite side of the starting point of the previous layer, i.e. a shift over π radians. The experiment illustrated in figure 5.28 was repeated, but now introducing this π-shift. Figure 5.30 shows a sequence of 1 to 20 layers of the cone deposited with π-shifted starting points. Comparing figure 5.28 and figure 5.30, the π-shift strategy leads to more uniform rings with more even top surfaces, so the deposition order definitely is of importance. This issue will be addressed later in this section. For now the π-shifted strategy will be adopted. To characterize the height evolution, the height of the rings in figure 5.30 was measured and plotted versus number of layers in figure 5.31. As the top surface of the rings is not smooth, the measured height was taken as the distance between the top of a pillar (top of a hill on the top surface of the ring, the red 'X' in figure 5.30) and the substrate. The height increases linearly up to 20 layers at a rate of 12 nm/layer. Note that this is about one third of the height of the building block of 35 nm, obviously caused by filling up the space between the well separated building blocks.

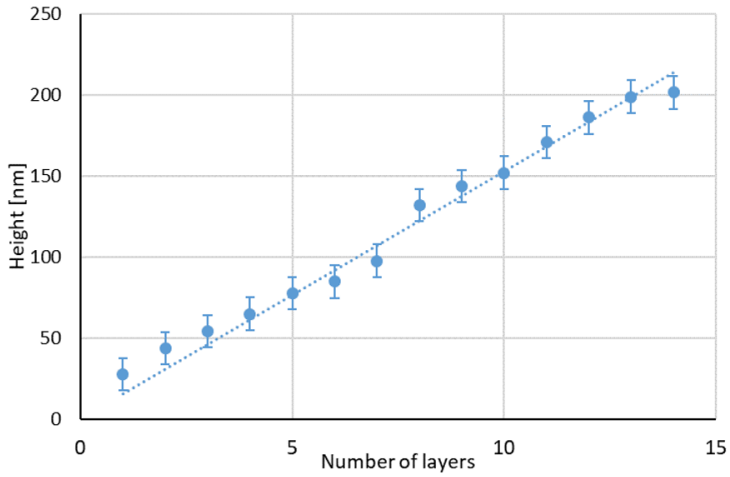

Figure 5.29: Height of the different number of layers for the cones in figure 5.28. The dotted blue line shows the best fit passing through the origin. The slope of the best fit line is 15 nm/layer. The error bars are ±10 nm uncertainties in the manual height measurements from the SEM images.

Next, the effect of the variation of both pt_{pitch} and r_{pitch} on the cone height and angle was studied. In this experiment the number of layers is kept constant at 60 layers. This means that r_t will necessarily vary while r_b remains fixed at 500 nm. As before, the dwell time per pixel is 20 ms (single pass). The π-shifted starting point strategy is used to have a more even growth and to minimize irregularities on the top of the cone. The SEM images of the 60 layer cones and a variation of r_{pitch} between 1 and 6 nm, are shown in figure 5.32 for a pt_{pitch} of 30 nm, in figure 5.33 for a pt_{pitch} of 50 nm, and in figure 5.34 for a pt_{pitch} of 70 nm. For the 30 nm pt_{pitch} smooth cone walls are obtained, but a

severe deformation is seen on top. So, the π-shifted strategy has not entirely solved the deformation issue. Increasing the value of pt_{pitch} results in more corrugated sidewalls but less deformation on top. This is an indication that the proximity of building blocks is an important factor in fabricating shapes that meet the design requirements. Figure 5.35 shows the height and the angle of the cones shown in figures 5.32, 5.33 and 5.34 as a function of r_{pitch} for the three values of the pt_{pitch}. The angles are measured using the angle measurement from the microscope software. The cross section tilt correction option is selected which calculates the corrected angle:

$$\tan \phi_c = \frac{\tan \phi_m}{\sin \alpha} \tag{5.3}$$

where ϕ_c is the corrected cone angle, ϕ_m is the measured cone angle and α is the tilt angle.

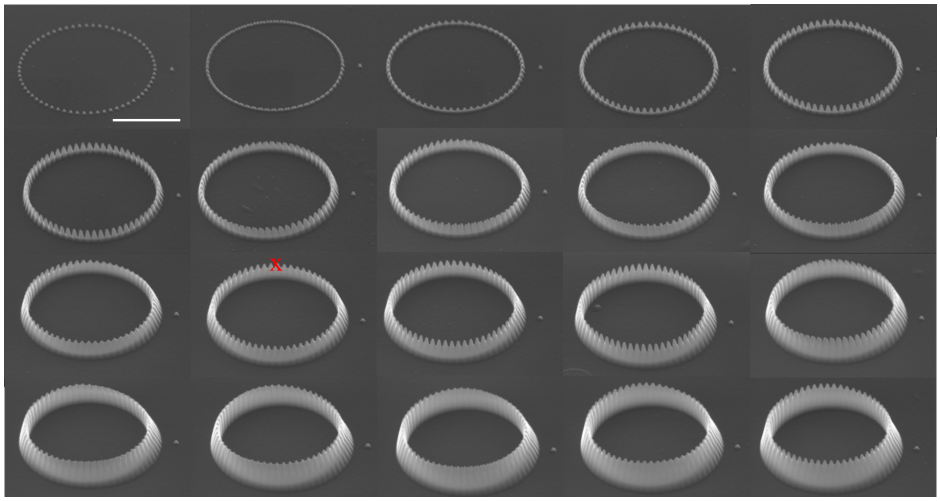

Figure 5.30: Successive layers of a cone deposited using larger building blocks at larger spacing and a π-shift between the starting point of successive layers. The beam energy is 10 keV, the beam current 80 pA, dwell time 20 ms (single pass), pt_{pitch} = 50 nm, r_{pitch} = 3 nm, r_b =500 nm. The red 'x' shows the position where the height is measured. The scale bar is 500 nm.

The height decreases more or less linearly with the radial pitch and also scales with the point pitch. The data can be described, assuming linear behavior, as, the height at layer 60, $h = 1614 - 43.8r_{pitch} - 12.46pt_{pitch}$ (all dimensions in nm). The average layer height in the first 60 layers is then given by $h/layer = 26.9 - 0.73r_{pitch} - 0.21pt_{pitch}$. In figure 5.35, the average layer height ranges between ≈ 8 and ≈ 20 nm depending on radial pitch and the pitch between points. The cone angle ϕ, assuming linear behavior, can be approximated as $\phi = 110.2 - 5.252r_{pitch} - 0.33pt_{pitch}$. Figure 5.35 compares the

measured data to the results of the model. The model for the angle fits well with the measured data for the 50 nm pt_{pitch} but not very well with the other values of pt_{pitch}. For most of the experiments performed, pt_{pitch} of 50 nm was used.

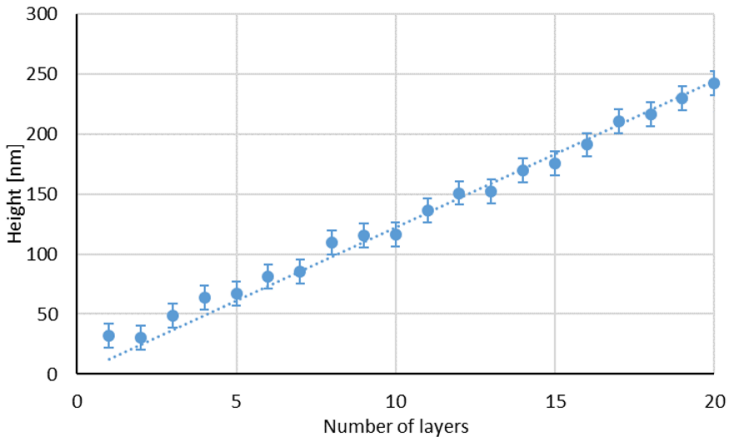

Figure 5.31: Height of the different number of layers for the cones in figure 5.30. The dotted blue line shows the best fit passing through the origin. The slope of the best fit line is 12 nm/layer. The error bars are ±10 nm uncertainties in the manual height measurements from the SEM images.

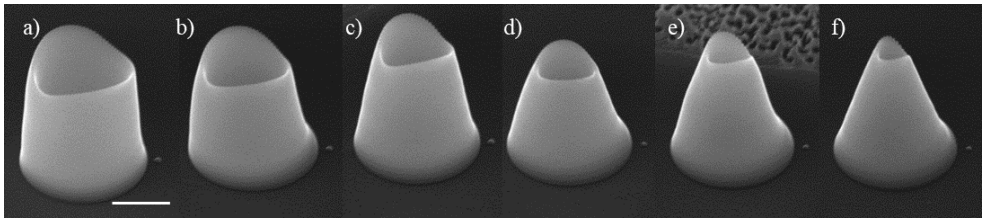

Figure 5.32: 60 layer cones with a 30 nm pt_{pitch} and r_{pitch} varying from 1 to 6 nm from a) to f). The beam energy is 10 keV, the beam current is 80 pA, dwell time =20 ms (single pass), r_b = 500 nm. There is a π-shift between the starting point of successive layers. The scale bar is 500 nm.

In the next experiment full cones are built, keeping $r_b - r_t$ constant and varying r_{pitch} such that the number of layers changes. r_b was fixed to 500 nm and r_t to 100 nm. This was repeated for three values of the pt_{pitch} 30, 50 and 70 nm. Figure 5.36 shows the height and angle of the cones as a function of the radial pitch. This serves as a rough guide for finding the required pitch for a design of a cone with a certain height and angle when the design requires fixed radii.

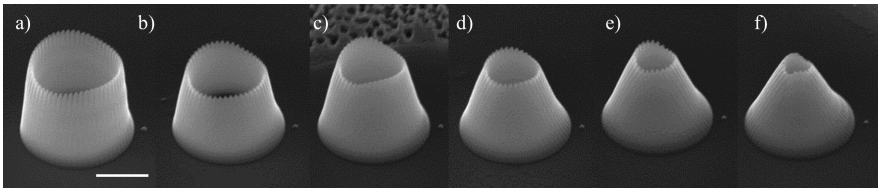

Figure 5.33: 60 layer cones with a 50 nm pt_{pitch} and r_{pitch} varying from 1 to 6 nm from a) to f). The beam energy is 10 keV, the beam current is 80 pA, dwell time =20 ms (single pass), r_b =500 nm. There is a π-shift between the starting point of successive layers. The scale bar is 500 nm.

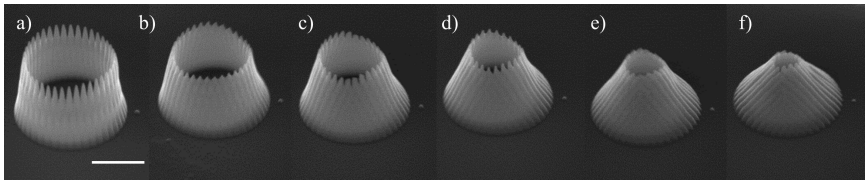

Figure 5.34: 60 layer cones with a 70 nm pt_{pitch} and r_{pitch} varying from 1 to 6 nm from a) to f). The beam energy is 10 keV, the beam current is 80 pA, dwell time =20 ms (single pass), r_b =500 nm. There is a π-shift between the starting point of successive layers. The scale bar is 500 nm.

From figure 5.36 (left) we can see that at a pt_{pitch} of 50 nm and for r_{pitch} ranging from 1 to 6 nm, corresponding to 400, 200, 133, 100, 80, 67 layers, respectively, the average layer height is 7, 9.5, 11.3, 13, 12.5, and 12 nm, respectively. For r_{pitch} of 3-6 nm the average layer height is approx. 12 nm, in agreement with the initial height increase seen in figure 5.31. However, for smaller values of r_{pitch} the average layer height is smaller, indicating a less efficient growth. This might be explained by the fact that for small r_{pitch} building blocks are deposited almost on top of each other, i.e. on a surface of smaller curvature than for larger values of r_{pitch}, where the deposition is on the steeper sidewalls of the building blocks. The latter leads to enhanced secondary electron emission and enhanced deposition. Indeed extending the fitted linear model from the 60 layers study to the full cones, by multiplying the average layer height obtained from the linear model by the number of layers, the inefficient growth at lower r_{pitch} (< 3 nm) becomes clearly visible (see figure 5.36). The angle model fits best for the 50 nm pt_{pitch}, same as for the 60 layers model in figure 5.35.

The cone with the desired dimensions of r_b = 500 nm and r_t= 100 nm with a height of 2 μm, is achieved for a value of r_{pitch} = 2 nm and a pt_{pitch} = 50 nm, as taken from figure 5.36. This cone takes about 2 minutes to deposit, about half the deposition time of the small-building block cones. This demonstrates the more efficient growth, enhanced by the proximity effects. To ensure that the cone is actually hollow, half a cone was deposited with the same parameters, which is shown in figure 5.37.

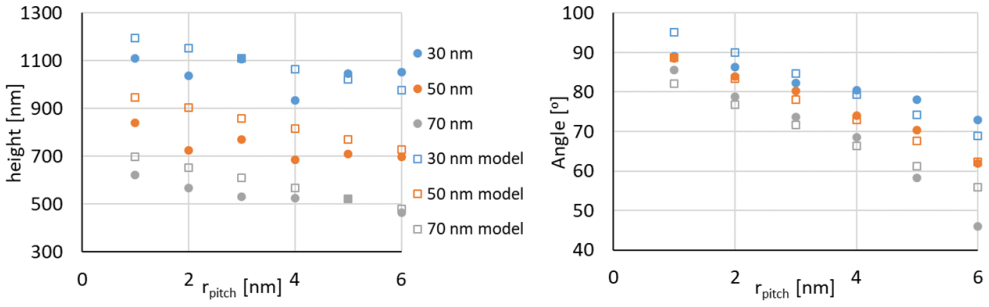

Figure 5.35: Heights (left) and angles (right) of 60 layer cones with r_{pitch} varying from 1 to 6 nm and a 30, 50 and 70 nm pt_{pitch}. The beam energy is 10 keV, the beam current is 80 pA, dwell time =20 ms (single pass), r_b =500 nm. There is a π-shift between the starting point of successive layers. The measured data is plotted as filled circles and the model data is plotted as empty squares.

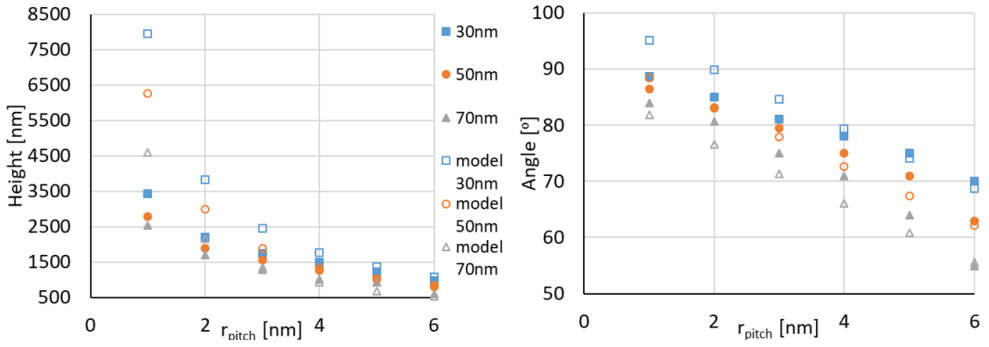

Figure 5.36: Heights (left) and angles (right) of full cones with r_b =500 nm and r_t =100 nm, with r_{pitch} varying from 1 to 6 nm and a 30, 50 and 70 nm pt_{pitch}. The beam energy is 10 keV, the beam current is 80 pA, dwell time =20 ms (single pass), r_b =500 nm. There is a π-shift between the starting point of successive layers. The model of the average height/layer is used to calculate the full cone height and is compared to the measured data. The angles from the model are plotted as well and compared with the measured data.

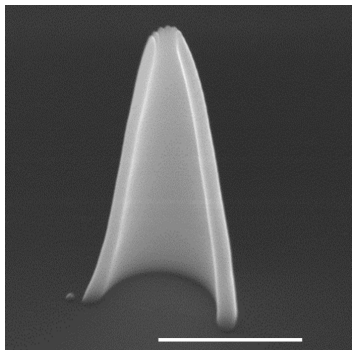

Figure 5.37: Half a cone deposited using 10 kV and 80 pA beam current. The pt_{pitch} = 50 nm, r_{pitch} = 2 nm, dwell time = 20 ms (single pass). The average wall thickness is about 120 nm ± 20 nm. The scale bar is 1 µm.

Shape irregularities

The irregularity problem at the top of the cone was further investigated. It seems that the π shift reduces the problem, but is this the optimum shift? Different shifts (0, π and random) were applied and the top parts of the cones were compared. Figure 5.38 shows the cones grown with different shifts. The π shift achieves the best result at the top. Figure 5.39 shows the top view of cones deposited with and without the π shift. The irregularity is also visible in the top view of the cone without the shift. The different shifts were simulated for smaller cones with less points using the NBD21 FEBID simulator [146]. Nebula is an open source Monte Carlo simulator that describes electron matter interaction and runs on a GPU to enhance the speed [147]. The Nebula dynamic simulator (NBD) was built upon Nebula in 2020 [148] and was further developed in 2021 to NBD21 [146]. The points of the cones where FEBID growth occurs in the simulations are shown in figure 5.40. The simulated cones have 425 points with r_{pitch} of 1.7 nm and a pt_{pitch} of 4 nm, r_t = 4 nm and r_b =30 nm. x and y cross sections of the simulated cones are shown in figure 5.41a,b,c and d,e,f respectively. A simulation of the top and 3D view of the full cones are shown in figure 5.41g,h,i and j,k,l respectively. From figure 5.41d, g and j, the asymmetry in the cone without a shift is clear which agrees with the deposited cone in figure 5.38a. In the case of random shift, the resulting cone is unpredictable, it can turn out successful or with some asymmetry. An example of a cone with random shift was simulated and is shown in figure 5.41. Even though this example seems successful, random shift is not always consistent. The experimentally deposited cone with random shift has shown asymmetry on the top. The cone with pi shift shows an improvement in the top part in the simulation and in the experiment when compared to the cone without shift. More shifts were simulated, namely π/2, π/4 and π/8. Of these simulations the π/4 showed the best performance, but there may be a more optimized choice. In the experiment no shift, random shift and π shift were tested, of which the latter seemed the one with the

best performance. It is important to note that in the simulations an abundant precursor flux was assumed, i.e. the precursor supply and surface diffusion were not taken into account.

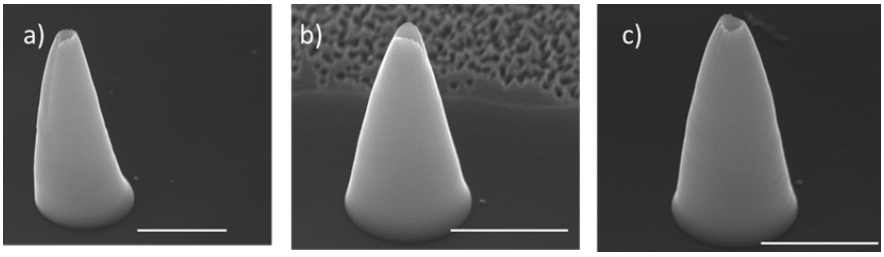

Figure 5.38: cones deposited using 10 kV, 80 pA beam. Dwell time is 20 ms, r_{pitch} =2 nm, pt_{pitch} = 50 nm. r_b = 500 nm and r_t = 100 nm. a) has no shift, b) has a random shift in each layer and c) has a π shift. Scale bars are 1 μm.

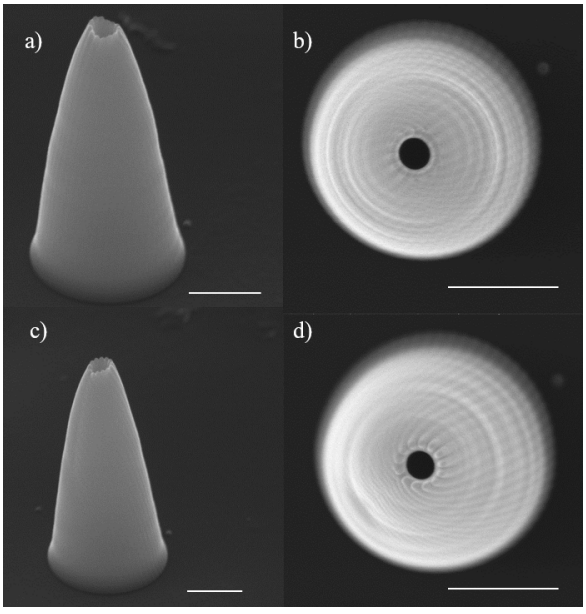

Figure 5.39: a) and c) 50° tilt image and b) and d) top down image of cones deposited using 10 kV and 80 pA beam current. pt_{pitch} is 50 nm, r_b was 500 nm and r_t was 100 nm, dwell time is 20 ms. Each layer is deposited in 100 passes. r_{pitch} was 2 nm. a) and b) are the same cones with the π shift applied. c) and d) are the same cones without any shift. The scale bars are 500 nm.

In the case of the previous approach with smaller building blocks, the pitches are much smaller and the points are overlapping, thus the π shift didn't result in a visible improvement.

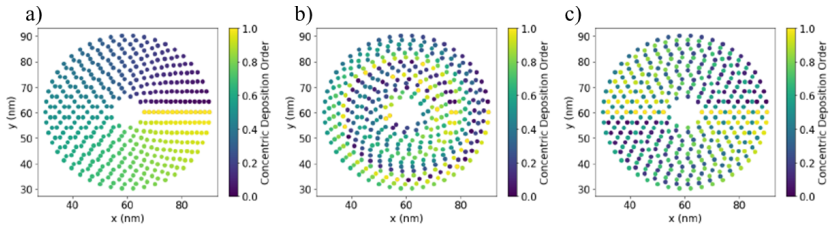

Figure 5.40: Points of cones where deposition occurs with a) the same starting point for every circle, b)a random shift between the starting points of every circle, c)a π shift between the starting point in each circle. Images are from [146]. The simulated cones have 425 points with r_{pitch} of 1.7 nm and a pt_{pitch} of 4 nm, r_t = 4 nm and r_b =30 nm. Normalized color grading for concentric depositions represent the order of deposition for each concentric deposition ring individually [146].

5

Applying the method to other shapes

It will now be demonstrated that the methods presented to fabricate hollow cones can be also used to build other closed wall hollow shapes such as cylinders and boxes. For shapes with vertical sidewalls (parallel to the electron beam) layers are placed exactly on top of each other (r_{pitch} = 0). As an example a box and a cylinder are grown using the same parameters as for the large-building block cones, i.e. 10 kV, 80 pA beam current, a pt_{pitch} of 50 nm and a dwell time of 20 ms. The results are shown in figure 5.42. Interestingly, a similar bulging out is seen at the lower right side of the cylinder as observed in the cones. And the top of the rectangular box is displaced to the left with respect to the bottom by approximately 70 nm. If this would be ascribed to stage drift during the deposition time of 1.2 minutes, the drift would amount to 58 nm/min., which is much larger than the observed stage drift as will be presented in the discussion and appendix sections. It is unclear presently what causes these deformations, and whether they are already present after deposition or are perhaps caused by the imaging. The cylinder shape in figure 5.42a shows a deformation of about 20 nm only during a deposition time of about 3 minutes (6-7 nm/min.), which could be due to stage drift. Both shapes also show an irregular rim at the top, resembling the ones observed in the cones, but not quite the same. It is very likely that this is due to the specific deposition order of the building blocks. For these shapes of constant cross section, the height is directly determined by the number of deposited layers. By growing a different number of layers and measuring the corresponding height, a curve of number of layers versus height can be constructed. From this graph, the number of layers can be determined for any desired height. For the cylinders with the specified parameters, the graph is shown in figure 5.43. The initial growth in figure 5.43 can be determined by the supply from the gas phase and a contribution from the surface. As the height increases further, the contribution from the surface will decrease because the molecules have to travel a longer path all the way up the growing structure. The supply

from the gas phase remains the same, but the total supply decreases with height. This leads to the growth decreasing with height.

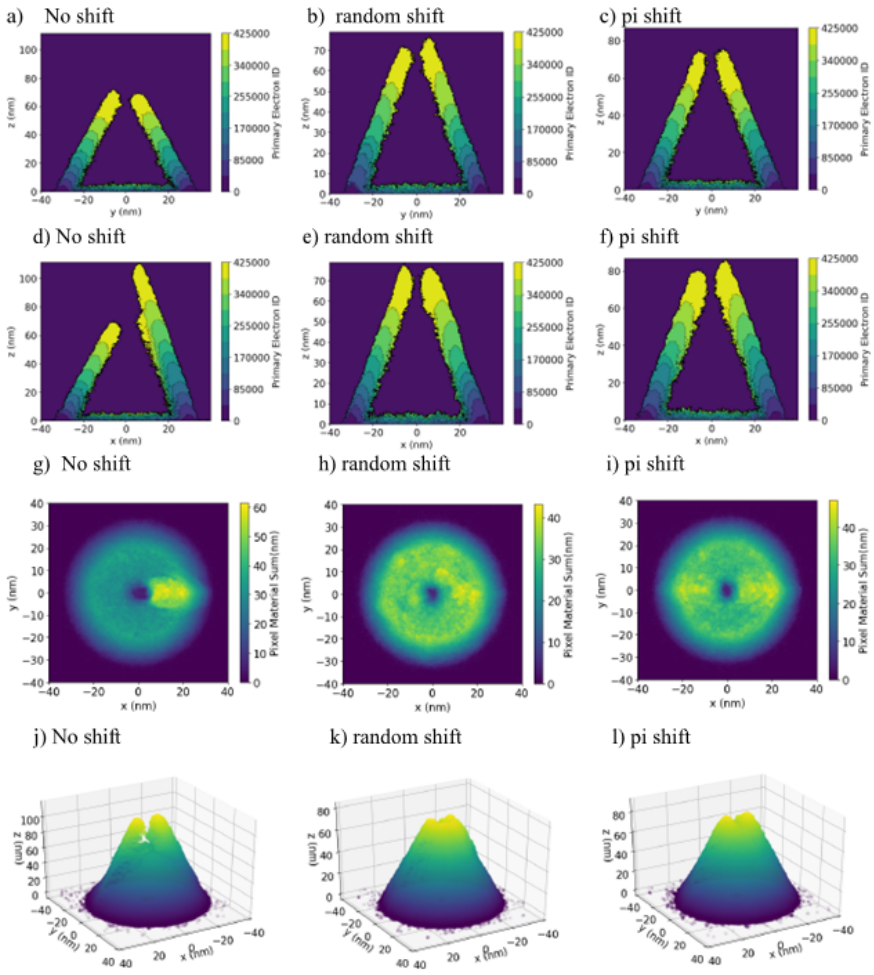

Figure 5.41: a), b) and c) show the cross section contour plots at x=0 of simulations done for deposition strategies shown in figure 5.40. d), e) and f) show the cross section contour plots at y=0. g), h) and i) show material sum maps indicating the amount of material deposited in each voxel column along the z-axis. j), k) and l) show 3D surface point clouds from scans in the +x, +y and +z directions. Coloring represents the height of points. Images are from [146].

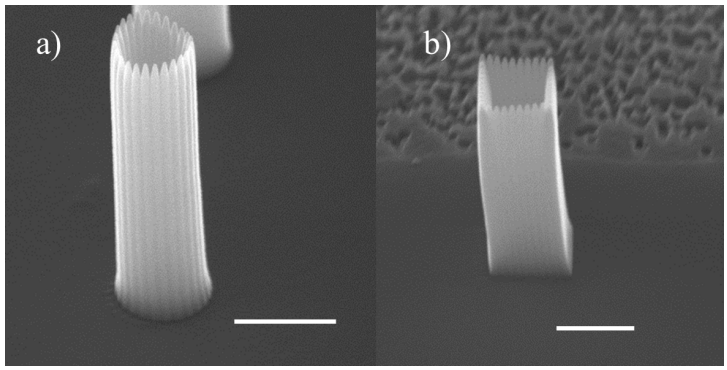

Figure 5.42: Example of a) cylinder and b) box deposited using the large building block approach using 10 kV and 80 pA beam current. pt_{pitch} = 50 nm and dwell time= 20 ms. The scale bars are 500 nm. The radius of the cylinder is 200 nm and it contained 100 layers. The height is 1578 nm. The side length of the square cross section of the box is 500 nm and it contained 100 layers. The height of the box is 1432 nm.

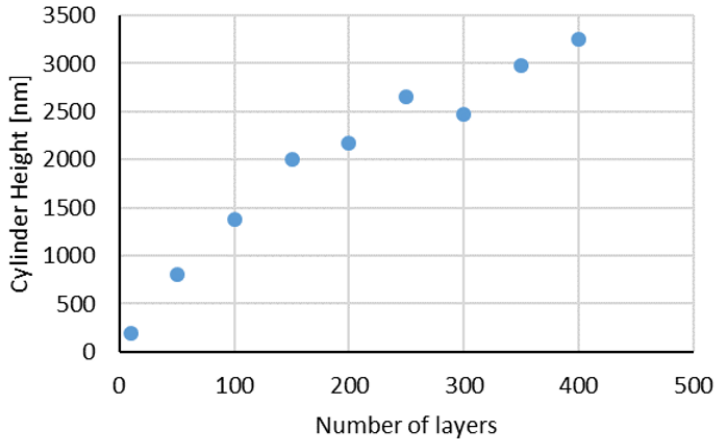

Figure 5.43: Cylinder heights as a function of the number of layers. All cylinders are deposited using beam energy and current of 10 kV and 80 pA, pt_{pitch} = 50 nm, dwell time per pixel = 20 ms.

5.5. Discussion

Two small problems remain in the way to achieve the perfect cone and it is important to address these to aim for better control over 3D FEBID. The first problem is the height irregularity at the top of some of the cones, such as seen in figure 5.20g. It was seen from simulations that the order in which the building blocks are arranged has an influence, but the perfect solution

was not yet found. There may be additional causes for the height irregularity problem. The second problem is that, at the beginning of the growth, many of the cones presented here seem to bend over towards the left (towards the GIS nozzle) as typically seen in figure 5.20h. Interestingly, the very small cones in figure 5.27 did not show this. A few experiments are now presented that were performed as an attempt to find the cause of these problems.

The first experiment was to test whether the precursor flux coming from one side might have an influence on the top irregularity. The precursor flux was varied, by increasing the working distance, i.e. by moving the stage in the z-direction. This increases the distance between the sample and the nozzle. The normal working distance is 4 mm and the nozzle is positioned at about 150 µm above the sample. The resulting cones are shown in figure 5.44. The irregularity at the top is already visible in figure 5.44a and becomes more pronounced in figure 5.44d at a working distance of 4.3 mm. It becomes larger when the distance increases and the locations of maximum height are shifting along the perimeter. When the distance is further increased the cone shape drastically changes because the precursor supply decreases rapidly. It is clear that the distance from substrate to nozzle is a critical parameter and it should stay below 450 µm. However, this experiment did not provide an explanation for the origin of the irregularity at the top. Other experiments were done changing the starting location of the deposition with respect to the nozzle and adding a refresh time to allow replenishment of precursor molecules. But both did not have any visible effect on the cone shape or the top irregularity.

A potential cause for the deformation of the cones shortly after the growth begins might be drift. Drift can have a variety of causes: stage drift, sample drift, and thermal drift due to heating effects by the beam. The amount of drift can differ from sample to sample or vary depending on how exactly samples are mounted. To get an idea of the typical size of the drift, after a stage move, it was measured in the Helios G3 dual beam SEM on two different samples. The measurements were performed using the iFast tool from Thermo Fisher Scientific which first moves the stage, then starts a measurement. The algorithm takes an image every few seconds and uses an image processing tool to characterize the movement of features present in the image in the x and y directions. The drift was measured on the same silicon sample where the FEBID experiments were performed. The drift results on the silicon sample are shown in figure 5.45. The drift in the y-direction calculated from the slope of the more linear part of the red curve (starting at 20 minutes) in figure 5.45 is about 3 nm/minute. Drift was also measured on a standard gold sample from Thermo Fisher Scientific and the results are shown in figure 5.46 in the Appendix section. The drift was larger for the gold sample (18-21 nm/minute) than for the Si sample. This measurement was repeated twice without removing the sample and the drift was found to be different in size. From these measurements, it is clear that the drift is not very predictable in size and in direction, and thus it is not possible to compensate for it accurately in the fabrication of a 3D shape. The bulging out near the bottom of the cones always occurred on the side near the starting point of the deposition (the small

dot). As the drift varies direction between measurements it is unlikely that this causes the observed deformation. The size of this deformation, as estimated from the misalignment between the top and bottom ring of the cone in figure 5.20h, is about 60 nm over the 4 minutes of deposition (average of 15 nm/minute) or about 30 nm in each (X and Y) direction for the cone in figure 5.22 over 4 minutes of deposition (average of 7.5 nm/minute). This is of the same order of magnitude as the drift measured on the gold sample, but the position of the deformation does not randomly vary as the drift does. So, it is questionable whether the drift can explain the observations.

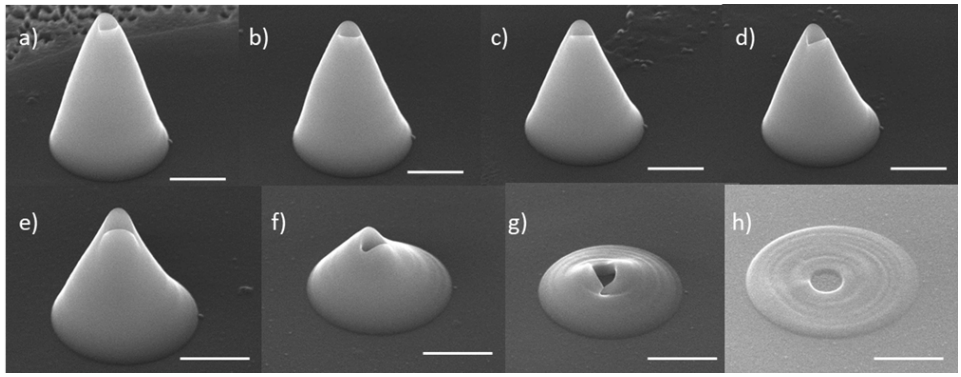

Figure 5.44: Cones deposited using 10 kV, 80 pA beam. The working distance was a) 4 mm (150 µm from the nozzle), b) 4.1 mm (250 µm from the nozzle), c) 4.2 mm (350 µm from the nozzle), d) 4.3 mm (450 µm from the nozzle), e) 4.5 mm (650 µm from the nozzle), f) 5 mm (1150 µm from the nozzle), g) 5.5 mm (1650 µm from the nozzle) and h) 6 mm (2150 µm from the nozzle).

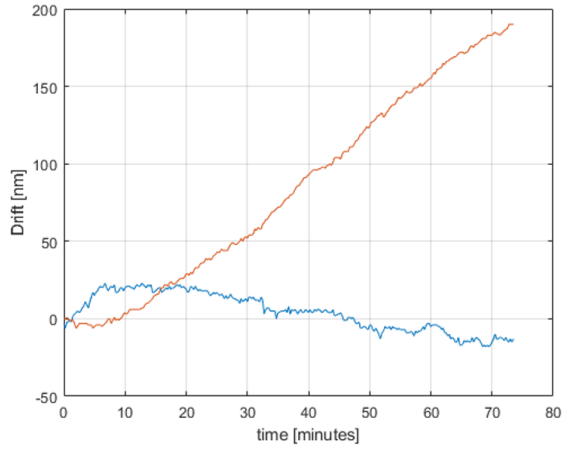

Figure 5.45: Drift in the x-direction (blue) and in the y-direction (red) measured on the silicon sample used to perform FEBID experiments.

5.6. Conclusion

In this study a procedure for building 3D shapes using FEBID was presented focusing on shapes with closed walls and especially hollow cones. The application for this specific shape was briefly explained in this chapter, but will be deeply discussed in the next chapter. Two approaches were presented, one using small building blocks, closely packed to have smooth layers, and the other with large building blocks, separated from each other, utilizing the proximity effects to enhance the growth rate. One of the main goals was to develop a simple procedure without the need to vary parameters continuously during the deposition of one shape. In addition to that, the parameters were chosen to optimize the growth rate without compromising the resolution. This was achieved through the choice of the beam energy and current of 10 kV and 80 pA, as opposed to what is most commonly used in literature (30 kV and 25 pA). The procedure does not include simulation or long calibrations and has also been used to build other shapes than cones, such as cylinders and boxes.

Both approaches start with choosing the parameters to deposit a suitable building block, i.e. the beam energy, beam current and dwell time. The dependence of the building block size on these parameters was studied such that a proper building block size can be chosen depending on whether the design shape requires high resolution or high deposition speed. In the former case small closely spaced building blocks are preferred (small dwell times) and in the latter case large building blocks, well separated from each other (larger dwell times). This guides the choice of the building block spacing, pt_{pitch}, to either create overlapping blocks or not. If the shape has sloped sidewalls, such as the cone, then the radial pitch r_{pitch}, i.e. the spacing between subsequent layers to be deposited, has to be chosen. It has to be less than the radius of the building block such that the layers of the shape can merge together. The r_{pitch} parameter mainly affects the slope of the shape. In order to choose the value of r_{pitch} that leads to the desired angle, a series of shapes needs to be deposited with different r_{pitch} (always less than the radius of the building block). With both approaches, we aim to achieve a simple design with the least possible variations of parameters. The dwell time and both pitches remain constant throughout the growth and only the number of points per layer automatically changes. The study highlights the importance of the writing strategy. There are multiple ways to deposit the same shape. In our approach, the shape is written in layers from bottom to top keeping the dwell time and both pitches constant to simplify the procedure. When choosing small building blocks the successful deposition of cones with smooth sidewalls was demonstrated in which preset dimensions and cone angle were achieved. The smallest cones deposited showed the best shape integrity. The larger ones, however, showed irregularities at the lower right sidewall and at the top rim. When using larger building blocks, cones were fabricated with more corrugated sidewalls, but growing at a larger speed. The same irregularities were observed as for small building block cones. In an attempt to remove the rim irregularity a π shift was applied in the starting position of each successive layer. This was not

entirely successful, although it indicated that the deposition strategy is an important parameter. Further research is required to unravel the cause of these rim irregularities.

In the future more research could also be done to expand our procedure to build other types of shapes. Moreover, it can be investigated how to further optimize the growth rate and to optimize the instrumentation. In regular SEM's there will always be drift, which could be minimized by installing an interferometrically controlled stage. The gas injection coming from one direction seems also a disadvantage. Gas supply, symmetrically arranged around the area of deposition, at a very well defined distance, would probably lead to better shape control. Further development of 3D FEBID opens the doors to build many shapes that are almost impossible to fabricate with other existing techniques. This will serve many fields such as plasmonics, sensors and more. Several simulation guided deposition methods have been recently developed and are still undergoing further improvements. In chapter 7, the simple cone fabrication procedure described in this chapter will be compared to cone fabrication using the two main simulation guided tools.

Appendix 5.1. Drift measurement

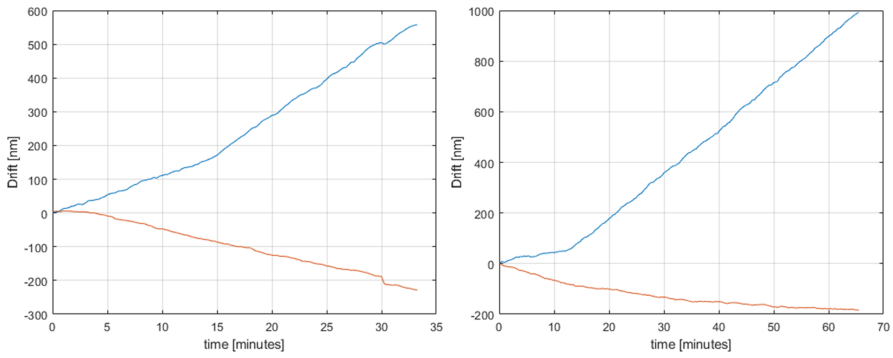

Figure 5.46: Drift measured twice on a standard gold sample from Thermo Fisher Scientific in the x-direction (blue) and in the y-direction (red).

6

Nano Aperture Ion Source (NAIS)

6.1. Introduction

The reason for the choice of studying the cone shape presented in the previous chapter is to apply it in a nano-aperture ion source (NAIS). This is an electron impact gas ionization source [149] in which an electron beam is focused into a small volume of gas, from which the created ions are extracted. In other words, the focused electron beam is used to create an ion source. In this chapter, an overview of the NAIS is presented, however, the focus remains on the fabrication of the cones using FEBID.

A special chip is fabricated to create a confined submicron sized gas chamber. The gas chamber needs to have a small ionization volume to achieve a small virtual source size and thus a high reduced brightness [127, 150]. The chip contains a hole to supply the gas (e.g. Ar, O_2, He, H_2, etc.) in between two thin membranes and a small hole that allows the focused electron beam to enter to ionize the gas [149] as shown in Figure 6.1. The focused electron beam is produced from a high brightness electron source such as a Schottky source [150]. On the other side of the chip there is another hole, 'aperture', for the ion beam to be extracted. To accelerate the beam an extractor is placed 0.5 mm away from the chip on a voltage of 2.5 kV compared to the chip voltage. This results in a 5kV/mm field which is considered the highest possible while minimizing the risk of arcing. The extractor extracts the ions. A high field strength means that the ions have more energy and will thus spend less time in the setup, which reduces aberrations. From the ion beam side, two concentric hollow cones, are built using the 3D FEBID method, as illustrated in the cross section shown in figure 6.1. The inner cone is deposited on the inner membrane, the outer one on the outer membrane looking from the ion side. Between the two cones a localized high gas pressure is created which does not affect the chamber pressure too much, and the gas is guided towards the ionization volume. In addition, the cone shape enhances the electrostatic field, which allows the ions to get extracted without having to apply a voltage between the two membranes. This particular design is expected to reduce ion neutral scattering and Coulomb interactions [150].

6.2. NAIS Chip Fabrication

The NAIS chip is a single chip with double membranes that create the gas chamber as shown in figure 6.1. The two membranes are realized by under-etching a sacrificial layer of 1 μm of SiO_2 in between two Si_3N_4 membranes as shown in figure 6.2. The under-etching is performed with a pattern of a group of 100 nm holes in the top membrane (looking from the ion side) leaving pillars every 20 μm to reduce the deformation or collapse of the membranes as shown in figure 6.3. Then an extra layer of Si_3N_4 membrane is deposited using PECVD for 8 minutes to close the holes. Thin conducting layers of Mo are applied on both sides to avoid electrical charging. A schematic of the cross section of the chip is shown in figure 6.2 and a SEM image of a FIB cross section of the membranes part is shown in figure 6.4.

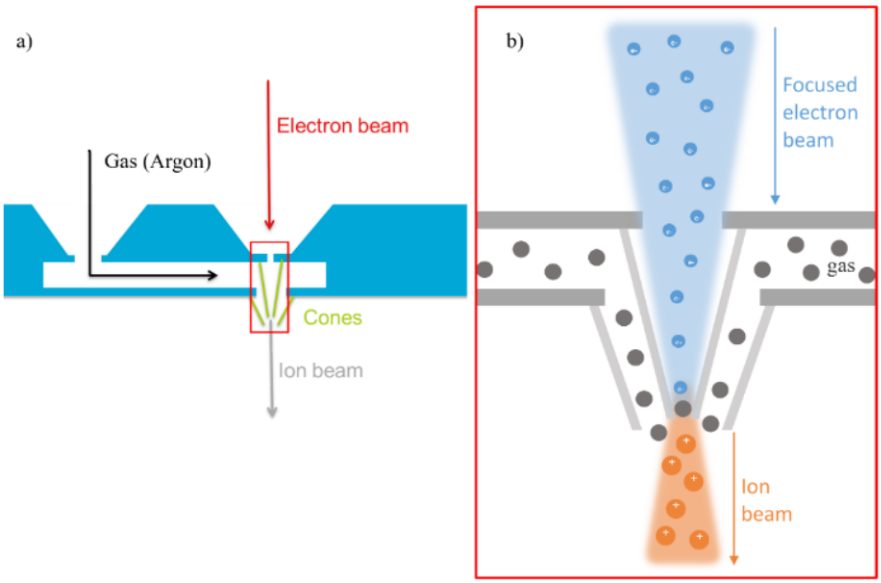

Figure 6.1: a) Illustration of the NAIS chip. Argon gas (as an example) is allowed in to the chip through a hole on one side of the chip. On the same side the electron beam is allowed through a small hole. The gas flows in between two thin membranes. The double cones are built on the two membranes. b) Magnification of the double cones part framed with a red rectangle in a). It shows a cross section of part of the ion source chip. The gas flows between the two cones. The cone shape of the double cone enhances the extraction field and ensures that the ions are extracted without having to apply a voltage between the two membranes.

6.3. Creating the gas inlet

To allow the gas to enter this small gas chamber between the two membranes a gas inlet was milled in the membrane from the electron side using the FIB. The size of the gas inlet is 50 µm x 50 µm square. The ion beam current used for milling was 9 nA. The milling should be stopped when the milling has broken through the first layer, which can be followed using the iSPY and the end point monitor (epm). The iSPY is a tool in the Thermo Fisher SEM that allows one to automatically in a periodic way, check the e-beam image to visualize the status of the milling. The user can specify how often the check is performed. The Si_3N_4 layer will break through at about 0.7 nC/µm^2 as shown in the epm in figure 6.5. The yellow line shows the stage current and the blue line shows the gray scale value. Both the gray scale value and the stage current decrease sharply when a layer is milled all the way through. The contrast changes when the next layer which is made from different material, starts to be measured. The result of the milling is shown in figure 6.6.

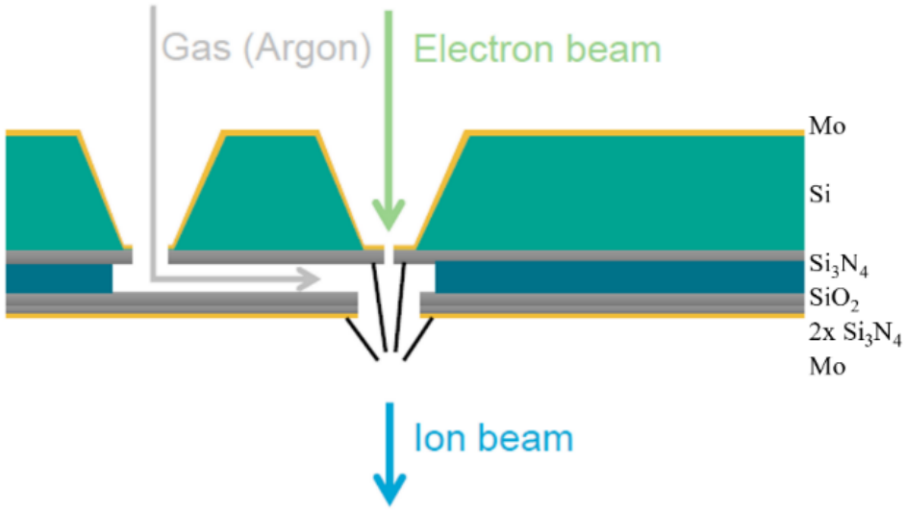

Figure 6.2: a) A cross section of the NAIS chip. The two membranes are realized by under-etching a sacrificial layer of 800 nm of SiO_2 in between two Si_3N_4 membranes. Then an extra layer of Si_3N_4 membrane is deposited using PECVD. Thin conducting layers of Mo are applied on both sides.

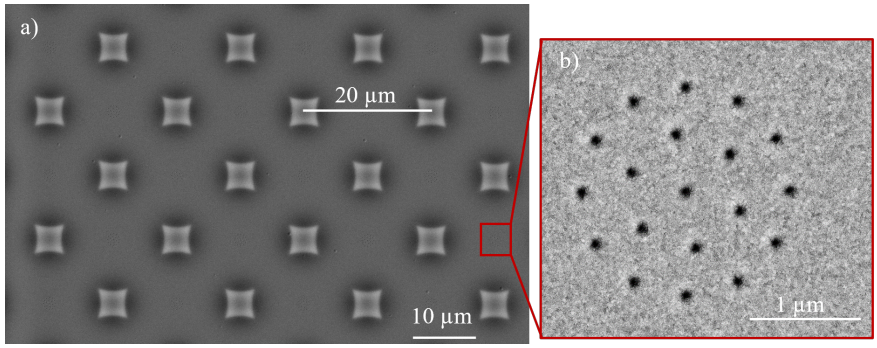

Figure 6.3: a) BSE image of the pillars and holes. b) magnified BSE image of the group of holes between the pillars.

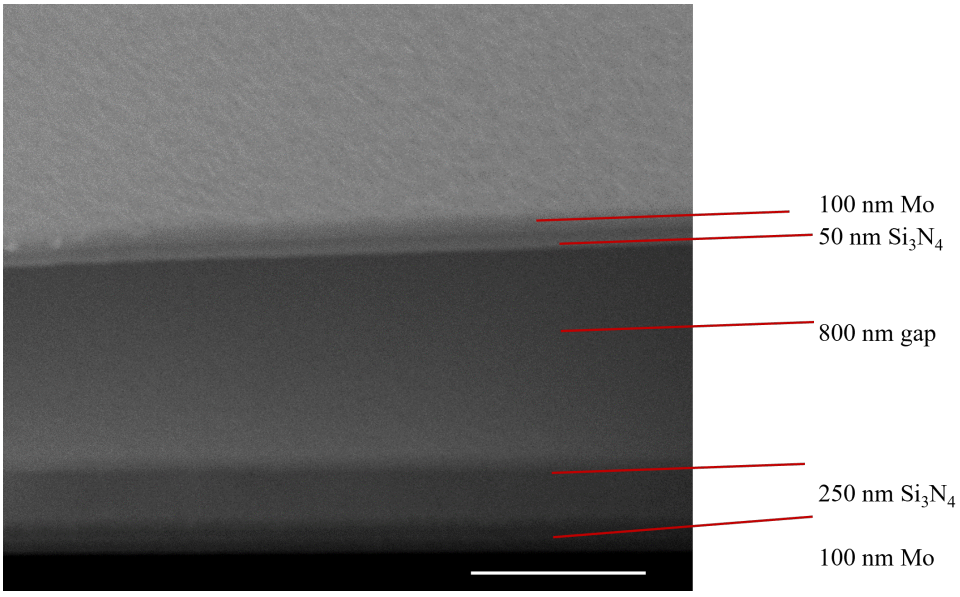

Figure 6.4: FIB cross section of the membranes part of the NAIS chip. The scale bar is 500 nm

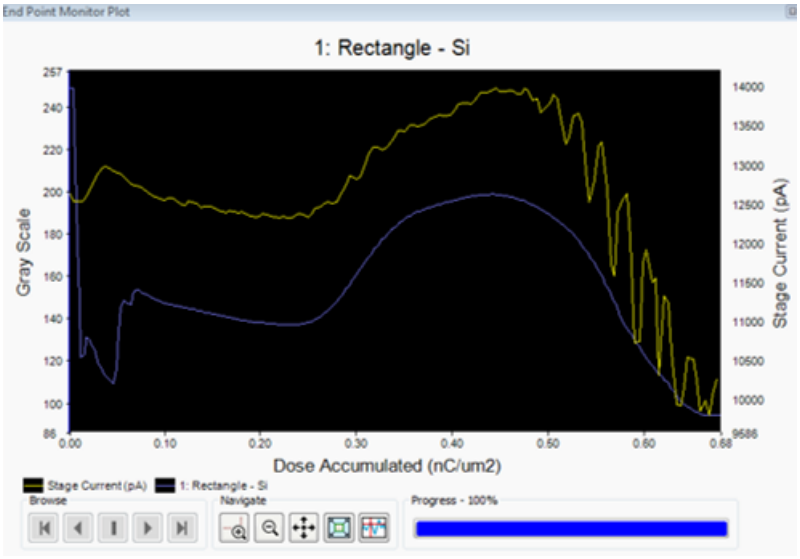

Figure 6.5: End point monitor (epm) showing the breaking of the Si_3N_4 membrane at about 0.7 nC/µm^2. The yellow line shows the stage current and the blue line shows the gray scale value. Both the gray scale value and the stage current decrease sharply when a layer is milled all the way through. The contrast changes because the next layer, made from different material, starts to be measured.

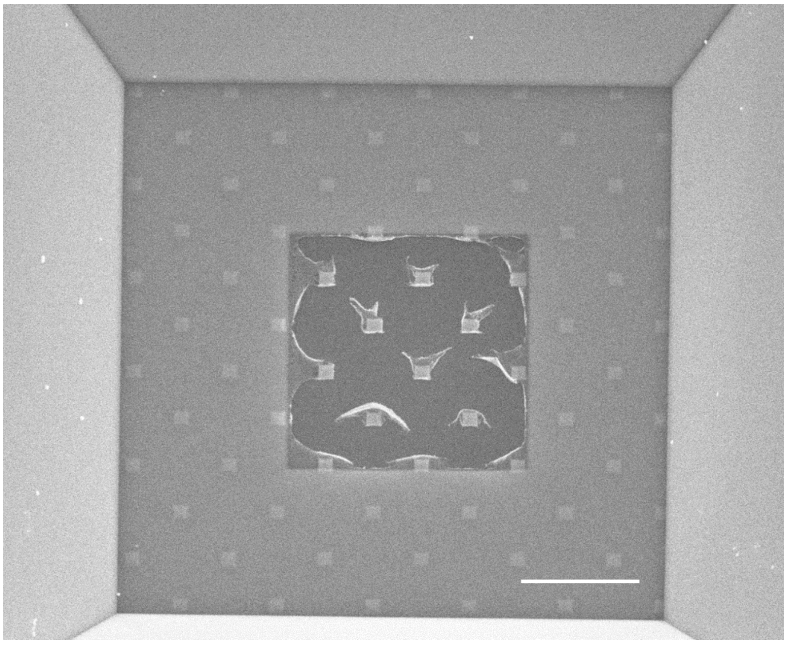

Figure 6.6: SE SEM image of the 50 µm x 50 µm gas entrance hole after milling. The scale bar is 25 µm. The pillars become clearly visible.

To mill away all the small remaining parts shown in figure 6.6, selective milling was used with a 2.5 nA ion beam. This process makes use of the gray level of each pixel to determine if the beam should mill at that point. A histogram is created with all the gray levels in the selected area. By choosing the correct part of the histogram including the gray levels of the areas to be milled, the pattern can be cleaned up. What appears in red in the milling pattern on the Ion image is where the beam will mill the sample. The user can vary the selection of the range of grey levels in the histogram and observe the parts that will appear in red on top of the selected area in the image until the desired areas are selected in red. Another way to automate the milling of the gas inlet was developed using the Nanobuilder tool [151]. Instead of milling a square gas inlet, an array of holes were milled to prevent the milling debris from entering the gas channel and blocking it which is a risk in case of the square shaped gas inlet. The Nanobuilder parameters for the array of holes of 4 µm diameter each, were: 2.5 nA ion beam current, 104 µm horizontal field width (HFW), passes: 1367, Fluence: 773 C/m^2, Time: 1:41, Dwell time, overlap, volume per dose: 1 µs, 50%, 0.22 µm^3/nC. The holes in the array are not all equally spaced, but are rather placed in a diagonal pattern to fit in the spaces between the pillars as shown in figures 6.7 and 6.8. The resulting gas inlet is shown in figure 6.8. The array is composed of circles shown in figure 6.7. The side length of a square of points is 14 µm as shown in figure 6.7.

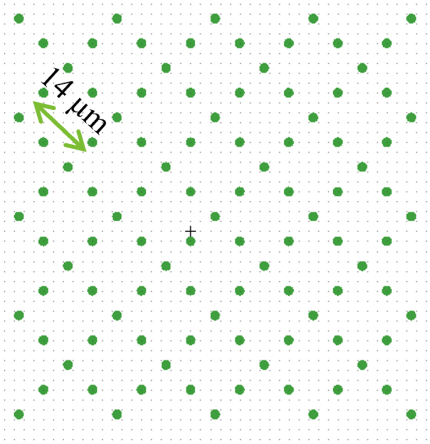

Figure 6.7: The nanobuilder holes array for the gas inlet. The array is composed of circles shown. The side length of a square of points is 14 µm.

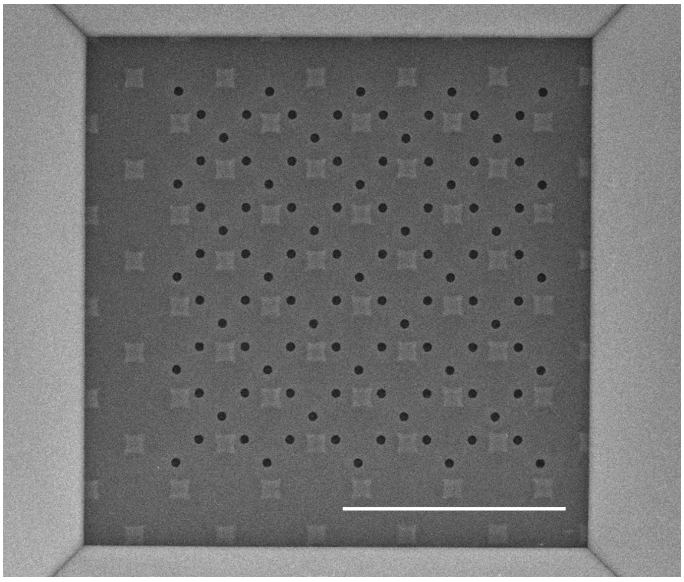

Figure 6.8: Array of 4 µm holes made using FIB milling controlled with NanoBuilder. The scale bar is 50 µm.

6.4. Milling the center holes

An example of the dimensions of the double cone structure to be deposited on the double membranes of the NAIS chip is shown in figure 6.9. Several chips were prepared with different hole diameters and different cone size to find out which will perform better in terms of the ion beam current and the maximum gas pressure the chip can withstand.

The holes were milled using the FIB from the ion side of the chip. Two concentric circular patterns are prepared, with a diameter of 1.8 and 1 µm, respectively. Hole 1, a 1.8 µm diameter disk was milled first, with a scan direction from outside-in, using a 30 kV, 7.7 pA gallium ion beam (10 pA measured) while keeping the smaller disk pattern inactive. The outside-in scan avoids that part of the membrane stays hanging and curls. The iSPI feature and the epm were used to see the progress. The Si_3N_4 layer breaks after about 1.1nC/µm^2. This takes about 6 minutes. Selective milling could be used to "clean up" the remaining, hanging, parts. Then hole 2, a 1 µm diameter disk, is milled afterwards for about 1 minute, keeping the larger disk pattern inactive. The result is shown in figure 6.10.

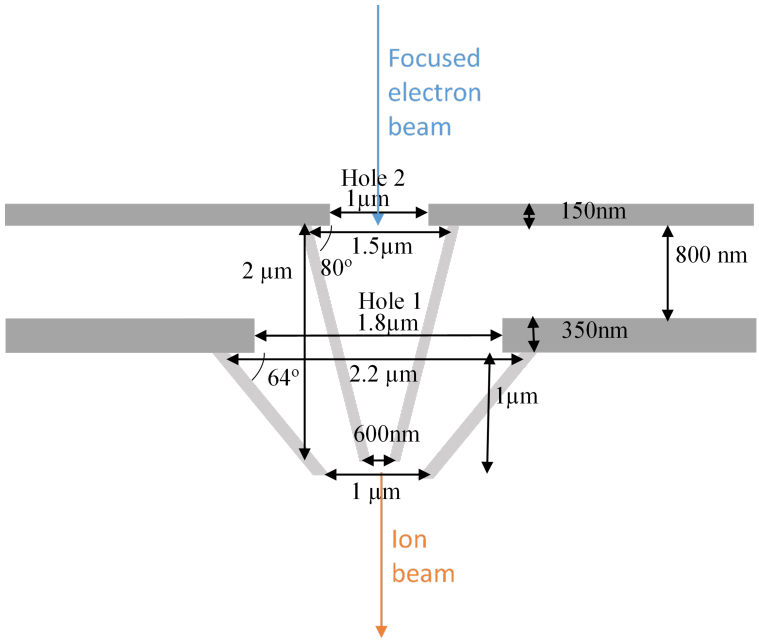

Figure 6.9: Cross section of the membranes with the dimensions of the holes and cones on an example NAIS chip.

In another chip, a larger outer hole was milled with a diameter of 2.4 µm, using the same process. In this case, the Si_3N_4 layer starts to break after about 1.5 nC/µm^2 and is fully broken at 1.8 nC/µm^2. This takes about 16 minutes. Then, the 1 µm diameter circle, was milled afterwards for about 1

minute, breaking at about 0.8 nC/μm^2. When the hole size increased, the milling time became more than 16 minutes. This can be shortened by using a higher ion beam current. The same process was repeated using a 24 pA beam (28 pA measured). In this case, the Si_3N_4 layer starts to break after about 1.3 nC/μm^2 and is fully broken at 1.8 nC/μm^2. This takes about 3 minutes and 17 seconds. Then, the 1 μm diameter circle, is milled afterwards for about 22 seconds, breaking at about 0.8 nC/μm^2 .

In order to automate milling these holes, a Nanobuilder file was created. The file was created by making 2 layers for the 2 circular hole patterns. A 24 pA beam and 10 μm horizontal field width (HFW) were chosen for both patterns. The Nanobuilder parameters for the 2.4 μm hole are as follows: passes: 1847, fluence: 1.06 fC/nm^2 , time: 3 minutes and 19 s, dwell time 1 μs, overlap 50%, volume per dose 0.15 μm^3/nC, milling direction from outside-in. The parameters for the 1 μm hole are: passes: 1156, fluence: 667 C/m^2, time: 22s, dwell time 1 μs, overlap 50%, volume per dose 0.15 μm^3/nC, milling direction from outside-in. The file was then loaded and started. The monitor shows the doses where the layers in the first membrane break, until the whole membrane breaks creating the large hole of 2.4 μm. The milling continues shortly after to get rid of any debris that is still hanging to the edges of the holes. Examples of holes milled on 2 different chips using nanobuilder are shown in figure 6.11 and figure 6.12.

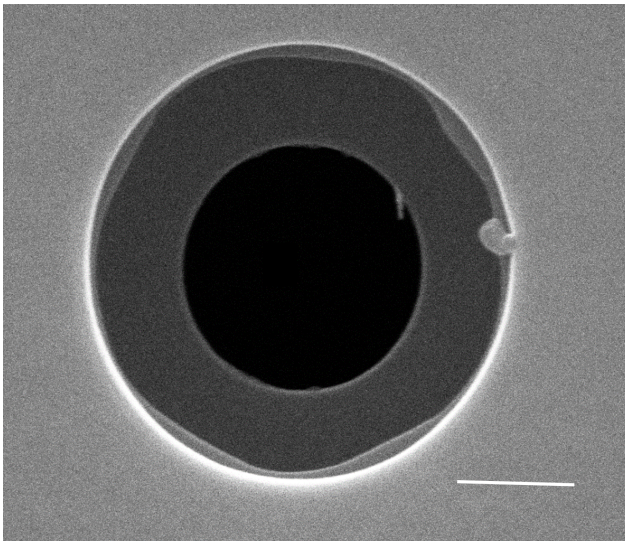

Figure 6.10: Top down SEM image of the two holes as viewed from the ion side. The holes were milled using the FIB. The bigger hole (1.8 μm diameter) was milled first, followed by the smaller one (1 μm diameter). The scale bar is 500 nm.

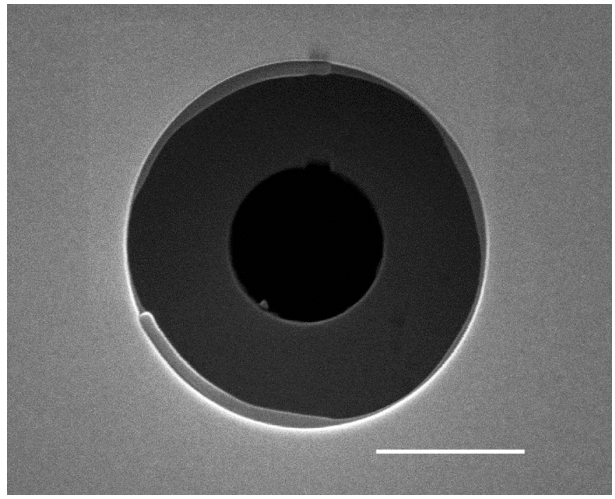

Figure 6.11: Two holes milled with nanobuilder using a 24 pA ion beam. The outer hole is 2.4 µm and the inner hole is 1 µm. The scale bar is 1 µm.

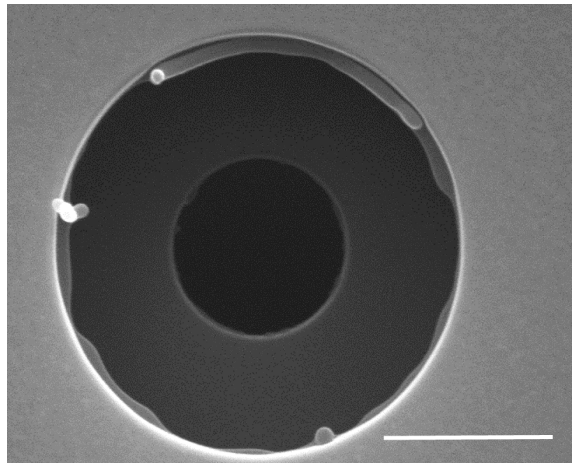

Figure 6.12: Two holes milled with nanobuilder using a 24 pA ion beam. The outer hole is 2.4 µm and the inner hole is 1 µm. The scale bar is 1 µm.

6.5. Double Cones

The requirement for this ion source is to construct two concentric cones on different membranes as shown in the cross section in Figure 6.10. After successfully building single cones as explained in the previous chapter, the next step was to build double cones. As a first step they were built on a single membrane and only after succeeding that, they were built on a double membrane structure. Some of the parameters used to fabricate a single cone were used to build the double cones as well. The same beam energy and current, total dwell time and the π-shift as used for the single cones made with approach 2 were taken. Approach 2 was used to speed up the growth rate and thus decrease the effect of drift. The r_{pitch} and pt_{pitch} were, for most of the double cones, the same as for the single cones or were slightly modified to achieve a different slope. The parameters will be specified for each experiment. Double cones of different sizes were deposited. There are various writing strategies that can be employed. The cones can be built sequentially or in a parallel fashion, and each layer of a cone can be written in a single pass or in multiple passes. It is expected that building two cones in parallel decreases the proximity effects and avoids blockage of the precursor supply by a first grown cone. Furthermore, writing each layer in multiple passes is expected to yield a better shape. This concept of 3D interlacing or intermittent exposure has been proven more efficient and successful in literature than continuous exposure [28, 30]. Depositing the points over multiple passes and depositing all points at the same height before moving to the next layer gives more time for the precursor to replenish before coming back to the same point again. This avoids a long continuous dwell time at the same point where precursor depletion may become prominent [30]. In addition to that, during long continuous exposure, drift can result in distortion or bending of structures and by interlacing, the drift effect will be minimized as the shape is more stable when growing in parallel [28]. To confirm these expectations, an experiment was performed to compare the different writing strategies.

Double cones were deposited using a beam energy and current of 10 kV and 80 pA with approach 2 and the π shift (as explained in the previous chapter) to compare the different writing strategies. Since this was a simple experiment to test the writing strategies, both cones were built with the same angle. The parameters for the double cones used are almost the same as the ones used for a single cone presented in the previous chapter. The double cones were built using approach 2 to speed up the growth and avoid long deposition times. The total dwell time per pixel is the same, 20 ms. The same pt_{pitch} of 50 nm is used. Only the r_{pitch} was increased to 3 nm instead of 2 nm (in the single cone) due to the increased proximity effects from having a second cone. The double cones are expected to grow more than a single cone. Thus, the r_{pitch} was slightly increased to decrease the total number of layers to compensate for the increase in the growth rate due to the proximity effects. The r_b and r_t were different than in the previous chapter depending on the potential holes sizes. For the inner cone, r_b = 700 nm and r_t = 200 nm and for the outer cone r_b = 900 nm and r_t = 400 nm. For the first experiments, the goal was to achieve

2 µm height, same as the single cone in the previous chapter. Figure 6.13 shows the difference between using 100 passes (a) and 1 pass (b) and between building the inner and outer cones simultaneously (a,b) and separately (c). Both a) and b) were deposited layer by layer, first a layer of the inner cone followed by a layer of the outer cone before moving to the next layer. Figure 6.13 c) shows the cones deposited separately, the inner cone first and then the outer one. The heights of the cones measured from the center of the inner cone in Figure 6.13 are 2.06, 2.28 and 2.31 µm for a), b) and c) respectively, the outer diameters at the bottom are 1.89, 1.92 and 1.87 µm for a), b) and c) respectively. The inner diameters of the top hole of the inner cones are 337, 286 and 312 nm for a), b) and c) respectively. The cones in figure 6.13 b) suffer from the irregularity on the top which was discussed in the previous chapter. In the previous chapter, the π shift was introduced to reduce this top irregularity. This experiment shows that writing the shape in multiple passes helps in further reducing the top irregularity. The drift and the lower growth in some parts due precursor depletion become more prominent in b) with the single pass exposure. The resulting shape was not successful when writing the inner cone first followed by the outer one (figure 6.13 c). The proximity effects from the deposition of the outer cone increased the thickness of the inner cone. A poor growth on the right part of the outer cone was observed. In the cones deposited in figure 6.13, the precursor nozzle is located on the top left. The inner cone causes a precursor shadowing effect, meaning that less precursor is able to reach the part behind the inner cone. Therefore this shadow effect led to a poor growth on the right part of the outer cone which was shadowed behind the inner cone. This is mostly visible in figure 6.13 c) where the right part grew at a lower rate and collapsed. The shape of the inner cone is not clear, but there is a gap that appeared on the left side. The reason for this is still unclear.

The double cones showed a better result when deposited using multiple passes and by building the inner and outer cones simultaneously together, one layer from the inner cone followed by one from the outer.

To further investigate the shape from the inside, a double cone was deposited using the successful writing strategy from the previous experiment and was milled using the FIB. The double cone was deposited using a beam energy and current of 10 kV and 80 pA, pt_{pitch} of 50 nm, dwell time of 20 ms and r_{pitch} of 3 nm. The two cones are deposited layer by layer in parallel, each layer written in 100 passes. For the inner cone r_b = 600 nm and r_t = 100 nm and for the outer cone r_b = 1000 nm and r_t = 500 nm. Figure 6.14 shows the double cone and a FIB-milled cross section to show the thickness of the walls. The π shift (explained in the previous chapter) has been applied between every layer. The resulting cone height is about 2.23 µm, the inner diameter of the top hole of the inner cone is 143 nm, the inner diameter of the top hole of the outer cone was 900 nm and the outer diameter of the bottom of the outer cone is 2.07 µm. The maximum wall thicknesses, measured at the bottom of the cones are 192 and 332 nm for the inner and outer cones respectively. The proximity effect of the outer cone on the inner cone is clearly visible in

the higher thickness of the inner cone wall compared to the outer one. The thickness of both walls is not uniform throughout the cone. Nonetheless, the cones were successful and the gap between the walls is clear. As concluded from the previous chapter, the growth rate decreases as the structure's height increases. It is important to be careful in the design with the diameters. The radii in the design define the positions were the beam will be positioned, therefore, the resulting inner diameter of any of the holes is expected to be less, depending on the wall thickness. The radius in the design should be chosen larger than the actual required radius to account for the wall thickness.

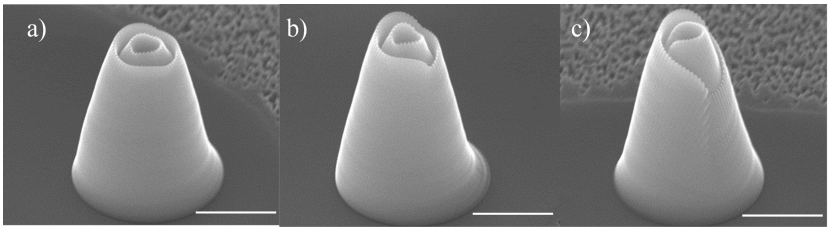

Figure 6.13: 50º tilted images of double cones deposited on the same surface using a beam energy and current of 10 kV and 80 pA with approach 2 and the π shift (explained in the previous chapter), a pt_{pitch} of 50 nm, dwell time of 20 ms and r_{pitch} of 3 nm. For the inner cone r_b = 700 nm and r_t = 200 nm and for the outer cone r_b = 900 nm and r_t = 400 nm. a) The two cones are deposited in parallel layer by layer, 100 passes of one layer from the inner cone followed by 100 passes of one layer from the outer cone, then repeat. b) as in a) but each layer is written in 1 pass. c) The two cones are deposited one after the other. The inner cone is deposited first followed by the outer one and each layer in each cone is written in 100 passes. The scale bars are 1 μm.

The next challenge was to build the cones on two membranes with a spacing in between, as shown in Figure 6.9. The difference in this case, is that the precursor gas has to diffuse not only on the surface of the chip but also in the space between the membranes to reach the lower membrane where the inner cone starts to be deposited. Due to this longer path, it is expected that the growth rate of the inner cone is lower than an identical cone grown on the top surface.

It is important to take into account the broadening of the walls of the cone and make sure that the inner diameter of the bottom of the cone is still wider than the small hole and the top half to be narrower than the bigger hole. To give some room for the broadening of the walls, the radii of the cones were chosen as follows: r_b = 750 nm and r_t =300 nm for the inner cone and r_b = 1100 nm and r_t = 600 nm for the outer cone. The goal for the inner cone is to be about 2 μm with an angle of about 80º. From previous experiments we see that choosing the r_{pitch} = 2 or 3 nm and the pt_{pitch} = 50 nm achieves the 80º angle. Due to the decrease in growth when being built on the lower

membrane, r_{pitch} of 2 nm was the one that led to a successful inner cone, 1 μm higher than the top membrane (from the ion side) . The outer cone needs to be about 1 μm high so that it is at least as high as the inner cone. This means that the angle is about 64°. According to previous experiments, r_{pitch} =5 or 6 nm can achieve this. Using pt_{pitch} of 50 nm, the cones didn't succeed and collapsed due to the larger size of the cone (compared to previously deposited cones) and the presence of the holes which changed the diffusion path of the precursor and thus the growth rate. Therefore, the pt_{pitch} was decreased to 30 nm. To find out the best r_{pitch}, single cones were deposited with r_{pitch} of 5 and 6 nm to find which will result in a height of at least 1 μm. As shown in figure 6.15, the cone with r_{pitch} of 6 nm resulted in a cone height of 894 nm while the one with r_{pitch} of 5 nm resulted in a cone with a height of 1155 nm, so the outer cone was deposited using 5 nm r_{pitch}. For both cones the dwell time was 20 ms divided over 100 passes. The deposition starts from the inner cone until the remaining number of layers is equal to the number of layers of the outer cone. At this point the deposition of both cones continues simultaneously, one layer from the inner cone followed by one from the outer. This ensures the stability of the shape and avoids the collapse shown in figure 6.13 c. The successfully built cones are shown in figure 6.16, for the inner cone r_b = 750 nm and r_t = 300 nm, pt_{pitch} of 50 nm and r_{pitch} of 2 nm and for the outer cone r_b = 1100 nm and r_t = 600 nm, pt_{pitch} of 30 nm and r_{pitch} of 5 nm. The measured inner diameter of the top of the inner and outer cones are 520 and 1150 nm. As explained earlier, it is important to choose the radii in the design larger than the actual required radii due to the wall thickness. Choosing the radius 50 nm larger than required led to a hole size that almost matches the design (as measured in the inner cone).

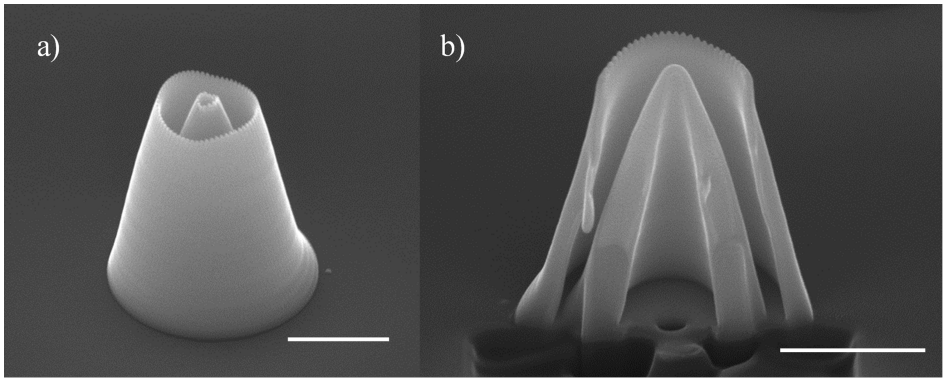

Figure 6.14: 50° tilted images of double cone deposited using a beam energy and current of 10 kV and 80 pA, pt_{pitch} of 50 nm, dwell time of 20 ms and r_{pitch} of 3 nm. The two cones are deposited layer by layer in parallel, each layer written in 100 passes. For the inner cone r_b = 600 nm and r_t = 100 nm and for the outer cone r_b = 1000 nm and r_t = 500 nm. a) the double cone shape. b) FIB cross section through the cones in a). The scale bars are 1 μm.

Then, the double cone shape was tested in the full setup, it was deposited on the test chip, then exposed to a 1 kV and 100 nA electron beam, 3 kV ion extraction and approximately 1 bar of Argon gas for about 3 hours. The outcome ion beam current was about 200 pA. Figure 6.17 shows the shape before and after exposure. The inner cone was more affected and appears to have become slightly shorter. Nonetheless, the shape seems to be quite robust.

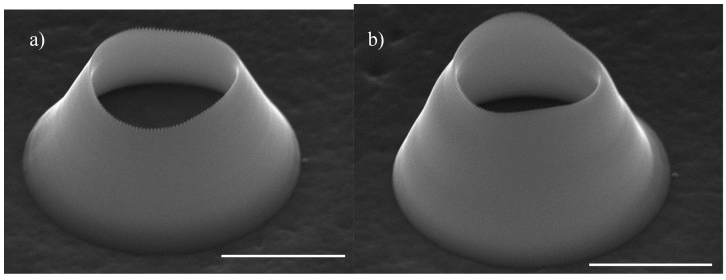

Figure 6.15: 50° tilted images of single cones deposited using 10 kV and 80 pA beam, dwell time of 20 ms over 100 passes. r_b = 1100 nm and r_t = 600 nm, pt_{pitch} of 30 nm and r_{pitch} of a) 6 nm and b) 5 nm. The cones resulting heights are a) 894 nm and b) 1155 nm. Scale bars are 1 µm.

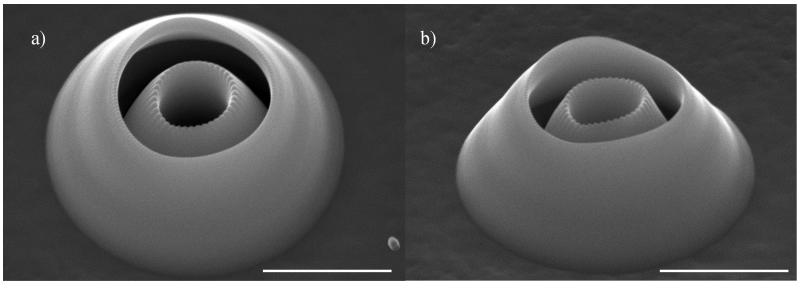

Figure 6.16: Double cones deposited on the double membranes with holes using 10 kV and 80 pA beam, dwell time of 20 ms. a) 30° tilted image and b) 50° tilted image. The two cones are deposited simultaneously, each layer in each cone is written in 100 passes. For the inner cone r_b = 750 nm and r_t = 300 nm, pt_{pitch} of 50 nm and r_{pitch} of 2 nm. For the outer cone r_b = 1100 nm and r_t = 600 nm, pt_{pitch} of 30 nm and r_{pitch} of 5 nm. The scale bars are 1 µm.

Another example of a successful double cone was built for another chip with the bigger hole (2.4 µm diameter) as shown in Figure 6.11. The cones are shown in figure 6.18. The inner cone was not changed, r_b = 750 nm and r_t = 300 nm, pt_{pitch} of 50 nm and r_{pitch} of 2 nm, but the outer cone diameter was increased to surround the now bigger hole. For the outer cone r_b = 1400 nm and r_t = 600 nm. The angle of the outer cone is now smaller (51°) and

thus r_{pitch} needs to be larger than 5 nm which resulted in 65° angle. The successful r_{pitch} was 8 nm. The diameters of the resulting cones were measured: 495 nm and 1.14 µm for the top holes of the inner and outer cones and 2.8 µm for the bottom diameter of the outer cone. The height of the outer cone is 2 µm. This specific double cone showed higher growth rate compared to previous cones deposited with the same parameters. For example, the inner cone has the same parameters as the ones in figure 6.16 and figure 6.17, but the height is about 3 µm. This could possibly be due to some contamination (condensed precursor for example) in the needle that was previously restricting the precursor flow and is now gone. However, this was not investigated further as this was only a first demonstration of a double cone structure to test the resilience to extend electron exposure.

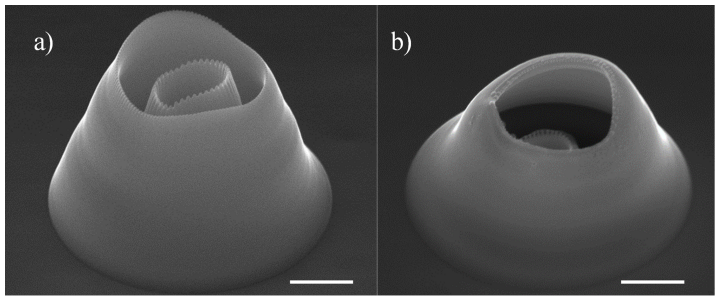

Figure 6.17: Double cone before a) and after b) exposure to a high current for several hours. Stage tilt is a) 50° and b) 45°. The scale bars are 500 nm.

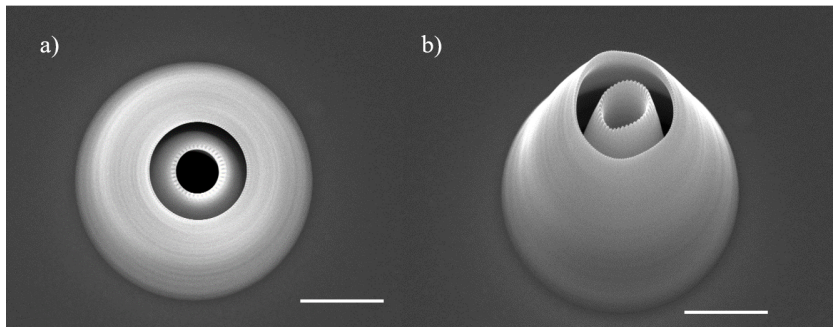

Figure 6.18: a) top down and b) 30° tilted image of the double cones deposited using 10 kV and 80 pA beam, dwell time of 20 ms . The two cones are deposited simultaneously, each circle in each cone is written in 100 passes. For the inner cone r_b = 750 nm and r_t = 300 nm, pt_{pitch} of 50 nm and r_{pitch} of 2 nm. For the outer cone r_b = 1400 nm and r_t = 600 nm, pt_{pitch} of 30 nm and r_{pitch} of 8 nm. The scale bars are 1 µm.

6.6. Conclusion

Double hollow cones were successfully deposited with multiple dimensions for the NAIS application. This demonstrates the ability of using FEBID for building 3D structures that are almost impossible to build using other existing techniques. The NAIS concept was explained and the fabrication process of the NAIS chips was described although that's not the main focus of this work. The main focus of this work is rather the fabrication of the double cones. Holes were milled using the FIB for the gas inlet and the center holes in the two different membranes of the NAIS chips, then the cones were deposited around these center holes. The procedure for milling of the holes was presented and was automated using the Nanobuilder tool. Several challenges were involved in the cone fabrication process. First, having a second cone induces proximity effects on the inner cone which leads to an increase in the growth rate of the inner cone. This was overcome by slightly adapting the r_{pitch} from that of a single cone. The second challenge was to build them around holes on two different membrane levels. The best strategy was to build both cones simultaneously. First the extra part of the inner cone is built alone till the remaining number of layers is equal to the number of layers of the outer cone and then the rest is built simultaneously, one layer from the inner followed by one from the outer cone. This increased the stability of the shape, minimized shadow effects and prevented the low growth on one side and the collapse of the shape. Additionally, each layer was built in multiple passes to avoid having long continuous exposure in one point where drift effect becomes more visible and the pillars start to bend and become unstable. The π shift is always applied as explained in the previous chapter to minimize any top irregularity, although it didn't completely remove it. The double cones were built using approach 2 to speed up the growth and decrease the effect of drift. Some chips were tested in the full setup and the cones were robust after exposure to a 1 kV and 100 nA electron beam, 3 kV ion extraction and approximately 1 bar of Argon gas for about 3 hours. The resulting ion beam current was about 200 pA. Work is still in progress for the NAIS setup. A special microscope setup is being built. In this setup proper brightness measurements can be performed and the quality of the generated ion beam can be assessed with and without the cones and the best cones and holes sizes can be found. FEBID offers a great flexibility to build this double cone shape locally with different sizes in a specified position on top of the holes. Creating this shape is almost impossible using existing lithography techniques. It is very difficult to achieve a thin sloped layer with lithography let alone the double sloped walls of the cones. Developments in FEBID techniques opens the doors to building localized complex 3D shapes in an efficient way all inside an SEM.

7

Comparing FDTM to simulation-guided deposition tools

7.1. Introduction

In chapter 5, two approaches were presented for building 3D shapes, either using small, closely spaced, building blocks or large, well separated, ones. The first approach ensures having very smooth layers while the second utilizes proximity effects to speed up the growth rate. Both approaches were used to successfully build closed wall hollow cones, cylinders and boxes. As mentioned earlier, simulation guided deposition methods were recently developed, attempting to compensate for broadening of structures, proximity and heating effects and surface diffusion of precursor molecules. This is quite a challenge as FEBID has a huge pool of parameters, which does provide flexibility but also makes it hard to account for in models and simulations. For example, just by varying the writing strategy or the order of writing, shape differences may occur. In addition to that, the FEBID process heavily depends on parameters such as the dissociation cross section, the temperature of the precursor reservoir and the substrate temperature. For instance, a different reservoir temperature leads to a different growth rate and the substrate temperature influences the precursor surface coverage. The dependency of FEBID growth on these parameters is often not very well known and also hard to determine, especially for newly synthesized precursors. The three main software solutions available are the layer by layer approach by Skoric et al. [29], CAD 3BID developed by Fowlkes et al. [30] and the pattern generation software developed by Keller and Huth [31]. The differences between the latter two were described in [31] and [32]. The layer by layer approach [29] was developed to fabricate complex 3D structures of arbitrary shape. The other two solutions [30] and [31] are based on a 'diving board' structure as a building block, as shown in figure 7.1, and are therefore more suited for the fabrication of open mesh-like structures[30]. Several calibration measurements are required for these simulation tools.

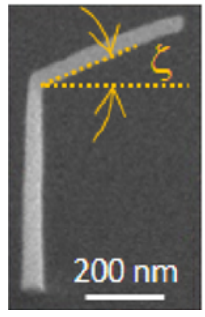

Figure 7.1: Diving board structure used as a building block for 3BID simulation tool. The figure is reprinted (adapted) with permission from [15]. Copyright 2018, American Chemical Society.

In this chapter, a comparison is presented to build a 3D hollow cone using the approach described in chapter 5, which will be referred to from now on as the fixed dwell time method (FDTM), and using both the CAD 3BID and layer by layer approach.

7.2. Design of the cone

The intention is to fabricate a hollow cone, with the same dimensions as in chapter 5, i.e. a height h of 2 µm, a bottom radius r_b of 500 nm, a top radius r_t of 100 nm, and consequently a sidewall angle ϕ of ~ 78.7 degrees. All deposition experiments were performed in the Helios G3 dual beam SEM (Thermo Fisher Scientific) under the same conditions as presented in chapter 5. First, a brief description will be given of the two simulation guided fabrication methods to provide some insight in the required preparatory work.

7.3. Experimental setup for simulation-guided FEBIP

7.3.1. Layer-by-layer approach

As described in [29] an algorithm was developed to create a stream file for the fabrication of a 3D shape from an stl (stereolithography) file format which can be generated from standard CAD software packages. The algorithm is based on the FEBID continuum model [104, 131, 152]. It compensates for proximity effects, beam-induced heating, changes in precursor flux and defocusing [29]. The algorithm divides the shape in layers, or slices, similar to the slicing software of 3D printers. The maximum layer height was set to 6 nm to ensure having thin layers. As the name suggests, the shape is built in layers (circles of points) from bottom to top. Slanted pillars were deposited to determine that the growth rate was independent of r_{pitch} for values of r_{pitch} below 3 nm. Thus, both r_{pitch} and pt_{pitch} were set to 3 nm [29]. The maximum dwell time per point is set to 5 ms and in case the total calculated time per point exceeds this, multiple passes will be applied in that layer. All their calibrations and experiments were performed at 30 kV and with a beam current of 21 pA. A single point deposit is modelled as a Gaussian shape as shown in figure 7.2. The model defines the dynamic height of the deposit as a function of the dwell time t and radial distance r from the center of the beam as:

$$h(t,r) = GR_0 e^{-kR_T} \exp\frac{-r^2}{2\sigma^2} t \tag{7.1}$$

where GR_0 is the growth rate in the center of the beam at a base deposition temperature, R_T is a geometrical factor accounting for the thermal resistance of the deposit, k is a thermal resistance scaling factor, and σ is the standard deviation of the deposit as shown in figure 7.2 which resembles the effective beam width. The values of GR_0 and k are determined from a first calibration experiment in which the length of pillars deposited at various dwell times is determined. A second calibration experiment is done to determine σ. A set of 45 degree tilted pillars were deposited with the same length, but varying the value of σ in the model. The angle of the pillars obtained at different values of σ were measured and plotted versus σ. The value of σ that results in an angle that matched a single pixel thin pillar built with the same conditions was taken to be the real value of σ [29]. The σ value determined from building

pillars takes into account proximity effects from points on the same line along the pillar length. However, the proximity effect from points in neighboring pillars, as present in closed wall structures, is not taken into account. This could be the reason for the thickening observed in the closed shapes that were deposited [29].

Although the software was not publicly available yet at the time of this work, the authors were so kind to provide the stream file for the deposition of a hollow cone. Very recently, the software is made available on github [153].

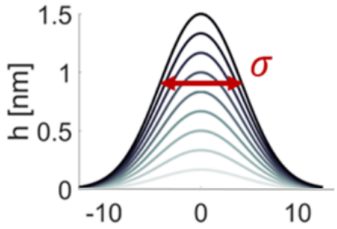

Figure 7.2: Deposit shape modelled as a Gaussian. The figure is from [29].

7.3.2. CAD 3BID

The CAD 3BID tool was developed with a GUI to generate the stream file required to build a 3D shape [30]. The GUI helps the user to design the shape by defining sets of vertices which can be connected via pillars (vertical) or segments (tilted). There is a segment auto-detection option to automatically connect vertices separated by a distance specified by the user. Vertices can be directly placed by the user in the GUI or their coordinates can be imported as a text file. A calibration file needs to be prepared, starting from an existing one. Segments and pillars, such as shown in figure 7.1, are deposited with different dwell times and the resulting angles are measured. The calibration file is a text file with the dwell time of the segment part and the corresponding segment angle. There is a procedure explained in the supporting information of [30] to fit the calibration curve. Besides the diving board structure calibration, another calibration is needed to measure the vertical growth rate VGR, which can be done by depositing vertical pillars without segments. The pitch between points in a segment is kept constant and is specified by the user and the software calculates the dwell time. The software is available for free with the guiding documentation.

In order to build the hollow cone geometry in the GUI, a text file was prepared containing the points of the top and bottom circles of the cone. This means that the pt_{pitch} between the points within a layer is not chosen by the software but rather by the user. Then, the auto segment detection can be used to connect the points of the two circles to form the wall of the cone. This auto segment detection requests the user to choose the length of the connecting segments.

7.4. Results and Discussion

7.4.1. Layer-by-layer approach

The first stream file, as kindly provided by the authors, was prepared for the default conditions of 30 kV and a 21 pA beam current. The shape was successfully deposited as shown in figure 7.3 in a total deposition time of about 30 minutes. The top irregularity discussed in chapter 5 is also present despite using a different deposition strategy. Moreover, the resulting height is lower than in the design. The height of this cone is about 1.5 µm while the designed height was 2 µm. A Focused Ion Beam (FIB) was used to create a cross section of the cone, as shown in figure 7.4. The cross section shows the absence of any separate co-deposition inside the cone. The wall thickness is considerable and decreases from bottom to top. The large thickness could be due to the use of 30 keV electrons for the deposition, with a high penetration depth. When a layer is exposed to the beam, electrons will also travel in to the layers underneath, leading to unwanted additional growth. Please note that the increase in thickness could also partially be caused by re-deposition during the FIB cutting process.

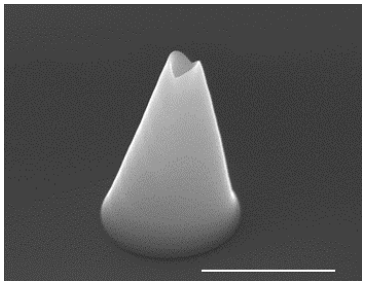

Figure 7.3: Cone deposited using the layer-by-layer approach. Beam energy and current are 30 keV and 21 pA. The radius of the bottom circle is 500 nm and it decreases with the radial pitch until the top radius reaches 100 nm. The deposition took about 30 minutes. The height of the cone is about 1.5 µm. The scale bar is 1 µm.

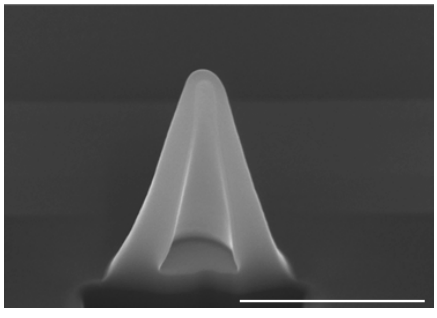

Figure 7.4: Focused Ion Beam (FIB) cross section of the cone shown in figure 7.3.

Another deposition experiment was performed using a 10 kV and 80 pA beam for a fair comparison with the FDTM. This time, several stream files were prepared with different growth rates and pillar widths, based on the estimated growth time under these conditions. The most successful cone, in matching the design dimensions, was the one with a growth rate of 700 nm/s and a pillar width of 7 nm. However, the resulting height was about 2.6 μm. Figure 7.5a shows the deposited cone which took 4 minutes and 17 seconds to deposit. Figure 7.5b shows a FIB cross section through the cone. The top irregularity is also still observed in this cone. The wall thickness is more uniform compared to the one fabricated with the 30 kV beam.

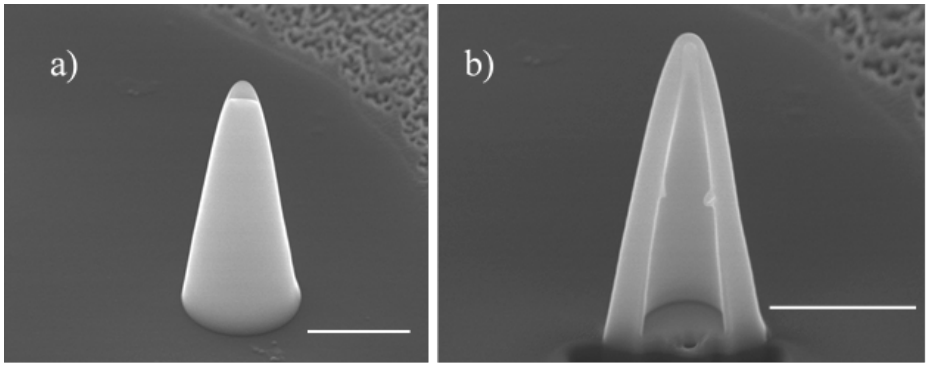

Figure 7.5: a) Cone deposited using the layer-by-layer approach. Beam energy and current are 10 keV and 80 pA. The bottom circle radius is 500 nm and it decreases with the radial pitch until the top radius reaches 100 nm. The deposition took about 4 minutes. The height of the cone is about 2.6 μm. b) Focused Ion Beam (FIB) cross section of the cone. The scale bars are 1 μm.

7.4.2. CAD 3BID

Calibrations

The first step is to find the VGR by depositing a few pillars and measuring the average height increase per unit time. For a 10 kV, 80 pA beam, it was calculated to be 464 nm/s. The VGR was inserted in the software GUI as shown in figure 7.6a. The beam energy and current were chosen as in chapter 5. Then, the stream files for the diving board calibration structures, shown in figure 7.7, were prepared using an existing calibration file. The stream files were used to deposit these diving board structures and the angle of the segment was measured for each structure from tilted images. The new calibration file is a text file with two columns, one with the dwell time of the segment part and the other with the segment angle. The calibration data was fitted using the instructions in the documentation. Only the simple instructions were used to fit the calibration data. The result is shown in figure 7.6b.

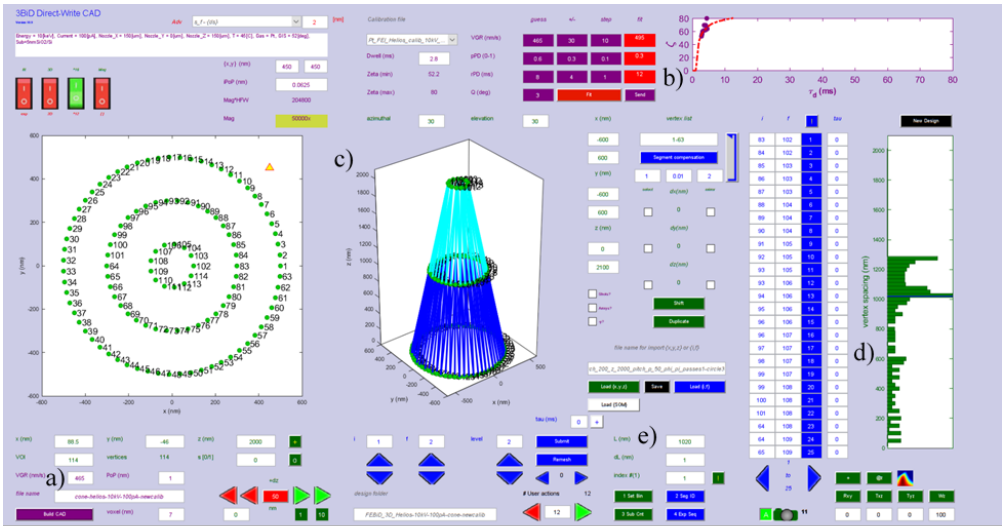

Figure 7.6: GUI of the CAD 3BID software. The VGR is inserted in a). The new calibrations are fitted and plotted in b). The vertices are imported in the software and auto segment detection was used to connect the vertices as shown in c). The lengths of possible segments are shown in the histogram in d). The required segment length for each level has been manually calculated and inserted in e).

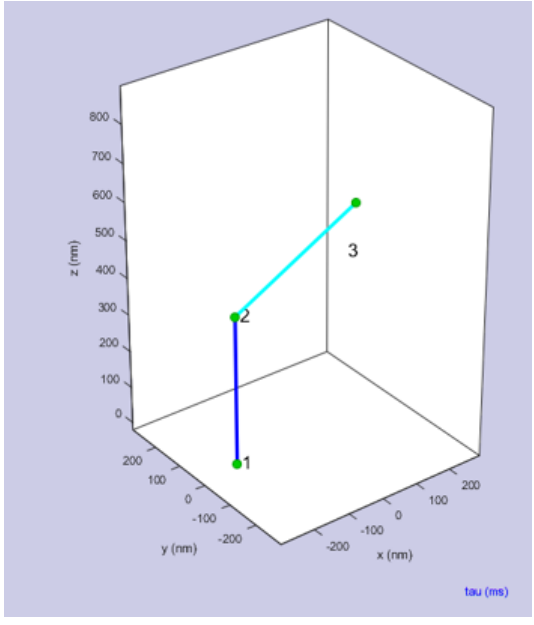

Figure 7.7: Diving board structure used for the calibration.

Geometry

After all the calibrations were done, the geometry of the shape was drawn. The program is designed mainly for structures that consist of a few vertices connected with segments: "3BID is designed to work best for mesh object deposition where a complete geometric description is provided by a list of vertices and interconnecting elements" [30]. However, the design of the hollow cone is different. It doesn't really have vertices, but in order to use CAD-3BID some vertices had to be defined. Thus, a text file with the coordinates of the bottom and top circles was created and imported in the software. To define the coordinates, a pitch between the points within the circle had to be chosen. Based on prior knowledge and experiments (explained in chapter 5) a pt_{pitch} of 50 nm was chosen. The pitch between the points in the segments was kept as default of 1 nm as shown in figure 7.6a labelled as PoP (point pitches). The user has to pay attention to some critical parameters such as the maximum number of vertices or segments per layer which needs to be changed in the code. Then, the auto segment detection was used to connect the vertices of the top and bottom circles to create the cone wall. The designed cone height is 2 μm. However, when only two circles with vertices were defined at a distance of 2 μm, no segments with that length were found. This could be caused by one of the critical parameters related to the maximum segment length, but after consultation with the authors, it was not clear how to fix this. Therefore, coordinates of a third circle in the middle of the cone were added such that the segment length becomes about 1 μm. This creates three layers and segments can be connected between the layers. The segments connecting different layers are colored differently in figure 7.6c. The possible segment lengths are shown in the histogram in figure 7.6d. The correct lengths of the segments required to create the cone wall were manually calculated for each level and inserted in the software as shown in figure 7.6e.

The segments connecting the layers of circles mean that at any cross section the number of points visited by the e-beam is the same. The dwell time is varied between the points to compensate for the proximity effects. This is a main difference between the FDTM and CAD 3BID. In FDTM, the number of points in each layer is adapted to keep the same ptpitch and dwell time while in CAD 3BID, the pt_{pitch} and dwell time are adapted to keep the number of points per layer the same. The pitch that is kept constant in CAD 3BID is the pitch between points within one segment (PoP).

Deposition

The stream file of the cone was generated and used for deposition. The result is shown in figure 7.8 and a FIB cross section of the cone is shown in figure 7.9. The cone height is about 1.8 μm and it took about 2 minutes to deposit. However, the top is very uneven. The main problem here is that the important information which is expected to be chosen by the software such as the pt_{pitch} was input to the software together with all the calibrations. This raises the question of whether the software will recalculate the dwell times and provide us with the correct shape if the pt_{pitch} was chosen different. The same proced-

ure was repeated but with a pt_{pitch} of 30 nm instead of 50 nm. The resulting cone is shown in figure 7.10 a. The deposition took about 5.5 minutes. The cone height is 3.2 µm. This means that the software did not compensate for the change in pt_{pitch} and did not change the dwell times and the growth has increased due to the increase in number of vertices and segments. Thus, for this kind of shape, the pitch has to be known before using the software. The authors of the CAD 3BID confirmed this and mentioned that the calibration structure doesn't have to be always the diving board shape. They explained that the calibration should include the most repeated element of the structure. In this case it could have been better to have several segments, without pillars, beside each other with the pitch defined by the user. If a specific angle is desired, it is advised to do the calibration just with segments without pillars with a small range of angles around this desired angle.

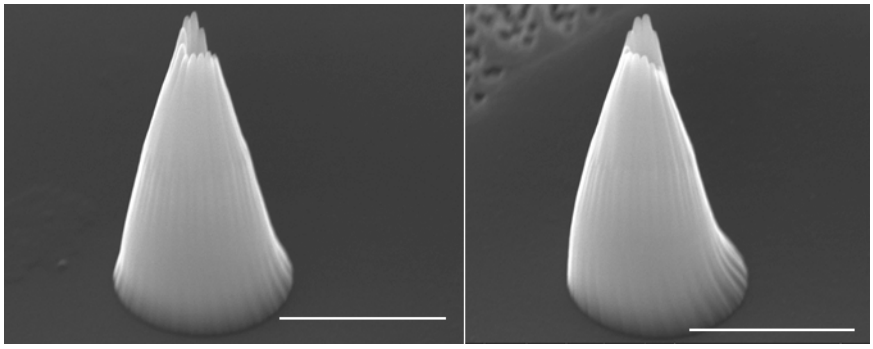

Figure 7.8: Cone deposited using the stream file generated with CAD 3BID. Beam energy and current used are 10 keV and 100 pA. The pitch between the points in the 3 circles inserted in the geometry file is 50 nm. The height of the cone is about 1.8 µm. The deposition time was about 2 minutes. Scale bars are 1 µm.

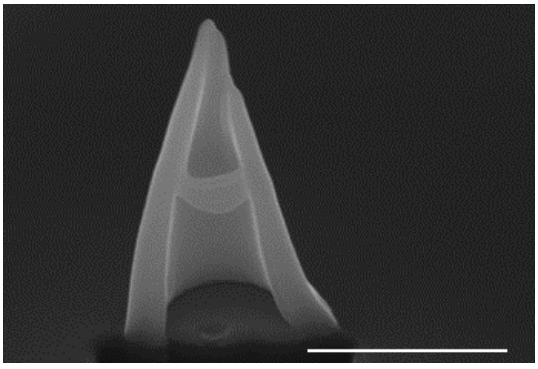

Figure 7.9: FIB cross section of the cone shown in figure 7.8. Scale bar is 1 µm.

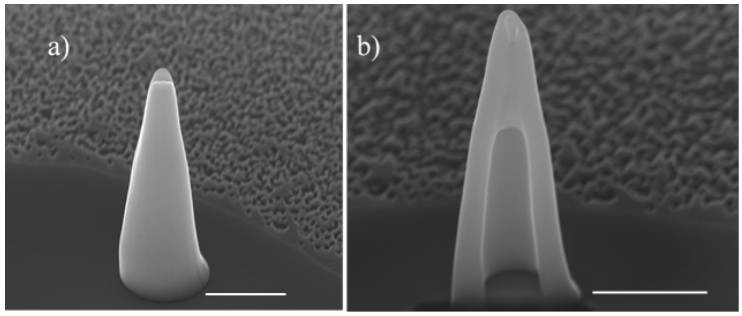

Figure 7.10: a) Cone deposited using the stream file generated with CAD 3BID. Beam energy and current used are 10 keV and 100 pA. The pitch between the points in the 3 circles inserted in the geometry file is 30 nm. The deposition time was about 5.5 minutes. b) FIB cross section of the cone deposited in a). Scale bars are 1 μm. Cone height is 3.2 μm. Scale bars are 1 μm.

7.4.3. Discussion

All methods were successful in depositing a closed wall cone, as shown in figure 7.11. The shape of the cones deposited using both FDTM and layer by layer approach are similar. The layer-by-layer approach resulted in successful cones, with dimensions close to the design and no visible problems in the shape, without having to provide values for the pitch or dwell time. The cones deposited using CAD 3BID had either a very irregular top c) or wrong dimensions d). Table 7.1 shows a comparison of the dimensions of the cones produced using the different methods. According to the table, the method that produced the cone with almost all dimensions closest to the design was the FDTM. All measurements done on the cones fabricated with the FDTM are averages over 9 cones deposited using approach 1 with r_{pitch} = 0.3 nm, pt_{pitch} = 1 nm, dwell time = 100 μs divided over 2 passes. The top looks uneven in all cones with the highest irregularity in the cone built using CAD 3BID and least irregularity using the FDTM. This could possibly be due to the difference in writing strategy with CAD 3BID fixing the number of points per layer and the points in each layer are deposited directly above the ones in the previous layer. In the FDTM case, the number of points per layer changes and π-shift is applied, so the points in one layer are not exactly on top of the ones in the previous layer. In the layer by layer approach, the points of one layer are also not directly on top of the previous layer. The positions of the points are based on the sliced layers from the stl file. An adaptive mechanism was used in choosing the slice thickness according to the local angle [29]. This means that the slice thickness for structures with smaller angles are chosen with a finer step [29]. The positions of the points in the first layers for the three methods are shown in figure 7.12. The points shown from the FDTM are using approach 2 to be able to clearly visualize the effect of the π-shift and the change in the number of points per layer. Only in CAD 3BID (figure 7.12a,

the points of a layer are built directly on top of the previous layer forming the segments as shown in figure 7.6. The shape of the segments is visible in figure 7.11c as well. On the other hand figure 7.12b and c show the variation in the orientation of a layer with respect to the neighboring layers in both the layer by layer approach and the FDTM.

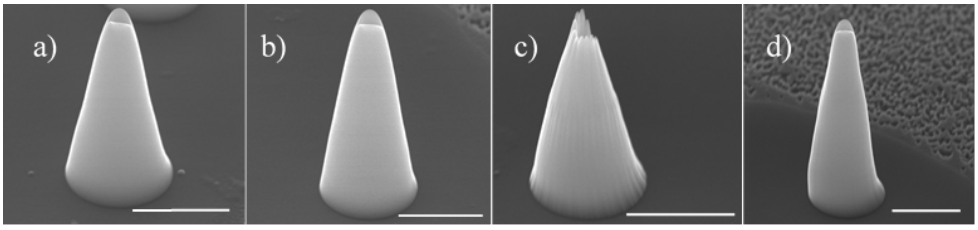

Figure 7.11: Comparison between cones deposited using a) FDTM, b) the layer-by-layer approach and the c) CAD-3BID with a pitch of 50 nm between points in the 3 circles input to the software and d) CAD-3BID with a pitch of 30 nm between points in the 3 circles input to the software. All cones are deposited using 10 kV and 80 pA beam current. The scale bars are 1 µm.

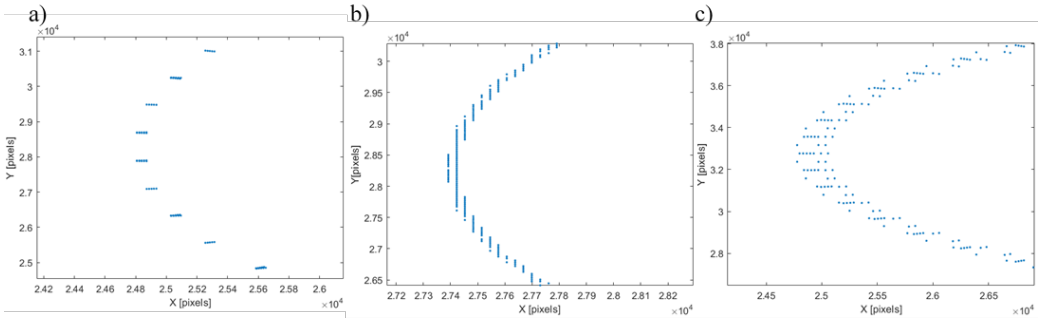

Figure 7.12: a) Points of the first layers in cones built using: CAD 3BID, b) layer by layer approach, c) FDTM (approach 2).

A huge amount of work was put in the development of these simulation tools. They required a thorough understanding of the FEBID process. Proximity effects, beam induced heating, defocusing and gas flux were taken into account. Judging from the closed wall cones fabricated using these methods one cannot clearly conclude that it is worth the effort to develop simulation guided FEBID tools for such structures. Especially CAD 3BID [30] and the pattern generator [31] are more tailored for mesh like structures consisting of pillars and segments. The layer by layer approach was more successful in the deposition of cones, providing a more general platform for the deposition of arbitrary shapes. However, it was not straightforward to achieve deposits

of dimensions equal to the designed dimensions. The deposits usually turned out to be broader and thicker than expected. All the published models have presented their experiments and tests being done at 30 kV and 21 pA aiming to achieve best resolution and least co-deposition [15]. However, this choice is not the most ideal for all types of shapes. The beam induced heating and dissipation depends on the cross section of the shape so if bending happens in the diving board calibration structure this doesn't mean that it will happen in the actual full shape to be deposited. Using 30 kV and 21 pA beam current leads to a very slow growth rate, wastes the precursor and increases the thickness of the previously deposited layers. As explained in chapter 5, these settings may be the best when very thin, small, high resolution structures are required. However, for higher growth rates it is a better to use a lower beam energy and higher beam current.

	Design	FDTM	Layer-by-Layer	Layer-by-Layer	Layer-by-Layer	Layer-by-Layer	CAD 3BID (pt_{pitch} = 50)	CAD 3BID (pt_{pitch} = 30)
height (nm)	2000	2015.7	1500	2742	3160	3854	1800	3150
angle (º)	78.7	80.5	81.8	82.45	84.1	86.5	82.5	85.7
top radius (nm)	100	101.9	112.7	139.2	139.2	134.4	99.6	120.3
bottom radius (nm)	500	553.9	531.7	585.7	585.4	590.6	547.8	570.2
deposition time (min)		03:45	30	04:17	6	08:31	2	05:30
Beam Energy (kV)		10	30	10	10	10	10	10
Beam Current (pA)		100	21	100	100	100	100	100
Growth rate (nm/s)			200	700	500	500		
σ (nm)				7	7	5		

Table 7.1: comparison of the design and measured parameters of the cones deposited using FDTM, layer by layer approach and CAD 3BID.

7.5. Conclusion

The cone shape was deposited using the FDTM, CAD 3BID and layer by layer approaches. The required calibration files were prepared for the CAD 3BID to

determine the VGR and the relation between the dwell time and the segment angle. The CAD 3BID tool is available for free as a Matlab script with GUI. The layer by layer approach tool is not yet available, however, the authors helped us in preparing the required stream files. FDTM resulted in the cones that best matched the design dimensions. For both other methods, some input had to be provided to create the stream file which was based on our previous knowledge from chapter 5. In the CAD 3BID, the pt_{pitch} was provided and when changed the code didn't adjust the dwell time or other parameters to achieve the required design. In the layer by layer approach, the total deposition time was provided to have an estimate of the VGR and σ, and several stream files were tried until cones with dimensions close to the design were achieved. The resulting shape deposited using the layer by layer approach was successful and close to the dimensions of the design. The cone produced by CAD 3BID had a very irregular top. As mentioned earlier, the CAD 3BID is optimized for mesh-like shapes that are based on the diving board structure and thus the calibrations become difficult in case of a closed wall shape and several extra inputs become required (such as the pt_{pitch} in the cone case). The development of tools for 3D FEBID is very promising. Our FDTM presents a simple method, mainly for closed wall shapes, with the least variation in parameters without the need for simulations or calibrations. To further develop the FDTM, other shapes need to be tested. The other tools seem to be promising as well, although not necessarily for simple closed wall shapes, especially when further optimized eliminating the need for prior knowledge of parameters. These tools require testing over different shapes and a range of parameters to find their problems and limitations. Furthermore, as explained earlier, the testing done by the authors of these tools was limited to 30 kV, 21 pA beam. This needs to be extended to a range of beam settings, as explained in chapter 5. When optimizing the growth or decreasing the wall thickness, lower beam energy and higher beam currents are required. These developments will pave the road for using FEBID for building 3D shapes for many applications such as sensors, plasmonic devices, electronics, etc.

8

Conclusion

In this thesis, three main challenges to the FEBID process have been addressed; deposit purity, deposition speed and 3D shape control. Two novel Pt precursors and 7 novel Au precursors have been synthesized by our partners and were tested in this work searching for the highest deposit purity. The possibility of purifying the deposits using water vapor was investigated. And the speed of the process was studied at increased precursor fluxes. The power of the FEBID process lies in the flexibility of building shapes without the need for "carving" the shape but rather to directly write it. This makes FEBID very attractive for fabricating complex 3D shapes, which was one of main focuses of this work. A method (referred to as FDTM, fixed dwell time method) was developed for fabricating 3D shapes using FEBID focusing on simplicity and efficiency. The method was successfully used to build hollow single and double cones which were used in a novel electron impact ion source. FDTM was compared with recently developed simulation guided fabrication methods by fabricating the same shape using the different methods.

In chapter 2, the synthesis and testing of the 2 novel precursors $PtCl_2(CO)_2$ and $PtBr_2(CO)_2$ were described. The synthesis was done by our partners at the university of Florida. From this study we conclude that both precursors can be used for FEBID in SEM. $PtCl_2(CO)_2$ provides an improvement in the metal content of the deposit of about 7 at% higher than the widely used $MeCpPtMe_3$ precursor provided that plasma cleaning has been performed prior to deposition. However, this is still far from what is desired, ideally a deposit as pure as possible is the goal. The comparison between the deposition in HV and UHV showed surprising results. Next to the metal content, in HV SEM deposits a large amount of carbon is present, while in UHV deposits mainly halogen is found, originating form the parent precursor molecule (either Cl or Br), and no carbon. The reasons for this are still unclear and further research is required to reveal possible explanations. Contrary to the expectations, deposits from $PtBr_2(CO)_2$ performed worse in terms of composition and growth rate than deposits from $PtCl_2(CO)_2$ and $MeCpPtMe_3$. It might be that a higher precursor temperature is required to perform better, however these experiments were done at 80°C which is already close to the limits of the GIS and

further increasing the temperature led to higher chamber pressure than the allowed high vacuum limits. We concluded that $PtCl_2(CO)_2$ can potentially be used in FEBID as it provides some improvement compared to the commercially available $MeCpPtMe_3$. Still, there is a need for exploring and designing more FEBID precursors that provide a higher metal content in the deposit, are volatile at temperatures that can be realized inside an SEM (preferably in a GIS), provide sufficient growth, are stable and easy to handle.

In chapter 3, more novel precursors were synthesized at the university of Oslo and tested, but for Au deposition. Seven Au(I) NHC low volatility precursors ((Y,R)AuX) were synthesized and tested. The low volatility might seem undesirable, however it provides the great advantages of stability, ease of handling and safety. A special reservoir-on-substrate setup was implemented to heat the precursor and substrate together. Testing the precursors showed that the most suitable organic ligand for the gold precursor is triazole-based ((N,Et)AuCl), resulting in 15 at% gold in the deposit. Out of X=Cl, Br, I and CF_3, the best purity was reached with Cl and CF_3, but CF_3 led to the highest growth rate of 0.01 nm^3/electron. This is similar to the results achieved for the Pt precursors, where the purity achieved using the Cl ligand was better than that with the Br ligand. For R, out of Me, Et and iPr, the Me group resulted in the highest Au content. This automatically raises the question of whether (N,Me)AuCl or (N,Me)$AuCF_3$ will achieve even better purity. This work provides a guide for choices of ligands in future novel precursor molecules. It also provides a solution to heat up low volatility precursors using the reservoir on-substrate setup safely for a wide range of temperatures (tested up to 160°C). Most researched gold FEBID precursors suffer from low stability or low purity. The compounds presented here provide a stable solution with a relatively comparable and even better purity than some of the gold precursors in literature. Nonetheless, there is a need for further exploring potential FEBID precursors to achieve higher purity of the deposits.

In chapter 4, the first and second FEBID challenge were addressed, purification of the deposits and to enhance the growth rate. The possibility of locally cleaning a sample by EBIE using water vapor was investigated in a desktop SEM which allows much higher vapor pressures than regular SEM's. The setup was modified to let in water vapor in the chamber. Indeed, EBIE using water vapor can locally clean the exposed part of the sample. This provides a simple and easy solution for in situ purifying of FEBID deposits. In addition, the full FEBID instrumentation was developed to deposit Pt using a high $MeCpPtMe_3$ precursor flux in a desktop SEM. The growth rate was measured and found to increase with increasing precursor flux. However, the metal content of the deposit is lower than in a HV SEM due to the worse vacuum conditions in the desktop SEM, leading to increased carbon contamination. Thus, if the growth rate is a priority, desktop SEM is a great solution for faster deposition.

In chapter 5, a simple method (FDTM) for the fabrication of 3D shapes using FEBID is reported. FDTM was developed for the deposition of 3D shapes with closed walls, particularly hollow cones. FDTM is simple and aimed at

3D shape control and enhanced growth rate. Throughout the deposition of a shape all deposition parameters remain constant. In this chapter, a study of the parameters is presented. Two approaches were followed, one aimed at utilizing proximity effects to enhance the growth, using large separate building blocks, and the other aimed at achieving smooth walls and high resolution by having very small closely packed building blocks. The hollow cones were successfully built matching the design parameters. A cone of 2 μm height and 1 μm base diameter was built in about 2 minutes. It is important to define the priorities required for a certain shape and to adjust the beam parameters accordingly to use the FEBID process in the most efficient way. Most of 3D FEBID shapes in literature have been deposited using a 30 kV and 25 pA beam. However, increasing the beam current and decreasing the beam energy can enhance the growth and avoid thickening of previously deposited parts. Furthermore, the writing strategy makes a big difference especially in 3D shapes. Depositing the building blocks in multiple passes gives time for precursor replenishment. If the shape has several parts that are independently growing from the surface of the substrate, interlacing between the points at the same height is important to avoid collapsing of the shape. A π shift was applied in the starting position of each successive layer to reduce the irregularity at the top of the cone. This did not entirely eliminate it, but it confirmed the importance of the writing strategy. The π shift showed an improvement in the top irregularity compared to having no shift in experiment and in Monte Carlo simulation [146]. According to experiments, applying a random shift was worse than the π shift. However, the simulation showed an improvement with the random shift compared to the π shift. The simulation showed even better results with a π/4 shift. More research is required to further investigate the cause of these irregularities and to find the best possible deposition order to minimize them. To further optimize the 3D FEBID process and increase the accuracy, the instrumentation needs more attention. Drift is a limiting factor to the shape integrity of the deposit which could be improved by using an interferometrically controlled stage. Changing the gas supply from the gas injection systems could improve the efficiency of the deposition too. Having a more uniform gas supply around the deposition area could help to get rid of undesired shadow effects and achieve better shape control. FDTM was successfully used to build other shapes as well such, as boxes and cylinders. Another very promising result with FDTM was the deposition of small cones (smallest deposited cone was about 100 nm high). In this case, the drift doesn't impose a problem anymore, since they take only a few seconds to deposit (the 100 nm high cone took about 10 s). Furthermore, the top irregularity is hardly visible in such small cones.

The reason to choose the cone shape was to use it in the NAIS chip which is part of a novel ion source. Details of the fabrication of the chip are described in chapter 6. The application required a double cone structure, each cone being built on a different membrane with a spacing between the membranes. The procedure for building the double cones was presented. Some of the chips were tested in the ion source test setup and the cones were exposed to a 1

kV and 100 nA electron beam, with 3 kV ion extraction and approximately 1 bar of Argon gas supplied in between the membranes. After exposure for about 3 hours, the shape didn't collapse or break, but the inner cone got shorter and the top part of the outer one slightly changed. This might be the result of a continued dissociation of parent precursor molecules built in to the cones, leading to shape deformation. The resulting ion beam current was about 200 pA. Work is still in progress and a special microscope setup is being built where further tests and brightness measurements will be performed to assess the generated ion beam. Then, the sizes of the holes and cones can be optimized accordingly. However, the focus of this work was on building the double cone structure.

In chapter 7, a comparison between FDTM and two simulation guided fabrication tools (CAD 3BID and layer-by-layer approach) was presented. Cones were deposited using the three methods and compared. With all methods, the cone shape was realized, but the exact design dimensions were not achieved right away. For FDTM, as presented in chapter 5, there was some fine tuning of the parameters to reach the best result closest to the design. For both CAD 3BID and layer-by-layer approach, some input had to be provided to create the stream file which was based on our previous knowledge and studies presented in chapter 5. It is expected that after the calibrations, the simulation tools would result in a shape that matches the design, but it was not the case. The resulting shape deposited using the layer-by-layer approach was successful and close to the dimensions of the design. The cone produced by CAD 3BID had a very irregular top. CAD 3BID is optimized for mesh-like shapes that are based on a diving board structure and therefore is not very suitable for closed wall shapes. As explained earlier, FDTM focuses on simplicity and minimal change of parameters during the deposition of a shape. Thus, the dwell time and pitch are kept constant and the number of points per layer decreases when the diameter of the layer decreases. In other methods the number of points is kept constant while the dwell time for each point is adapted. This generates a lot of variation across the deposition points which can complicate the design. For building a simple closed wall shape, FDTM is the simplest method out of the three which generates a stream file without complicated simulation and with only small parameter variations the right dimensions were achieved. This does not make one choice better than the other, but the important message here is to choose the method that suits the desired shape and the priorities (for example growth rate, type of shape, resolution, simplicity, etc.). All three methods still require certain deposition tests within a range of parameters to find the set of parameters that results in the designed shape. The development of tools for 3D FEBID is very promising and facilitates building more complex shapes that were not possible to build before.

With all the existing challenges, FEBID remains a very promising technique for 2D and 3D nano-fabrication with its great flexibility, high resolution and the possibility to directly write structures in one step. Although the purity remains a big challenge, some applications actually made use of having gran-

ular metal in a carbonaceous matrix [11, 154] or used FEBID to make support structures with a deposited layer of the desired composition on top [27] or used FEBID to create sub-10 nm masks for NIL [19], to name a few. Furthermore, pure gold was deposited by FEBID while simultaneously injecting water vapor [61]. With the current FEBID technology, speed is still incomparable with resist-based lithography and thus FEBID remains mostly suited for local deposition of small shapes. With advancements in the field of multi-beam SEMs, the deposition speed achieved by FEBID will increase, but resolution might be sacrificed.

Acknowledgements

First of all, I would like to express my huge thanks to Kees, who gave me the opportunity to do this PHD project and to be part of not only the MINT group but also the ELENA network. With his long experience in FEBID, I have learnt so much, not only about my specific project, but about many different advancements in the field of FEBID. Thank you for your daily support and for your availability to answer my questions. I would like to thank Pieter as well for his help, advice and for all the valuable information in the charged particle optics course.

Special thanks to Niels Noordzij for introducing me to the field and art of 3D FEBID. Thank you for your help when I was starting. Your pioneering work in the field on 3D nano-fabrication is highly appreciated.

All my experimental work wouldn't have been possible without the help and support of Dustin. He was always there to help fix problems in the microscopes and was always patient and generous with his time. I learned a lot from his vast knowledge about all parts of the microscope. In addition to that, working together on the NAIS project was always fun and added a lot of perspective to my research. Big thanks to Mike as well for all the help throughout the NAIS project. I would like to thank all other technicians for taking care of many things such as chemicals and some fabrication steps. Thanks to Martin, Carel, Johan and Han.

My PHD was not only fully at the TU Delft, but thanks to ELENA, I had the chance to do part of my research in Phenom World (part of Thermofisher Scientific). It wouldn't have been possible without the help and guidance of Jeroen van de Water. Thank you for being patient and for all our trials until the success of our setup. Big thanks to Wouter for all the software support and help you have given me and more important, for the nice discussions and laughter. Even though, he was not fully working at Phenom world, Karel van der Mast has helped me a lot and made sure I had a fast and good start. Thanks to all the applications team for the help and fun times as well: Karl, Willem, Antonis, Luigi and Rogier.

This project wouldn't have been possible without the ELENA network. This network has provided me with multiple trainings, conferences, company visits, endless networking opportunities and more important, the great fellow students I met. Oddur, thank you so much for managing such a huge project with all the heavy loads of it. Cristiano, it was a pleasure working with you, I really enjoyed, I always saw your passion in research and in our project and this only motivated me more. Thank you for all the efforts in the synthesis of the gold precursors. Furthermore, I would like to thank Lisa McElwee-White and her group including Hang Lu for the synthesis of the platinum precursors

and for the great collaboration. Can't thank enough all the other students for the fun times at trainings, conferences and for the long-lasting friendships we made! Thank you Ali, Reza, Elif, Najmeh, Jakub, Ashish, Chris, Rene, Abid Ali, Po Yuan, Linh, Maria, Dominik and of course Maicol (despite not being actually part of ELENA but was heavily involved).

I would like to thank Jason Fowlkes, Amalio and Lucas for their help and support to guide me to be able to use their 3D FEBID simulation tools.

During my PHD, I got the chance to supervise two passionate and smart students, Sietse and Richard. I really enjoyed working with you. Thank you for your contributions and efforts, it was always fun to spend time in the lab together. I wish you all the success in your careers.

Of course, I can't thank enough my colleagues and the PIs in the MINT group. Ryan and Luc, my officemates, thank you for all the fun times, jokes and for going through this journey day by day together. Thank you Jakub for all your help and support in many ways. I will always remember the day you took us to the blueberry fields and we had the best fries in the Netherlands! Thanks Daan, Elizabeth and Ali. Thank you Ali for helping me a lot during moving to Eindhoven for my internship and it's great that we can still meet at TFS now! Vidya, Nicolo, Xin, Marco, Gaudham, Kerim, Zhenzhen, Qiangrui, Yoram, Arent, Mathijs, Maurice, Aditi, Wilco, Neda, Xiaoli, Linxin, Gerward, Sangeetha and Marijke, I really enjoyed working with you and all the fun activities we did outside of work. Neda thanks for being a great friend and landlord! Huma, thank you for all your love, care and support. It is really a pleasure to meet someone ambitious and hardworking like you, you always inspired me. Laura, I can't thank you enough, I gained not only a colleague but an amazing friend. We started at about the same date and we went through this journey all together. Thank you for your endless support and love and for all the time we spent together.

Of course, I would like to thank my friends out of MINT and ELENA as well. My dearest Wietske, thank you for always being there for me and for always understanding. Utrecht is a very special place to me because of the time we spent there. To more fries and appelsap (from glass bottle only!) together! Myrna, thank you for all the love, support, and motivation and for your lovely company, our long walks and all the fun things we did and will do together! Maimuna thank you for being supportive and for all the fun we had together in Delft and Eindhoven! My roommates in Delft, thank you all for the fun time and for your love and support. Veronica, Maria, Hong, Iolanda, Lorena, Marianna, Yamuna, Angeliki, Camila, Anna, Hamra and Philia thank you! I wouldn't have been able to go through this journey without the support of my lovely family. Thank you my mum and dad for all your love and support. I want to thank my sister Sohaila and my brother Abdulla for always being there for me as well. Huge thanks to Rana and Begad for designing my thesis cover!

Bibliography

[1] G. Moore, *Lithography and the future of Moore's law*, SPIE, **1995**.

[2] J. T. M. Stevenson, A. M. Gundlach, *Journal of Physics E: Scientific Instruments* **1986**, *19*, 654–667.

[3] A. J. M. Mackus, A. A. Bol, W. M. M. Kessels, *Nanoscale* **2014**, *6*, 10941–10960.

[4] D. Mailly, C. Vieu in *Nanoscience: Nanotechnologies and Nanophysics*, (Eds.: C. Dupas, P. Houdy, M. Lahmani), Springer Berlin Heidelberg, Berlin, Heidelberg, **2007**, pp. 3–40.

[5] C. Wagner, N. Harned, *Nature Photonics* **2010**, *4*, 24–26.

[6] S. Okazaki, *Microelectronic Engineering* **2015**, *133*, 23–35.

[7] T. Manouras, P. Argitis, *Nanomaterials* **2020**, *10*, 1593.

[8] N. Mojarad, J. Gobrecht, Y. Ekinci, *Scientific Reports* **2015**, *5*, 9235.

[9] C. Vieu, F. Carcenac, A. Pépin, Y. Chen, M. Mejias, A. Lebib, L. Manin-Ferlazzo, L. Couraud, H. Launois, *Applied Surface Science* **2000**, *164*, 111–117.

[10] H. Schift, *Journal of Vacuum Science & Technology B: Microelectronics and Nanometer Structures Processing Measurement and Phenomena* **2008**, *26*, 458–480.

[11] M. Huth, F. Porrati, C. Schwalb, M. Winhold, R. Sachser, M. Dukic, J. Adams, G. Fantner, *Beilstein Journal of Nanotechnology* **2012**, *3*, 597–619.

[12] I. Utke, P. Hoffmann, J. Melngailis, *Journal of Vacuum Science & Technology B: Microelectronics and Nanometer Structures Processing Measurement and Phenomena* **2008**, *26*, 1197–1276.

[13] W. F. van Dorp, C. W. Hagen, *Journal of Applied Physics* **2008**, *104*, 081301.

[14] W. F. van Dorp, C. W. Hagen, P. A. Crozier, B. van Someren, P. Kruit, *Microelectronic Engineering* **2006**, *83*, 1468–1470.

[15] R. Winkler, B. B. Lewis, J. D. Fowlkes, P. D. Rack, H. Plank, *ACS Applied Nano Materials* **2018**, *1*, 1014–1027.

[16] T. Bret, T. Hofmann, K. Edinger, *Industrial perspective on focused electron beam-induced processes, Vol. 117*, **2014**, pp. 1607–1614.

[17] I. Utke, B. Dwir, K. Leifer, F. Cicoira, P. Doppelt, P. Hoffmann, E. Kapon, *Microelectronic Engineering* **2000**, *53*, 261–264.

[18] J. A. Bieber, J. F. Pulecio, W. A. Moreno in 2008 7th International Caribbean Conference on Devices, Circuits and Systems, pp. 1–6.

[19] M. Scotuzzi, M. Kamerbeek, A. Goodyear, M. Cooke, C. Hagen, *Journal of Micro/Nanolithography MEMS and MOEMS* **2015**, *14*, 031206.

[20] M. Moczała, K. Kwoka, T. Piasecki, P. Kunicki, A. Sierakowski, T. Gotszalk, *Microelectronic Engineering* **2017**, *176*, 111–115.

[21] G. Arnold, R. Winkler, M. Stermitz, A. Orthacker, J.-H. Noh, J. D. Fowlkes, G. Kothleitner, M. Huth, P. D. Rack, H. Plank, *Advanced Functional Materials* **2018**, *28*, 1707387.

[22] M. Huth, F. Porrati, O. V. Dobrovolskiy, *Microelectronic Engineering* **2018**, *185-186*, 9–28.

[23] D. S. Widyaratih, P.-L. Hagedoorn, L. G. Otten, M. Ganjian, N. Tümer, I. Apachitei, C. W. Hagen, L. E. Fratila-Apachitei, A. A. Zadpoor, *Nanotechnology* **2019**, *30*, 20LT01.

[24] P. C. Post, A. Mohammadi-Gheidari, C. W. Hagen, P. Kruit, *Journal of Vacuum Science & Technology B* **2011**, *29*, 06F310.

[25] J. A. Spencer, S. Rosenberg, M. Barclay, Y. C. Wu, L. McElwee-White, H. Fairbrother, *Applied Physics A* **2014**, *117*, 1631–1644.

[26] J. J. L. Mulders, *Nanofabrication* **2014**, *1*, 74–79.

[27] D. Sanz-Hernández, R. F. Hamans, J. Osterrieth, J.-W. Liao, L. Skoric, J. D. Fowlkes, P. D. Rack, A. Lippert, S. F. Lee, R. Lavrijsen, A. Fernández-Pacheco, *Nanomaterials* **2018**, *8*, 483.

[28] R. Winkler, F. P. Schmidt, U. Haselmann, J. D. Fowlkes, B. B. Lewis, G. Kothleitner, P. D. Rack, H. Plank, *ACS Applied Materials & Interfaces* **2017**, *9*, 8233–8240.

[29] L. Skoric, D. Sanz-Hernández, F. Meng, C. Donnelly, S. Merino-Aceituno, A. Fernández-Pacheco, *Nano Letters* **2020**, *20*, 184–191.

[30] J. D. Fowlkes, R. Winkler, B. B. Lewis, A. Fernández-Pacheco, L. Skoric, D. Sanz-Hernández, M. G. Stanford, E. Mutunga, P. D. Rack, H. Plank, *ACS Applied Nano Materials* **2018**, *1*, 1028–1041.

[31] L. Keller, M. Huth, *Beilstein Journal of Nanotechnology* **2018**, *9*, 2581–2598.

[32] R. Winkler, J. D. Fowlkes, P. D. Rack, H. Plank, *Journal of Applied Physics* **2019**, *125*, 210901.

[33] C. W. Hagen, *Applied Physics A* **2014**, *117*, 1599–1605.

[34] S. J. Randolph, J. D. Fowlkes, P. D. Rack, *Critical Reviews in Solid State and Materials Sciences* **2006**, *31*, 55–89.

[35] H. Miyazoe, I. Utke, J. Michler, K. Terashima, *Applied Physics Letters* **2008**, *92*, 043124.

[36] I. Utke, S. Moshkalev, P. Russell, *Nanofabrication Using Focused Ion and Electron Beams : Principles and Applications*, Oxford University Press, Incorporated, Cary, UNITED STATES, **2012**.

[37] N. Silvis-Cividjian, C. W. Hagen in *Electron-Beam-Induced Nanometer-Scale Deposition*, Advances in Imaging and Electron Physics, Elsevier, **2006**, pp. 1–235.

[38] J. J. L. Mulders, L. M. Belova, A. Riazanova, *Nanotechnology* **2010**, *22*, 055302.

[39] O. Ingólfsson, *Low-Energy Electrons: Fundamentals and Applications*, 1st ed., Jenny Stanford Publishing, **2019**.

[40] J. J. L. Mulders, J. M. Veerhoek, E. G. T. Bosch, P. H. F. Trompenaars, *Journal of Physics D: Applied Physics* **2012**, *45*, 475301.

[41] I. Utke, P. Hoffmann, B. Dwir, K. Leifer, E. Kapon, P. Doppelt, *Journal of Vacuum Science & Technology B: Microelectronics and Nanometer Structures Processing Measurement and Phenomena* **2000**, *18*, 3168–3171.

[42] T. Brintlinger, M. S. Fuhrer, J. Melngailis, I. Utke, T. Bret, A. Perentes, P. Hoffmann, M. Abourida, P. Doppelt, *Journal of Vacuum Science & Technology B: Microelectronics and Nanometer Structures Processing Measurement and Phenomena* **2005**, *23*, 3174–3177.

[43] J. A. Spencer, S. G. Rosenberg, M. Barclay, Y.-C. Wu, L. McElwee-White, D. Howard Fairbrother, *Applied Physics A* **2014**, *117*, 1631–1644.

[44] F. Ferreira da Silva, R. M. Thorman, R. Bjornsson, H. Lu, L. McElwee-White, O. Ingólfsson, *Physical Chemistry Chemical Physics* **2020**, *22*, 6100–6108.

[45] R. Thorman, P. A. Jensen, J.-C. Yu, S. J. Matsuda, L. McElwee-White, O. Ingolfsson, D. H. Fairbrother, *The Journal of Physical Chemistry C* **2020**, *124*, 10593–10604.

[46] J. A. Spencer, J. A. Brannaka, M. Barclay, L. McElwee-White, D. H. Fairbrother, *The Journal of Physical Chemistry C* **2015**, *119*, 15349–15359.

[47] M. Cipriani, R. M. Thorman, C. R. Brewer, L. McElwee-White, O. Ingólfsson, *The European Physical Journal D* **2019**, *73*, 227.

[48] K. Wnorowski, M. Stano, C. Matias, S. Denifl, W. Barszczewska, Š. Matejčík, *Rapid Communications in Mass Spectrometry* **2012**, *26*, 2093–2098.

[49] S. G. Rosenberg, M. Barclay, D. H. Fairbrother, *The Journal of Physical Chemistry C* **2013**, *117*, 16053–16064.

[50] J. A. Spencer, M. Barclay, M. J. Gallagher, R. Winkler, I. Unlu, Y. C. Wu, H. Plank, L. McElwee-White, H. Fairbrother, *Beilstein Journal of Nanotechnology* **2017**, *8*, 2410–2424.

[51] J. A. Spencer, Y. C. Wu, L. McElwee-White, H. Fairbrother, *Journal of American Chemical Society* **2016**, *138*, 9172−9182.

[52] F. Bagnoli, D. B. D. Amico, F. Calderazzo, U. Englert, F. Marchetti, G. E. Herberich, N. Pasqualetti, S. Ramello, *Journal of the Chemical Society Dalton Transactions* **1996**, 4317–4318.

[53] F. Calderazzo, *Journal of Organometallic Chemistry* **1990**, *400*, 303–320.

[54] F. Bagnoli, D. Belli Dell'Amico, F. Calderazzo, U. Englert, F. Marchetti, A. Merigo, S. Ramello, *Journal of Organometallic Chemistry* **2001**, *622*, 180–189.

[55] M. Faust, M. Enders, M. Bruns, S. Bräse, K. Gao, M. Seipenbusch, *Surface and Coatings Technology* **2013**, *230*, 19th European Conference on Chemical Vapor Deposition (EuroCVD19), Varna, Bulgaria, 1st - 6th September 2013, 284–289.

[56] J. D. Fowlkes, P. D. Rack, *ACS Nano* **2010**, *4*, 1619–1629.

[57] S. Mehendale, J. J. L. Mulders, P. H. F. Trompenaars, *Nanotechnology* **2013**, *24*, 145303.

[58] J. L. Campbell, J. A. Maxwell, T. Papp, G. White, *X-Ray Spectrometry* **1997**, *26*, 223–231.

[59] Z. Warneke, M. Rohdenburg, J. Warneke, J. Kopyra, P. Swiderek, *Beilstein Journal of Nanotechnology* **2018**, *9*, 77–90.

[60] B. Geier, C. Gspan, R. Winkler, R. Schmied, J. D. Fowlkes, H. Fitzek, S. Rauch, J. Rattenberger, P. D. Rack, H. Plank, *The Journal of Physical Chemistry C* **2014**, *118*, 14009–14016.

[61] M. M. Shawrav, P. Taus, H. D. Wanzenboeck, M. Schinnerl, M. Stöger-Pollach, S. Schwarz, A. Steiger-Thirsfeld, E. Bertagnolli, *Scientific Reports* **2016**, *6*, 34003.

[62] M. Rohdenburg, H. Boeckers, C. R. Brewer, L. McElwee-White, P. Swiderek, *Scientific Reports* **2020**, *10*, 10901.

[63] F. Schmidt, P. Swiderek, J. H. Bredehöft, *ACS Earth and Space Chemistry* **2019**, *3*, 1974–1986.

[64] A. Fernández-Pacheco, L. Serrano-Ramón, J. M. Michalik, M. R. Ibarra, J. M. De Teresa, L. O'Brien, D. Petit, J. Lee, R. P. Cowburn, *Scientific Reports* **2013**, *3*, 1492.

[65] J. H. Noh, M. G. Stanford, B. B. Lewis, J. D. Fowlkes, H. Plank, P. D. Rack, *Applied Physics A* **2014**, *117*, 1705–1713.

[66] J. Brown, P. Kocher, C. S. Ramanujan, D. N. Sharp, K. Torimitsu, J. F. Ryan, *Ultramicroscopy* **2013**, *133*, 62–66.

[67] B. J. Rodriguez, S. Jesse, K. Seal, A. P. Baddorf, S. V. Kalinin, P. D. Rack, *Applied Physics Letters* **2007**, *91*, 093130.

[68] I. Utke, P. Hoffmann, R. Berger, L. Scandella, *Applied Physics Letters* **2002**, *80*, 4792–4794.

[69] K. Höflich, J. M. Jurczyk, K. Madajska, M. Götz, L. Berger, C. Guerra-Nuñez, C. Haverkamp, I. Szymanska, I. Utke, *Beilstein journal of nanotechnology* **2018**, *9*, 842–849.

[70] N. Liu, M. L. Tang, M. Hentschel, H. Giessen, A. P. Alivisatos, *Nature Materials* **2011**, *10*, 631.

[71] S. Graells, S. Aćimović, G. Volpe, R. Quidant, *Plasmonics* **2010**, *5*, 135–139.

[72] J. M. De Teresa, A. Fernández-Pacheco, *Applied Physics A* **2014**, *117*, 1645–1658.

[73] L. Keller, M. K. I. Al Mamoori, J. Pieper, C. Gspan, I. Stockem, C. Schröder, S. Barth, R. Winkler, H. Plank, M. Pohlit, J. Müller, M. Huth, *Scientific Reports* **2018**, *8*, 6160.

[74] D. S. Widyaratih, P.-L. Hagedoorn, L. G. Otten, M. Ganjian, N. Tümer, I. Apachitei, C. W. Hagen, L. E. Fratila-Apachitei, A. A. Zadpoor, *Nanotechnology* **2019**, *30*, 20LT01.

[75] W. G. Carden, H. Lu, J. A. Spencer, D. H. Fairbrother, L. McElwee-White, *MRS Communications* **2018**, *8*, 343–357.

[76] S. Barth, M. Huth, F. Jungwirth, *Journal of Materials Chemistry C* **2020**, *8*, 15884–15919.

[77] A. Folch, J. Servat, J. Esteve, J. Tejada, M. Seco, *Journal of Vacuum Science & Technology B: Microelectronics and Nanometer Structures Processing Measurement and Phenomena* **1996**, *14*, 2609–2614.

[78] M. G. Jenke, D. Lerose, C. Niederberger, J. Michler, S. Christiansen, I. Utke, *Nano Letters* **2011**, *11*, 4213–4217.

[79] M. V. Puydinger dos Santos, A. Szkudlarek, A. Rydosz, C. Guerra-Nuñez, F. Béron, K. R. Pirota, S. Moshkalev, J. A. Diniz, I. Utke, *Beilstein Journal of Nanotechnology* **2018**, *9*, 91–101.

[80] H. W. P. Koops, J. Kretz, M. Rudolph, M. Weber, G. Dahm, K. L. Lee, *Japanese Journal of Applied Physics* **1994**, *33*, 7099–7107.

[81] I. Utke, M. G. Jenke, C. Röling, P. H. Thiesen, V. Iakovlev, A. Sirbu, A. Mereuta, A. Caliman, E. Kapon, *Nanoscale* **2011**, *3*, 2718–2722.

[82] D. Belić, M. M. Shawrav, E. Bertagnolli, H. D. Wanzenboeck, *Beilstein journal of nanotechnology* **2017**, *8*, 2530–2543.

[83] P. Hoffmann, I. Utke, F. Cicoira, B. Dwir, K. Leifer, E. Kapon, P. Doppelt, *MRS Proceedings* **2000**, *624*, 171.

[84] W. F. van Dorp, X. Wu, J. J. L. Mulders, S. Harder, P. Rudolf, J. T. M. De Hosson, *Langmuir* **2014**, *30*, 12097–12105.

[85] A. Marashdeh, T. Tiesma, N. J. C. van Velzen, S. Harder, R. W. A. Havenith, J. T. M. De Hosson, W. F. van Dorp, *Beilstein journal of nanotechnology* **2017**, *8*, 2753–2765.

[86] W. G. Carden, R. M. Thorman, I. Unlu, K. A. Abboud, D. H. Fairbrother, L. McElwee-White, *ACS Applied Materials & Interfaces* **2019**, *11*, 11976–11987.

[87] M.-C. Brandys, M. C. Jennings, R. J. Puddephatt, *Journal of the Chemical Society Dalton Transactions* **2000**, 4601–4606.

[88] F. O. Elnajjar, J. F. Binder, S. C. Kosnik, C. L. B. Macdonald, *Zeitschrift für anorganische und allgemeine Chemie* **2016**, *642*, 1251–1258.

[89] V. Levchenko, C. Glessi, S. Øien-Ødegaard, M. Tilset, *Dalton Transactions* **2020**, *49*, 3473–3479.

[90] G. Jeevanandam, V. van der Meijden, L. D. Birnie, P. Kruit, C. W. Hagen, *Microelectronic Engineering* **2020**, *224*, 111239.

[91] L. Berger, K. Madajska, I. B. Szymanska, K. Höflich, M. N. Polyakov, J. Jurczyk, C. Guerra-Nuñez, I. Utke, *Beilstein Journal of Nanotechnology* **2018**, *9*, 224–232.

[92] W. G. Carden, J. Pedziwiatr, K. A. Abboud, L. McElwee-White, *ACS Applied Materials & Interfaces* **2017**, *9*, 40998–41005.

[93] N. Marion, S. P. Nolan, *Chemical Society Reviews* **2008**, *37*, 1776–1782.

[94] M. Porchia, M. Pellei, M. Marinelli, F. Tisato, F. Del Bello, C. Santini, *European Journal of Medicinal Chemistry* **2018**, *146*, 709–746.

[95] J.-F. Longevial, A. Langlois, A. Buisson, C. H. Devillers, S. Clément, A. van der Lee, P. D. Harvey, S. Richeter, *Organometallics* **2016**, *35*, 663–672.

[96] D. Marchione, L. Belpassi, G. Bistoni, A. Macchioni, F. Tarantelli, D. Zuccaccia, *Organometallics* **2014**, *33*, 4200–4208.

[97] M. N. Hopkinson, C. Richter, M. Schedler, F. Glorius, *Nature* **2014**, *510*, 485–496.

[98] A. Mahgoub, H. Lu, R. M. Thorman, K. Preradovic, T. Jurca, L. McElwee-White, H. Fairbrother, C. W. Hagen, *Beilstein Journal of Nanotechnology* **2020**, *11*, 1789–1800.

[99] A. Solovyev, S.-H. Ueng, J. Monot, L. Fensterbank, M. Malacria, E. Lacôte, D. P. Curran, *Organic Letters* **2010**, *12*, 2998–3001.

[100] P. de Frémont, R. Singh, E. D. Stevens, J. L. Petersen, S. P. Nolan, *Organometallics* **2007**, *26*, 1376–1385.

[101] M. V. Baker, P. J. Barnard, S. K. Brayshaw, J. L. Hickey, B. W. Skelton, A. H. White, *Dalton Transactions* **2005**, 37–43.

[102] M. Blaya, D. Bautista, J. Gil-Rubio, J. Vicente, *Organometallics* **2014**, *33*, 6358–6368.

[103] B. Pinter, L. Broeckaert, J. Turek, A. Růžička, F. De Proft, *Chemistry – A European Journal* **2014**, *20*, 734–744.

[104] M. Toth, C. Lobo, V. Friedli, A. Szkudlarek, I. Utke, *Beilstein journal of nanotechnology* **2015**, *6*, 1518–1540.

[105] J. I. Goldstein, D. E. Newbury, J. R. Michael, N. W. M. Ritchie, J. H. J. Scott, D. C. Joy in *Scanning Electron Microscopy and X-Ray Microanalysis*, Springer New York, New York, NY, **2018**, pp. 173–185.

[106] D. Stokes, *Principles and Practice of Variable Pressure / Environmental Scanning Electron Microscopy (VP-ESEM) : Environmental Scanning Electron Microscopy (VP-ESEM)*, John Wiley & Sons, Incorporated, New York, UNITED KINGDOM, **2008**.

[107] A. A. Martin, M. Toth, I. Aharonovich, *Scientific Reports* **2014**, *4*, 5022.

[108] A. A. Martin, M. R. Phillips, M. Toth, *ACS Applied Materials & Interfaces* **2013**, *5*, 8002–8007.

[109] J. Bishop, Thesis, University of Technology Sydney, **2018**, pp. 49–71.

[110] M. Toth, C. J. Lobo, G. Hartigan, W. R. Knowles, *JOURNAL OF APPLIED PHYSICS* **2007**, *101*, 054309.

[111] M. Toth, *Applied Physics A* **2014**, *117*, 1623–1629.

[112] A. A. Martin, G. McCredie, M. Toth, *Applied Physics Letters* **2015**, *107*, 041603.

[113] M. Toth, C. J. Lobo, W. R. Knowles, M. R. Phillips, M. T. Postek, A. E. Vlada, *Nano Letters* **2007**, *7*, 525–530.

[114] S. Hari, Thesis, Delft University of Technology, Netherlands, **2017**.

[115] M. Toth, C. J. Lobo, M. J. Lysaght, A. E. Vladár, M. T. Postek, *Journal of Applied Physics* **2009**, *106*, 034306.

[116] B. Thiel in *Springer Handbook of Microscopy*, (Eds.: P. W. Hawkes, J. C. H. Spence), Springer International Publishing, Cham, **2019**, pp. 319–344.

[117] S. V. Zaitsev, S. Y. Kupreenko, E. I. Rau, A. A. Tatarintsev, *Instruments and Experimental Techniques* **2015**, *58*, 757–764.

[118] N. Erdman, D. C. Bell, R. Reichelt in *Springer Handbook of Microscopy*, (Eds.: P. W. Hawkes, J. C. H. Spence), Springer International Publishing, Cham, **2019**, pp. 229–318.

[119] Thermo Fisher Scientific Phenom-World BV, Topographic and Compositional Analysis in SEM with Backscattered Electron Imaging, **2014**.

[120] A. Ul-Hamid, *A Beginners' Guide to Scanning Electron Microscopy*, Springer International Publishing, **2018**, pp. 15–128.

[121] Thermo Fisher Scientific, Phenom XL G2 Desktop SEM, DS0328, **2020**.

[122] V. Friedli, I. Utke, *Journal of Physics D: Applied Physics* **2009**, *42*, 125305.

[123] N. Sharma, PhD thesis, Eindhoven university of technology, **2017**.

[124] F. Niessen, M. J. B. Nancarrow, *Nanotechnology* **2019**, *30*, 435301.

[125] L. v. Kouwen, P. Kruit, *Journal of Vacuum Science & Technology B* **2018**, *36*, 06J901.

[126] L. van kouwen, Thesis, TU Delft, **2017**.

[127] D. S. Jun, V. G. Kutchoukov, C. T. H. Heerkens, P. Kruit, *Microelectronic Engineering* **2012**, *97*, 134–137.

[128] V. Tondare, Thesis, TU Delft, **2006**.

[129] D. S. Jun, Thesis, TU Delft, **2014**.

[130] I. Utke, V. Friedli, M. Purrucker, J. Michler, *Journal of Vacuum Science & Technology B: Microelectronics and Nanometer Structures Processing Measurement and Phenomena* **2007**, *25*, 2219–2223.

[131] A. Szkudlarek, W. Szmyt, C. Kapusta, I. Utke, *Applied Physics A* **2014**, *117*, 1715–1726.

[132] R. M. Thorman, R. Kumar T. P, D. H. Fairbrother, O. Ingólfsson, *Beilstein Journal of Nanotechnology* **2015**, *6*, 1904–1926.

[133] W. F. van Dorp, J. D. Wnuk, J. M. Gorham, D. H. Fairbrother, T. E. Madey, C. W. Hagen, *Journal of Applied Physics* **2009**, *106*, 074903.

[134] D. A. Smith, J. D. Fowlkes, P. D. Rack, *Small* **2008**, *4*, 1382–1389.

[135] D. A. Smith, J. D. Fowlkes, P. D. Rack, *Nanotechnology* **2007**, *18*, 265308.

[136] D. A. Smith, J. D. Fowlkes, P. D. Rack, *Nanotechnology* **2008**, *19*, 415704.

[137] J. I. Goldstein, D. E. Newbury, J. R. Michael, N. W.M. Ritchie, J. Henry J. Scott, D. C. Joy, *Scanning Electron Microscopy and X-Ray Microanalysis*, Springer New York, NY, **2018**.

[138] A. Botman, D. A. M. de Winter, J. J. L. Mulders, *Journal of Vacuum Science & Technology B: Microelectronics and Nanometer Structures Processing Measurement and Phenomena* **2008**, *26*, 2460–2463.

[139] R. Schmied, J. D. Fowlkes, R. Winkler, P. D. Rack, H. Plank, *Beilstein Journal of Nanotechnology* **2015**, *6*, 462–471.

[140] W. F. van Dorp, S. Lazar, C. W. Hagen, P. Kruit, *Journal of Vacuum Science & Technology B: Microelectronics and Nanometer Structures Processing Measurement and Phenomena* **2007**, *25*, 1603–1608.

[141] D. J. Burbridge, S. N. Gordeev, *Nanotechnology* **2009**, *20*, 285308.

[142] J. D. Fowlkes, R. Winkler, B. B. Lewis, M. G. Stanford, H. Plank, P. D. Rack, *ACS Nano* **2016**, *10*, 6163−6172.

[143] E. Mutunga, R. Winkler, J. Sattelkow, P. D. Rack, H. Plank, J. D. Fowlkes, *ACS Nano* **2019**, *13*, 5198–5213.

[144] I. Utke, V. Friedli, J. Michler, T. Bret, X. Multone, P. Hoffmann, *Applied Physics Letters* **2006**, *88*, 031906.

[145] H. Plank, D. A. Smith, T. Haber, P. D. Rack, F. Hofer, *ACS Nano* **2012**, *6*, 286–294.

[146] R. de Jong, Master Thesis, TU Delft, **2021**.

[147] L. van Kessel, C. W. Hagen, *SoftwareX* **2020**, *12*, 100605.

[148] J. Dingemanse, Bachelor Thesis, TU Delft, **2020**.

[149] L. van Kouwen, P. Kruit, *Journal of Vacuum Science & Technology B* **2018**, *36*, 06J901.

[150] Pieter Kruit, Vipin Nagnath Tondare (Fei Company, Hillsboro), *patent*, US 7772564 B2, **2010**.

[151] Thermofisher Scientific, *Nanobuilder*, **2018**.

[152] A. Weitzer, M. Huth, G. Kothleitner, H. Plank, *ACS Applied Electronic Materials* **2022**, *4*, 744–754.

[153] L. Skoric, FEBID 3D Algorithm for Stream File generation (F3AST), **2022**, `https://github.com/Skoricius/f3ast` (visited on 22/11/2022).

[154] F. Porrati, R. Sachser, C. H. Schwalb, A. S. Frangakis, M. Huth, *Journal of Applied Physics* **2011**, *109*, 063715.

Curriculum Vitæ

Aya Mahgoub

17-01-1993 Born in Cairo, Egypt.

Education

2009–2014 Bachelor in Electronics and communication engineering
The American University in Cairo
Cairo, Egypt
Thesis: Stolen car detector
Promotor: dr. Karim Seddik

2014–2017 Master in Electrical Engineering
Eidgenössische Technische Hochschule Zürich
Zürich, Switzerland
Thesis: Design and Fabrication of High Efficiency Blazed Grating Couplers
Promotor: Prof. dr. Juerg Leuthold

2017–2021 PHD in Applied Physics
Delft University of Technology
Delft, Netherlands

Work Experience

2022–present Operations Engineer
Thermo Fisher Scientific
Eindhoven, Netherlands

List of Publications

1) Mahgoub, Aya ; Lu, Hang ; Thorman, Rachel M. ; Preradovic, Konstantin ; Jurca, Titel ; McElwee-White, Lisa ; Fairbrother, Howard ; Hagen, Cornelis W. *Electron beam-induced deposition of platinum from $PtCl_2(CO)_2$ and $PtBr_2(CO)_2$. Beilstein Journal of Nanotechnology.* **11, 1789-1800** (2020)

2) Glessi, Cristiano ; Mahgoub, Aya ; Hagen, Cornelis W. ; Tilset, Mats.*Gold(I) N-heterocyclic carbene precursors for focused electron beam-induced deposition. Beilstein Journal of Nanotechnology.* **12, 257–269** (2021)